Raul Gonzalez Lima

Tecnologia de Tomografia por Impedância Elétrica para Monitorar o Pulmão

Texto apresentado à Escola Politécnica da Universidade de São Paulo como requisito para obtenção do Título de Professor Livre Docente, junto ao Departamento de Engenharia Mecânica.

São Paulo
2009

Raul Gonzalez Lima

Tecnologia de Tomografia por Impedância Elétrica para Monitorar o Pulmão

Texto apresentado à Escola Politécnica da Universidade de São Paulo como requisito para obtenção do Título de Professor Livre Docente, junto ao Departamento de Engenharia Mecânica.

Área de concentração: Engenharia Mecânica
Especialidade: Biomecânica

São Paulo
2009

Ficha Catalográfica

Lima, Raul Gonzalez
Tecnologia de Tomografia por Impedância Elétrica para Monitorar o Pulmão. São Paulo, 2009. xiii p.

Tese (Livre Docência) — Escola Politécnica da Universidade de São Paulo. Departamento de Engenharia Mecânica.

1. Pulmão. 2. Tomografia por Impedância Elétrica. I. Universidade de São Paulo. Escola Politécnica. Departamento de Engenharia Mecânica. II. Título.

UNIVERSIDADE DE SÃO PAULO

CJ.P.0271/10
MWBS/ecdi

Autos n.º 87.1.32597.1.9
Interessado: RAUL GONZALEZ LIMA
Assunto: Contrato docente

Tema: Concurso para a obtenção do título de livre-docente — Inexistência de irregularidades procedimentais que obstem à outorga do título

PARECER

Examinados os autos n.º 2009.1.1773.3.8 de "concurso de livre-docente", e os autos de n.º 87.1.32597.1.9, em particular as informações de fls. 282 verso, conclui-se que o procedimento de concurso não apresenta irregularidades que obstem se ratifique a homologação do relatório final da comissão julgadora e se acolha a proposta de outorga do título.

Encaminhem-se os autos ao Gabinete do Magnífico Reitor.

Consultoria Jurídica, 29 de janeiro de 2010

MÁRCIA WALQUIRIA BATISTA DOS SANTOS
Procuradora Chefe

À Liani e Raquel

Agradecimentos

Meu caloroso agradecimento aos colaboradores que compartilharam este desenvolvimento, Agenor de Toledo Fleury, Claudia Natalia Lara Herrera, Daniel Aruca Miranda, Erick León, Fernando de Silva Moura, Flávio Celso Trigo, Harki Tanaka, Iara Kazue Ike, Joyce Bevilacqua, Julio Cesar Ceballos Aya, Marcelo Britto Passos Amato, Miguel Fernando Montoya, Nelson Molina Vanegas, Olavo Luppi, Pedro Bertemes, Stephan Bohm e Thaís Samed.

Agradeço ainda o apoio financeiro proveniente da Fapesp, do CNPq, da Capes e da FINEP que foram inestimáveis e espero ter bem utilizado estes recursos públicos.

Resumo

Este texto é uma sistematização crítica da linha de pesquisa que foi iniciada há dez anos por sugestão do Prof. Dr. Marcelo Britto Passos Amato do Departamento de Pneumologia da Faculdade de Medicina da USP. Estratégias protetivas do pulmão de pacientes submetidos a ventilação artificial requeriam o ajuste da pressão positiva no final da expiração (PEEP) em uma faixa estreita. Estas estratégias deveriam recrutar o maior número possível de alvéolos e, portanto, o ventilador deveria impor uma pressão elevada, mas não deveriam traumatizar os alvéolos por excesso de pressão, causando barotrauma. Requeria-se um equipamento que permitisse detectar a presença de tecido pulmonar colapsado, condição conhecida como atelectasia, e tecido pulmonar sobre-estendido. A Tomografia por Impedância Elétrica (TIE) gera um gráfico da distribuição da impeditividade de um domínio. Era uma técnica promissora na década de noventa, uma vez que o tecido pulmonar colapsado e o tecido pulmonar sobre-estendido possuem impeditividade consideravelmente distinta. Deu-se início a um projeto de pesquisa para tornar a TIE utilizável na beira de leito, o que tornaria viável a monitoração de ventilação e possibilitaria estimar a perfusão no tecido pulmonar. Este projeto caracterizou-se, desde o início, por uma *competição de métodos* de solução de problemas inversos. Implementaram-se inicialmente algoritmos clássicos de comunidades científicas diversas, como, por exemplo, observadores de estado e a retroprojeção. A incorporação de idéias efetivas de cada algoritmo clássico permitiu desenvolver algoritmos com características originais. Nestes dez anos a tecnologia evoluiu do estágio em que imagens de variações de resistividade eram de baixa resolução e pouco valiosas em aplicações médicas para o estágio em que as imagens de variações de resistividade são úteis em aplicações de pneumologia, mesmo no ambiente de Unidades de Terapia Intensiva. O texto descreve de forma sucinta a trajetória desta linha de pesquisa e serve de roteiro para o detalhamento do desenvolvimento, que pode ser acompanhado através das publicações nos anexos. Este trabalho faz parte dos requisitos do concurso de livre docência na Escola Politécnica da Universidade de São Paulo, Departamento de Engenharia Mecânica.

palavras-chave: Tomografia por Impedância Elétrica, Pulmão, Problema Inverso, Estimação de parâmetros.

Abstract

The present text describes the research line entitled *Algorithms for Electrical Impedance Tomography (EIT) for lung monitoring*, which begun ten years ago following a suggestion placed by Prof. Dr. Marcelo Britto Passos Amato from the Pneumology Department of the School of Medicine of The University of São Paulo. Protective maneuvers of the lungs of patients under artificial ventilation required fine adjustments of the Positive End-Expiration Pressure (PEEP). Using protective maneuvers a large number of alveoli should be kept open and the artificial ventilator should work with high pressures, but, on the other hand, it should not cause trauma to the overinflated alveoli, sometimes called barotrauma. An equipment able to detect collapsed lung tissue, a condition called atelectasis, was requested. The Electrical Impedance Tomography generates a graph of impeditivity distribution of a domain. It was a promising technology at the 90's, since the collapsed lung tissue and the over-inflated lung tissue have considerably distinct impeditivity. An investigation was initiated to make the EIT technology effective as a lung monitoring tool at bedside, estimating ventilation and perfusion in the lungs. The investigation was characterized since the beginning by a *competition of methods* for solving inverse problems. Classical methods from diverse scientific communities were implemented, like state observers and the back-projection algorithm. Blending effective features of the algorithms allowed the development of novel algorithms. During the last ten years the technology evolved from low resolution images with few medical applications to become effective tools in Intensive Care Units. The text describes in broad lines the trajectory of the investigation and the details may be followed through the publications in the appendices. This work is part of the prerequisites for the public contest to become *Livre-docente* at the Mechanical Engineering Department of The Escola Politécnica of The University of São Paulo.

keywords: Electrical Impedance Tomography, Lungs, Inverse Problems, Parameter Estimation.

Sumário

Lista de Abreviaturas

2D Duas dimensões

3D Três dimensões

ACT *Adaptive Tomograph*

APT Applied Potential Tomograph

FDA *Food and Drug Administration*

FEK *Filtro Estendido de Kalman*

MCMC *Monte Carlo com Cadeias de Markov*

NIC Negative impedance converter

PEEP *Positive end expiration pressure*

PL *Programação Linear*

SA Simulated Annealing

SPECT *Single photon emission computed tomography*

TIE *Tomografia por Impedância Elétrica*

UKF Unscented Kalman Filter

UTI Unidade de Terapia Intensiva

1 Introdução

A Tomografia por Impedância Elétrica (TIE) gera imagens que são gráficos de distribuição estimada de resistividade e/ou permitividade de um domínio físico. Utiliza correntes elétricas para excitar o sistema e mede potenciais elétricos no contorno do domínio. Considera-se conhecida a geometria do domínio e a estrutura de um modelo do domínio. Procura-se a distribuição de resistividade e/ou permitividade.

Neste trabalho utilizaremos a TIE para estimar apenas a distribuição de resistividade e o termo *imagem* será utilizado como sinônimo de distribuição de resistividade estimada. O problema de estimar a imagem de TIE será abordado através de diferentes pontos de vista: ora será encarado como a solução de um problema de *estimação de parâmetros*, ora será encarado como um problema de *observação de estados* de um sistema dinâmico e às vezes será encarado como um *problema inverso*. Desta forma podemos utilizar resultados da Teoria de Estimação de Parâmetros, da Teoria de Controle e da solução de Problemas Inversos.

A seguir, nesta introdução, descreve-se o contexto em que esta linha de pesquisa foi originada, do ponto de vista da Pneumologia, do ponto de vista da Eletrônica e do ponto de vista dos algoritmos. Nos capítulos subsequentes serão descritos os desafios e os avanços na ótica de cada classe de algoritmo e na ótica de algumas aplicações médicas, por exemplo, a detecção de pneumotórax, a detecção de atelectasia e a estimação de perfusão local no pulmão. O termo atelectasia refere-se ao fechamento de alvéolos e tem importância clínica em função de complicações associadas a esse fechamento.

Os algoritmos de TIE podem ser distinguidos pela sua capacidade de gerar *imagens de diferença* ou por gerar *imagens absolutas*. Imagens de diferença nada mais são que a gráficos de variação de distribuição de resistividade que tomam um instante de tempo como referência; as imagens absolutas são gráficos de distribuição de resistividade.

Se acaso for utilizada informação instantânea, caracterizada por medidas de

potencial elétrico simultâneas, o algoritmo é dito *estático*. Se for utilizada informação de vários instantes, levando em consideração algum modelo de variação temporal, o algoritmo é dito *dinâmico*.

Neste texto, quando uma referência estiver em anexo, haverá uma mensagem na lateral da página indicando sua localização nos apêndices. O leitor poderá encontrar nestas referências os detalhes dos trabalhos e argumentação mais completa.

1.1 Contexto na Pneumologia

Na pneumologia iniciava-se o uso de estratégias protetivas do pulmão. Em casos de atelectasia massiva do tecido pulmonar, procurava-se *recrutar* (abrir) o maior número possível de alvéolos e mantê-los abertos. Era necessário elevar a pressão no final da expiração (PEEP) para que os alvéolos não tornassem a se fechar. Simultaneamente, para manter a mesma taxa de absorção de oxigênio, elevava-se a frequência do ciclo de ventilação artificial. Devido ao uso de pressões elevadas, corria-se o risco de causar algum trauma ao tecido pulmonar, inclusive iniciar um pneumotórax. Mesmo sem ter equipamento adequado para ajustar os parâmetros do ventilador artificial, foi possível mostrar que o índice de mortalidade era reduzido em 47% quando esta estratégia protetiva era utilizada (AMATO et al., 1998).

A manobra de recrutar alvéolos requeria PEEP diferente para diferentes pacientes e mesmo para um mesmo paciente em momentos distintos. O ideal seria que houvesse um equipamento de beira de leito que permitisse identificar regiões do tecido pulmonar que estivessem fechadas ou sobre-estendidas, o que permitiria um ajuste do ventilador artificial para cada paciente e para cada instante.

A tomografia por raio-X não era adequada por utilizar radiações ionizantes e por requerer salas especiais revestidas por chumbo, distantes dos leitos de Unidades de Terapia Intensiva. O traslado de pacientes de uma UTI para a sala de Tomografia por raio-X envolvia riscos e a retirada de alguns equipamentos de auxílio à vida. As imagens de ultrassom não permitiam distinguir o tecido pulmonar sobre-estendido do tecido em condições normais. Entretanto, a tomografia por impedância elétrica, apesar de sua baixa resolução espacial, apresentava elevada sensibilidade a variações do conteúdo de ar no tecido pulmonar (RAPP et al., 1993; NOPP et al., 1997).

1.2 Contexto na Eletrônica

O primeiro tomógrafo de TIE de pesquisa foi desenvolvido na Universidade de Sheffield por Barber e Brown (BARBER; BROWN, 1984). O equipamento possuía 16 eletrodos, uma placa de aquisição de dados, uma fonte de corrente alternada e um microcomputador para a reconstrução da imagem. As medidas de potenciais elétricos eram realizadas de forma diferencial. Mais especificamente, o aparelho media a diferença de potencial entre eletrodos adjacentes, evitando assim problemas decorrentes da variabilidade do potencial elétrico de referência, que flutua em função da atividade dos profissionais de saúde e de interferência eletromagnética. A principal característica deste aparelho era a tecnologia de blindagem contra interferências eletromagnéticas, utilizavam-se duas malhas de blindagem. A primeira malha era ativa e tratava de anular a capacitância do cabo; a segunda blindagem era mais externa e estava ligada ao potencial de referência. A relação sinal ruído era de 60 dB. Havia uma única fonte de corrente. A corrente devia ser imposta a cada eletrodo através de um de-multiplexador (BARBER; BROWN, 1984).

Posteriormente, no Rensselaer Polytechnic Institute (RPI) foi desenvolvido um aparelho com outra característica: as medidas eram tomadas em relação a uma referência comum, eram medidas ditas *single-ended*. O tomógrafo contava com 32 eletrodos e 32 fontes de corrente. Os cabos ligados aos eletrodos eram também duplamente blindados, a blindagem mais interna era ativa e a blindagem externa era passiva, ligada ao potencial de referência. Para minimizar a capacitância das fontes de corrente utilizava-se um *Negative Impedance Converter* (NIC) (COOK et al., 1994). O procedimento de calibração deste aparelho era demorado, tornando-o inviável como aparelho de beira de leito.

Ambos equipamentos dependiam de conversores de sinal analógico para digital e da compensação da capacitância dos cabos elétricos que ligavam fontes de corrente aos eletrodos e dos eletrodos aos conversores de sinal analógico para digital. A precisão era caracterizada pela relação sinal/ruído, que era de 60 dB. A baixa acurácia das medidas era compensada através de normalizações das medidas (ADLER; GUARDO, 1996).

1.3 Contexto na Estimação de Parâmetros

As aplicações da TIE na Medicina eram incipientes e restritas ao ambiente de pesquisa. Inicialmente, o único algoritmo empregado em pesquisas médicas era o

Back-projection (SANTOSA; VOGELIUS, 1990). Apesar de inúmeras tentativas de incluir informação *a priori* no *Backprojection*, os algoritmos baseados no Método dos Elementos Finitos eram uma plataforma mais favorável à inclusão de informação *a priori*. A geometria do domínio é variável de indivíduo para indivíduo, o mapa que relaciona potencial elétrico com resistividade é não linear e a variação de resistividade é elevada para ser estimada por um estimador linearizado, como ocorre com o *Backprojection*. Por fim, não foi desenvolvida uma generalização do *Back-projection* para domínios em 3D (METHERALL, 1998). A utilização de domínios 2D para representar um fenômeno 3D provocava significativas distorções na localização dos objetos da imagem (BORSIC et al., 2001).

Duas técnicas de discretização da equação de Laplace generalizada pareciam promissoras pela facilidade de inclusão de informação *a priori*: o Método dos Elementos Finitos (MEF) e o Método das Diferenças Finitas. A informação *a priori* pode ser de origem geométrica, pode ser a respeito da faixa de variação de resistividade que ocorrem em organismos vivos e pode ser a respeito de variações espaciais da resistividade que ocorrem em cada órgão (YORKEY; WEBSTER; TOMPKINS, 1987; ADLER; GUARDO, 1996). Os trabalhos que utilizaram o Método dos Elementos Finitos geravam artefatos, inclusive pelo uso de malhas de elementos finitos inadequadas.

1.4 Dificuldades para tornar a TIE efetiva na monitoração dos pulmões

No início desta pesquisa haviam dificuldades que impediam a efetiva utilização da TIE para monitorar os pulmões:

- a resolução espacial era insuficiente, cerca de 1/8 do diâmetro médio do tórax humano;
- a localização das estruturas anatômicas não era correta;
- pequenos movimentos dos eletrodos causavam artefatos na imagem;
- variações na impedância de contato entre eletrodo e pele provocavam artefatos na imagem;
- não era possível obter imagens absolutas em aplicações de pneumologia;
- em geral, as regularizações eram globais, tinham o mesmo valor no domínio, independente da região anatômica;

- o potencial elétrico de referência variava com elevada amplitude e de forma imprevisível no ambiente de Unidades de Terapia Intensiva, introduzindo não-linearidades no procedimento de medida, seja pela saturação de amplificadores operacionais, seja por não-linearidades na rejeição de modo comum nos amplificadores operacionais diferenciais.

Estas dificuldades foram sendo abordadas pela linha de pesquisa através de uma competição de métodos. Os objetivos da linha de pesquisa podem ser melhor definidos.

1.5 Objetivo da Linha de Pesquisa

A linha de pesquisa *Tecnologia de Tomografia por Impedância Elétrica para Monitorar o Pulmão* tinha e ainda tem como objetivo desenvolver a tecnologia de TIE para que ela possa ser utilizada em aplicações médicas e, em particular, na monitoração da ventilação e perfusão pulmonar.

Este objetivo principal vem acompanhado de objetivos particulares, como:

- aumentar a resolução espacial das imagens;
- aumentar a acurácia das estimativas de resistividade e/ou permitividade;
- diminuir a relação sinal/ruído da resistividade estimada;
- estimar a impedância de contato eletrodo-pele;
- estimar a posição dos eletrodos para corrigir a posição deles no modelo numérico do domínio, este erro de posição é causa alguns artefatos;
- otimizar a posição dos eletrodos e determinar as formas ótimas de excitação por corrente elétrica para maximizar a observabilidade da distribuição de resistividade;
- desenvolver a eletrônica de forma a obter medidas com elevada acurácia e elevada relação sinal/ruído.

2 Avanços durante a pesquisa

Apresentam-se neste capítulo os avanços tecnológicos que foram sendo alcançados ao longo da investigação, fazendo referência aos artigos que contém os detalhes e dão suporte a cada afirmação. Assim como na Economia, a falta de algum recurso pode restringir o crescimento econômico, o desenvolvimento desta tecnologia depende de vários aspectos: algoritmos, eletrônica, informação *a priori* anatômica e correção de modelo numérico que representa o domínio. A descrição dos avanços será apresentada do ponto de vista destes aspectos.

2.1 Desenvolvimento do hardware de TIE

O primeiro tomógrafo experimental foi construído na Escola Politécnica, logo no início da investigação. Apresentava 16 canais *single-ended*, com blindagem passiva, 10 kHz de frequência de excitação, fonte de corrente monopolar de 1 mA pico a pico, de-multiplexador de 16 canais para injetar a corrente e outro de-multiplexador de 16 canais para definir qual eletrodo seria o terra analógico. As medidas de potencial eram realizadas por intermédio de uma placa de aquisição de dados com 16 canais *single-ended*. Sobrepostos à senóide que se esperava encontrar nas medidas, apareciam considerável ruido, média não nula e tendência. Utilizava-se, um algoritmo de demodulação para estimar a amplitude de uma senóide num conjunto de medidas (cerca de 300 medidas), subtraindo a média não nula e a tendência.

O tomógrafo experimental seguinte foi construído por uma empresa alemã, Helzel Gmbh, especializada em eletrônica de alta frequência. A proposta era utilizar fontes de corrente e amplificadores de sinal em cada um dos 32 eletrodos. Embora cada eletrodo operasse bem em separado, o sistema tornava-se instável quando os 32 eletrodos eram ligados ao domínio, tanto num manequim com solução salina quanto num um voluntário. A partir desta experiência decidiu-se utilizar uma única fonte de corrente bipolar e conectá-la aos eletrodos através de de-multiplexadores e cabos com dupla blindagem. A tecnologia de blinda-

gem ativa e cancelamento de capacitância em cabos precisava ser desenvolvida
anexo A (BERTEMES-FILHO; LIMA; AMATO, 2004).

A especificação do tomógrafo passou a ser mais realista. O tomógrafo deveria ter pelo menos 32 eletrodos, uma fonte de corrente de 125 kHz e amplitude de até 4 mA pico a pico. Através de resultados de simulação numérica sabia-se que a precisão das medidas deveria ser de 1/100000. Optou-se por utilizar uma placa de aquisição de dados com 32 canais diferenciais e com conversão de analógico para digital simultânea. A frequência de 125 kHz minimizava os efeitos causados pela impedância de contato eletrodo-pele. As medidas diferenciais simultâneas cancelavam parte da interferência eletromagnética e eletrostática captada nos cabos de alta impedância. A placa de aquisição utilizava conversores A/D de 14 bits de precisão. A rotina de demodulação processava 2500 amostras para estimar a amplitude do sinal na precisão de 1/100000. A tecnologia de blindagem ativa e cancelamento de capacitância nos cabos e de-multiplexadores causou uma deterioração da informação de fase do sinal de potencial elétrico. Procurava-se precisão na medida de amplitude. Ao utilizar injeção de corrente bipolar e medidas diferenciais, as medidas eram pouco afetadas pelas consideráveis mudanças no potencial de referência analógico que ocorrem no ambiente de U.T.I. A seguir, a demodulação passou a ser feita em um circuito integrado fpga, *field-programmable gate array*, e o tomógrafo passou a coletar dados em velocidade suficiente para gerar 50 imagens por segundo. Este tomógrafo permitiu avanços nos algoritmos de obtenção de imagens e nas aplicações médicas associadas à monitoração do pulmão.

Foram produzidos cerca de 15 destes tomógrafos pela Dixtal Biomédica Ltda. Ao calibrar, testar e utilizar este tomógrafo experimental ao longo de dois anos, ficou claro que a acurácia das medidas e a fase das medidas também influenciam a resolução espacial e a resolução em resistividade. Em particular, quando a capacitância não cancelada dos cabos passa a ser maior que 5 pF, a resolução espacial se deteriora. Desta forma, os tomógrafos experimentais que estão sendo projetados na Escola Politécnica utilizam diferentes conceitos de eletrodos ativos. Outro fator que influencia de forma decisiva a resolução espacial e em resistividade do tomógrafo é o conhecimento da posição dos eletrodos.

2.2 O desenvolvimento dos algoritmos de imagens de diferenças

As imagens de diferenças são as mais fáceis de serem geradas porque, ao subtrair duas imagens, erros persistentes (de modelagem ou de medidas), que se somam ao sinal, são cancelados ao subtrair dois sinais. Adicionalmente, estas imagens utilizam medidas normalizadas, utilizam a diferença entre duas medidas, dividida por uma delas. Desta forma, erros persistentes (de modelagem ou de medidas), que se multiplicam ao sinal, acabam sendo cancelados. São imagens mais robustas e decorrem de algoritmos não iterativos, em geral.

2.2.1 O algoritmo Backprojection

Ao implementar e testar o algoritmo Back-projection (NAN; AYA; LIMA, 2007), conforme descrito por Santosa e Vogelius, foi possível verificar, por comparação com o algoritmo Matriz de Sensibilidade (YORKEY; WEBSTER; TOMPKINS, 1987), que a normalização das medidas é um fator que aumenta a qualidade das imagens e que estava faltando na formulação original do algoritmo Matriz de Sensibilidade.

anexo B

2.2.2 O algoritmo Matriz de Sensibilidade

A formulação do algoritmo Matriz de Sensibilidade (YORKEY; WEBSTER; TOMPKINS, 1987) baseia-se na teoria de estimação de parâmetros. A estrutura do modelo é considerada conhecida, a excitação do sistema é conhecida e imposta, e a resposta do sistema é conhecida porque foi medida com certa precisão. A estrutura do modelo foi definida pela equação parcial de Laplace generalizada, caso particular das equações de Maxwell, e pelo Método dos Elementos Finitos. Restava determinar os parâmetros do modelo, um conjunto de resistividades, uma resistividade para cada elemento finito. A determinação da resistividade é realizada de forma linear e algébrica utilizando uma série de Taylor truncada do mapa de resistividade para potencial elétrico, que decorre do modelo de elementos finitos.

Nos trabalhos de Roberto Guardo foi introduzida uma normalização nos moldes da normalização utilizada no Backprojection (ADLER; GUARDO, 1996). A normalização trouxe melhorias para a imagem; entretanto, as imagens subestimavam variações de resistividade superiores a 10%, que são variações facilmente encontradas no tecido pulmonar (que pode variar de 4 a 8 Ωm (GABRIEL; LAU;

GABRIEL, 1996)).

2.2.3 O algoritmo Caixa-Preta

Com base na experiência de ter implementado e testado o Backprojection e o Matriz de Sensibilidade em manequins de meio salino, em animais e em humanos, foi proposto um método que procurava identificar diretamente uma matriz que relacionasse variação de potencial elétrico nos eletrodos com variação de resistividade (AYA et al., 2007). Esta matriz foi *treinada* com variações de resistividade ortogonais e suas correspondentes variações de potencial elétrico, calculadas através de um modelo de elementos finitos. Como as colunas desta matriz formam uma base do espaço das variações de resistividade, para restringir o espaço solução em frequência espacial, bastava restringir as colunas da matriz. A regularização do método é realizada, portanto, simultaneamente ao cálculo das colunas da matriz. Este algoritmo foi denominado Caixa-Preta por decorrer da busca de uma matriz que relaciona entrada e saída de um sistema multivariável, sem preocupação com a estrutura interna do sistema.

anexo C

O algoritmo Caixa-Preta gerou imagens com maior acurácia nas variações de resistividade acima de 10%. Verificou-se, comparando as hipóteses do Backprojection e do Matriz de Sensibilidade com as do Caixa-Preta, que a hipótese que os distinguia era a expectativa de obter variações finitas ou infinitesimais de resistividade. Esperar variações finitas permite obter maior acurácia nos valores de resistividade.

2.3 O desenvolvimento dos algoritmos de imagens absolutas

Embora as imagens de diferenças permitam detectar diversas emergências clínicas no tecido pulmonar em algumas circunstâncias (como, por exemplo, atelectasia massiva, trombo-embolismo, efusão pleural e pneumotorax), isto é possível somente quando o paciente vem sendo monitorado desde antes do início da emergência. Distinguir efusão pleural de uma hemorragia só pode ser realizável se houverem sido captados potenciais elétricos anteriores ao evento (LEITE et al., 2008; COSTA et al., 2009).

anexo D

O problema inverso associado à obtenção de imagens absolutas gera um sistema de equações algébricas pior condicionado que o sistema de equações gerado na obtenção de imagens relativas. Desta forma, na busca de melhores imagens ab-

solutas acaba-se desenvolvendo tecnologia que melhora a qualidade das imagens de diferenças.

2.3.1 Algoritmos baseados em Gauss-Newton

Os algoritmos absolutos baseados em Gauss-Newton (VAUHKONEN, 2004) são rápidos quando comparados aos métodos de busca probabilísticos como o Recozimento Simulado, *Simulated Annealing* (SA) (HERRERA et al., 2007) e o Monte Carlo Cadeias de Markov (MCMC) (KAIPIO; SOMERSALO, 2004). Entretanto, nos algoritmos tipo Gauss-Newton há a necessidade de cálculo de uma derivada do modelo de elementos finitos com respeito à resistividade. Esta derivada introduz significativos erros no sistema de equações algébrico. Estes erros acabam por se manifestar deteriorando qualidade da imagem (MIRANDA, 2002; HERRERA et al., anexo E 2007; LIMA et al., 2007; MELLO et al., 2007).

2.3.2 Algoritmos baseados em Programação Linear

Impor limites inferiores e superiores nos valores de resistividade constitui uma regularização, que embora não seja precisa, não costuma introduzir informação *a priori* falsa se os limites estiverem de acordo com a realidade. Esta regularização é, por vezes, chamada de regularização tipo *caixa*. Trata-se, portanto, de uma regularização segura do ponto de vista clínico (HERRERA et al., 2007; VALLEJO et anexo F al., 2007; VALLEJO, 2007; LIMA et al., 2007; MELLO et al., 2007).

Ao utilizar uma regularização tipo caixa em conjunto com uma regularização que restringe altas frequências espaciais na imagem, notas-se que o parâmetro de regularização pode ser significativamente diminuído e que a qualidade da imagem melhora. Por melhoria na qualidade de imagem entende-se melhor uniformidade de sensibilidade, melhor localização de objetos e contornos dos objetos mais fidedignos (HERRERA et al., 2007; VALLEJO et al., 2007; VALLEJO, 2007; LIMA et al., anexo H 2007; MELLO et al., 2007).

Algoritmos de otimização (que neste trabalho são utilizados na busca de uma imagem) baseados em Programação Linear, permitem impor restrições tipo caixa sem modificar a função objetivo que se deseja otimizar. Mesmo que a função objetivo seja não linear, ou que as restrições sejam não lineares, é possível utilizar a Programação Linear Sequencial (LIMA et al., 2007; MELLO et al., 2007).

É possível, ainda, através da definição de modelos de materiais (técnica amplamente utilizada na Otimização Topológica (BENSOE; SIGMUND, 2003)), intro-

duzir informação *a priori* sobre valores esperados de resistividade. Resultam imagens com distribuição de resistividade com elevada amplitude e boa localização de objetos (LIMA et al., 2007; MELLO et al., 2007).

anexo G

2.3.3 Técnicas probabilísticas de solução de problemas inversos

A TIE tem que lidar, necessariamente, com uma série de incertezas, erros de medida e erros de modelagem. A imagem deve ser procurada em um sentido probabilístico. Informação *a priori* probabilística regulariza o problema inverso mal posto, que caracteriza a TIE, restringindo a função densidade de probabilidade definida pela verossimilhança (KAIPIO; SOMERSALO, 2004).

Três algoritmos de solução de problemas inversos probabilísticos se destacam: o Recozimento Simulado, ou *Simulated Annealing* (SA), o Monte Carlo com Cadeias de Markov (MCMC) e as variantes do Filtro de Kalman. O SA e o MCMC são algoritmos lentos e mais apropriados para obtenção de imagens estáticas. O SA, quando comparado ao Gauss-Newton com informação semelhante, gera imagens com maior resolução espacial e em resistividade (HERRERA, 2007), provavelemente porque o SA utiliza a função objetivo diretamente, não requer o cálculo de sua derivada com respeito à resistividade e pela presença de uma regularização tipo caixa ao invés de apenas a regularização que restringe elevadas frequências espaciais.

Os filtros de Kalman permitem resolver problemas inversos dinâmicos e probabilísticos, nos quais o estado do sistema varia com o tempo e segue um modelo, mesmo que impreciso. Nos filtros de Kalman a estimativa do estado atual é feita com base em estimativas passadas e medidas passadas, em um modelo de evolução e em um modelo de observação. A monitoração do tecido pulmonar pode ser abordada como um problema de observação probabilística não linear de estado ou como um problema inverso dinâmico e probabilístico (VAUHKONEN, 1997).

2.3.4 Algoritmos baseados em Filtros de Kalman

O primeiro trabalho que abordou o problema de TIE como um observador de estados utilizou o Filtro de Kalman para sistemas lineares (VAUHKONEN, 1997). Decorre deste trabalho que as variações de resistividade no pulmão têm amplitude elevada para poder ser tratadas por um observador linear. Em seguida, foi implementado uma variante do Filtro de Kalman para sistemas não lineares, o

Filtro Estendido de Kalman (FEK) (KIM et al., 2001), mostrando que, de fato, observadores não-lineares eram mais adequados para monitorar o pulmão. Antes desta publicação já se desenvolvia na Escola Politécnica uma implementação do FEK (TRIGO, 2001).

Além de estimar a distribuição de resistividade, é preciso estimar a impedância do contato entre eletrodo e pele e a distância entre eletrodos em uma monitoração de pulmão em condições de UTI. Quando a impedância de contato ou a distância entre eletrodos é informada erroneamente ao modelo de elementos finitos, ocorre um viés na estimativa da resistividade do torax. Ao implementar o FEK definindo como estado o conjunto das resistividades dos elementos da malha e as impedâncias de contato entre eletrodos e pele, ocorreu uma dificuldade de ajuste do FEK para que tivesse sensibilidade equilibrada entre estes dois conjuntos de parâmetros de significados físicos distintos. Uma solução foi implementar dois filtros FEK interligados (TRIGO, 2001; TRIGO; LIMA; AMATO, 2004). Esta solução foi encorajadora e, posteriormente, foi implementado um algoritmo que estimava em paralelo e interligados três conjuntos de parâmetros: resistividades do torax, impedâncias de contato e distâncias entre eletrodos (VALLEJO et al., 2006).

anexo I

Sabe-se pela Teoria de Controle que, para que um observador de estado possa efetivamente acompanhar as variações de estado, ele deve ter uma velocidade de seguimento igual ou superior às variações do estado da *planta* (neste trabalho o pulmão). O FEK apresentava baixa velocidade de seguimento. Duas modificações foram implementadas, estimar o modelo de evolução de cada paciente em um intervalo de tempo recente (MOURA et al., 2007, 2008, 2009, Em revisão, IEEE Transaction on Biomedical Engineering) e utilizar uma matriz covariância do ruído de processo adaptativa que dirigisse o resíduo de estimação a ter média nula e distribuição próxima de Gaussiana (TRIGO; LIMA; FLEURY, 2009; TRIGO, 2005). As duas alternativas causaram um aumento significativo na velocidade de seguimento do FEK. Verifica-se que a resistividade das imagens está de acordo com a resistividade dos tecidos do pulmão, da coluna vertebral e da caixa torácica de seres humanos medidas após a retirada do corpo humano (GABRIEL; LAU; GABRIEL, 1996; MOURA et al., 2009). Este resultado indica que é possível a obtenção de imagens absolutas em ambiente de U.T.I. em um futuro próximo. Resta melhorar a resolução espacial destas imagens e testar a confiabilidade da técnica.

anexo J

anexo K

2.3.5 Sobre o posicionamento ótimo dos eletrodos

Ao definir como índice de observabilidade modal alguns autovalores da matriz resultante do produto da transposta da matriz de sensibilidade por ela mesma, foi investigada a posição ótima dos eletrodos que maximizam a soma destes autovalores. Ou seja, procura-se a localização dos eletrodos no domínio que maximizam a obsservabilidade de algumas componentes principais das imagens. Os resultados preliminares indicam que, quando a distribuição de resistividade é não uniforme e não simétrica, a posição ótima dos eletrodos não é equi-espaçada (MELLO et al., 2008). anexo L

2.3.6 Técnica direta de reconstrução de imagens

Em 1996 foi demonstrada a existência e a unicidade de solução da equação generalizada de Laplace (NACHMAN, 1995). A demonstração é construtiva e gerou um caminho teórico para obter imagens de forma direta, isto é, sem iterações. Este método vem sendo desenvolvido ao longo dos anos com resultados encorajadores e é o único método de TIE para imagens absolutas não iterativo, no momento (SILTANEN; MUELLER; ISAACSON, 2000). Baseia-se em uma transformação de variáveis que leva a equação generalizada de Laplace na equação de Schrödinger. Na equação de Schrödinger, uma função não linear da condutividade, porém conhecida e determinística, é uma variável que pode ser determinada de forma direta e linear, sem iterações. Duas teses de doutorado da Escola Politécnica dedicam-se ao desenvolvimento deste método com a co-orientação da Profa. Jennifer Mueller da Colorado State University.

2.4 O desenvolvimento de aplicações na Pneumologia

2.4.1 Sobre a detecção de pneumotórax

A detecção precoce de pneumotorax na beira de leito já é uma realidade(??). O pneumotorax se carateriza por ter baixa ventilação, ventilação mais baixa que o tecido sobre-estendido. Uma imagem de desvio padrão da variação da resistividade, obtida através de um algoritmo gerado nesta linha de pesquisa, permite quantificar a ventilação. Utilizando imagens de diferenças, somente é possível identificar um pneumotorax quando ele ocorre ou cresce durante o período de monitoração do torax. Com imagens de resistividade, ditas absolutas, será pos-

sível detectar a ocorrência de um pneumotórax que começou antes do período de monitoração.

anexo D

2.4.2 Determinação da pressão no final da expiração PEEP

Através do mapa de desvio padrão da variação de resistividade, desenvolvido nesta linha de pesquisa, é possível identificar as regiões em que está ocorrendo colapso do tecido pulmonar. E por consequência, é possível estimar a pressão positiva no fim da expiração, o PEEP, que evita novo colapso do tecido pulmonar, atelectasia (BERALDO et al., 2006; COSTA et al., 2009). Manobras de recrutamento alveolar recuperam regiões do tecido pulmonar que estavam colapsadas; entretanto, se a pressão for reduzida abaixo de certo limite, o tecido volta a colapsar. É necessário determinar esta pressão mínima, chamada de pressão positiva no final da expiração (PEEP). A TIE tem sido considerada a técnica mais precisa de terminação do PEEP, entre aquelas que são possíveis de realizar na beira de leito.

2.4.3 Sobre a perfusão no pulmão

Inicialmente pensava-se que, ao subtrair das imagens de diferenças imagens de ventilação (separação realizada por média coerente sincronizada com sinal de Eletrocardiograma (ECG)), resultavam imagens de perfusão. Verificou-se que a separação da imagem de ventilação da imagem completa resulta em uma imagem que contém predominantemente a pulsatilidade dos grandes vasos. O estudo utilizou comparações de imagens de perfusão através de *Single Photon Emission Computed Tomography* (SPECT) com a perfusão obtida via TIE com contraste de solução salina hipertônica (FRERICHS et al., 2002). A discrepância entre estimativas de perfusão regional via SPECT e via TIE é de apenas 5% (SIPMANN et al., 2008). Desta forma, a TIE permite avaliar a perfusão regional no pulmão.

3 Comentários Finais e Trabalhos Fututros

Esta investigação, que contou com a colaboração estreita do Departamento de Pneumologia da Faculdade de Medicina da USP, através do desenvolvimento da tecnologia de TIE, tornou possível a monitoração do pulmão em ambiente de U.T.I.

- É possível a detecção precoce de pneumotórax e atelectasia a beira de leito. Pneumotórax com volume de 20 ml podem ser detectados.
- É possível determinar o PEEP para ajustar ventiladores de pulmão em ambiente de UTI.
- Esta linha de pesquisa contribuiu para que a tecnologia de TIE obtivesse um aumento de resolução espacial que agora é de 1/10 do diâmetro médio, no centro do domínio, e de 1/20 do diâmetro médio, na periferia do tórax, através de modelagem mais precisa do tórax, normalizações e regularizações com maior sentido clínico.
- O erro de localização das estruturas anatômicas diminuiu graças ao uso de modelos 3D de elementos finitos. A distância entre eletrodos é estimada em tempo real.
- A impedância do contato eletrodo-pele também pode ser estimada e seu valor pode ser corrigido no modelo do tórax, minimizando o artefato associado.
- Imagens absolutas dinâmicas do tórax humano foram obtidas, das quais é possível extrair imagens de diferença com informação sobre a ventilação local e sobre pulsatilidade local. Este resultado indica a viabilidade de obtenção de imagens absolutas na beira de leito.
- A perfusão pode ser estimada com discrepância de 5% em relação à estimativa por tomografia SPECT, pelo uso de solução salina hipertônica

como contraste. Injeta-se 5 ml de solução salina no sistema vascular e acompanham-se os íons quando eles passam pelo pulmão, revelando assim a perfusão de sangue local no pulmão. Foi demonstrado ainda que a pulsatilidade não revela a perfusão local.

O desenvolvimento desta tecnologia deve ainda continuar por vários anos: no campo da eletrônica, no campo da solução de sistemas lineares, no campo dos problemas inversos, na determinação de atlas anatômicos cada vez mais específicos e precisos e nas aplicações, da medicina e na engenharia.

Na eletrônica, espera-se um aumento de precisão pelo emprego de eletrodos ativos. Cinco tomógrafos experimentais serão construídos na Escola Politécnica nos próximos meses para testar configurações de eletrodos ativos. Quanto às regularizações, está em andamento o desenvolvimento de uma atlas anatômico humano, em cooperação com a Universidade de Kuopio, Finlândia e a Faculdade de Medicina da USP.

No campo dos algoritmos, ocorre o desenvolvimento da uma variante do filtro de Kalman chamada *Uscented Kalman Filter* (UKF), também em cooperação com a Universidade de Kuopio. Planeja-se ainda a implementação de algoritmos do tipo *Kaczmarz - Level Sets* e estão em andamento duas teses de doutorado sobre o D-Bar em colaboração com a Profa. Jennifer Mueller, Colorado State University. O UKF é um observador de estado probabilístico que tem demonstrado elevada velocidade de seguimento; esta velocidade pode ser ainda aumentada se associada à identificação do modelo de evolução. O segundo algoritmo, *Kaczmarz Level Sets*, deve gerar imagens constantes por trechos de forma rápida e eficiente, imagens com elevada importância clínica, pois é uma maneira de delimitar os tecidos, e adequadas para a inicialização de métodos iterativos probabilísticos. Finalmente, o desenvolvimento do Método D-Bar pode tornar rotineiro o uso de imagens absolutas, ao invés de imagens de diferenças nas aplicações médicas.

Outro desafio para o futuro próximo é a determinação em tempo real da posição dos eletrodos e a geometria externa do domínio. A correção da malha de elementos finitos deve permitir um aumento de resolução espacial e em resistividade.

Trata-se, portanto, de uma linha de pesquisa que tem o potencial de modificar práticas na área da saúde, em particular, nas estratégias protetivas do pulmão, e diminuir a taxa de mortalidade de pacientes em U.T.I. com deficiência respiratória aguda. Espera-se que esta tecnologia, com algumas modificações, seja efetiva na monitoração da perfusão do cérebro e na estimativa do débito cardíaco, para citar

algumas aplicações mais viáveis no momento.

Referências

ADLER, A.; GUARDO, R. Electrical impedance tomography: regularized imaging and contrast detection. *IEEE Transactions on Medical Imaging*, IEEE, USA, v. 15, n. 2, p. 170–179, 1996.

AMATO, M. B. P. et al. Effect of a protective-ventilation strategy on mortality in the acute respiratory distress syndrome. *New England Journal of Medicine*, v. 338, n. 6, p. 347–354, 1998.

AYA, J. C. C. et al. Regularizations for a black box back-projection eit algorithm. *ABCM Symposium Series in Bioengineering*, v. 1, 2007.

BARBER, D. C.; BROWN, B. H. Applied potential tomography. *Journal of Physics E: Scientific Instruments*, v. 17, p. 723–733, 1984.

BENSOE, M. P.; SIGMUND, O. *Topology Optimization: Theory, Methods and Application*. Berlin, Heidelberg, New York: Springer Verlag, 2003.

BERALDO, M. A. et al. Peep titration by eit (electric impedance tomography): correlation with multislice ct. In: *ATS - 2006 International Conference and Special Issue of the Am. J. Respir. Crit. Care Med.* San Diego, California: ATS, 2006. v. 3, p. A64.

BERTEMES-FILHO, P.; LIMA, R.; AMATO, M. B. P. Capacitive-compensated current source used in electrical impedance tomography. In: *12th International Conference on Electrical Bio-Impedance*. Gdansk: Gdansk University of Technology, 2004. p. 645–648.

BORSIC, A. et al. Relastic 2d human thorax modelling for eit. *Physiol. Meas.*, v. 22, p. 77–83, September 2001.

COOK, R. D. et al. Act3: a high-speed, high-precision electrical impedance tomograph. *IEEE Transactions on Biomedical Engineering*, v. 41, n. 8, p. 713–722, 1994.

COSTA, E. V. L. et al. Bedside estimation of recruitable alveolar collapse and hyperdistension by electrical impedance tomography. *Intensive Care Medicine*, v. 35, p. 1132–1137, 2009.

FRERICHS, S. I. et al. Regional lung perfusion as determined by electrical impedance tomography in comparison with electron beam ct imaging. *Physics In Medicine And Biology*, v. 21, n. 6, p. 646–652, 2002.

GABRIEL, S.; LAU, R. W.; GABRIEL, C. The dielectric properties of biological tissues: Ii. measurements in the frequency range 10 hz to 20 ghz. *Physics In Medicine And Biology*, v. 41, p. 2251–2269, 1996. Disponível em: <http://niremf.ifac.cnr.it/tissprop/>.

HERRERA, C. N. *Algoritmo de Tomografia por Impedancia Eletrica baseado no Simulated Annealing.* Dissertação (Mestrado) — Escola Politécnica da Universidade de São Paulo, São Paulo, 2007.

HERRERA, C. N. L. et al. Electrical impedance tomography algorithm based on simulated annealing search method. In: *Proceeedings of the 19th International Congress of mechanical Engineering.* Brasília: ABCM, 2007.

KAIPIO, J.; SOMERSALO, E. *Statistical and Computational Inverse Problems.* 1º. ed. New York: Springer, 2004.

KIM, K. Y. et al. Image reconstruction in time-varying electrical impedance tomography based on the extended kalman filter. *Measurement Science and Technology*, n. 12, p. 1032–1039, 2001.

LEITE, E. V. C. et al. Real-time detection of pneumothorax using electrical impedance tomography. *Critical Care Medicine*, v. 36, p. 1230–1238, 2008.

LIMA, C. R. de et al. Electrical impedance tomography through constrained sequential linear programming: a topology optimization approach. *Measurement Science and Technology*, v. 18, p. 2847–2858, 2007.

MELLO, L. A. M. et al. On the design of electrodes through the topology optimization method applied to electrical impedance tomography. In: *Proceedings of EngOpt 2008 - International Conference on Engineering Optimization, 2008.* Rio de Janeiro: COPPE/UFRJ, 2008.

MELLO, L. M. et al. Three-dimensional electrical impedance tomography: a topology optimization approach. *IEEE Transactions on Biomedical Engineering*, 2007.

METHERALL, P. *Three Dimensional Electrical Impedance Tomography of the Human Torax.* Tese (Doutorado) — Department of Medical Physics and Clinical Engineering, University of Sheffield, 1998.

MIRANDA, D. A. A. *Tomografia por Impedância Elétrica utilizando o Método de Newton-Raphson.* Dissertação (Mestrado) — Escola Politécnica da Universidade de São Paulo, São Paulo, 2002.

MOURA, F. S. et al. On line transition matrix identification of the state evolution model for the extended kalman filter in electrical impedance tomography. In: *Proceedings of the AIP 2007/IPIA Conference on Applied Inverse Problems 2007: Theoretical and Computational Aspects, 2007.* Vancouver: Pacific Institute for the Mathematical Sciences/University of British Columbia, 2007.

MOURA, F. S. et al. On line transition matrix identification of the state evolution model for the extended kalman filter in electrical impedance tomography. *Journal of Physics: Conference Series*, v. 124, 2008.

MOURA, F. S. et al. Dynamic imaging of a human chest using the kalman filter in electrical impedance tomography. In: *Proceedings of the 10th International Conference on Biomedical Applications of Electrical Impedance Tomography (EIT 2009).* Manchester: University of Manchester, 2009.

MOURA, F. S. et al. Dynamic imaging of a human chest using the kalman filter in electrical impedance tomography. *IEEE Transactions on Biomedical Engineering*, Em revisão, IEEE Transaction on Biomedical Engineering.

NACHMAN, A. A global uniqueness for a two-dimensional inverse boundary value problem. *Annals of Mathematics*, EUA, v. 142, p. 71-96, 1995.

NAN, P. C.; AYA, J. C. C.; LIMA, R. G. An implementation of the back-projection algorithm according to santosa and vogelius. *ABCM Symposium Series in Bioengineering*, v. 1, 2007.

NOPP, P. et al. Model for the dielectric properties of human lung tissue against frequency and air content. *Med. Biol. Eng. Comput.*, v. 35, n. 6, p. 695–702, 1997.

RAPP, P. N. bnd E. et al. Dieletric properties of lung tissue as a function of air content. *Physics in Medicine and Biology*, v. 38, n. 6, p. 699–716, 1993.

SANTOSA, F.; VOGELIUS, M. Backprojection algorithm for electrical impedance imaging. *SIAM Journal on Applied Mathematics*, v. 50, p. 216–243, 1990.

SILTANEN, S.; MUELLER, J.; ISAACSON, D. An implementation of the reconstruction algorithm of a. nachman for the 2d inverse conductivity problem. *Inverse Problems*, v. 16, p. 681–699, 2000.

SIPMANN, F. S. et al. Analysis of global v/q and regional distribution of ventilation in an ali model. In: *American Thoracic Society International Conference*. Toronto: ATS, 2008.

TRIGO, F. C. *Filtro Estendido de Kalman Aplicado à Tomografia por Impedância Elétrica*. Dissertação (Mestrado) — Escola Politécnica da Universidade de São Paulo, São Paulo, 2001.

TRIGO, F. C. *Estimação não linear de parâmetros através dos filtros de Kalman na tomografia por impedância elétrica*. Tese (Doutorado) — Escola Politécnica da Universidade de São Paulo, São Paulo, 2005.

TRIGO, F. C.; LIMA, R. G.; AMATO, M. B. P. Electrical impedance tomography using the extended kalman filter. *IEEE Transactions on Biomedical Engineering*, v. 51, n. 1, p. 72–81, 2004.

TRIGO, F. C.; LIMA, R. G.; FLEURY, A. T. Adaptive iterated extended kalman filter for electrical impedance tomography. In: *Proceedings of 10th International Conference on Biomedical Applications of Electrical Impedance Tomography (EIT 2009)*. Manchester, UK: University of Manchester, 2009.

VALLEJO, M. F. M. *Algoritmos para Tomografia por Impedância Elétrica utilizando Programação Linear*. Dissertação (Mestrado) — Escola Politécnica da Universidade de São Paulo, São Paulo, 2007.

VALLEJO, M. F. M. et al. The use of linear programming as search method of images in electrical impedance tomography. In: *Proceeedings of the 19th International Congress of mechanical Engineering*. Brasília: ABCM, 2007.

VALLEJO, M. F. M. et al. An algorithm for real time estimation of electrode position in electrical impedance tomography. In: *Proceedings of the Technology and Medical Sciences International 4*. Dundee: ABCM, 2006.

VAUHKONEN, M. *Electrical Impedance Tomography and Prior Information.* Tese (Doutorado) — University of Kuopio, Finland, 1997.

VAUHKONEN, P. J. *Image Reconstruction in Three-Dimensional Electrical Impedance Tomography.* Tese (Doutorado) — Department of Applied Physics, University of Kuopio, 2004.

YORKEY, T. J.; WEBSTER, J. G.; TOMPKINS, W. J. Comparing reconstruction algorithms for electrical impedance tomography. *IEEE Transactions on Biomedical Engineering*, v. BME-34, n. 11, p. 843–852, 1987.

ANEXO A – Cancelamento de capacitância

CAPACITIVE-COMPENSATED CURRENT SOURCE USED IN ELECTRICAL IMPEDANCE TOMOGRAPHY

P. Bertemes-Filho[1a], R.G. Lima[a], M. B. P. Amato[b]

[a]Escola Politecnica da USP, Av. Prof. Luciano Gualberto 380, Butanta, Sao Paulo, SP, Brasil
[b]Faculade de Medicina da USP, Av. Dr. Arnaldo 455, São Paulo, Sp, Brasil

ABSTRACT: Electrical impedance tomography is a promising technique for imaging the conductivity distribution within the body. Yet no high quality anatomical image has been reported. This is partially related to the inaccuracies of the instrumentation, particularly to the low performance of the current source. A brief overview in the literature show that current source with capacitive compensation is a recent technique applied to increase its output impedance, but still suffering with instability and process control. This paper shows a multiplexed bipolar current source using negative impedance converter. The measured output impedance was greater than 20 MΩ and stable on a period of 15 hours.

Keywords: current source, impedance converter, electrical impedance tomography

1. INTRODUCTION

Over 20 years the Electrical Impedance Tomography (EIT) has been under investigation as a promising imaging technique. This technique consists on imaging the distribution of the impedance within the body (anatomical imaging) or the variation in impedance during a physiological change (dynamic imaging). Anatomical EIT is of great interest in the clinical environment to be used as an alternative to X-rays, CT or MRI. Forming an image of this impedance is technically difficult. Some difficulties are related to the inaccuracies of the instrumentation used in the data acquisition system [2].

Many EIT groups have used multifrequency recording as a possible solution for obtaining anatomical image, where the set of voltage measurements at one frequency is used as a reference for measurements at another. However, there is still the problem of deciding which of the images best represents the underlying anatomy [2]. Images of the anatomy can be based only on the measurements of voltage at one frequency. If the objective in single frequency EIT is to produce absolute images, highly accurate measurements are needed. The maximisation of the output impedance, Z_{out}, of the current source and the input impedance of the recording amplifier has been frequently attempted to overcome inaccuracy problems.

In theory, the Z_{out} of the current source should be thousands times greater than the load (i.e. the combination of the skin/electrode-interface impedance with the biological one). However, parasite capacitance in the output of the current source decreases significantly the Z_{out} of the current source. One possible solution is to use a Negative Impedance Converter (NIC) [1]. Table1 brings some important characteristics of some EIT hardware with particular emphasis on the current source. Measured output impedance as high as 37 MΩ at 100 kHz can be achieved by using a Generalised Impedance Converter (GIC) [3], but a sophisticated and a permanent trimming process is required. It has to be emphasised that a clinical EIT system has to be robust and safe, capable of generating real time images and stable over time.

This paper compares the output impedance of a multiplexed bipolar current source, with and without a negative impedance converter, intended to be used in a single frequency EIT system.

[1] pedro.bertemes@poli.usp.br; phone 55 11 3091-9643; fax 55 11 3813-1886;

Tab.1. Comparative table of some EIT system found in the literature, where SE= single-ended and DB= dual balanced.

Authors	*Electrodes*	*Design Frequency*	*CURRENT SOURCE*		
			Z_{out} (kΩ)	I_{out} (mA_{p-p})	*Configuration*
Brown et al 1987	16	50	13	-	SE
Shi et al 1990, Rigaud et al 1990	16	11.5-92	5,000 at 50 kHz	-	SE
Cook et al 1994	32	30	25,000-50,000	1	multiple SE*
Jossinet et al 1994	16	32-2048	1,000 at 128 kHz	2	multiple SE
Wang et al 1992	16	75-153.6	5,500 at 76.8 kHz	-	-
Bragós et al 1994	-	10-500	1,000	0.3	-
Goovaerts et al 1998	-	4-1024	1,013 at 64 kHz	0.85	isolated DB
Wilson et al 2001	8	2-1600	>1,000 at 100 kHz	0.85	multiple DB
Ross et al 2003	-	0.1-1000	37,000 at 100 kHz	-	SE**
Bertemes-Filho et al 2003	32	125	20,000	2	DB*

*using NIC circuit, **using GIC circuit

2. METHODOLOGY

A Bipolar-Hownald-Current-Source (BHCS) and two negative impedance converters, one for each side of the current source, attached to a 32 channel multiplexer were built. The complete system is shown in figure 2.

The output impedance of the BHCS circuit was measured by varying the load from 0.2 to 1.2 kΩ, which was done by two relays (S_1 and S_2 in figure 2). The measurements were made by using an acquisition board (DAQ-2010, ADLink Technology Inc.) at 2 MS/s. The load voltages were demodulated using 2.000 samples and then the output impedance were calculated by using a virtual bench developed in LabVIEW 6i (National Instruments Inc.). Measurements were made with and without the NIC circuit. The stability of the BHCS circuit was investigated by calculating the Z_{out} over 15 hours of acquisition.

3. RESULTS

Figure 3 shows the output impedance of the multiplexed bipolar current source with and without a NIC circuit. Data are averaged every 24 seconds of acquisition up to about 5.5 minutes. It can be seen that the Z_{out} decreases from approximatly 23 to 2 MΩ when the 32-channel multiplexer is connected to the circuit. The drop in Z_{out} was certainly caused by capacitances of the multiplexer. However, when connecting and adjusting the NIC circuit, the magnitude of the Z_{out} is on average 20 MΩ.

Figure 4 shows the stabilily of the measurements when the equipament was running over a period of 15 hours. It can be seen that the magnitude of Z_{out} is over 20 MΩ.

It must be mentioned that the input voltage signal to the current source was generated by an integrated circuit (MAX038 from Maxim), which contributed to some inaccuracies to the load current. In order to measure higher output impedance than 20 MΩ, accurate input signal and data acquisition board of at least 14 bits resolution should be considered.

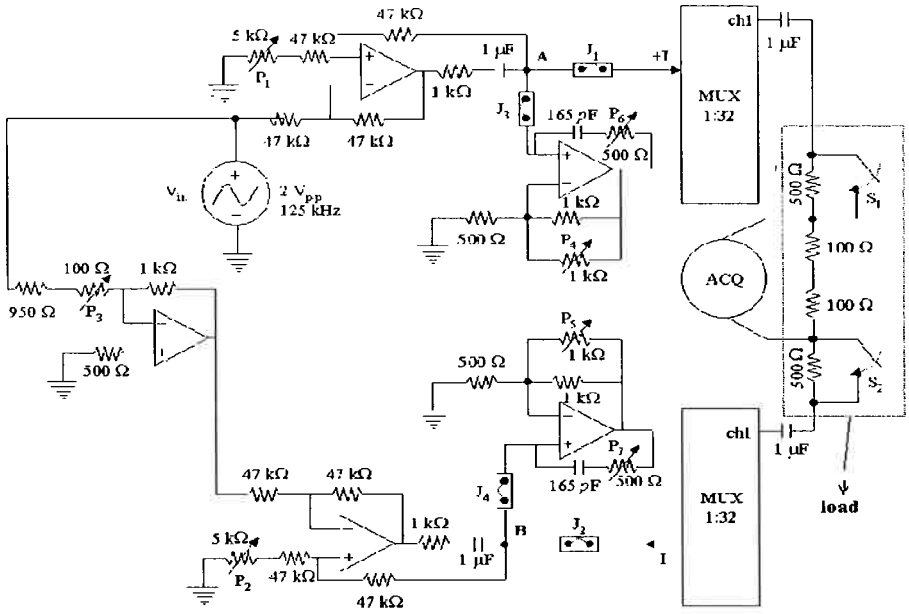

Fig. 2. Diagram of the multiplexed BHCS circuit implemented for measuring the Z_{out}.

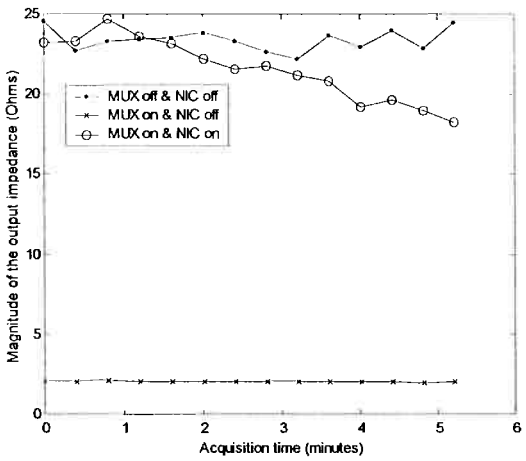

Fig.3. The magnitude of the output impedance switching on and off both multiplexer and the NIC circuit.

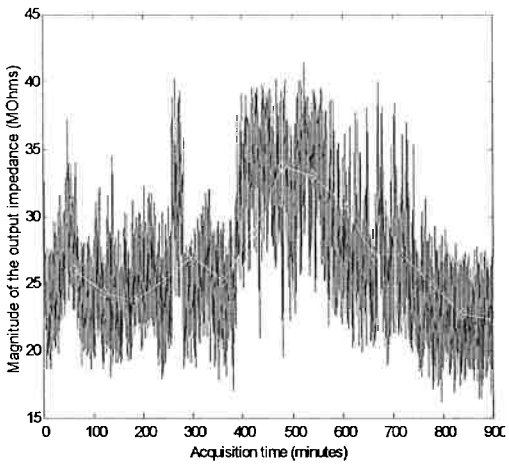

Fig.4. Output impedance, showing the raw data over 15 hors of acquisition and the respective mean values.

4. CONCLUSIONS

The output impedance of 32-channel multiplexed BHCS with capacitive compensation was measured an its output current stability over time was also investigated. It was shown that the current source is quite stable over a long period of time when driving a resistive load through a 32-channel multiplexer. The measured output impedance was on average greater than 20 MΩ within the first 15 hours of acquisition time, using a load variation of 1 kΩ. It can be concluded that the accuracy of the load current is about 86 dB at 125 kHz.

ACKNOWLEDGEMENTS

We would like to thank FAPESP for financial support, grants 03/1917-3 and 01/05303-4.

REFERENCES

1. Bertemes-Filho, P., Lima, R. G., Tanaka, H., A Current Source using a Negative Impedance Converter (NIC) for Electrical Impedance Tomography (EIT), *17th Int. Congress of Mechanical Eng.*, São Paulo (Brasil), 83-87, 2003.
2. Boone, K., Barber, D. and Brown, B. H., Review Imaging with electricity: Report of the European Concerted Action on Impedance Tomography, *Journal of Medical Engineering & Technology*, 21(6), 201-231, 1997.
3. Ross, A. S., Saulnier, G. J., Newell, J. C. and Isaacson, D., Current source design for electrical impedance tomography, *hysiological Measurement*, 24:509-516, 2003.

ANEXO B – Backprojection na Escola Politécnica

ABCM Symposium Series in Bioengineering, Vol. 1

AN IMPLEMENTATION OF THE BACK-PROJECTION ALGORITHM ACCORDING TO SANTOSA AND VOGELIUS

Pai Chi Nan
Department of Mechanical Engineering - Polytechnic School of University of São Paulo Av. Prof. Mello de Moraes, 2231 - São Paulo - SP - 05508-900, Brazil
paichinan@yahoo.com

Julio C. C. Aya
Department of Mechanical Engineering - Polytechnic School of University of São Paulo Av. Prof. Mello de Moraes, 2231 - São Paulo - SP - 05508-900, Brazil
jccaya@usp.br

Raul Gonzalez Lima
Department of Mechanical Engineering - Polytechnic School of University of São Paulo Av. Prof. Mello de Moraes, 2231 - São Paulo - SP - 05508-900, Brazil
rauglima@usp.br

Corresponding author: Raul Gonzalez Lima

Abstract. *Electrical Impedance Tomography (EIT) is a technique to estimate the impedance distribution of a domain of interest, for instance, a section of the human body. It uses the boundary electrical potential measurements of the section to estimate the image. One of the early image reconstruction algorithms is called back-projection, duo to Barber and Brown, but there is a lack of articles about it. Santosa and Vogelius proposed an implementation of the Barber-Brown algorithm with interpolation of the boundary data and low-pass filter the image.*
The present work shows an implementation of this improvement with a particular choice of interpolation of the boundary data and an interpretation of the resulting image in terms of resistivity instead of conductivity.

Keywords: *back-projection, Electrical Impedance Tomography*

1. Introduction

The back-projection algorithm, developed by Barber and Brown in 1983, is an efficient algorithm with relative low computer cost [1, 2], and this is the reason for being one of the most well known image reconstruction algorithms for Electrical Impedance Tomography. However, there are few articles describing how is this algorithm. One of these articles was written by Santosa and Vogelius [3]. The vast literature on Backprojection reports its performance or clinical applications.

Backprojection is a two dimensional reconstruction algorithm and, initially, the domain was restricted to be circular. Extensions for non-circular domains were proposed. A three dimensional direct extension of the Barber and Brown Backprojection was not accomplished [4], although some conceptually closely related 3D algorithms were developed [5].

An posterior development, called filtered backprojection [4, 6], improved the spatial resolution and the conductivity resolution pre-processing the electric potential data before the use of the backprojection algorithm. The pre-processing, or filtering procedure, used the first derivative of a finite elements model of the domain under analysis.

The objective of the present work is to describe an implementation the back-projection algorithm according to Santosa and Vogelius, with a particular choice of interpolation of the boundary data and an interpretation of the resulting image in terms of resistivity instead of conductivity using concepts from the calculus of variations.

2. Sheffield's back-projection algorithm

The mathematical representation of the problem is supposed to be [4]

$$\nabla.(\sigma \nabla U) = 0 \; in \; \Omega \tag{1}$$

$$\sigma \frac{\partial U}{\partial n} = J \; on \; \partial\Omega \tag{2}$$

where σ is the conductivity profile, U is the electric potential, J is the boundary current density and Ω is the domain of interest.

Taking the first variation of eq. 1 and eq. 2, denoting the first variation of the conductivity by $\delta\sigma$ and the first variation of the electric potential by δU, results,

$$\nabla.(\sigma\nabla\delta U) + \nabla.(\delta\sigma\nabla U) = 0 \; in \; \Omega \tag{3}$$

$$\sigma\frac{\partial(\delta U)}{\partial n} + \delta\sigma\frac{\partial U}{\partial n} = 0 \; on \; \partial\Omega \tag{4}$$

With the following hypotheses

1. Ω is the unit two dimensional ball;
2. the conductivity is unitary $\sigma = 1$;
3. $\delta\sigma = 0$ near the dipole

the linearized problem reduces to

$$\nabla^2\delta U = -\nabla(\delta\sigma).\nabla U \; in \; \Omega \tag{5}$$

$$\frac{\partial(\delta U)}{\partial n} = 0 \; on \; \partial\Omega \tag{6}$$

The linearized inverse problem associated with equations 5 and 6 becomes
Given a variation of electric potential along the boundary, $\delta U\mid_{\partial\Omega}$, for various choices of dipole positions along the boundary, determine a consistent increment $\delta\sigma$.

To solve this problem, Barber and Brown used a change of variables that mapped the circular domain into a rectangular domain.

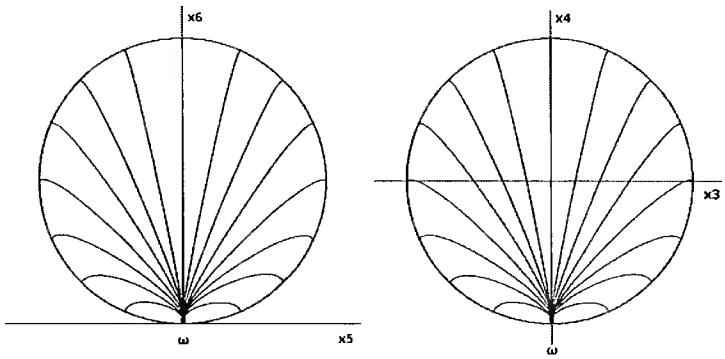

(a) (b)

Figure 1. (a) coordinates (x5,x6) (b) coordinates (x3,x4)

Using the reference frame shown on Fig. 1(a), with ω representing the position of current injecting dipole, which is located between two electrodes, the equation for the voltage equipotential lines is

$$U = \frac{x_5}{x_5^2 + x_6^2} \tag{7}$$

and the equation for the current equipotential lines is

$$V = \frac{x_6}{x_5^2 + x_6^2} \tag{8}$$

With a translation on the reference frame, see Fig. 1(b), equations 7 and 8 become

$$U = \frac{x_3}{x_3^2 + (x_4+1)^2} \tag{9}$$

$$V = \frac{(x_4+1)}{x_3^2 + (x_4+1)^2} \tag{10}$$

With the equations 9 and 10, the domain Ω can be mapped to the upper half plane P defined by the rectangular region where $V > 1/2$. The problem represented by equations 5 and 6 simplifies, using the new coordinates (U, V), to

$$\nabla^2 \delta U = -\frac{\partial(\delta\sigma)}{\partial U} \; in \; P \tag{11}$$

$$\frac{\partial(\delta U)}{\partial V} = 0 \; on \; \partial P = \{V > \frac{1}{2}\} \tag{12}$$

Barber and Brown suggest that the average

$$\delta\sigma = \frac{1}{m}\sum_{j=1}^{m} W(s,\omega_j)\,|_{s=U(s,\omega_j)}\,(2V\,(x,\omega_j) - 1) \tag{13}$$

as the discrete solution for $\delta\sigma$, where m is the number of the electrodes, W is the voltage measurement on the boundary, ω represent the position of the electrode and V is the current intensity function. Santosa and Vogelius have shown that eq. 13 is a simplification of the one consistent with the Radon Transform [?].

Since the voltage measurement is affected by the resistivity/conductivity of the whole of the body, Barber and Brown suggest the use of a normalized voltage measurement to obtain a normalized conductivity.

The Sheffield back-projection algorithm assumes that the region between two adjacent potential lines has the same voltage measurement. Rotating the position of the current injection dipole, it obtains m sets of voltage measurements. These sets of electric potential measurements, , previously normalized, adjusted by the corresponding weight, which is $2V - 1$, is the desired normalized conductivity.

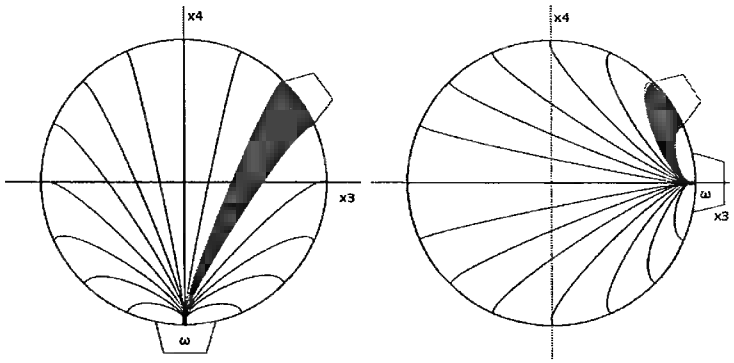

(a) (b)

Figure 2. Different positions of current injection electrode

3. Improvement of back-projection by Santosa and Vogelius

Santosa and Vogelius suggested that instead of using the region between two equipotential lines, the algorithm should find the corresponding electric potential measurement for a certain point inside the domain, according to the equipotential lines. Since there is a limited number of electric potential measurements on the boundary, they suggest a linear interpolation to find these measurements.

From the orientation and position of the electrode shown on Fig. 1(b), it is possible to find the point on the boundary of the domain with the same electric potential measurement of the point desired by equations 14 and 15

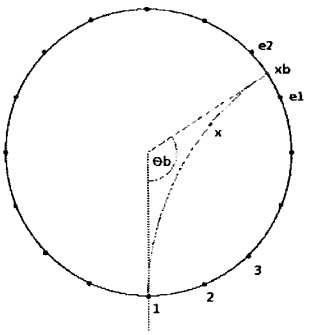

Figure 3. The electric potential measurement of certain point x

$$x_{b3} = \frac{4U}{4U^2 + 1} \tag{14}$$

$$x_{b4} = \frac{2}{4U^2 + 1} - 1 \tag{15}$$

Using the equations 14 and 15, and linear interpolation between electrodes $e1$ and $e2$, we obtain the electric potential measurements, which are differential measurements, of all the pixels inside the domain. Rotating the current injection pattern, other sets of measurements can be obtained. And the normalized conductivity distribution is

$$\frac{\delta\sigma_i}{\sigma_i} = -\frac{1}{m}\sum_{j=1}^{m}\frac{\delta U_j}{U_j}\left(2V_{i,j} - 1\right) \tag{16}$$

where i represent the pixels, j represent a pair of electrodes, $\delta\sigma_i$ is the perturbed conductivity, σ_i is the conductivity of reference, m is the total number of pair of electrodes, δU_j is the perturbed electric potential, U_j is the electric potential of reference, and $V_{i,j}$ is the equipotential line corresponding to the current passing through the desired point.

The equations 14 and 15 are for dipole at position 1, or $-\pi/2$. With the rotation of the current injecting electrodes, it is necessary to change coordinates according to

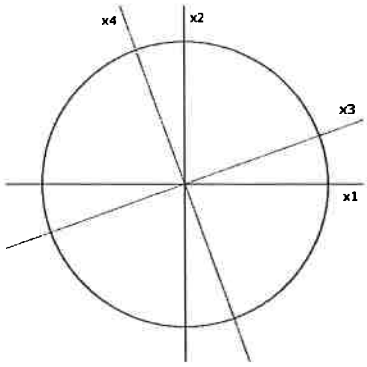

Figure 4. Relation between (x3,x4) and (x1,x2)

$$x_3 = x_1 * cos\theta + x_2 * sin\theta \tag{17}$$

$$x_4 = -x_1 * sin\theta + x_2 * cos\theta \tag{18}$$

4. Conductivity X Resistivity

The two methods described before give images of distribution of conductivity. For medical interpretation, images given in term of distribution of resistivity are better. Using concepts of calculus of variations, the relation of both images is straightforward

$$\frac{\delta\sigma}{\sigma} = \frac{\delta\left(\frac{1}{\rho}\right)}{\frac{1}{\rho}} = \frac{\frac{-\delta\rho}{\rho^2}}{\frac{1}{\rho}} = -\frac{\delta\rho}{\rho} \tag{19}$$

Therefore, equation 19 is rewritten as

$$\frac{\delta\rho}{\rho} = \frac{\mathbf{1}}{\mathbf{m}}\sum_{\mathbf{j=1}}^{\mathbf{m}}\frac{\delta\mathbf{U}}{\mathbf{U}}\left(\mathbf{2V} - \mathbf{1}\right) \tag{20}$$

5. Results

Five images resulting from experimental data are presented. All of them were obtained through the back-projection algorithm as described by Santosa and Vogelius (1990), with the interpretation in terms of resistivity. These images were obtained using a cylindrical acrylic object placed at the center of an experimental cylindrical container, then 30 mm apart from the center, then 60 mm apart from the center, then 90 mm apart from the center and, finally, 120 mm apart from the center of the container, as shown on Fig. 5.

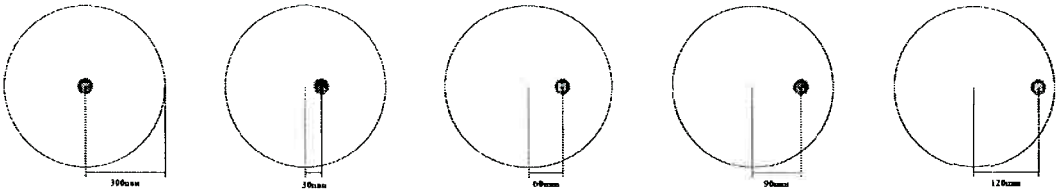

(a) at the center (b) 30 mm apart from the center (c) 60 mm apart from the center (d) 90 mm apart from the center (e) 120 mm apart from the center

Figure 5. An acrylic object placed inside an cylindrical container with 300mm of diameter

The cylindrical object has 30 mm of diameter, the experimental cylindrical container has 300 mm of diameter and the container was filled with 20 mm of 0.9% saline solution. On the border of the container there are 30 electrodes placed at equal distances. The electrodes were used to measure the electric potential variation due to a disturbance caused by the presence of the acrylic object and the injection of current through an adjacent of these electrodes. These electric potential measurements have accuracy of 2.5 mV and the results are shown in Fig. 6.

(a) at the center (b) 30 mm apart from the center (c) 60 mm apart from the center (d) 90 mm apart from the center (e) 120 mm apart from the center

Figure 6. Images estimated

The results show clearly the non-uniform sensitivity of the algorithm. The increasing blurring of the object when the object is closer to the center of the domain is one of the performance problems of this method. The filtered Backprojection has better performance in terms of resolution and sensitivity matrix based algorithms have, to some extent, more uniform sensitivity and spatial resolution [7, 8, 9].

6. Final Comments

The back-projection algorithm was implemented and described. The algorithm was tested and some of its performance characteristics were confirmed. The algorithm has non-uniform sensitivity, as can be seen on the resulting images. At the center of the container, the acrylic object is seen blurred, while at the boundary the image is better defined. The mapping from conductivity distribution into resistivity distribution is simply a multiplication by minus one, when the images are characterized by small deviations from a uniformly distributed value of conductivity or resistivity.

7. Acknowledgments

Financial Supports by The State of São Paulo Research Foundation, process 01/05303-4 is gratefully acknowledged.

8. References

Yorkey, T.J. and Webster, J.G.,1986, "Comparison Of Impedance Tomographic Reconstruction Algorithms", Clinical Physics and Physiological Measurement, vol.8 supp A, pp.55 - 62.

Brown, B.H., Barber D.C. and Seagar A.D., 1988, "Applied potential tomography: possible clinical applications", Clinical Physics and Physiological Measurement, vol. 6 num. 2, pp.109 - 121.

Santosa, F. and Vogelius, M.,1990, "Backprojection algorithm for electrical impedance imaging", SIAM Journal on Applied Mathematics, vol.50, No. 1, pp.216 - 243.

Metheral, P., 1998, "Three Dimensional Electrical Impedance Tomography of the Human Thorax", phD thesis, University of Sheffield

Kotre, C. J. 1994, EIT Image Reconstruction using sensitivity weighted filtered backprojection, Physiological Measurements, vol. 15, pp. A125-A136.

Avis, N.J. and Barber, D.C., 1995, "Incorporating a priori information into the Sheffield filtered backprojection algorithm", Physiological Measurements, vol.16 supp A, pp.111-122.

Adler, A. and R. Guardo 1996, "Electrical Impedance Tomography: Regularized Imaging and Contrast Detection", IEEE Trans. on Medical Imaging, vol. 15, no. 2, April, 1996, pp. 170-179. Clinical Physics and Physiological Measurement, vol.8 supp A, pp.55 - 62.

Aya,J.C.C., de Moura,F.S., Pai,C.N., Bevilacqua, J.C., Lima, R.G., 2005,"Back-Projection Resolution Improvement Through Measurement Interpolation Using The Finite Element Method", Proceedings of TMSi 2005.

Wedberg, T.C., Stamnes, J.J. and Singer, W., 1995, "Comparison of the filtered backprojection and the filtered backprojection algorithms for quantitative tomography", Applied Optics, vol.34, num.38, pp.65-75.

9. Responsibility notice

The authors are the only responsible for the printed material included in this paper

ANEXO C – Algoritmo Caixa-Preta: regularizações

ABCM Symposium Series in Mechatronics

Regularizations for a Black Box Back-projection EIT algorithm

Julio C. C. Aya
Department of Mechanical Engineering - Polytechnic School of University of São Paulo Av. Prof. Mello de Moraes, 2231 - São Paulo - SP - 05508-900, Brazil
jccaya@usp.br

Fernando Silva de Moura
Department of Mechanical Engineering - Polytechnic School of University of São Paulo Av. Prof. Mello de Moraes, 2231 - São Paulo - SP - 05508-900, Brazil
fernando.moura@poli.usp.br

Pai Chi Nan
Department of Mechatronic and Mechanical Systems Engineering - Polytechnic School of University of São Paulo Av. Prof. Mello de Moraes, 2231 - São Paulo - SP - 05508-900, Brazil
pai.nan@poli.usp.br

Ronaldo K. Schweder
Department of Mechanical Engineering - Polytechnic School of University of São Paulo Av. Prof. Mello de Moraes, 2231 - São Paulo - SP - 05508-900, Brazil
ronaldo.schweder@poli.usp.br

Raul Gonzalez Lima
Department of Mechanical Engineering - Polytechnic School of University of São Paulo Av. Prof. Mello de Moraes, 2231 - São Paulo - SP - 05508-900, Brazil
rauglima@usp.br

Abstract.
One of the objectives of Electrical Impedance Tomography (EIT) is to estimate the resistivity distribution based on measurements of electrical potential on the boundaries of a domain of interest. In this work we propose an algorithm that identifies directly the back-projection matrix given known perturbations of the resistivity distribution and their associated boundary electrical potential perturbations, called Black Box Algorithm, two new regularizations for the Black Box Algorithm, one of the new regularizations have his performance compared to two classical regularization methods, truncation of singular values and Tikhonov regularization.
Keywords: *black-box, back-projection, Electrical Impedance Tomography, forward problem*

1. Introduction

The Electrical Impedance Tomography (EIT) is a method for estimating the impedance distribution in a domain. The domain can be modeled through the Finite Elements Method. The variable of interest is the impedance distribution or variations in time of the impedance distribution. The problem of estimating the impedance distribution knowing the injected current, measuring electrical potentials on the boundary and knowing the structure of the model characterizes an inverse problem.

The value of the electric of the impedance of the different biological tissues is governed fundamentally by the concentration of different fluids (blood, water, air, etc. ..), this is the reason why EIT has being applied to monitor gastric functions, the oesophagus, lung ventilation, pulmonary edemas and brain clots, for instance. It is possible possible to say that the lung is a privileged tissue for being monitored by EIT, because is a function of the air content and blood content, which suffer changes during the respiratory and cardiac cycles.

Initial work by Brown (Barber and Brown, 1984) used an isopotential approach for solving the inverse problem. The backprojection method is based on linearization and delivers difference images. This algorithm can be described as follows. Two different sets of measurements are required. The first set voltage is V_0, is a reference set of measurements. The second set of measurements V_1 is related to the modified impedance distribution. An estimate of the normalized resistivity can be computed from the formula

$$\Delta\rho = \mathrm{B}\Delta V \tag{1}$$

where

$$\Delta\rho = \frac{\rho_1 - \rho_0}{\rho_0}$$
$$\Delta V = \frac{V_1 - V_0}{V_0},$$

and $\mathbf{B}$ is so-called *backprojection matrix*, the construction of which can be found in (Santosa and Vogelius, 1990).

The objective of this work is to obtain an algorithm to identify directly the *backprojection matrix*, using a set of independent, known difference images, and a set of accurately computed boundary data through a Finite Elements model FEM. Four procedures can be used to directly identify the back-projection matrix $\mathbf{B}$, to follow:

1. truncation of singular values decomposition
2. Tikhonov regularization

and one new regularization

3. Heuristic
4. Filtered columns of B

2. Theory

Consider a domain with unknown electromagnetic properties. The objective of the EIT is to estimate the distribution of impedance of the domain, given the excitation current imposed of the boundary, and known the electric potentials measured in regions of the contour of domain. In order to estimate the impedance distribution, a set of electrodes they are attached to the boundary of the domain and electric currents are applied in some electrodes. A particular choice of current intensities applied to the electrodes will be called of a "current pattern". For each current pattern, the electrical potential between pairs of electrodes are measured. After gathering the potential data it is possible resistivity distribution of the domain.

It is common to define two problems in EIT. In the *Forward Problem* are known the resistivity distribution, the current patterns, the structure of the model and the electrode potentials are desired. In the Inverse Problem, are known the electrode potentials, the patterns of excitation, and it is desired to know the resistivity distribution of the domain.

2.1 Forward Problem

The forward problem in the EIT calculates the potentials in the electrodes, known the resistivity distribution and the current patterns. The electric model, using the Finite Elements Method, of a domain is the matrical equation (Logan, 1986) and (Sadiku, 1992)

$$Y(\rho) \cdot V = C, \tag{2}$$

where $Y(\rho)$ is the condutivity matrix, $V = [v_1, \ldots, v_q]$ is a matrix of potentials, each column of this matrix is composed by nodal potentials, $C = [c_1, \ldots, c_q]$ is a matrix of current patterns each column represents a current pattern. Both c_i and v_i are vectors with ne elements, where ne is the number of nodes of the mesh.

In order to solve eq.2 it is necessary to remove the singularity of the matrix $Y(\rho)$. This is done imposing the potential of a node, for example, with null value (Yorkei et. al, 1987).

2.2 Inverse Problem

The inverse problem consists on estimate the resistivity distribution of of the domain, from a set of current patterns, measures of voltages in the electrodes and the structure of the model.

In the equation: Eq. (2) the condutivity matrix $Y(\rho)$ has known structure, however the parameters of resistivity are not known. Denoting the vector of electric resistivity $\rho \in \Re^m$, where m it is the number of elements of the mesh, the equation Eq. (2) can be rewritten in the next form:

$$V(\rho) = [Y(\rho)]^{-1} \cdot C. \tag{3}$$

It is possible to define a nonlinear map $\vec{f} : \rho \rightarrow V_j$ where V_j is a vector of electrodes potentials related to the j-th current pattern. Therefore, the vectors of electrodes potentials are nonlinear functions of the distribution of resistivity.

3. Black-Box

The main idea of the black-box back-projection method is that if good images, relative variations of resistivity, and good measurements, relative variations of electrode potentials, are available, then a matrix that relate measurements and images may be estimated. The method forms a set of difference images and computes, using a finite element model, the respective variations on electrode potentials. From this two sets of information it estimates the back-projection matrix.

The black-box back-projection algorithm estimates directly the $\mathbf{B}$ matrix of back-projection given the variation of potential on the boundary of the domain when the resistivity of each finite element of domain varies. The method assumes linearity between variation of potentials at the electrodes and variation of electrical resistivity.

First, it is assumed an initial resistivity distribution which will be used as reference. With this reference, the electrical potentials are calculated, using a Finite Element model, for each current injection pattern. A perturbation is imposed on each finite element, one at a time. The potentials at the electrodes are calculated and normalized with respect to the potential corresponding to the reference value. The perturbed potentials are arranged as vectors. A matrix of perturbed potentials is formed such that each column of this matrix is a perturbed potential vector. Through the perturbed potential matrix and a matrix of resistivity perturbation, the matrix $\mathbf{B}$ can be determined.

The procedure to determine $\mathbf{B}$ is:

1. assume a known electrical resistivity at each one of n elements of domain, arrange as vector ρ^0. The linearization of the model is performed around ρ^0.
2. each current injection pattern is denoted by $\{c_j\}_{e\times 1}$ for $j = 1, 2, \ldots, e$;
3. the potentials at the electrodes, v_j^0, are determined from the direct problem,

$$\mathbf{Y}|_{\rho^0} v_j^0 = c_j \quad , \quad j = 1, 2, \ldots, e. \tag{4}$$

4. a known perturbation on the resistivity element of the i-*th* element of ρ^0, is denoted by $\delta\rho_i$ and $i = 1, 2, \ldots, n$;
5. vectors $\{\delta\rho^i\}_{n\times 1}$ are formed such that all elements are null but the i-*th* element that contains $\delta\rho_i$, i. e., ${\delta\rho^i}_i = \delta\rho_i$;
6. for each current pattern c_j, the potentials at electrodes, $\{v_j^i\}$ related to a resistivity perturbation $\delta\rho^i$ are determined by the direct problem,

$$\mathbf{Y}|_{(\rho^0+\delta\rho^i)} v_j^i = c_j \quad , \quad j = 1, 2, \ldots, e \quad , \quad i = 1, 2, \ldots, n. \tag{5}$$

7. let $\{v^0\}_{e^2\times 1}$ be an augmented vector formed of $\{v_j^0\}_{e\times 1}$ for $j = 1, 2, \ldots, e$, such that,

$$v^0 = \begin{bmatrix} v_1^0 \\ v_2^0 \\ \cdots \\ v_e^0 \end{bmatrix} . \tag{6}$$

8. let $\{v^i\}_{e^2\times 1}$ be an augmented vector formed of $\{v_j^i\}_{e\times 1}$ for $j = 1, 2, \ldots, e$, such that

$$v^i = \begin{bmatrix} v_1^i \\ v_2^i \\ \cdots \\ v_e^i \end{bmatrix} \tag{7}$$

9. form a normalized vector $\{\psi^i\}_{n\times 1}$ such that each element, for $j = 1, 2, \ldots, n$, is

$$\{\psi^i\}_j = \frac{{\delta\rho^i}_j}{\rho_j^0} \tag{8}$$

10. form a normalized vector $\{\theta^i\}_{e^2\times 1}$ such that each element, for $j = 1, 2, \ldots, e$, is

$$\{\theta^i\}_{e^2\times 1} = \frac{{v^i - v^0}_j}{{v^0}_j}, \tag{9}$$

11. define a matrix $\Psi_{n\times n}$ such that

$$\Psi_{n\times n} = \left[\begin{array}{cccccc} \psi^1 & \dots & \psi^i & \dots & \psi^n \end{array} \right], \tag{10}$$

observe that this matrix is diagonal;

12. define a matrix $\Theta_{e^2\times n}$ such that

$$\Theta_{e^2\times n} = \left[\begin{array}{cccccc} \theta^1 & \dots & \theta^i & \dots & \theta^n \end{array} \right] \tag{11}$$

13. since each column of Ψ is an image and can be related to a column of Θ by a back-projection matrix, one can say,

$$\Psi_{n\times n} = \mathbf{B}_{n\times e^2}\Theta_{e^2\times n} \tag{12}$$

14. finally, determine the matrix $\mathbf{B}$ that minimizes an error index, eq. 24.

Once the matrix $\mathbf{B}$ is obtained, estimation of a difference image is performed multiplying B and a normalized vector of variation of electrode potentials related to each current injection pattern, according to eq. 13

$$\Delta\rho = \mathbf{B}\Delta V \tag{13}$$

where $\{\Delta\rho\}_{n\times 1}$ is such that the j-*th* element is $\frac{\rho-\rho^0{}_j}{\rho^0{}_j}$ for $j = 1, 2, \dots, n$, and $\{\Delta V\}_{e^2\times 1}$ is such that the j-*th* element is $\frac{V_{measured}-V^0_{measured\,j}}{V^0_{measured\,j}}$ for $j = 1, 2, \dots, e^2$.

4. Determination of B

This paper describes four procedures to obtain the black-box back-projection matrix B. This matrix is not square and the problem is ill-conditioned.

Methods for developed for estimation of B:

1. the first method consist on using *pseudo-inverse* calculation. This calculation is done using singular value decomposition (SVD), the calculation is controlled by the number or singular values.
2. the second method uses a Tikhonov regularization. which is determination of a smoother approximated solution compatible with the datas observed for a certain level of noise, inputting a priori information, that changes the matrix to well-posed.
3. the third method will be denominated *Heuristic regularization*
4. the four method will be called *Filtered B reguarization*

4.1 Truncating the Singular Values

Any matrix can be decomposed into three matrices U, Σ and V (Watkins 1991),

$$\Theta = USV^T \tag{14}$$

where

$\Rightarrow$ $U \in \Re^{e^2\times m}$ is an ortonormal matrix

$\Rightarrow$ $S \in \Re^{m\times m}$ is a diagonal matrix containing singular values of Θ

$\Rightarrow$ $V \in \Re^{m\times m}$ is an ortonormal matrix

with the matrix decomposed, its pseudo-inverse is computed as

$$\Theta^+ = VS^{-1}U^T, \tag{15}$$

where S^{-1} is computed as

$$S^{-1}(i,i) = \left\{ \begin{array}{ll} \frac{1}{S(i,i)} & \text{if } S(i,i) > \xi \\ 0 & \text{if } S(i,i) \leq \xi \end{array} \right. \tag{16}$$

and ξ is the parameter to determine which singular values will be used.

Now, the matrix $\mathbf{B}$ is determined as

$$\mathbf{B} = \Psi\Theta^+ \tag{17}$$

4.2 Tikhonov Regularization

To solve an ill-posed problem is necessary adicional information. Tikhonov and Arsenin (1977) started a general formulation for ill-posed problems, called regularization or method of regularization. The inverse problem is formulated as an optimization problem with restrictions.

The error can be defined as

$$\mathbf{E} = \mathbf{\Psi}^T - \mathbf{\Theta}^T\mathbf{B}^T \tag{18}$$

and the error index is defined as

$$IE = \mathbf{E}^T\mathbf{E} + \lambda\mathbf{B}\mathbf{B}^T, \tag{19}$$

the error index is minimized in respect to $\mathbf{B}$ when

$$\mathbf{B} = \mathbf{\Psi}^T\mathbf{\Theta}^T\left[\mathbf{\Theta}\mathbf{\Theta}^T + \lambda\mathbf{I}\right]^{-1} \tag{20}$$

where $\mathbf{I} \in \Re^{e^2 \times e^2}$ is the identity matrix and λ is a scalar parameter.

4.3 Heuristic Regularization

The matrix $\mathbf{\Theta}^T\mathbf{\Theta}$ is ill-conditioned. The inversion of $\mathbf{\Theta}^T\mathbf{\Theta}$ for $\mathbf{B}$ determination introduce great numerical errors. Therefore, to determine $\mathbf{B}$, a regularization is necessary.

An error index is defined as,

$$IE = tr\left\{\mathbf{E}^T\mathbf{E} + \alpha\mathbf{B}^T\mathbf{F}^T\mathbf{F}\mathbf{B} + \beta\mathbf{B}^T\mathbf{M}^T\mathbf{M}\mathbf{B}\right\}, \tag{21}$$

where $\mathbf{F}$ is a high pass spatial filter considering each column of $\mathbf{B}$ like an image, $\mathbf{M}$ is a matrix for improving the uniformity of the sensitivity, α and β are regularization parameters, and matrix $\mathbf{E}$ is defined as

$$\mathbf{E} = \mathbf{\Theta}(\mathbf{\Psi} - \mathbf{B}\mathbf{\Theta}). \tag{22}$$

The matrix $\mathbf{M}$ is a diagonal matrix such that each element of the diagonal is

$$M_{ii} = r(i)^p, \tag{23}$$

where $r(i)$ is the distance of the geometrical center of the i-*th* finite element to the center of the domain, divided by the radius of the domain. And p is an experimentally adjusted real parameter, to attenuate localization error and non-uniform sensitivity.

The minimum of the error index with respect to $\mathbf{B}$ is achieved when,

$$\mathbf{B} = (\mathbf{\Theta}^T\mathbf{\Theta} + \alpha\mathbf{F}^T\mathbf{F} + \beta\mathbf{M}^T\mathbf{M})^{-1}\mathbf{\Psi}\mathbf{\Theta}^T. \tag{24}$$

4.4 Filtered columns of B

The error index is defined at the equation Eq. (21), the matrix $\mathbf{E}$ is redefined as

$$\mathbf{E} = (\mathbf{\Psi} - \mathbf{B}\mathbf{\Theta}). \tag{25}$$

The minimum of the error index with respect to $\mathbf{B}$ is achieved when,

$$\mathbf{B}\mathbf{\Theta}\mathbf{\Theta}^T + (\alpha\mathbf{F}^T\mathbf{F} + \beta\mathbf{M}^T\mathbf{M})\mathbf{B} = \mathbf{\Psi}\mathbf{\Theta}^T. \tag{26}$$

Note that the equation above is like the Sylvester equation

$$AXB^T + CXD^T = E, \tag{27}$$

where A and C has the sizes $m \times m$, B and D are $n \times n$, and E is $m \times n$.

The Sylvester problem is resolved by Bartels (et.al) (1972) and Gardiner (et.al) (1992). To determine $\mathbf{B}$, $A = \alpha\mathbf{F}^T\mathbf{F} + \beta\mathbf{M}^T\mathbf{M}$, $B = I$, $C = I$, $D = \mathbf{\Theta}\mathbf{\Theta}^T$ e $E = \mathbf{\Psi}\mathbf{\Theta}^T$.

5. Parameters and methodology

The mesh used to create the matrix $\mathbf{B}$ has 300.0 mm of diameter, $n = 2034$ pentahedrical elements (prisms of triangular base), divided equally in three layers, 30.0 mm of total height and $e = 30$ electrodes. The Figure 1 shows the top view of the mesh.

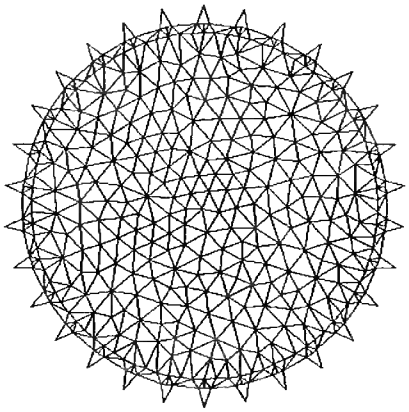

Figure 1. Finite Element Mesh.

Figure 2. Experimental Container.

The initial distribution of electrical resistivity ρ_0 was homogeneous and equal to $3.0\,\Omega m$. The electrodes parameters were all equal to $0.02\,\Omega m^2$. The imposed perturbation $\delta\rho_i$ was $+30\%$ of initial value.

The electrical potential data set was collected from an experimental cylindrical container shown on Fig. 2 filled with 0.5% saline solution. An acrylic cylinder with 32 mm of diameter was used to simulate a region with different electrical resistivity. The object will be analyzed on two positions. Position 1 has the object placed at the center of the container. Position 2 has the object placed 120 mm apart from the center of the container.

6. Results

Eight images resulting from experimental data are presented. The first two images were obtained through the back-projection algorithm as described by Santosa and Vogelius (1990).

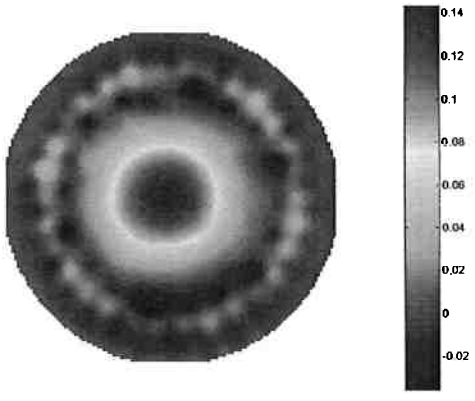

(a) Object in position 1

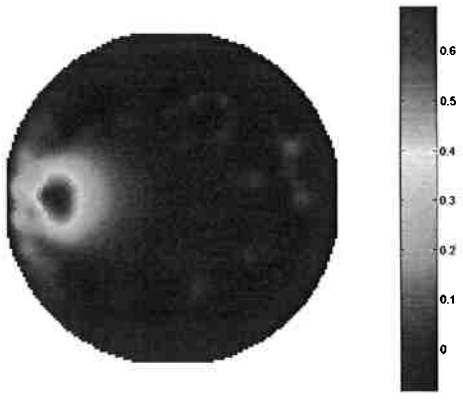

(b) Object in position 2

Figure 3. Images using Santosa and Vogelius algorithm.

6.1 Truncation of Singular Values

The following images were obtained from experimental data using truncation of singular values. The image at Fig. 4(a) represent the object placed at position 1 with $\xi = 0.01$ which represent the use of only 8% of all the singular values and the image at Fig. 4(b) represent the object placed at position 2 with $\xi = 0.0006$ witch represent the use od only 15%

of all singular values.

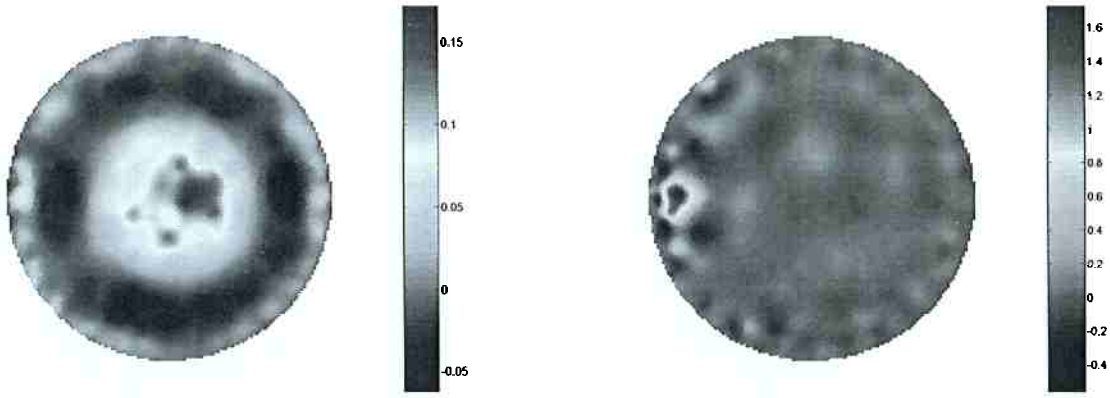

(a) Object in position 1 (b) Object in position 2

Figure 4. Images using truncation of singular values.

6.2 Tikhonov Regularization

The following images were obtained from experimental data using Tikhonov regularization. The image at Fig. 5(a) represent the object when placed at position 1 with $\lambda = 1.0\,\text{e-}5$ and the image at Fig. 5(b) represent the object when placed at position 2 with $\lambda = 1.0\,\text{e-}4$.

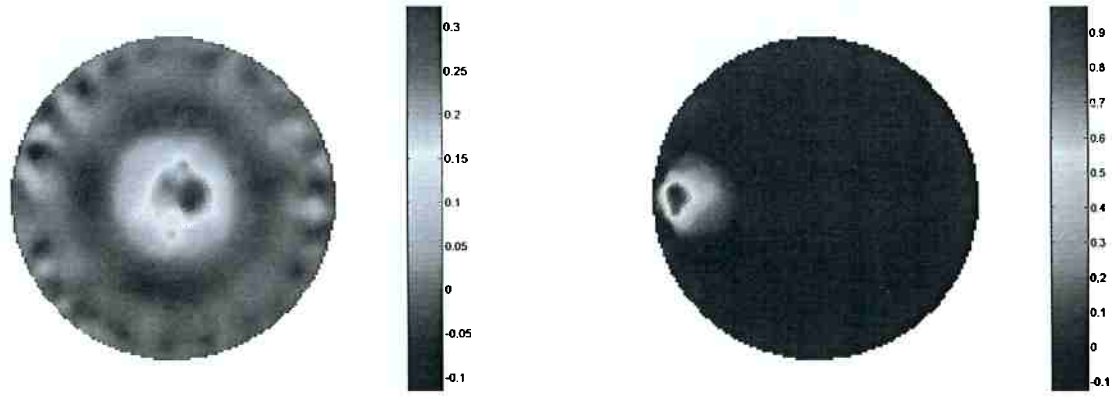

(a) Object in position 1 (b) Object in position 2

Figure 5. Images using Tikhonov Regularization

6.3 Heuristic Regularization

The following images were obtained from experimental data using heuristic regularization. For this regularization, $\alpha = 1.0\,\text{e-}4$ and $\beta = 4.0\,\text{e-}3$ were chosen. The image at Fig. 6(a) represent the object when placed at position 1 and the image at Fig. 6(b) represent the object when placed at position 2.

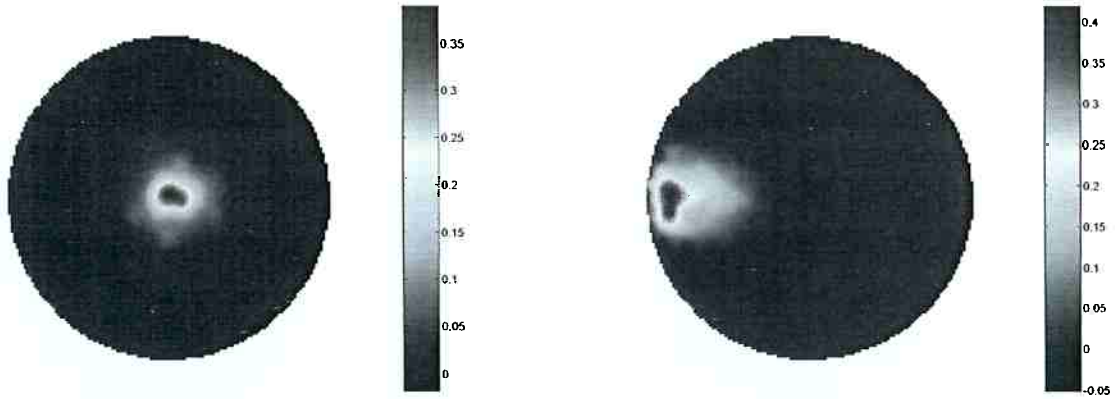

(a) Object in position 1 (b) Object in position 2

Figure 6. Images using Heuristic Regularization

7. Conclusion

It can be seen that the images obtained by these algorithms are compatible with the correct positions of the objects, and the best resolution is obtained using the Heuristic regularization. The numerical solution of the *Filtered column of B* regularization is under development.

The regularization for improving the uniformity of the sensitivity proved to be efficient. The maximum values of pixels for images when the object is at the boundary or at the center using heuristic algorithm, are similar due to parameter β, which reduces the non-uniform sensitivity. The non-uniform is present at the other algorithms

8. Acknowledgements

Financial Supports by The State of Sao Paulo Research Foundation, process 01/05303-4 are gratefully acknowledged.

9. References

Adler, A.,1995, "Measurement of Pulmonary Function with Electrical Impedance Tomography", Ph.D., Université de Montréal.

Barber, D.C. and Brown, B.H.,1984, "Applied Potential Tomography", Journal of Physics E: Scientific Instruments, vol. 17, No. 9, pp.723 - 733.

Bartels R.H. and Stewart G.W., 1972, "Solution of the Matrix Equation $AX + XB = C$" Communications of ACM, Vol. 15, No. 9, pp. 820-826.

Brown, B.H.,2003, "Electrical impedance tomography (EIT): A review", Journal of Medical Engineering and Technology, vol. 27, No. 3, pp.97 - 108.

Gardiner J.D., Laub, A.J., Amato, J.J. and Moler C.B., 1992, " Solution of the Sylvester Matrix Equation $AXB^T + CXD^T = E$", ACM Transactions on Mathematical Software, Vol 18, No 2, pp. 223-231.

Hua, P., Woo, E.J., Webster, J.G. and Tompkins, W.J.,1993, "Finite element modeling of electrode-skin contact impedance in electrical impedance tomography", IEEE Transactions on Biomedical Engineering, vol.40, No. 4, pp.335 - 343.

Logan, D., 1986, A First Course in the Finite Element Methods, Boston : PWS Engineering.

Sadiku, N., 1992, Numerical Techniques in Electromagnetics, Boca Raton : Crc Press.

Santosa, F. and Vogelius, M.,1990, "Backprojection algorithm for electrical impedance imaging", SIAM Journal on Applied Mathematics, vol.50, No. 1, pp.216 - 243.

Tikhonov, A. and Arsenin, V., 1977, *Solution of Ill-posed Problems*. New York : John Wiley & Sons.

Yorkey, T.J. and Webster, J.G.,1986, "Comparison Of Impedance Tomographic Reconstruction Algorithms", Clinical Physics and Physiological Measurement, vol.8 supp A, pp.55 - 62.

Yorkey, T., Webster, J. and Tompkins, W., 1987. "Comparing reconstruction algorithms for electrical impedance tomography", Transactions on Biomedical Engineering, vol.BME-34, No. 11, pp.843 - 852.

Watkins, D.S., 1991, Fundamental of Matrix Computation. New York : Johm Wiley & Sons.

10. Responsibility notice

The author(s) is (are) the only responsible for the printed material included in this paper

ANEXO D - Detecção de Pneumotórax

Real-time detection of pneumothorax using electrical impedance tomography*

Eduardo L. V. Costa, MD; Caroline N. Chaves; Susimeire Gomes; Marcelo A. Beraldo, RRT; Márcia S. Volpe, RRT; Mauro R. Tucci, MD, PhD; Ivany A. L. Schettino, MD, PhD; Stephan H. Bohm, MD, PhD; Carlos R. R. Carvalho, MD, PhD; Harki Tanaka, Eng, MD; Raul G. Lima, Eng, PhD; Marcelo B. P. Amato, MD, PhD

Objectives: **Pneumothorax is a frequent complication during mechanical ventilation. Electrical impedance tomography (EIT) is a noninvasive tool that allows real-time imaging of regional ventilation. The purpose of this study was to 1) identify characteristic changes in the EIT signals associated with pneumothoraces; 2) develop and fine-tune an algorithm for their automatic detection; and 3) prospectively evaluate this algorithm for its sensitivity and specificity in detecting pneumothoraces in real time.**

Design: **Prospective controlled laboratory animal investigation.**

Setting: **Experimental Pulmonology Laboratory of the University of São Paulo.**

Subjects: **Thirty-nine anesthetized mechanically ventilated supine pigs (31.0 ± 3.2 kg, mean ± SD).**

Interventions: **In a first group of 18 animals monitored by EIT, we either injected progressive amounts of air (from 20 to 500 mL) through chest tubes or applied large positive end-expiratory pressure (PEEP) increments to simulate extreme lung overdistension. This first data set was used to calibrate an EIT-based pneumothorax detection algorithm. Subsequently, we evaluated the real-time performance of the detection algorithm in 21 additional animals (with normal or preinjured lungs), submitted to multiple ventilatory interventions or traumatic punctures of the lung.**

Measurements and Main Results: **Primary EIT relative images were acquired online (50 images/sec) and processed according to a few imaging-analysis routines running automatically and in parallel. Pneumothoraces as small as 20 mL could be detected with a sensitivity of 100% and specificity 95% and could be easily distinguished from parenchymal overdistension induced by PEEP or recruiting maneuvers. Their location was correctly identified in all cases, with a total delay of only three respiratory cycles.**

Conclusions: **We created an EIT-based algorithm capable of detecting early signs of pneumothoraces in high-risk situations, which also identifies its location. It requires that the pneumothorax occurs or enlarges at least minimally during the monitoring period. Such detection was operator-free and in quasi real-time, opening opportunities for improving patient safety during mechanical ventilation. (Crit Care Med 2008; 36:1230–1238)**

KEY WORDS: pneumothorax; electric impedance; diagnostic imaging; artificial respiration; catheterization

Pneumothorax is a common complication of routine interventions on intensive care units. For example, it complicates mechanical ventilation in 10% to 42% of patients (1–3) and appears following the placement of a central venous catheter in 2% (4, 5). In the scenario of positive pressure ventilation, pneumothorax tends to progressively increase and lead to cardiovascular depression if not promptly recognized (6, 7).

There is no available method, however, for continuous pneumothorax surveillance in high-risk situations. Late diagnoses can thus be common even when sensitive methods are employed (e.g., computed tomography [CT] or lung ultrasound) (8, 9) because clinical suspicion at the bedside is required to decide the timing of these exams.

Electrical impedance tomography (EIT) is a noninvasive monitoring tool that allows real-time imaging of ventilation (10, 11). It reconstructs a cross-sectional image of the lung's regional conductivity using electrodes placed circumferentially around the thorax. It has been shown that EIT images correlate well with regional ventilation within the thorax (11, 12). Its noninvasiveness, low cost, and high sensitivity

*See also p. 1380.

From the Respiratory Intensive Care Unit, University of São Paulo School of Medicine, Brazil (ELVC, CNC, SG, MAB, MSV, MRT, IALS, SHB, CRRC, HT, MBPA); and Department of Mechanical Engineering, Polytechnic Institute of the University of São Paulo, Brazil (RGL).

For additional information regarding this article, please see the supplementary video, which can be viewed at www.ccmjournal.org.

Supported, in part, by grants from Fundação de Amparo à Pesquisa do Estado de São Paulo (FAPESP) (São Paulo State Research Support Foundation), Conselho Nacional de Desenvolvimento Científico e Tecnológico (CNPq) (National Council for Scientific and Technological Development), and Financiadora de Estudos e Projetos (FINEP) (Studies and Projects Financial Support Provider).

Dr. Bohm has consulted for Dixtal Biomedica and is the inventor and owner of patents for EIT technology. Dr. Schettino received honoraria for supporting the EIT project as a clinical specialist in intensive care medicine. Dr. Tanaka received honoraria for supporting the EIT project as an expert electronic engineer. In addition to financial support from FAPESP and FINEP, Drs. Lima and Amato received grant support from Dixtal Biomedica. The remaining authors have not disclosed any potential conflicts of interest.

Address requests for reprints to: Marcelo Amato, MD, Laboratório de Pneumologia LIM09, Faculdade de Medicina da USP, Av. Dr Arnaldo 455 (Sala 2206, 2nd floor), São Paulo 01246-903, Brazil. E-mail: amato@unisys.com.br

DOI: 10.1097/CCM.0b013e31816a0380

to changes in thoracic air content make EIT a promising real-time screening method for pneumothoraces in high-risk situations.

The purpose of this study was to 1) identify characteristic changes in EIT signals associated with pneumothoraces; 2) develop and fine-tune an algorithm for their automatic detection; and 3) prospectively evaluate the algorithm for its sensitivity and specificity in detecting pneumothoraces in real time.

MATERIALS AND METHODS

Experimental Setup

Experiments were performed on 39 anesthetized supine Landrace pigs (31.0 ± 3.2 kg, mean body weight ± SD) following the guidelines of animal experimentation after approval by the local animal care committee (details in Appendix).

Electric Impedance Tomography

EIT data were acquired using the impedance tomography platform called *enlight*, which was developed by our group (Experimental Pulmonology Laboratory, Polytechnic Institute of the University of São Paulo and Dixtal Biomedica Ltd, São Paulo, Brazil) capable of producing 50 online images per second. After measuring the thoracic perimeter, 32 self-adhesive electrodes were placed equidistantly around the circumference of the thorax just below the level of the axilla. Small amounts of electrical currents (5–8 mA; 125 kHz) were injected in a rotating sequence through pairs of electrodes, with one noninjecting electrode interposed between the injecting electrodes. During an injection pattern, the noninjecting electrodes were used to measure 29 differential voltages between electrode pairs. One complete acquisition cycle of 32 current patterns produced 928 voltage measurements comprising one "raw voltage frame" used as an input for a relative EIT image. These images were generated by a reconstruction algorithm for a cross section of the thorax, which is based on a sensitivity matrix derived from a three-dimensional finite element model (14) (Appendix). A "primary relative image" is created by comparing the most recent raw voltage frame with a reference or baseline frame chosen by the investigator. Output pixel values represent percentage changes in local tissue impedance, from reference to present time.

As shown previously, the average (or simple sum) of all pixel values within each output image can be plotted against the timeline, producing a global EIT plethysmographic signal. Such signal is linearly related to changes in parenchymal air content (11, 15). This concept can be applied regionally, within regions of interest, producing regional EIT plethysmographic signals. Details about the resolution/precision and noise of our EIT device can be found in the Appendix.

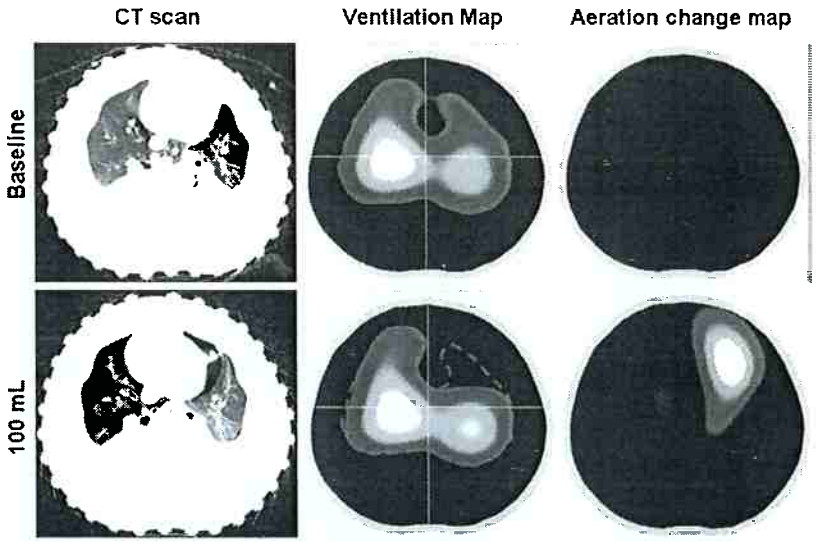

Figure 1. Computed tomography (*CT*), ventilation map, and aeration change map obtained at baseline (*top*) and after injecting 100 mL of air into the pleural space of the left upper quadrant (*bottom*). The arrow points to the induced pneumothorax (*left, bottom*).

Concept of Pneumothorax Detection by EIT

Ventilation Maps. Victorino et al. (11) showed that tidal oscillations in pixel values are proportional to tidal oscillations in tissue aeration. By calculating the amplitude of these oscillations (tidal ΔZ = delta impedance) along a sequence of primary relative images for a fixed pixel, one can estimate the local rate of ventilation and represent it by a color code. Such a procedure generates yet another derived image henceforth called a *ventilation map*, which is similar to the concept of functional images introduced by Frerichs (16) (Fig. 1).

During this study, ventilation maps were repeatedly refreshed every 9 secs, corresponding to the accumulation of 450 new primary relative images in an accrual image buffer. Perturbations caused by perfusion artifacts were attenuated in such maps by frequency-dependent filtering (Appendix).

Aeration Change Maps. Similarly to the image buffers described previously, the most recent raw voltages frames were also sent to an accrual voltage buffer containing 9 secs of data. Aeration change maps can be considered as secondary relative images derived from the comparison between one current raw voltage buffer, still in the random access memory, and a reference buffer previously stored. Voltages within both buffers were averaged along the time, producing two single averaged-voltage frames representing current and baseline conditions, respectively, which then served as inputs for a relative-image reconstruction. The current buffer was constantly refreshed, while the reference was maintained to represent the moment just before any intervention or pneumothorax induction. The relative image produced by such inputs represented sustained changes in thoracic impedance and easily identified regional changes in functional residual capacity. The averaging process filtered out transient changes in impedance produced by tidal breathing.

Interpreting the Maps and Detecting Pneumothoraces. Our algorithm for detecting pneumothoraces is based on the online analysis of ventilation maps and aeration change maps repeatedly refreshed after the accumulation of new image/voltage buffers (typically encompassing the last two to three complete respiratory cycles). In preliminary experiments, we observed that pneumothoraces caused characteristic perturbations in both maps: a localized bright spot in the aeration change map—close to the site of air injection—with a corresponding defect in the ventilation map (Figs. 1 and 2; see also supplemental online video). We reasoned that the former perturbation reflected a localized fixed increment in impedance caused by air pockets forming in the pleural space, whereas the latter represented the diminution of tidal ventilation and local compliance in this area due to the extrapulmonary air.

After computing the magnitude of such perturbations in each quadrant of the maps (see Experimental Protocol Section, part 1), we created a quasi online algorithm for determining the presence/absence of a pneumothorax as well as its location (Appendix). After some brief data collection during stable baseline conditions, the algorithm was

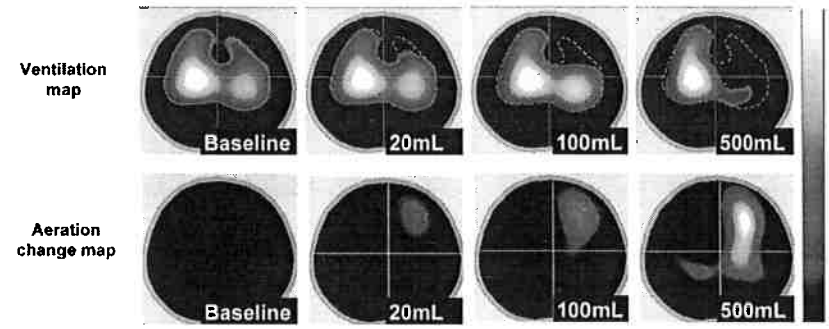

Figure 2. Ventilation maps (*top*) and aeration change maps (*bottom*) of one representative animal. From left to right, the baseline images are shown as well as those after injecting 20, 100, and 500 mL of air through the chest tube into the left upper quadrant. The color scale on the right shows in lighter tones either increased ventilation (*top*) or increases in aeration (*bottom*).

ready to run in real time and the animals were submitted to multiple interventions. Every two breaths, after processing the recently buffered information, the algorithm had to display a refreshed message and, in case of positive detection, to indicate the quadrant in which the pneumothorax was developing.

Experimental Protocol

Throughout the protocol, ventilation was delivered in pressure control mode, inspiratory-to-expiratory ratio of 1:2, F_{IO_2} of 1.0, respiratory rate of 20–30 cycles/min, and driving pressure of 15 cm H_2O.

Part 1: Designing the Detection Algorithm. Ten animals were used to design the detection algorithm (Fig. 3). A chest tube was inserted into the right (two animals) or left (eight animals) hemithorax to allow controlled induction of the pneumothorax (as well as its drainage afterward). Preliminary experiments were performed in the CT room to acquire the skills of positioning the tube along the most anterior part of the chest wall. After baseline data collection (EIT, mechanics, blood gas, and hemodynamics) at 5 cm H_2O positive end-expiratory pressure (PEEP), we injected 20-mL aliquots of air up to a total volume of 500 mL into the pleural space via the chest tube, waiting 1 min at each step. After reaching the maximal volume, we connected the chest tube to a water seal to allow the spontaneous drainage of the pneumothorax. In one animal, we simultaneously collected CT images during the entire protocol (Fig. 1). In five animals, the whole procedure was repeated after induction of diffuse lung injury (lavage with 25 mL/kg warm saline repeated as many times as needed to obtain a P_{O_2} <100 mm Hg, for ≥10 mins, at PEEP of 5 cm H_2O and a F_{IO_2} of 1.0).

Part 2: Optimizing Sensitivity and Specificity of Algorithm. It had to be ruled out that our algorithm inadvertently took the impedance perturbations caused by marked elevations in PEEP (simulating lung overdistension) (17) for a pneumothorax. Typically, high PEEP caused a sustained increment in impedance in the nondependent lung with corresponding defects in regional ventilation due to parenchymal overdistension and decreased regional compliance (>25% decrease in nondependent lung compliance, compared with a PEEP of 5 cm H_2O).

With the aim of determining specificity of our algorithm, eight additional animals were submitted to large step changes in PEEP after lung injury. Keeping a constant driving pressure of 15 cm H_2O, PEEP was either increased gradually in steps of 2 cm H_2O (from 5 to 25 cm H_2O) or abruptly from 5 to 25 cm H_2O. In total, 88 acute PEEP changes, including small and large steps, were tested in eight animals.

After analyzing the data, a highly sensitive and specific algorithm was calibrated to detect pneumothorax volumes of ≥20 mL in all EIT raw-voltage data files played back, simulating real-time acquisitions.

Part 3: Prospective Validation of Algorithm. Once the algorithm was calibrated (100% sensitivity and 100% specificity), we tested its accuracy in a prospective series of 21 additional pigs. During the monitoring of these animals, the algorithm was applied quasi real-time, displaying a refreshed diagnosis every 9 secs or once every two respiratory cycles (Fig. 3).

Statistical Analysis

Data are presented as mean ± SEM or median and interquartile range where appropriate. For comparing variables at different amounts of injected air, we used either repeated-measurements analysis of variance or the Friedman test of SPSS 10.0 (SPSS, Chicago, IL). We considered $p < .05$ as statistically significant.

RESULTS

Part 1: Detection Algorithm: Stepwise Increments of Intrapleural Air

Electrical Impedance Tomography Findings. There was a significant increase in the global EIT plethysmographic signal after the injection of 20 mL of air into the pleural space ($p < .001$) followed by further increases in mean impedance with every aliquot of air injected. The increase was confined to the thoracic quadrant where the air was injected (Figs. 1 and 2), producing visible changes in the aeration change maps. In contrast, there was a progressive decrease in regional ventilation (pixel impedance oscillations, or tidal ΔZ, observed in ventilation maps) within the quadrant containing the pneumothorax, which reached statistical significance when pneumothoraces were ≥100 mL ($p = .035$) (Fig. 4). The anatomical correspondence between EIT and CT slices can be observed in Figure 1.

Respiratory System Mechanics. Despite increasing amounts of air in the pleural space, up to 100 mL of injected air, the average behavior of the entire lung was that of enhanced ventilation due to better compliance ($p = .04$) (Fig. 5). Beyond 100 mL, the compliance behavior was heterogeneous: in eight of ten animals, compliance showed an initial increase, reaching a peak at different pneumothorax volumes in each of the animals (median, 200 mL; interquartile range, 80–400 mL) and decreasing thereafter. In two animals, compliance improved progressively until the maximum amount of air was injected (500 mL).

Arterial Blood Gases and Hemodynamics. P_{aCO_2} showed a nonsignificant decrease ($p = .17$) until a volume of 300 mL was injected. After that, there was a tendency to return to baseline levels ($p = .34$). P_{aO_2} presented a slight deterioration ($p = .34$) from baseline to 100 mL and a significant decrease from 100 mL to 500 mL ($p = .036$). The initial P_{aO_2} was 306.8 ± 171.4 mm Hg and the final 221.7 ± 207.6 mm Hg.

Mean arterial pressure started to decrease only after injection of ≥200 mL of air ($p = .01$). Heart rate showed no significant changes.

Part 2: Specificity of Algorithm: Animals Submitted to PEEP Steps Without Concurrent Pneumothorax

As opposed to the induction of pneumothoraces, which showed a sharp concentration of impedance perturbations in one of the thoracic quadrants, the EIT behavior in this control situation (PEEP

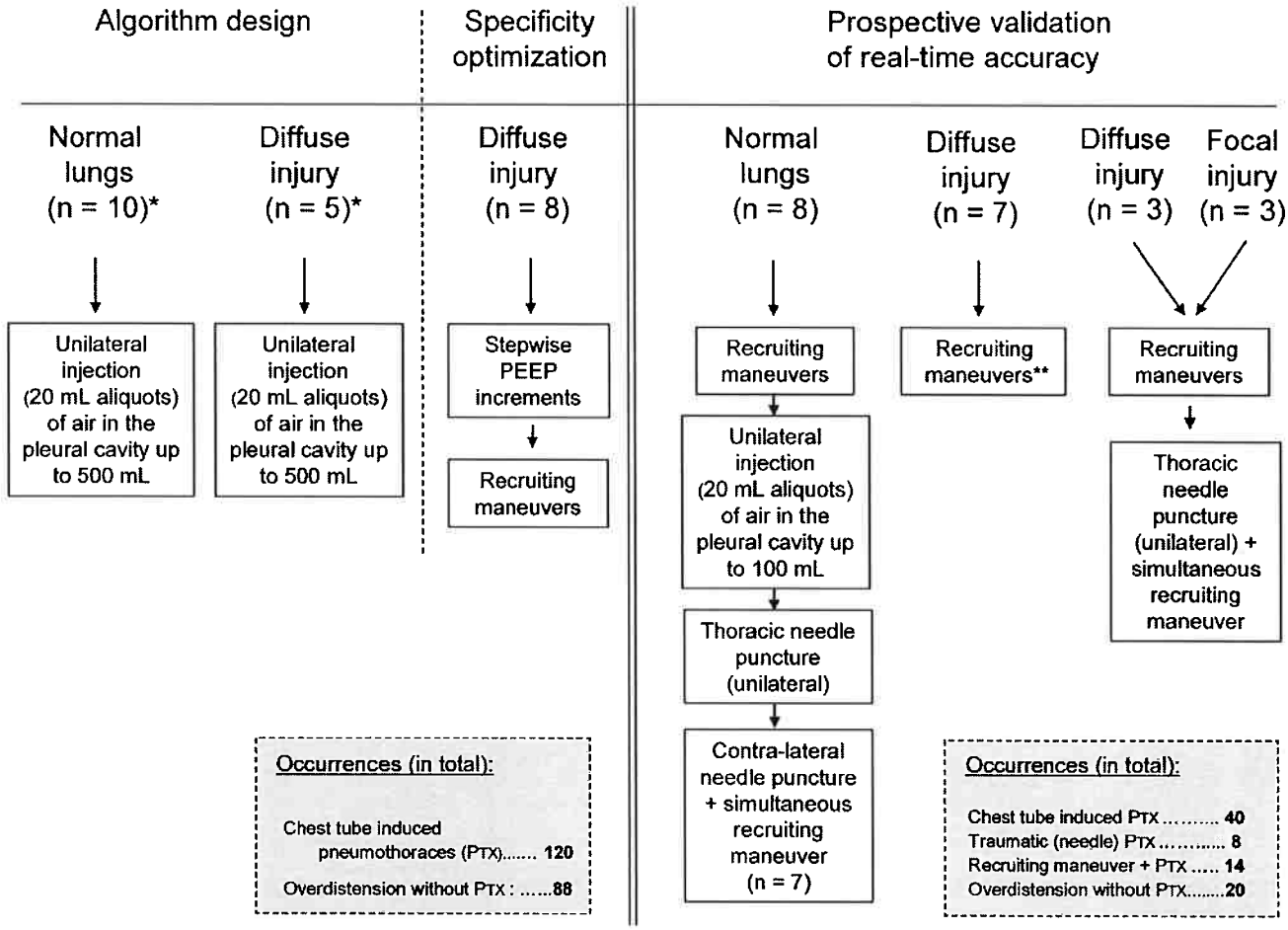

Figure 3. Study design. *Five animals were sequentially used for testing both the normal and later the diffuse injury condition with superimposed pneumothorax. **A unilateral pneumothorax was detected immediately after the recruiting maneuver, without any other associated intervention. *PEEP*, positive end-expiratory pressure. *Prx*, pneumothorax.

step) was characterized by a striking right-left symmetry (Fig. 6, right). This could be observed by analyzing the regional EIT plethysmographic signals or by visual inspection of aeration change and ventilation maps.

Part 3: Prospective Validation of Algorithm

Recruitment Maneuvers. Eight normal animals and 13 lung-injured animals were submitted to a recruitment maneuver, and there was one accidental barotrauma (in a bilaterally lavaged animal). In that animal, we were able to recognize the pneumothorax by EIT within seconds, much before any other variable was significantly affected. The algorithm had a specificity of 21 of 22 with one single false-positive result. In that case, a pneumothorax was detected in the lower left quadrant where an outlier and asymmetric increment in aeration was observed, in conjunction with a decrease in regional compliance.

Pneumothorax Generation Through the Chest Tube. In all animals, a pneumothorax was detected after the first injection of 20 mL, and always in the correct position. The automatic detector also confirmed the presence of pneumothoraces with all the other volumes of air injected. There was no false-negative result in any of the 40 different situations (each of the eight animals had pneumothoraces of five different volumes from 20 to 100 mL induced) resulting in a sensitivity of 100% for detecting volumes ≥20 mL.

Traumatic Pneumothoraces. By puncturing the thorax during a recruitment maneuver or during constant PEEP, we induced a total of 15 pneumothoraces in normal animals and six in injured animals. The detector identified correctly all of the pneumothoraces (sensitivity = 100%) with a mean delay of 3.1 ± 0.6 ventilatory cycles. The unplanned pneumothorax associated with a recruiting maneuver was also properly detected.

DISCUSSION

In this study, we found that EIT had a sensitivity of 100% to detect pneumothoraces as small as 20 mL in volume, with a diagnostic delay of ~3 respiratory cycles, which is not likely to be clinically relevant. The correct quadrant of the pneumothorax—potentially helpful information during emergency conditions—could be identified under all circumstances. All pneumothoraces induced by needle punctures were immediately diagnosed as was the unplanned one, which occurred during a recruitment maneuver.

Such early diagnosis could be accomplished due to the surprisingly large changes in the aeration change maps caused by even small volumes of air in the pleural space (Fig. 4*B*). The perturbations were localized enough to allow the development of a detection algorithm, which indicated also the location (quadrant) where the pneumothorax was taking place. We further optimized the

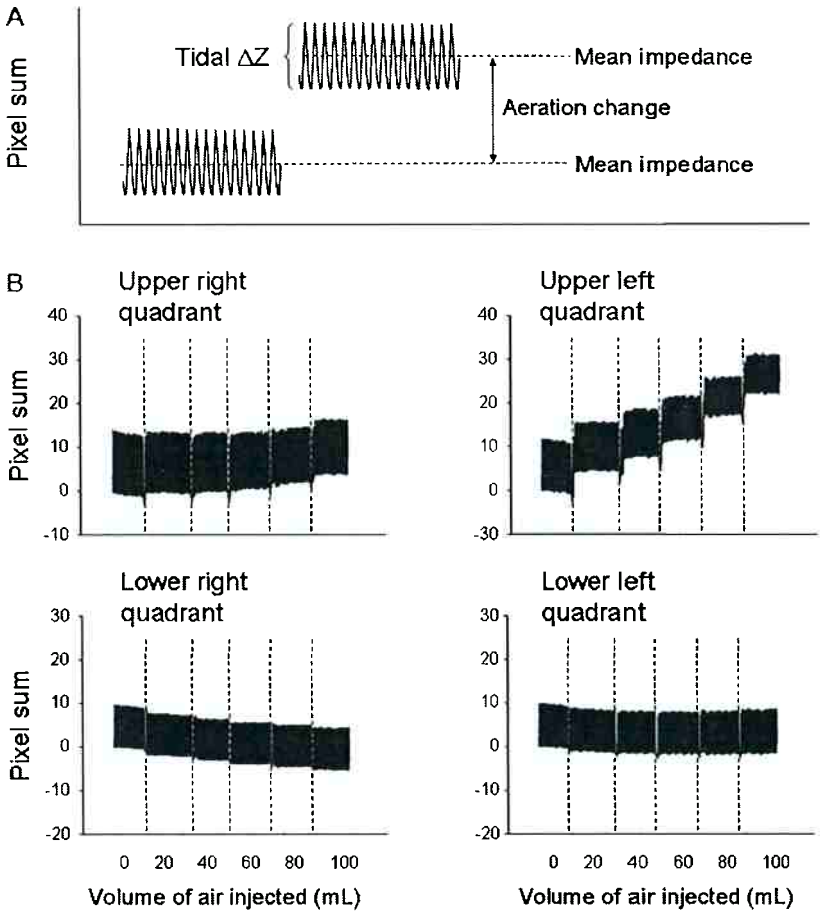

Figure 4. Typical changes in the regional electrical impedance tomography (*EIT*) plethysmographic signals for each of the four quadrants during pneumothorax induction. *A*, whereas the aeration change maps represent local changes in mean impedance, the ventilation maps represent local tidal ΔZ. *B*, variations in the sum of pixel values for each quadrant are displayed over time. As in the previous figures, free air was injected into the upper left quadrant. Note the progressive increment in pixel values in this quadrant containing the pneumothorax, as opposed to the remaining quadrants. Note also the decrease in the magnitude of impedance oscillations (tidal ΔZ).

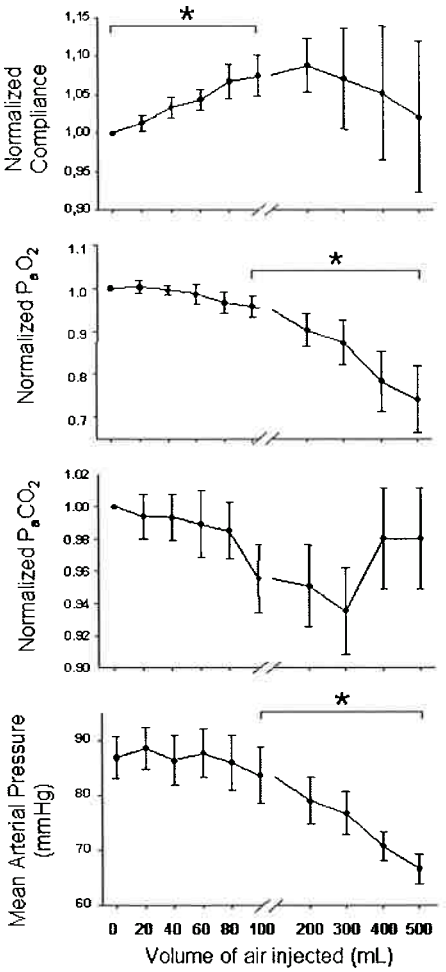

Figure 5. Behavior of compliance, Pao_2, $Paco_2$, and mean arterial pressure during the induction of pneumothorax for the ten animals used in part 1 of the study. *Statistical significance either from baseline to 100 mL or from 100 mL to 500 mL.

performance of the algorithm by introducing two additional criteria that increased specificity, differentiating pneumothoraces from the large perturbations caused by PEEP increments or recruiting maneuvers (Appendix). The first criterion was an associated decrease in regional ventilation (Fig. 6, *bottom*), since we frequently observed that recruiting maneuvers resulted in an increase in mean impedance plus an increase in regional ventilation, especially in the dependent lung regions. The second associated criterion was an associated asymmetry, since we consistently observed that extreme lung overdistension—even when predominant in one side of the thorax—could never produce the asymmetric perturbations seen during pneumothoraces, even the smallest ones (Fig. 6).

After such adjustments during algorithm calibration, we observed no more false-positive results in our retrospective series and only one case (specificity of 21 of 22) in the prospective evaluation. Such results indicate that the algorithm can differentiate the large impedance perturbations caused by pneumothorax from other large perturbations in parenchymal impedance, as those occurring during extreme overdistension (i.e., recruiting maneuvers).

During pressure-controlled ventilation with a fixed driving pressure, sustained changes in pixel tidal ΔZ (which reflect the tidal ventilation per pixel) necessarily reflect sustained changes in regional lung compliance. Accordingly, when we tracked the behavior of the nondependent pixels in the normal animals, we observed a decrease in regional compliance of >70% during extreme PEEP conditions (data not shown). In contrast, the lung-injured animals presented a nondependent decrease in regional compliance of only ~40%. This observation suggests that the nondependent overdistension (18) was much more pronounced in the animals with normal lungs, a situation that might potentially mimic a pneumothorax condition in terms of impedance perturbations. Our results demonstrated, however, that the proposed algorithm was specific enough for pneumothorax detection in normal or previously injured animals and in diffusely as well as focally injured animals.

All other traditional variables monitored, including global respiratory compliance, arterial blood gases, arterial pressure, and heart rate, were not as sensitive as EIT. Our data are in accordance with other authors who have shown that lung mechanics, oxygenation, and hemodynamics are not sensitive enough to screen for pneumothoraces (19, 20, 21).

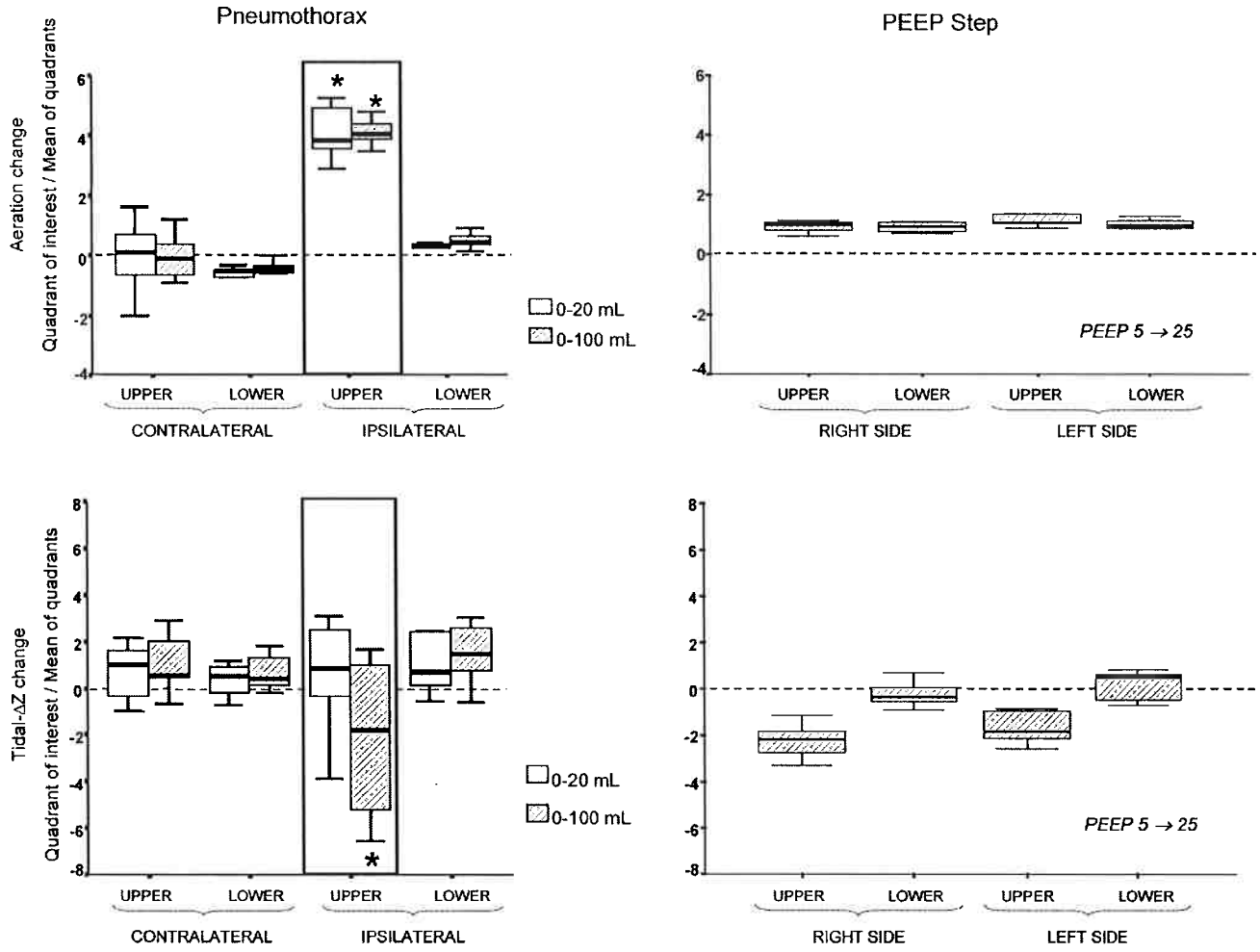

Figure 6. Mean impedance changes (*upper graphs*), extracted from aeration change maps, and tidal ΔZ changes (*lower graphs*), created by subtracting two ventilation maps taken at two different moments (at baseline vs. after 20 mL, or at baseline vs. after 100 mL). The changes determined in each quadrant were normalized to the mean change in all four quadrants. The graphs on the left (part 1 of the experiment) represent the impedance changes following the induction of pneumothoraces of 20 and 100 mL, and those on the right (part 2 of the experiment) show the impedance changes after an increase in positive end-expiratory pressure (*PEEP*) from 5 to 25 cm H_2O. Pixel ΔZ values were calculated after filtering out the high-frequency component of perfusion.

There are some limitations of our study: One is that we did not use any imaging method to control our results. Nevertheless, we used a model with controlled induction of pneumothorax in which the precise amount of air injected during each step of the protocol was known, obviating the need for a comparison with other imaging techniques. In the prospective phase, we always confirmed the presence of the traumatic pneumothoraces by their later drainage. Another potential limitation is the unblinded fashion of the pneumothorax detection. During the time period of detection, however, we could not interact with the pneumothorax detector since it is fully automated. The detector was kept running throughout the protocol while the various interventions were being performed (pneumothorax, recruitment maneuver, drainage). We therefore think that blinding the investigators would not have influenced the results obtained.

Perhaps the most important limitation of our study is that we used baseline data (without pneumothorax) for comparison with the situations of interest. Our online algorithm was using these baseline data as reference repeatedly, necessarily requiring previous data acquisition. One previous investigation suggested that the use of an absolute image generation algorithm, which is able to perceive the presence of air in the pleural space without the need for a baseline image (22), might be more appropriate. The advantage of our procedure, however, is its robustness, since the use of relative images makes it possible to eliminate artifacts caused by patient manipulation or electrode misplacement. In the intensive care unit, this is an important advantage. By using the approach we presented, the EIT cannot be used for diagnosing pneumothoraces of constant volume that are already present at the moment they are suspected. However, EIT may work well in the scenario of a preexisting pneumothorax that is increasing in volume, which is, in fact, the most dangerous situation.

These limitations also do not preclude the application of such an algorithm to high-risk situations, when physicians choose to attentively monitor the appearance of a pneumothorax. Thus, our results seem applicable to two of the most common and important clinical scenarios involving the risk of barotrauma: central venous catheter placement and mechanical ventilation. In these situations, phy-

sicians could easily start the EIT monitoring before proceeding with their interventions, automatically collecting the baseline data.

The placement of central venous catheters carries an important risk of developing a pneumothorax (4, 23). This is especially important when the patient is under positive-pressure ventilation or when he or she has a low respiratory reserve. In these situations, the progression of a pneumothorax can be lethal if not promptly treated. We are starting a clinical trial testing whether such an EIT-based algorithm might allow early detection of pneumothorax in high-risk selected patients, obviating the need for routine radiographic imaging.

Recruitment maneuvers are widely used to reverse hypoxemia, especially in the context of acute lung injury and acute respiratory distress syndrome (24–26). The lung is submitted to high pressures in an attempt to reopen collapsed alveoli, carrying the risk for barotrauma. EIT monitoring could, therefore, be very useful to increase the safety of such maneuvers, making it possible to abort the maneuver once a pneumothorax has been detected. This study intentionally tested such specific situation, demonstrating the good sensitivity of the algorithm to detect pneumothoraces during recruiting maneuvers.

CONCLUSION

We created an algorithm based on electrical impedance tomography that was operator-free and capable of detecting early signs of pneumothoraces in high-risk situations, such as central venous catheterization or mechanical ventilation. We could also indicate the quadrant of occurrence, which might be particularly helpful in emergency conditions requiring prompt drainage. Pneumothoraces could be clearly distinguished from lung overdistension and PEEP-induced changes in intrathoracic air.

ACKNOWLEDGMENTS

We are indebted to Dr. João Batista Borges, Júlio César Ceballos Aya, and Fernando Souza Moura for their contribution in the theoretical background of algorithms.

REFERENCES

1. Schnapp LM, Chin DP, Szaflarski N, et al: Frequency and importance of barotrauma in 100 patients with acute lung injury. *Crit Care Med* 1995; 23:272–278
2. Amato MB, Barbas CS, Medeiros DM, et al: Effect of a protective-ventilation strategy on mortality in the acute respiratory distress syndrome. *N Engl J Med* 1998; 338:347–354
3. Weg JG, Anzueto A, Balk RA, et al: The relation of pneumothorax and other air leaks to mortality in the acute respiratory distress syndrome. *N Engl J Med* 1998; 338:341–346
4. de Lassence A, Timsit JF, Tafflet M, et al: Pneumothorax in the intensive care unit: Incidence, risk factors, and outcome. *Anesthesiology* 2006; 104:5–13
5. Eisen LA, Narasimhan M, Berger JS, et al: Mechanical complications of central venous catheters. *J Intensive Care Med* 2006; 21: 40–46
6. Moss HA, Roe PG, Flower CD: Clinical deterioration in ARDS—An unchanged chest radiograph and functioning chest drains do not exclude an acute tension pneumothorax. *Clin Radiol* 2000; 55:637–639
7. Rankine JJ, Thomas AN, Fluechter D: Diagnosis of pneumothorax in critically ill adults. *Postgrad Med J* 2000; 76:399–404
8. Pelosi P, Brazzi L, Gattinoni L: Diagnostic imaging in acute respiratory distress syndrome. *Curr Opin Crit Care* 1999; 5:9–16
9. Rowan KR, Kirkpatrick AW, Liu D, et al: Traumatic pneumothorax detection with thoracic US: Correlation with chest radiography and CT—Initial experience. *Radiology* 2002; 225:210–214
10. Brown BH, Barber DC, Seagar AD: Applied potential tomography: Possible clinical applications. *Clin Phys Physiol Meas* 1985; 6:109–121
11. Victorino JA, Borges JB, Okamoto VN, et al: Imbalances in regional lung ventilation: A validation study on electrical impedance tomography. *Am J Respir Crit Care Med* 2004; 169:791–800
12. Wolf GK, Arnold JH: Noninvasive assessment of lung volume: Respiratory inductance plethysmography and electrical impedance tomography. *Crit Care Med* 2005; 33: S163–S169
13. Caramez MP, Borges JB, Tucci MR, et al: Paradoxical responses to positive end-expiratory pressure in patients with airway obstruction during controlled ventilation. *Crit Care Med* 2005; 33:1519–1528
14. Pai C, Mirandola L, Scweder R, et al: A black-box back-projection algorithm for electrical impedance tomography. *In:* Proceedings of the 18th International Congress of Mechanical Engineering; 2005; Ouro Preto, MG, Brazil
15. Nopp P, Harris ND, Zhao TX, et al: Model for the dielectric properties of human lung tissue against frequency and air content. *Med Biol Eng Comput* 1997; 35:695–702
16. Frerichs I, Hahn G, Schroder T, et al: Electrical impedance tomography in monitoring experimental lung injury. *Intensive Care Med* 1998; 24:829–836
17. Rouby JJ, Lu Q, Goldstein I: Selecting the right level of positive end-expiratory pressure in patients with acute respiratory distress syndrome. *Am J Respir Crit Care Med* 2002; 165:1182–1186
18. Adler A, Shinozuka N, Berthiaume Y, et al: Electrical impedance tomography can monitor dynamic hyperinflation in dogs. *J Appl Physiol* 1998; 84:726–732
19. Murray JM, Seaberg DC, Menegazzi JJ: Demand valve ventilation in a swine pneumothorax model. *Am J Emerg Med* 1996; 14: 13–15
20. Bitto T, Mannion JD, Stephenson LW, et al: Pneumothorax during positive-pressure mechanical ventilation. *J Thorac Cardiovasc Surg* 1985; 89:585–591
21. Barton ED, Rhee P, Hutton KC, et al: The pathophysiology of tension pneumothorax in ventilated swine. *J Emerg Med* 1997; 15: 147–153
22. Hahn G, Just A, Dudykevych T, et al: Imaging pathologic pulmonary air and fluid accumulation by functional and absolute EIT. *Physiol Meas* 2006; 27:S187–S198
23. Mansfield PF, Hohn DC, Fornage BD, et al: Complications and failures of subclavian-vein catheterization. *N Engl J Med* 1994; 331:1735–1738
24. Barbas CS, de Matos GF, Okamoto V, et al: Lung recruitment maneuvers in acute respiratory distress syndrome. *Respir Care Clin N Am* 2003; 9:401–418, vii
25. Barbas CS, de Matos GF, Pincelli MP, et al: Mechanical ventilation in acute respiratory failure: Recruitment and high positive end-expiratory pressure are necessary. *Curr Opin Crit Care* 2005; 11:18–28
26. Borges JB, Okamoto VN, Matos GF, et al: Reversibility of lung collapse and hypoxemia in early acute respiratory distress syndrome. *Am J Respir Crit Care Med* 2006; 174: 268–278

APPENDIX

Experimental Setup

Animals were initially sedated (acepromazin 0.1 mg/kg, midazolam 0.5 mg/kg, and ketamine 5.0 mg/kg) while receiving oxygen via facial mask, subsequently tracheostomized, and maintained with continuous intravenous anesthesia (ketamine 2.0 mg/kg/hr, pancuronium 0.35 mg/kg/hr, midazolam 0.45 mg/kg/hr, and thiopental 2.0 mg/kg/hr). Controlled mechanical ventilation was initiated with pressure-controlled mode (Servo 300 A, Siemens-Elema, Sweden). All animals were monitored with a continuous arterial blood gas sensor inserted through the carotid artery (Paratrend MPM7000, Dia-

metrics Medical, Roseville, MN). Invasive systemic arterial and central venous pressures were monitored (Portal DX 2020 Monitor, Dixtal, Manaus, Brazil). Proximal airway pressures were measured with a differential pressure transducer open to atmosphere (Validyne MP45; ±100 cm H_2O; Validyne, Northridge, CA). Airway flow was measured by a differential pressure pneumotachograph (Hans Rudolph; 0–160 L/min; Kansas City, MO; connected to a Validyne MP30; ±2 cm H_2O transducer) placed between the ventilator circuit and the tracheal tube. A customized software calculated respiratory system mechanics breath by breath (13).

EIT Image Reconstruction Algorithm

Images were generated by a reconstruction algorithm for a cross section of the thorax, which is based on a sensitivity matrix derived from a three-dimensional finite element model of the thorax with approximately 8,000 elements (Fig. A1), including electrodes and contact impedance models. The model assumes that the major part of the electrical current passes through a thoracic slice 5 cm thick. The thoracic slice contour was extracted from an average CT image of the pig thorax. Images were originally reconstructed in a raw matrix of 32 by 32 pixels and subsequently interpolated.

Noise

Noisy voltages during the experiments were discarded using statistical criteria. The rejection rate, however, was never allowed to exceed 5% of the total number of measurements. The resulting random noise in sequential pixel values was determined after killing the animal, thereby eliminating the periodic oscillations due to lung perfusion and ventilation. It was <0.001 across the lung regions (i.e., 1:1000th of the raw pixel value during maximum lung inflation).

Preconditioning of Raw Voltage Files

During *in vivo* experiments, perturbations caused by pulsatile perfusion of lung capillaries can affect local impedance, although usually contributing to <10% of cyclic impedance changes related to ventilation. During low tidal volume ventilation, however, such perfusion-related perturbations can be relatively larger, introducing some errors in the analysis. Thus, to correctly calculate the pixel-by-pixel amplitude of a ventilation map, we always preconditioned the voltage data according to a low-pass temporal filter (cutoff frequency around 0.8 Hz), attenuating the energy of impedance perturbations at frequencies close to the heart rate. This way it was usually possible to eliminate 90% to 95% of perfusion-related perturbations, without losing the original amplitude of respiratory oscillations.

Image Resolution

Preliminary tests of our EIT device in a phantom of 30 cm diameter revealed a maximum image resolution (analyzed as area at half maximum height of a perturbation) of 1:10th the phantom diameter at the center and 1:20th at peripheral locations.

During typical incremental inflation of healthy pig lungs from functional residual to total lung capacity using a super-syringe, pixels representing lung tissue showed a stepwise linear increment in resistivity ($R^2 > .99$) from 0 to ~1.1, indicating that the lung's air content had increased by ~110% (when functional residual capacity was the reference condition).

Developing the Pneumothorax Detection Algorithm

To optimize the use of data obtained from living experimental animals, raw

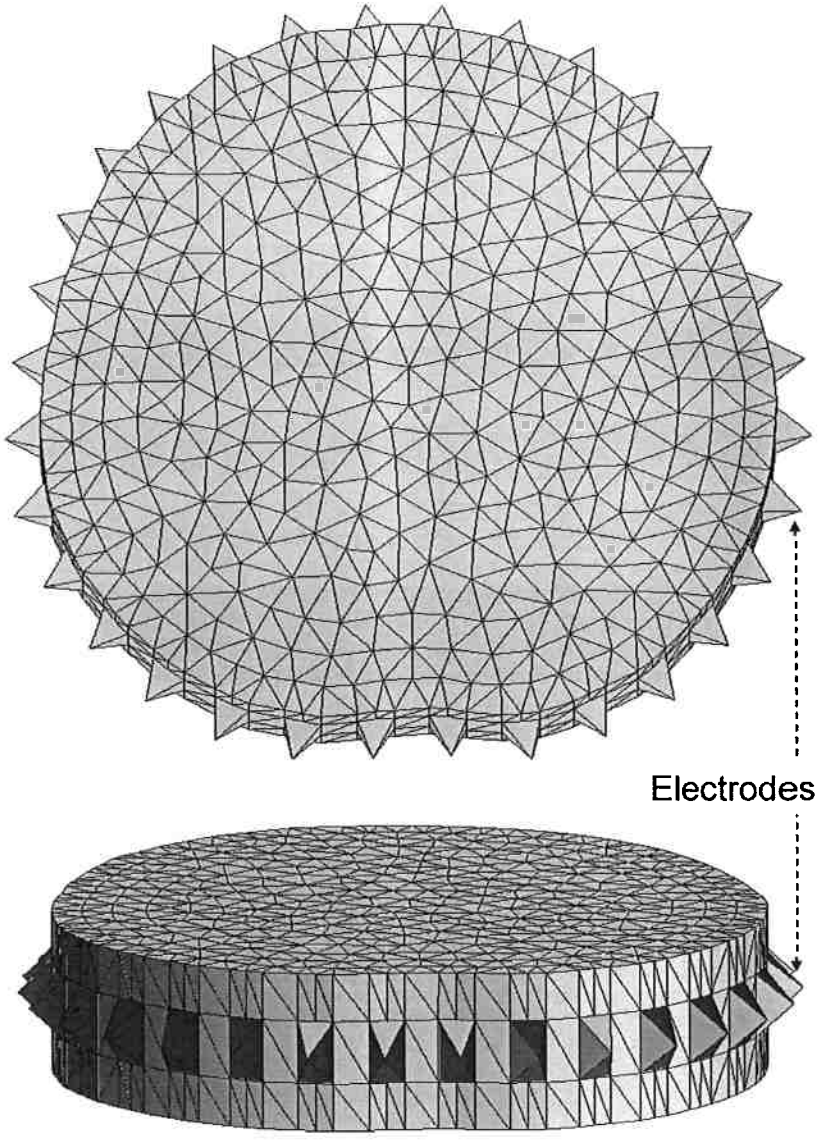

Figure A1. The three-dimensional finite element mesh used for reconstructing electrical impedance tomography images, simulating the pig's thorax.

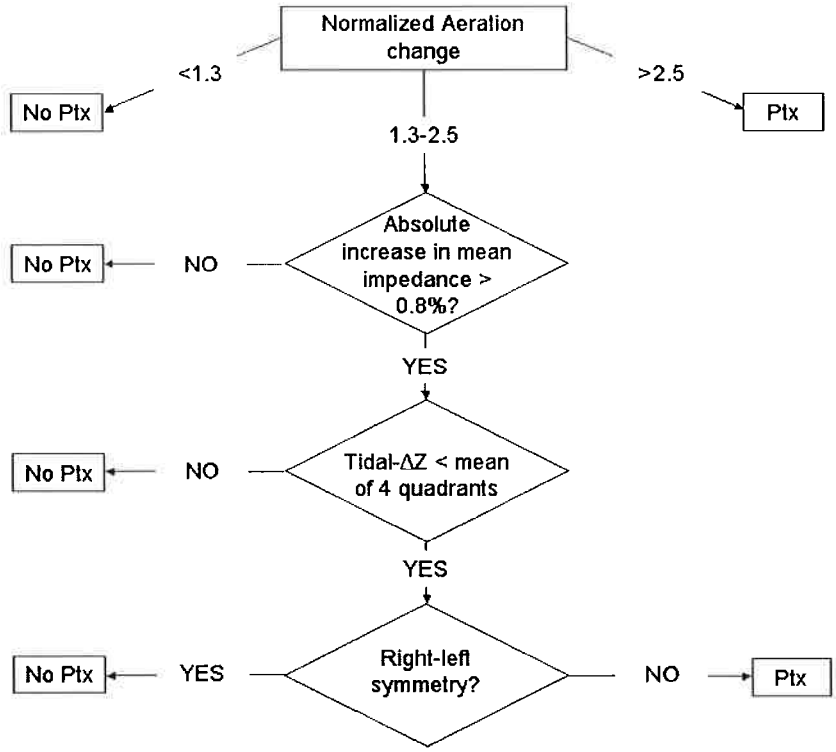

Figure A2. The final pneumothorax (*Ptx*) detection algorithm.

EIT data were continuously recorded during the first phase of the study (18 animals) and later used for designing and bench testing different versions of the algorithm. Files of acquired data were repeatedly used to simulate real-time conditions: Instead of receiving voltage inputs from an acquisition system, the EIT microprocessor received voltage inputs from the hard disk at the same frame rate as during acquisition. This way, modifications of the algorithm could be tested reproducibly without having to use more animals than necessary.

Through repeated analysis of the data gathered in the first two parts of the experimental protocol, we were able to iteratively define thresholds for aeration changes and for tidal ΔZ changes that could best differentiate a pneumothorax from the control situations (lung distension/overdistension). To improve the specificity of the algorithm, we later included an additional symmetry criterion (Fig. A2).

ANEXO E - Recozimento Simulado

ELECTRICAL IMPEDANCE TOMOGRAPHY ALGORITHM BASED ON SIMULATED ANNEALING SEARCH METHOD

Claudia Natalia Lara Herrera, natylara@gmail.com
Miguel Fernando Montoya Vallejo, montovall@gmail.com
Fernando Silva de Moura, fernandosmoura@gmail.com
Julio Cesar Ceballos Aya, jccaya@gmail.com
Raul Gonzalez Lima, lima.raul@gmail.com
Department of Mechanical Engineering - Polytechnic School of University of São Paulo Av. Prof. Mello Morães, 2231 - São Paulo - SP - 05508-900, Brazil

Abstract. *Electrical impedance tomography (EIT) is a noninvasive monitoring technique to produce images that represent the cross-sectional distribution of the electrical resistivity within an object (for instance the human thorax) from measurements on its boundary. Mathematically, the absolut resistivity distribution estimation is a nonlinear ill-posed inverse problem. This paper presents a probabilistic reconstruction algorithm based on Simulated annealing method for the solution of the absolut EIT inverse problem. The advantage of this algorithm is that no evaluation of function derivatives is needed and the possibility to escape from local minimus. This work contributes to the development of image estimation algorithms applied to monitor mechanical ventilation of lungs. Using simulated data, the localization of object, the size of object and the resistivity of the object are well inside the accuracy of EIT obtained by classical methods, but using experimental data the spatial resolution of the object is not good, because of only restrictions of the solution space are imposed and a regularization technique is necessary to obtain more stable solutions. In both, simulated and experimental tests, the computational effort is large. This results verify the advantages and feasibility of the proposed algorithm.*

Keywords: *Electrical Impedance Tomography, simulated annealing, inverse problems, finite elements method*

1. INTRODUCTION

Electrical Impedance Tomography (EIT) is a noninvasive technique used to produce images that represent the cross-sectional electrical resistivity distribution (or conductivity) within a domain (for instance the human thorax) from electrical measurements made through electrodes distributed on its boundary. A low amplitude alternated electrical current is applied by two or more electrodes with a constant intensity and the difference of electrical potential generated (voltage) is measured in all the rest of the electrodes equally spaced between each other. The way of injecting currents and reading voltages are called of current pattern and voltage pattern, respectively. The pair of electrodes used in the current injection is changed successively until a enough number of observations allows the estimation of an image. The image is the most likely resistivity distribution on the domain in study.

EIT is an innovative monitoring tool for applications on fields like medicine, geophysical, environmental science and non-destructive materials tests. Currently, the research focus and more common use of the TIE is for monitoring and medical diagnosis where it is used to image an internal section of human body based on the nonuniformity of the electrical properties of different living tissues as lung, blood, muscle, bone, etc. [1]. Some examples of medical applications of the EIT are the detection of pulmonary embolism [2, 3, 4], monitoring of apnea [5], monitoring of brain function [6], monitoring of heart function and blood flow [7] and the detection of breast cancer [8].

As well as being a noninvasive technique without collateral effect, its cost electronic hardware requirements are relatively cheap, any radiation type is used and its equipment is portable, if compared with the others techniques as Computer Tomography, Magnetic Resonance or ultrasound [9]. Unfortunately, the biggest limitation of this technique is its low spatial resolution that is related with the number of used electrodes.

The Resistivity distribution search can be made with the aid of models that depend or not on the time generating *static* or *dynamic* methods. The static are used when the changes of electrical properties of the domain do not vary significantly in the time interval where the necessary data for the image estimation are collected. Instead in the situations where faster changes of the electrical properties of the domain at the moment of the data collecting, the effects of the dynamic of the system must be taken in account and a dynamic method must be used. Depending on the type of estimated image static methods can further be divided in two categories: *difference* imaging and *absolute* imaging. In difference imaging two voltages data sets are measured corresponding to two different target resistivity distributions. Based on the difference between these measurements the difference of the resistivity distributions can be estimated. In absolute imaging the estimation is based on a single data set of voltage measurements only, and the aim is to estimate the absolute resistivity distribution.

On the other hand, the problem of EIT is seriously complicated by the nonlinearity of the governing equation. Moreover, the measurement electrodes are far from the internal objects, and only boundary measurements are available

which makes the problem mathematically inherently ill-posed. This inverse problem is also ill-conditioned, because the boundary measurements are very sensitive to resistivity changes in the periphery and relatively insensitive to changes at the center. Therefore to get stable solutions of the problem is necessary to use some *regularization technique*. Generically, these techniques allow the inclusion of *a priori* information that is all known information about the resistivity distribution in the domain.

1.1 Features of EIT

In general, EIT system consists of the hardware part to apply currents and then measure resulted voltages and the software part contains the image reconstruction algorithm to estimate resistivity images. The mathematical approximation to solve the whole estimation problem is divided in two parts [11, 12]. The first part, the *forward problem* of EIT consists of modeling the boundary voltages as an explicit function of the resistivity (or conductivity) in the domain. The second part, the *inverse problem* of EIT consists of inverting the relation of forward problem to calculate the internal resistivity distribution.

Approaches to solve the inverse problem for reconstruction of EIT fall into several categories like: the *noniterative* methods that frequently are used to obtain difference images of EIT, are generally fast and of low computational cost, however, these ignore the effect of the nonlinearity of the problem leading with inexact results and limiting its application to solve qualitative problems like the organs functioning [1, 13, 14]; the *iterative* methods consider the nonlinear relation that exists between the electrical potentials and electrical resistivity and are promising for obtaining more accurate results, but the computational cost are very higher than in the noniterative methods. The iterative solutions generally follow similar strategies [23, 16, 17].

The present work evaluates the performance of a probabilistic algorithm based on Simulated Annealing method (SA) to obtain absolute resistivity distributions in a 2-D domain. SA differs from the traditional search methods, no evaluation of objective function derivatives is needed and the possibility to escape from a local minimum through the use of Metropolis criterion for acceptance of new points in the search space. The developed algorithm solves the inverse problem of EIT while resolving iteratively a direct problem by using random resistivity distributions. The random search is accomplished by the metropolis algorithm [18]. It is assumed that the random image that minimizes the difference between the measured voltage on the boundary and calculated voltage is the closest to the distribution of real resistivity, thus, the algorithm supplies a final solution near to the optimal solution. This makes the method especially attractive when the functions to be optimized present multiple local minimums [19]. SA allows to include that reduce the solution space and works as a type *a priori* information.

The next sections of the paper are organized as follow. Section 2.shows the mathematical governing equations of EIT. In section 3.is briefly explained how the domain and the electrodes are discretized using FEM. Section 4.describes in more details the Simulated Annealing method and its formulation for the application in EIT. The methodology of performed tests and its results are shown in section 5and 6.respectively. Finally, section ?? draws the conclusions.

2. Mathematical model of the domain and electrodes

The study domain is considered a bidimensional region closed Ω and limited by a contour surface $\partial\Omega$. The resultant electrostatic field is governed by the Maxvell's equations. To reduce the complexity of the EIT problem some simplification hypotheses must be adopted. If the domain is related to a body section, then low frequencies and small field strengths the electromagnetic properties of living tissue allow these to be simplified to the Poisson's equation that governs the electrical potential $\phi(x,y)$ inside of Ω.

$$\nabla \cdot (\sigma \nabla \phi) = 0 \tag{1}$$

To limit the infinite number of solutions of $\phi(x,y)$ that has the Eq. (1) are applied boundary conditions that specify the value of certain parameters in $\partial\Omega$. In EIT the voltages measurements and currents injection are made thought l electrodes fixed on certain points of $\partial\Omega$, thus, can be established the following boundary conditions

$$\sigma \frac{\partial \phi(\sigma)}{\partial \hat{n}} = \begin{cases} J_i, & i = 1, 2, \cdots, l \\ 0, & \text{in the other points of } \partial\Omega \end{cases} \tag{2}$$

where$\hat{n}$ is an outward normal vector to $\partial\Omega$. The Eq. (1) is a complicated nonlinear differential, such that it is impossible to get a general analytic solution for an arbitrary resistivity distribution and irregular boundary shape. Therefore, numerical techniques are indicated.. The Finite Elements Method (FEM) is a well accepted and powerfid numerical method to solve de EIT problem.

To model the whole domain Ω it is necessary modeling the interaction of the electrodes in $\partial\Omega$ too. The complete electrode model takes into account both the shunting effect of the electrode and the contact impedance between the

electrodes and the domain. Besides of the Eq. (1) the rest of the equations of this model are

$$\int_{\partial\Omega_j} \sigma \frac{\partial \phi}{\partial \hat{n}} = I_j, \qquad j = 1, 2, \cdots, l \tag{3}$$

$$\sigma \frac{\partial \phi}{\partial \hat{n}} = 0, \tag{4}$$

$$\phi + z_j \sigma \frac{\partial \phi}{\partial \hat{n}} = V_j, \qquad j = 1, 2, \cdots, l \tag{5}$$

where I_j in Eq. (3) represents the electrical current that crosses the j^{th} electrode. In Eq. (5) z_j is the effective contact impedance between the j^{th} electrode and medium and V is the electrical potential in the electrodes.

3. Use of FEM in EIT

An inverse problem can be solved iteratively using the solution of its corresponding forward problem. In the particular case of EIT a model that predicts the internal voltage distribution given the electrical current stimulates and the internal resistivity distribution of the domain, must be adopted as forward problem. We use the FEM to discretize the domain and the electrodes and solve both problems, forward and inverse, numerically.

The finite elements meshes used to divide Ω have m nodes and n triangular plain finite elements with constant resistivity ρ_i, $i = 1, 2, \cdots, n$ and linear interpolation functions [11]. The domain is discretized in such a way that regions experimenting high modification in the resistivity have smaller elements, it results in a more accurate model. These great changes in the resistivity occur mainly in $\partial\Omega$ due to intensity of the current injected. The domain is divided in FE by using the mesh generation software

The matrix $\tilde{Y}_i(\rho_i^{-1}) \in \mathbb{R}^{3\times 3}$ is denominated *local resistivity matrix* of the i^{th} element. Considering e the element height, $\mathbb{A}_i$ the element area and the resistivity being homogeneous and isotropic the components of the local resistivity matrix are given by

$$[\tilde{Y}_i(\rho_i^{-1}]_{(k,m)} = \frac{e\rho_i^{-1}}{4\mathbb{A}_i}(\xi_k \xi_m + \tau_k \tau_m) \qquad (k, m = 1, 2, 3) \tag{6}$$

with

$$\begin{aligned} \xi_1 &= (y_2 - y_3) \ , \ \tau_1 = (x_3 - x_2) \\ \xi_2 &= (y_3 - y_1) \ , \ \tau_2 = (x_1 - x_3) \\ \xi_3 &= (y_1 - y_2) \ , \ \tau_3 = (x_2 - x_1) \end{aligned} \tag{7}$$

The electrodes are discretized in 2-D finite elements following the work proposed by [20], in which are solved the Eq. (3) and Eq. (4) and Eq. (5) with the aid of FEM. Electrode model take into account the high metal resistivity and the contact impedance between metal and medium. The interface between the electrode and medium is discretized using two quadrangular finite elements with 6 nodes in total. To determine the *local resistivity matrix of the electrode* it is followed the same procedure used to find the local resistiviy matrix of the elements of Ω then

$$\tilde{Y}_j^{\,e} = \frac{b\,\rho_j^{-1}}{t} \begin{bmatrix} \frac{a}{2} & 0 & 0 & \frac{-a}{2} \\ & a & 0 & -a \\ \textit{sim} & & \frac{a}{2} & \frac{-a}{2} \\ & & & 2a \end{bmatrix} \tag{8}$$

where a is element width, t is the thickness of contact interface and b is the interface thickness (perpendicular to a and t).

It is defined

$$z_j = \frac{\rho_{j-1}}{t} \tag{9}$$

as the effective contact impedance em $[\Omega m^2]^{-1}$. The matrix $\bar{Y}_j^{\,e}$ represents the local resistivity matrix of the electrode writed in terms of global coordinates of the finite elements mesh which was discretized Ω. Then, the summation of all the local matrices of the elements and the electrodes is equivalent to the application of the variational principle in the discretized domain [22] and the global resistivity matrix $Y(\rho^{-1}) \in \mathbb{R}^{m\times m}$ is determined

$$Y(\rho^{-1}) = \sum_{i=1}^{n} \left[\tilde{Y}_i(\rho_i^{-1})\right] + \sum_{j=1}^{l} \left[\bar{Y}_j^{\,e}(z_j)\right] \tag{10}$$

After assembling the global element matrix (Eq. (10)) we have m nodes, l electrodes and n elements in which p currents are injected. Thus, the matrix containing unknown nodal voltages $v(\rho^{-1}) = [v_1 \cdots v_j \cdots v_p]$, $v_j \in \mathbb{R}^m$ corresponding to each applied current pattern is solved through the linear system equations given by

$$YV = C \tag{11}$$

where $\rho_p \in \mathbb{R}^{n+l}$ is any particular resistivity distribution for which it is calculated y, and $c = [c_1 \cdots c_j \cdots c_p]$, $c_j \in \mathbb{R}^m$ is the matrix of linearly independent bipolar current patterns. On numerical simulations and experimental tests c is

$$C = \begin{bmatrix} -I & 0 & \cdots & +I \\ 0 & -I & \cdots & 0 \\ +I & 0 & \cdots & 0 \\ 0 & 0 & \cdots & 0 \\ \vdots & \vdots & \ddots & \vdots \\ 0 & 0 & \cdots & -I \\ 0 & 0 & \cdots & 0 \end{bmatrix} \tag{12}$$

To solve the Eq. (11) that governs the forward problem it is necessary to eliminate the singularity of matrix Y, this can be made by choosing an arbitrary node with null value (ground). The imposition of this boundary condition it is made by equaling to zero the row and column of the matrix Y corresponding to selected node and attributing to the intersection element the unitary value [?].

4. Simulated Annealing

In 1953, the *Simulated Annealing* (SA) method was first proposed by [18] and it is known as Metropolis Algorithm (MA). It is an algorithm for the efficient simulation of the evolution of a solid to thermal equilibrium. In short, the SA algorithm is based on the analogy between the simulation of the annealing of solids and the problem of solving large combinatorial optimization processes [?, ?]. The annealing denotes a thermal cooling process that starts with the liquidification of a crystal at high temperature followed for the slow and gradual reduction of the temperature until the solidification point is reached when the system achieves a state of "minimal energy". Minimal states of energy are characterized for a structural perfection of the material undergone to annealing that would not be obtained if the cooling was not gradual. In conditions less careful of cooling the material would be crystallized by an "locally minimal energy", in other words, the atomic structure of the material would be irregular and weak, with imperfections.

The physical analogy between the annealing of solids and an optimization problem would be the next:

- The system energy $\varepsilon \Leftrightarrow$ objective function F of the optimization problem,
- system state $\Leftrightarrow$ solution of optimization problem,
- current system state $\Leftrightarrow$ candidate solution,
- minimal energy configuration $\Leftrightarrow$ optimal solution,
- the system temperature $T \Leftrightarrow$ control parameter

The central point of the algorithm is focused on the process of probabilistic acceptation of a nearby solution although presents an increase in F (higher cost). Summarizing, the algorithm is basically characterized by two operations: the first one is the reduction of the value of the control parameter T successively along the iterations based on a determined *annealing function* ; the second one is the realization of the cycle of generation and acceptation of solutions and equivalent to the MA, in such a way that the solutions corresponding to the thermal equilibrium be found to each temperature. The algorithm ends when a determined *stopping criterion* is satisfied.

The heuristical parameters should be well syntonized to improve the performance (i.e, efficiency, convergence, speed) as also the efficacy (i.e, quality of the found solutions) of the algorithm. Amongst these parameters are:

- The initial value for the temperature, T_0, must be a value high enough such that all the candidate solutions in the neighborhood (both: the ones which improve and the ones that get worse the objective function) have a probability next to 1 of being chosen.
- It is required to determine a (*cooling schedule*) that defines the evolution of T during an limited number of iterations. In this work the geometric cooling is used, whose general formula is given by

$$T_{k+1} = \alpha T_k \tag{13}$$

The factor α is a constant next to the unitary value and is the temperature decay rate. The value of the cooling factor α is determinative in the convergence of the SA. If α is sufficiently high, the probability to converge to an optimal point it is increases but the computational time increases unnecessarily. The values more commonly used are between 0.9 and 0.99 [25].

- the number of iterations to reach the equilibrium at certain temperature, N_t. The simplest criterion is to make a fixed number of iterations before the temperature is changed.
- the simplest stopping criterion is the pre-definition of the total number of iterations N to execute by the algorithm. However, this criterion needs to be chosen carefully together with the other parameters so that the algorithm reaches sufficiently low temperatures that guarantee the convergence.

4.1 SA and the EIT inverse problem

It is assumed that for the minimization of the difference between the measured voltages v_m and calculated voltages v_c in the computational model, the estimate image will converge to the requested original image. In that way, the quadratic error between these voltages was chosen as objective function and the problem is described with the next nonlinear optimization model

$$\min_{\rho \in \Omega} \quad F(\rho)$$
$$F(\rho) = \frac{1}{2}\left\| V_m - V_c(\rho) \right\|_2^2 \tag{14}$$

In EIT it is possible to include additional information in the reconstruction problem. In this work the fact of being able to include restrictions in the space solution in SA to introduce this additional information is taken advantage. The search covers the entire domain of the impedance distribution restricting the space solution between a limited superior vector and limited inferior vector whose values are defined according to information that is had about the problem.

The restrictions are imposed to obtain the new candidate point (candidate configuration). New candidate point is generated around the current point applying random moves along each coordinate direction, in turn and satisfying the imposed limits [26]. Let $F(\rho)$ be the function to minimize and let $a_1 < \rho_1 < b_1$, $a_2 < \rho_2 < b_2, \ldots$, $a_n < \rho_n < b_n$ be its variables, each ranging in a finite, continuous interval. Therefore, starting from the point ρ_i, generate a random point ρ' along the direction h

$$\rho' = \rho_i + r\gamma_h \beta_h \tag{15}$$

where r is a random number generated in the range $[-1, 1]$ by a pseudorandom number generator; β_h is the vector of the h^{th} coordinate direction; and γ_h is the component of the step vector γ along the same direction.

If the h^{th} coordinate of ρ' lies outside the definition domain of $F(\rho)$, that is, if $\rho'_h < a_h$ or $\rho'_h > b_h$, then a new random point in this direction must to be generated. With this, it is guaranteed the probability of accepting a new point that is out of the imposed limits is null and that whole defined domain is covered.

For each direction u, $u = 1, 2, \cdots, n$, the new step vector component γ'_u is

$$\gamma'_u = \begin{cases} \gamma_u \left(1 + \zeta \frac{M_{a_u}/M_t - 0.6}{0.4}\right) & \text{if} \quad M_{a_u} > 0.6 M_t, \\ \dfrac{\gamma_u}{1 + \zeta \frac{0.4 - M_{a_u}/M_t}{0.4}} & \text{if} \quad M_{a_u} < 0.4 M_t, \\ \gamma_u & \text{otherwise} \end{cases} \tag{16}$$

where ζ is a constant parameter that controls the step variation along each u^{th} direction. The aim of these variations in step length is to maintain the average percentage of accepted moves M_a at about one-half of the total number of moves M_t, both for a same value of T. [26, 27, 28] give a more detailed discussion about it.

The values of the objective function for ρ' and ρ_i configurations denoted as $F(\rho_i)$ and $F(\rho')$ are calculated through Eq. (14). In the minimization problem, if

$$\Delta F = F(\rho') - F(\rho_i) < 0 \quad \text{(i.e., } \rho' \text{ is better)} \tag{17}$$

then, the new movement is accepted, otherwise, it is accepted with a probability $P(i)$

$$P(i) = exp\left(-\frac{\Delta F}{T_i}\right) \tag{18}$$

where T_i is the control parameter (temperature) in the i^{th} iteration.

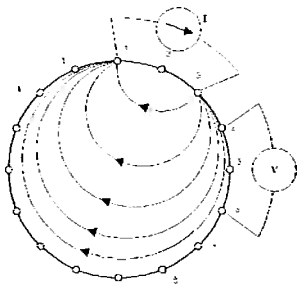

Figure 1. Adopted method for injecting currents and reading voltages

The EIT forward problem is used to calculate $V_c(\rho)$ that through of Eq. (14) is part of Eq. (17). This means that for each transition in the space of solutions Eq. (11) is solved first to get $v_c(\rho)$, then, it is calculated $F(\rho)$ based on Eq. (14). After this, the metropolis criterion is used to accept or rejecting a new configuration as it was mentioned above.

After $(N_t * n)$ iterations, it is changed the value of T according to the chosen annealing function and the cooling factor α as defined in Eq. (13), and a new step vector γ is calculated by the Eq. (16).

5. Methodology and tests

5.1 numerical phantom

A numerical phantom was used to simulate the data set acquisition made by the EIT system and thus to test the image reconstruction algorithm. This method consists of a discretized arbitrary domain in finite elements, whose distribution of resistivity ρ^* is chosen. It allows to get the voltages measured V_m em $\partial\Omega$ through the l electrodes for each one of the p injected current patterns. That is, to find the voltages measured in the electrodes the forward problem for each p injected current patterns is solved by Eq. (11) and the vector v_m contains only the electrodes voltages. Then, these voltages are used for the image estimation through the implemented algorithm which is compared with the image of resistivity distribution ρ^* chosen for the numerical phantom. The noises coming from the hardware and external agents as electrical fields can or not be simulated in the phantom.

The algorithm for solving the inverse problem in both, numerical and experimental tests, is implemented using C language and the FE meshes are made in the software Gmsh with system Linux. In order to simulate a situation similar to the real one the mesh used to discretized the phantom domain must have more elements than the mesh used to solve the inverse problem.

5.2 Numerical data tests

To simulate the measured voltages is used the numerical phantom. The aim of these numerical data tests is to identify an stable algorithm to be used in experimental evaluations. All tests are made with a circular domain with 300 mm of diameter and the interior perturbed region is also circular with 60mm of diameter. The injected current is 2mA, bipolar and the method shown in Fig. 1 (this figure corresponds to one current load case) is adopted for injecting currents and reading voltages.

5.2.1 Test 1

For solving the forward problem with the numerical phantom the domain is discretized by 222 nodes, 362 2-D triangular elements and 16 electrodes and the resistivity value of the background is 17Ωm. The resistivity value of the perturbed region (target) is 1000Ωm. The finite elements mesh used to solve the inverse problem has 122 nodes, 170 elements and 16 electrodes. Figure 2(a) shows the image that will be reconstructed, the background (blue) and target (red) regions, and Fig. 2(b) presents the finite elements mesh of the inverse problem. The initial temperature T_0 is 0.05, the cooling factor α is 0.8, stopping criterion is 40 iterations, the number of iterations at each temperature N_t is 15, the parameter ζ that controls the step variation is 1, the resistivity limits are between 17Ωm and 1000 Ωm and the initial value for resistivity distribution of whole domain ρ_0 is 20Ωm and 0.02Ωm^2 for the electrodes..

5.2.2 Test 2

The aim of this test is to get that the algorithm identifies the target region when it is changed to other position of the domain. The resistivity value of the background is 10Ωm and for the target region is 500Ωm. For solving the forward problem with the numerical phantom the domain is discretized by 547 nodes, 980 elements and 16 electrodes. The finite

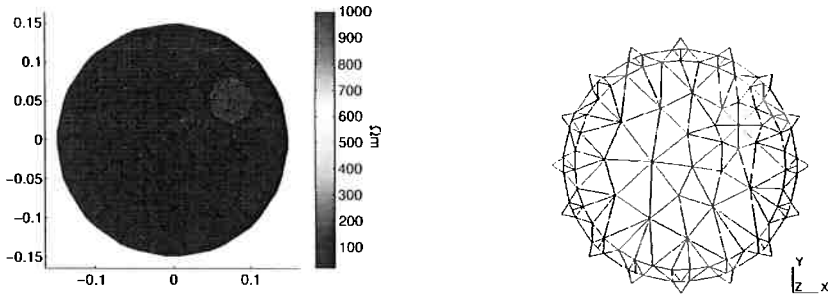

(a) (b)

Figure 2. (a) requested original image and (b) FE mesh of inverse problem to test 1.

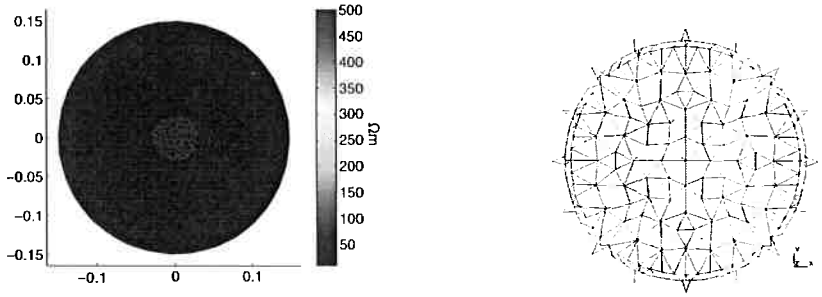

(a) (b)

Figure 3. (a) requested original image and (b) FE mesh of inverse problem to test 2

elements mesh used to solve the inverse problem has 229 nodes, 344 elements and 16 electrodes. Figure 3(a) shows the image that will be reconstructed, the background (blue) and target (red) regions, and Fig. 3(b) presents the finite elements mesh of the inverse problem. T_0 is 100, α is 0.9, stopping criterion is 20 iterations, N_t is 30, ζ is 2, the resistivity limits are between 10Ωm and 600 Ωm and ρ_0 is 12Ωm and 0.02Ωm^2 for the electrodes.

5.3 Experimental data tests

Followed procedure for the experimental data tests is similar to the used one for the numerical data, except for collecting the measured voltages data $\boldsymbol{V_m}$ where is used a current font that injects current on the electrodes positioned at the boundary of a cylindrical container with 300mm of inner diameter containing a 0.3 g/L saline solution (NaCl) inside. Its resistivity is approximately 17Ωm. The currents are injected and voltages are read on computer through an acquisition data system and adopting the method shown in Fig. 1. The aim of these tests is to identify a circular glass object with 32mm of diameter and resistivity equal to $10^6\Omega$m approximately, which is immersed into the container. The data are obtained through 30 bar electrodes with 35mm high and 10mm wide and the injected current is 2mA.

To obtain the voltages in the electrodes, a pair of them is electrically excited following the current pattern seen in Fig. 1. The pair of excited electrodes is successively changed until a satisfactory number of observations (or until enough information as voltage values) under different angles is obtained, thus providing the necessary data for a high quality image. 30 current load cases are applied following this pattern.

5.3.1 Test 3

The used configuration of the domain with the object positioned at the center of container as showed in Fig. 4(b). The FE mesh used for the inverse problem has 409 nodes, 636 elements and 30 electrodes (see Fig. 4(a)). T_0 is 5, α is 0.99, stopping criterion is 50 iterations, N_t is 30, ζ is 1, the resistivity limits are between 10Ωm and 200 Ωm and ρ_0 is 25Ωm and 0.02Ωm^2 for the electrodes.

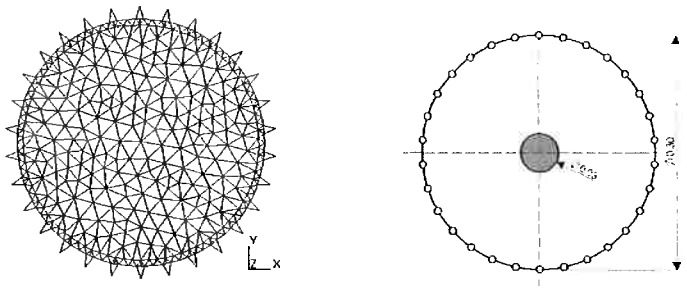

(a) (b)

Figure 4. (a) FE mesh for the inverse problem and (b) used configuration for test 3

6. Results

Figures 5(a), 5(b), 6(a) and 6(b) show image and converge curve obtained by SA algorithm for the test 1 and 2. In tests 1 and 2 the position and size of the virtual object were recovered properly and the amplitude reached the expected value (both basal and perturbed region). However due to the not very discretized meshes and to the difficulty to tune the SA parameters some elements did not reach the upper limit. For test 1 the elapsed time was 468 minutes and final objective function was 0.48, and for test 2 was 605 minutes and 0.0015. The objective function of test 2 converges faster than the one of test 1.

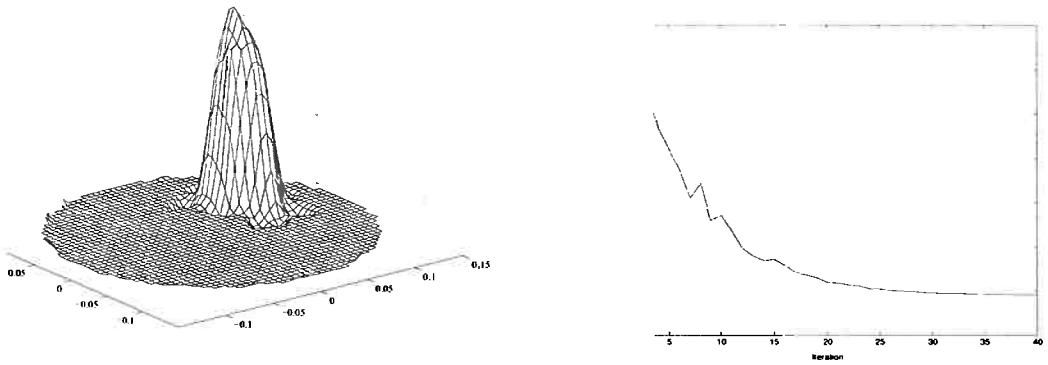

(a) (b)

Figure 5. (a) FE mesh for the inverse problem and (b) used configuration for test 3

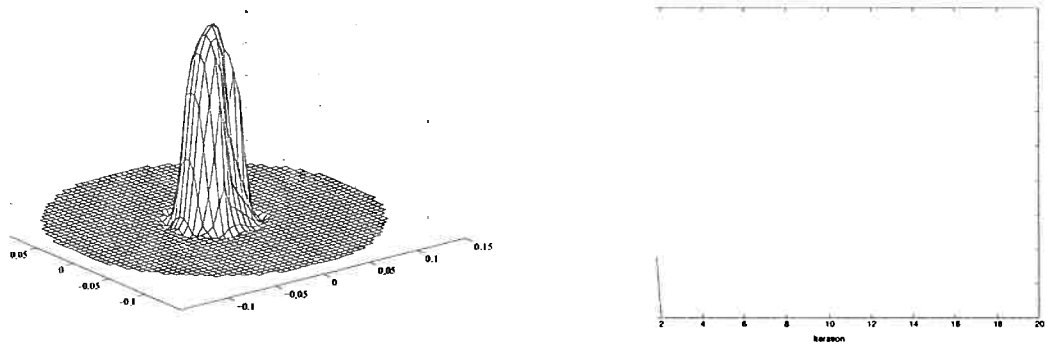

(a) (b)

Figure 6. (a) FE mesh for the inverse problem and (b) used configuration for test 3

Figures 7(a) and Fig. 7(b) show image and converge curve obtained by SA algorithm for the test 3. The position of the object was recovered properly but its diameter and resulted bigger than expected, it is probably related to the not very discretized mesh and to the absence of *a priori* information. The region of higher resistivity was identified but some

elements around this region (that would not have) acquired a resistivity value upper than expected one. However due to the discretization and to the difficulty to tune the SA parameters not all of elements reached the upper limit. The elapsed time was 503 minutes and final objective function was 6.35.

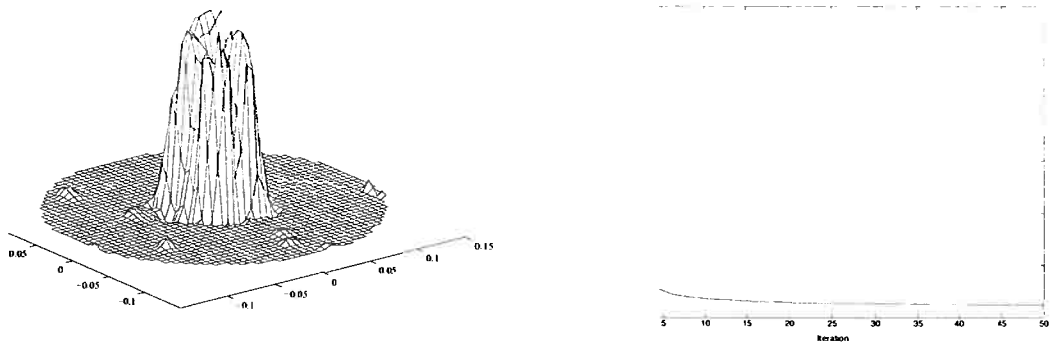

(a) (b)

Figure 7. (a) FE mesh for the inverse problem and (b) used configuration for test 3

7. Conclusions

An EIT algorithm based on SA method was proposed and implemented for image estimation. With numerical tests excellent results were obtained, so the stability of the algorithm was demonstrated. The evaluation of the experimental data was good because the algorithm identified the bigger resistivity region even having a poor discretization. The SA algorithm studied in this work allows to include restrictions limiting the solution space and introducing additional information with no need to use regularización techniques. In general, the results obtained here are comparable to the gotten ones with other absolute algorithms like Gauss-Newton, UKF or MCMC in similar conditions, however the processing time are very bigger. In order to improve the performance of the algorithm it should be worked specifically with the choice of *a priori* information, the optimization of its velocity, to use FE meshes more discretized and some tests must be made to find the way to reduce the effort of tunning the SA parameters.

8. Acknowledgement

First author thanks the financial support of FAPESP through master scholarship with process number $04/11159 - 1$.

9. REFERENCES

Barber, D.C., Brown, B.H., 1984, "Applied Potential Tomography", Journal of Physics E:Scientific Instruments, Vol.17, pp. 723-733.

Cheney, M., Isaacson, D. and Newell, J.C. and Goble, J. and Simske, S., 1999, "Electrical Impedance Tomography", SIAM Journal on Applied Mathematics, Vol.41, No. 1, pp. 85-101.

Harris, N.D, Sugget, A.J. and Barber, D.C. and Brown, B.H., 1987, "Applications of applied potential tomography (APT) in respiratory medicine", Clin. Phys. Physiol. Meas., Vol.8, pp. 155-165.

Holder, D., 1993, "Clinical and Physiological Applications of Electrical Impedance Tomography", Londres: UCL Press, Vol.8, 310 p.

Akbarzadeh, M.R., Tompkins, W.J. and Webster, J.G., 1990, "Multichannel Impedance Pneumography For Apnea Monitoring", Proceedings of the Twelfth Annual International Conference of the IEEE Engineering in Medicine and Biology Society, Vol.12, No. 3, pp. 1048-1049.

Bagshaw, A.P., Liston, A.D. and Bayford, R.H. and Tizzard, A. and Gibson, A.P. and Tidswell, A.T. and Sparkes, M.K. and Dehghani, H. and Binnie, C.D. and Holder, D.S., 2003, "Electrical impedance tomography of human brain function using reconstruction algorithms based on the finite element method", NeuroImage, Vol.20, pp. 752-764.

Noordegraaf, A.V., Faes, T.J. and Janse, A. and Marcus, J.T. and Bronzwaer, J.G. and Postmus, P.E. and de Vries, P.M., 1997, "Noninvasive assessment of right ventricular diastolic function by electrical impedance tomography", CHEST, Vol.111, pp. 1222-1228.

Cherepenin, V., Karpov, A. and Korjenevsky, A. and Kornienko, V. and Kultiasov, Y. and Ochapkin, M. and Trochanova, O. and Meister, D., 2002, "Three-dimensional EIT imaging of breast tissues: system design and clinical testing", IEEE Trans. Medical Imaging, Vol.21, No. 6, pp. 662-667.

Barber, D.C., 1990, "Quantification in impedance imaging", Clin. Phys. Physiol. Meas., Vol.11, pp. 45-56.

Asfaw, Y.W., 2005, "Automatic detection of detached and erroneous electrodes in Electrical Impedance Tomography", School of Information Technology and Engineering, University of Ottawa.

Murai, T., Kagawa, Y., 1985, "Electrical Impedance Computed Tomography based on a finite element model" , IEEE Transactions on Biomedical Engineering, Vol.32, No. 3, pp. 177-184.

Kallman, J.S., Berryman, J.G., 1992, "Weighted least-squares criteria for electrical impedance tomography", IEEE Trans. Medical Imaging, Vol.11, pp. 284-292.

Calderón, A.P., 1980, "On an Inverse Boundary Value Problem", Proceedings of Seminar on Numerical Analysis and its Applications to Continuum Physics, Brazil: Soc. Brasileira de Matemática, pp. 65-73.

Connolly, T.J., Wall, D.J.N., 1998, "On an inverse problem, with boundary measurements for the steady state diffusion equation", Inverse Problems, Vol.4, pp. 995-1012.

Kim, Y., Webster, J.G. and Tompkins, W.J., 1983, "Electrical impedance imaging of the thorax", Journal of Microwave Power, Vol.18, pp. 245-257.

Yorkey, T.J., Webster, J.G. and Tompkins, W.J., 1987, "Comparing Reconstruction Algorithms for Electrical Impedance Tomography", IEEE Trans. on Biomed. Eng., Vol.34, No. 11, pp. 843-852.

Adler, A., Guardo, R., 1996, "Electrical Impedance Tomography: Regularized imaging and Contrast Detection", 1996, IEEE Trans. Medical Imag., Vol.15, pp. 170-179.

Metropolis, N., Rosenbluth, A.W. and Rosenbluth, M.N. and Teller, A.H. and Teller, E., 1953, "Equation of state calculation by fast computing machines", Journal of Chemistry Physics, Vol.21, pp. 1087-1091.

Lutfiyya, H., McMillin, B. and Poshyanonda, P. and Dagli, C., 1992, "Composite Stock Cutting Through Simulated Annealing", Mathematical and Computer Modelling, Vol.34, pp. 111-124.

Hua, P., Woo, J. and Webster, J.G. and Tompkins, W., 1993, "Finite element modeling of electrode-skin contact impedance in Electrical Impedance Tomography", IEEE Transactions on Biomedical Engineering, Vol.40, No. 4, pp. 335-343.

Cheng, K.S., Isaacson, D. and Newell, J.C. and Gisser, D.G., 1989, "Electrode models for electric current computed tomography", IEEE Trans Biomed Eng., Vol.36, No. 9. pp. 918-924.

Logan, D.H., 1986, "A First Course in the Finite Element Methods", Boston: PWS Engineering.

Kim, Y., Webster, J.G. and Tompkins, W.J., 1983, "Electrical impedance imaging of the thorax", Journal of Microwave Power, Vol.18, pp. 245-257.

Cerny, V., 1985, "Thermodynamical aproach to the traveling salesmanproblem: an efficient simulation algorithm", Journal of Optimization Theory and Applications, Vol.45, No. 1, pp. 41-51.

Elliott, S.J., 2001, "Signal Processing for Active Control", Academic Press Inc., 511 p.

Corana, A., Marchesi, M. and Martini, C. and Ridella, S., 1987, "Minimizing Multimodal Functions of Continuous Variables with the Simulated Annealing Algorithm", ACM Transactions on Mathematical Software, Vol.13, pp. 262-280.

Vanderbilt, D., Louie, S.G., 1984, "A Monte Carlo Simulated Annealing Approach to Optimization over Continuous Variables", Journal of Comput. Phys., Vol.56, pp. 259-271.

Bohachewsky, I.O., Johnson, M.E. and Stein, M.L., 1986, "Generalised simulated annealing for function optimization", Technometrics, Vol.28, pp. 209-217.

ANEXO F - Programação Linear Sequencial

THE USE OF LINEAR PROGRAMMING AS SEARCH METHOD OF IMAGES IN ELECTRICAL IMPEDANCE TOMOGRAPHY

Miguel Fernando Montoya Vallejo, montovall@gmail.com
Claudia Natalia Lara Herrera, natylara@gmail.com
Fernando Silva de Moura, fernandosmoura@gmail.com
Julio Cesar Ceballos Aya, jccaya@usp.br
Raul Gonzalez Lima, lima.raul@gmail.com
University of São Paulo, Escola Politécnica da USP, Department of Mechanical Engineering, Av. Prof. Luciano Gualberto, no. 2231 - CEP - 05508 - 900 - São Paulo - SP

Abstract. *Electrical Impedance Tomography allows to monitor the lungs under forced ventilation and it is a non invasive procedure. It uses electrical potentials of electrodes attached to the thorax, when electrical current is imposed on some electrodes. The measurements allow estimating the electrical resistivity distribution inside the thorax, which, in turn, can be related to the lungs state. The present work evaluates the use of Linear Programming (LP) as a method to search images in Electric Impedance Tomography. Linear Programming is used to solve an ill-conditioned linear system in the Sensitivity Matrix algorithm, imposing restrictions in the solution space. These restrictions reduce the solution space to a closed region, with clinical and physical meaning. The tests were performed using numerically simulated data and experimental data. The images using Linear Programming are compared to images obtained using Lower Upper Triangular Decomposition (LU Decomposition). The use of LP and restrictions of the solution space generated images with better spacial solution, better resistivity resolution and more uniform sensitivity in the center of the domain compared to the use of the LU Decomposition and a small regularizing term*

Keywords: *Electrical Impedance Tomography, Linear Programming, Linear System*

1. INTRODUCTION

The necessity to visualize the interior of a domain whose access with devices like micro-cameras is difficult, impracticable, or impossible, led to the development of methods of estimation of images based in the variations of electric properties of the domain. Such methods are currently used in a variety of applications that involve from the control of industrial processes to the aid in medical diagnostics. Electrical Impedance Tomography (EIT) is well known among the different methods.

EIT can monitor the lungs in a continuous and non invasive way during the forced ventilation. In this technique the domain is discretized using a finite element mesh, electrodes are placed in the border of the domain, known currents are injected and electric potentials are measured through these electrodes. The electric potentials measurement makes possible to estimate the distribution of resistivity or conductivity in the interior of the domain. In medical diagnosis, EIT are being applied in different areas, such as the monitoring of cerebral blood flow and blood volume changes [9], study of cerebral haemodynamics in the newborn for many years [7] and detection and monitoring of apnea and edema [12].

Some industrial applications of the EIT are the monitoring of the solid distribution inside hidrociclone [11], images of industrial flows, volumetric flow's alterations in oil and gas [3], measures of material's distribution in two phases flows [4], images of volcanic magma [8] and detection of antitank mines [2].

In EIT, it is common to speak about the Forward Problem and Inverse Problem. In the forward problem the electric properties of the domain are defined, the currents injected and the structure of the model is known beforehand. The objective is to calculate the electric potentials in the electrodes. To calculate the electric potential in the electrodes is necessary to solve "Eq (1)"

$$[Y]\{V\} = \{C\} \tag{1}$$

where $[Y_{(\rho)}] \in \Re^{m \times m}$ is the matrix of global rigidity in function of resistivity $\{\rho\} \in \Re^n$ and $\{V_{(\rho)}\} \in \Re^m$ is a matrix of corresponding voltages to each current pattern injected. The term *current pattern* is defined as the way how the current is injected, equally the term *voltage pattern* is defined as the way how the voltage is measured. In the literature, various works present different forms to inject current and to measure potentials, in the present work the patterns method *jump an electrode* was adopted.

To solve a "Eq (1)" is necessary to eliminate the singularity of the rigidity matrix, the article *Comparing reconstruction algorithms for electrical impedance tomography* [13] describes the procedure to eliminate the singularity of the rigidity matrix.

In the inverse problem the potentials in the electrodes are known as well as the currents, the structure of the model and it aims to know the electric properties distribution. For the solution of the inverse problem, exists in the literature the absolute methods and the methods that generate images of variation of the electrical properties.

For the absolute methods, the images are in absolute values of resistivity, as example it is cited topological Optimiza-

tion Method [6], The Newton Raphson Method [1] and variants of the Filter of Kalman [10]. In the methods that generate images of variation of the electric properties, the images are the difference between two values of absolute resistivities, or either, the equivalent to an absolute value in a reference system whose zero has been translated to any chosen point as zero, as an example is cited Sensitivity Matrix method which is implemented in the present work.

Variations of the resistivity distribution are the result of the solution of a linear system of the type $[A]\{x\} = \{b\}$. The objective of the present work is to evaluate the performance of the Linear Programming (LP) in the solution of the linear system, from the point of view of numerical errors propagation and the easiness to restrict the solution to the region of interest.

This paper is organized as follows, in section II the mathematical formulation of the domain is presented, also the modeling of the domain and the electrodes by means of the Finite Elements Method (FEM). In section III Sensitivity Matrix is described which is implemented to solve the inverse problem. The use of the Linear Programming in EIT and the implementation of this technique in the Sensitivity Matrix is shown in section IV. In section V it is explained the data utilized for testing LP. The results with the different generated data are shown in section VI and finishing in section VII the results are discussed.

2. Finite Element Model

Having a domain with unknown electric properties, EIT allows estimate his distribution of resistivity, given the excitation of the system consisting in current imposed in the contour of the domain and the electrical potentials are measured in regions of the contour of the domain. It is known that different tissues of the human body have different electrical properties, the relations that govern the iterations between the electricity and the magnetism are summarized in the Maxwell's equations.

The Maxwell's equations can be simplified in the following elliptic partial differential equation:

$$\nabla \cdot (\frac{1}{\rho}\nabla V) = 0 \quad in \ \ \Omega \tag{2}$$

where ρ is the electrical resistivity, V is the electrical potential and Ω is the domain in study. The "Eq (2)" is also known as forward problem, the solution of this equation determines the electrical potentials that are used in the implementation of the algorithms. The solution of the forward problem can be determined with the knowledge of the conditions of Newmann and Dirichlet on the surface of the domain $\partial\Omega$. To be able to apply the conditions of Newmann and Dirichlet the domain Ω was discretized using the finite elements method (FEM).

The domain of interest Ω is discretized in a mesh of m nodes and n triangular elements (triangular elements of three nodes), the electrical potential in each element is approximated by a function of linear interpolation that depends on the electric potential values on nodes of the element. The electric potential is described by a finite dimensional space and the problem of finding the nodal electric potentials, $\{V\}$, turns into an algebraic problem or the following linear system of equations: where $\{V\}$ is the vector of nodal electric potentials, $\{I\}$ is the vector of nodal electric currents and $[K]$ is the matrix of global rigidity in function of electrical resistivity. With the electrodes placed in the surface of the domain, the effect of the contact impedances electrode-skin must be taken into account. In this work, we considered the complete electrode model [5] to represent these effects. The considered model generates a matrix $[Y_i^e]$ and a vector Ie correspondent to each electrode placed in the surface of the domain $\partial\Omega$, the new matrix and the new vector are added in $[K]$ and $\{I\}$, respectively. The matrix $[Y_i^e]$ is

$$[Y_i^e] = \frac{ab}{3t\rho}\begin{bmatrix} 1 & \frac{1}{2} & 0 & -\frac{3}{2} \\ & 2 & \frac{1}{2} & -3 \\ sim & & 1 & -\frac{3}{2} \\ & & & 6 \end{bmatrix} \tag{3}$$

It is assumed that the potential in the metallic part of the electrode is equal, the thickness of the interface of the electrode t is smaller that the width of the electrode a ($t \ll a$).

Adding the matrix of the electrode model in the matrix of global rigidity, we obtain the following system: (1)", we obtain the following system:

$$[K_T]\{V_T\} = \{I_T\} \tag{4}$$

Once the electric potential of a reference node is chosen, the system can be solved for the vector $\{V_T\}$, a non-linear function of the resistivity distribution.

3. Sensitivity Matrix

A domain Ω that represents a distribution resistivity not-uniform $\rho(x,y)$ is discretized using FEM. Under these hypotheses, it can define the transformation $h_j : (\rho, I) \longrightarrow \{v_j\}$ for vector $\{v_j\}$ (vector of nodal electrical potentials for which current pattern), $j = 1, \ldots, p$ (p number of current patterns)

$$\{v_j(\rho)\} = h_j(\rho) = [Y(\rho)]^{-1}\{I_j\} \tag{5}$$

where $\{I_j\} \in \Re^m$ is the current pattern injected.

From the "Eq. (5)", can be concluded that the vectors of nodal voltages are nonlinear functions of the distribution of resistivity in the domain. Applying series of Taylor and truncating the series from the linear term and around a distribution ρ_0, we obtain:

$$\{v_j(\rho)\} \approx \{v_j(\rho_0)\} + \frac{\partial h_j\,|_{(\rho_0)}}{\partial \rho}[\rho - \rho_0] \Longrightarrow \underbrace{\{v_j(\rho)\} - \{v_j(\rho_0)\}}_{\{\Delta V\}} = \underbrace{\frac{\partial h_j\,|_{(\rho_0)}}{\partial \rho}}_{H_j} \underbrace{[\rho - \rho_0]}_{\{\Delta\rho\}} \tag{6}$$

Calculating the partial derivative of the transformation h_j with respect the resistivity of each element for

$$H_j(\rho_0) = \frac{\partial h_j\,|_{(\rho_0)}}{\partial \rho} = -[Y]^{-1}\frac{\partial\,[Y]}{\partial \rho}[Y]^{-1}[I_j] \tag{7}$$

$$H_j(\rho_0) = \left[-[Y]^{-1}\frac{\partial [Y]}{\partial \rho_1}[Y]^{-1}\{I_j\} \quad -[Y]^{-1}\frac{\partial [Y]}{\partial \rho_2}[Y]^{-1}\{I_j\} \quad \cdots \quad -[Y]^{-1}\frac{\partial [Y]}{\partial \rho_n}[Y]^{-1}\{I_j\}\right], j = 1, \ldots, p \tag{8}$$

where $[H_j] \in \Re^{p\times n}$ is called *Sensitivity Matrix*,

To find the resistivity from the equation "Eq (7)" it is necessary to define the following performance index

$$IP = \frac{1}{2}\Big([H]|_{\rho_0}\{\Delta\rho\} - \{\Delta V_m\}\Big)^T\Big([H]|_{\rho_0}\{\Delta\rho\} - \{\Delta V_m\Big) + \alpha\{\Delta\rho\}^T[F]^T[F]\{\Delta\rho\} \tag{9}$$

where $[F] \in \Re^n$ is a regularization matrix and α is a regularization parameter. It is necessary to determine the resistivity variation that minimizes the difference between the measured voltage and the calculated voltage, for such objective is necessary derived the performance index with respect $\{\Delta\rho\}$ and to equal to zero

$$\frac{\partial IP}{\partial \Delta\rho} = 0 \Longrightarrow [H]|^T_{\rho_0}\Big([H]|_{\rho_0}\{\Delta\rho\} - \{\Delta V_m\}\Big) + \alpha[F]^T[F]\{\Delta\rho\} = 0 \tag{10}$$

Grouping terms in the "Eq (10)" we obtain the expression of interest

$$\Big([H]|^T_{\rho_0}[H]|_{\rho_0} + \alpha[F]^T[F]\Big)\{\Delta\rho\} = [H]|^T_{\rho_0}\{\Delta V_m\} \tag{11}$$

4. Using Linear Programming to Electrical Impedance Tomography

Linear Programming (LP) is used in TIE in the solution of linear systems of the type $[A]\{\vec{x}\} = \{b\}$ taking advantage of the fact that it is possible to impose restrictions in the variables $\{\vec{x}\}$.

The problem of identifying the resistivity distributions inside of the thorax has natural restrictions, resistivity cannot be negative and cannot exceed a characteristic maximum value of a biological tissue. These restrictions become the convex space solution, simplifying the solution of the inverse problem.

To solve the linear system is necessary to rewrite the classic LP problem. An arbitrary vector is chosen $\{\vec{x}_0\} \in \Re^n$ and then is proceeded to determine the vector $\{\vec{e}\} \in \Re^n$ as $\{\vec{e}\} = [A]\{\vec{x}_0\} - \{b\}$.

The original system of restrictions in the form $[A]\{\vec{x}\} = \{b\}$ is rewritten as presented in the following equation

$$[A]\{\vec{x}\} - \{b\} + \delta\{\vec{e}\} = 0 \tag{12}$$

The original problem is reformulated of the following form form

$$\begin{aligned} &\text{Minimize} \quad \delta \\ &\text{Subject to} \\ &[A]\{\vec{x}\} - \{b\} + \delta\{\vec{e}\} = 0 \\ &\{\vec{x}_{min}\} \leq \{\vec{x}\} \leq \{\vec{x}_{max}\} \\ &0 \leq \delta \leq \epsilon \end{aligned} \tag{13}$$

when $\delta \approx 0$, the solution vector $\{\vec{x}\}$ satisfies $[A]\{\vec{x}\} = \{b\}$.

Examining the "Eq (11)", it represents a linear system in the form $[A]\{x\} = \{b\}$, then by comparison we can identify our matrix $[A]$ and vectors $\{x\}$ and $\{b\}$

$$[A]\{x\} = \{b\} \Longrightarrow \underbrace{\left([H]|_{\rho_0}^T[H]|_{\rho_0} + \alpha[F]^{\mathsf{T}}[T][F]\right)}_{[A]} \underbrace{\{\Delta\rho\}}_{\{x\}} = \underbrace{\left([H]|_{\rho_0}^T\{\Delta V_m\}\right)}_{\{b\}} \tag{14}$$

Applying the previously mentioned procedure for the Sensitivity Matrix, we obtain

$$\begin{aligned} &\text{Minimizar} \quad \delta \\ &\text{Sujeito a} \\ &\left([H]|_{\rho_0}^T[H]|_{\rho_0} + \alpha[F]^T[F]\{\Delta\rho\} - ([H]|_{\rho_0}^T\{\Delta V_m\}\right) + \delta\{\vec{e}\} = 0 \\ &\Delta\rho_{min} \leq \Delta\rho \leq \Delta\rho_{max} \\ &0 \leq \delta \leq \epsilon \end{aligned} \tag{15}$$

Where

$$\{\vec{e}\} = \left([H]|_{\rho_0}^T[H]|_{\rho_0} + \alpha[F]^T[F]\{\Delta\rho_a\}\right) - \left([H]|_{\rho_0}^T\{\Delta V_m\}\right)$$

The imposition of limits in the "Eq (14)" is having in account a prior information, the value of resistivity found for the algorithm has that to be positive for the case of tank and the object, then the value zero is fixed for the inferior limit and the value for the superior limit can be fixed for the maximum value of resistivity that can be found, for ours study case this value is the resistivity of the object. For medical applications, the resistivities inside the thorax [14], they are positive values that vary since $4\Omega m$ for the heart (muscle) even $1 \times 10^5\Omega m$ for the present air in the lungs. Leaving of this known information as a prior, is possible to impose the limits in the variable to get medical images.

5. Simulated and Experimental data

The numerical phantom used to generate the simulated data consists of a circular domain with a 2D mesh. The resistivity distribution is known as a prior. Two sets of data are generated, one set will be called *basal* and the other set will be called *with-object*. To generate the *basal* set of simulated electrical potentials, the resistivity distribution is uniform. To generate the set *with-object* of simulated electrical potentials, the resistivity distribution of the domain is uniform except for a cylindrical region, called object, that has a higher resistivity.

The experimental data was obtained from a cylindrical container with 30 electrodes attached to its boundary with 35 mm high and 10mm wide (the thickness of each electrode is not necessary for the algorithm). The electrodes are equally spaced along the container's boundary, which was filled up to 35 mm with a $0.3g/L$ saline solution (NaCl). Its resistivity is approximately $17\Omega m$. The inner diameter of the container is $300mm$. The object, a glass cillinder, has $32mm$ of diameter and resistivity close to $10^6\Omega m$.

To obtain the electrical potentials in the electrodes, a pair of them was electrically excited following the current pattern seen in the section 1. Then, the relative potentials were measured, except for those which share current carrying electrodes, due to hardware limitations. The pair of electrodes used for current injection was successively changed until a satisfactory number of observations was obtained, providing the necessary data for the estimation of an image. Thirty current patterns were applied.

6. Results

To obtain the simulated data it was used a phantom with uniform resistivity in a cylindrical domain and a cylindrical inclusion placed in two different positions. The first position of the object is $0.11m$ off the center "Fig.1(a) " and the second position of the object is at the center of domain "Fig.1(b) ". The resistivity of the object was $100\Omega m$. The other

elements of the domain had $10\Omega m$ of resistivity. The initial estimate of resistivity was $10\Omega m$ for the elements and the initial electrode parameters were $0,02\Omega m^2$. The injected current was $2mA$. The meshes to solve the inverse problems are shown in "Fig.2(b) and "Fig.3(b) ". The meshes to solve the direct problems are shown in "Fig.2(a)" and "Fig.3(a) ".

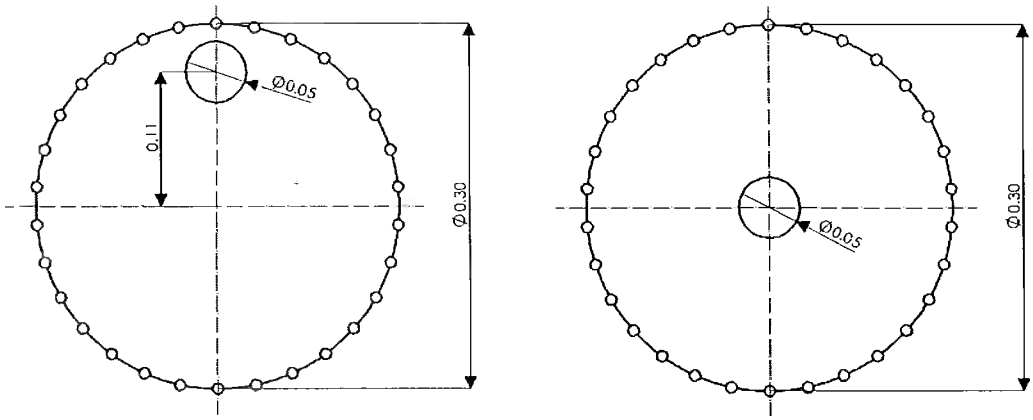

(a) (b)

Figure 1. Object located at (a) the boundary (b) the center

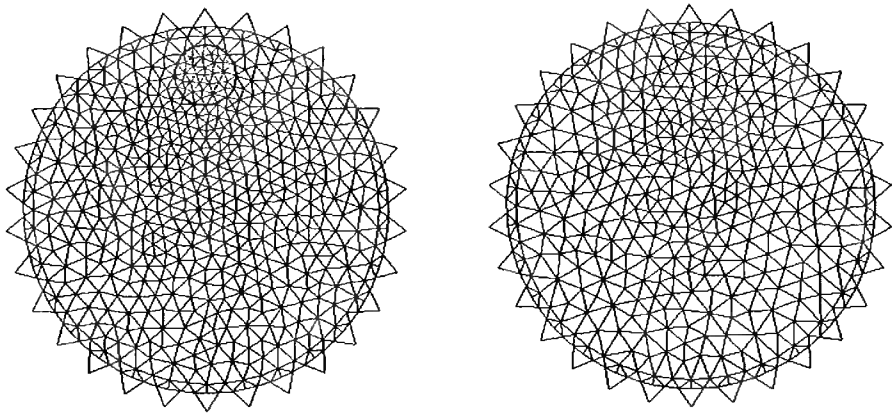

(a) (b)

Figure 2. Finite elements meshes to solve the (a) forward and (b) inverse problem, inclusion close to the boundary

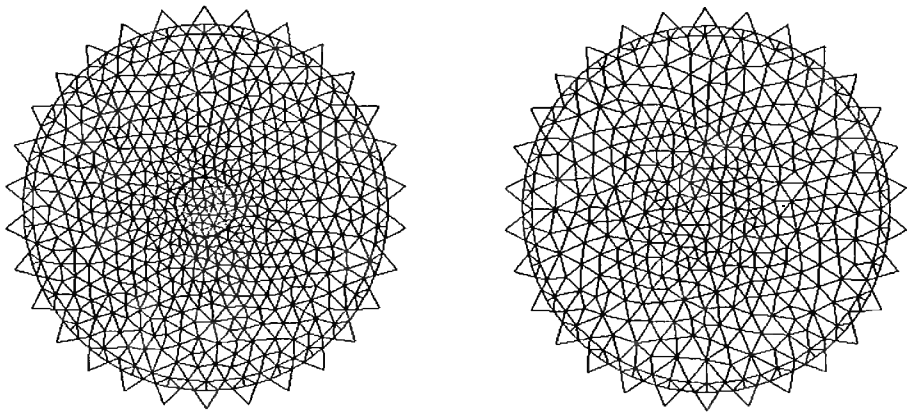

(a) (b)

Figure 3. Finite elements meshes to solve the (a) forward and (b) inverse problem, inclusion close to the center

To obtain experimental data, the object was located in two positions, near the border and in the center of the cillindrical

vessel. The adopted electrode parameters were $0.02\Omega m^2$ and the initial resistivity of the saline solution was $20.0\Omega m$. The injected current was $2mA$ peak in amplitude and $125kHz$ in frequency. The finite elements mesh used to solve the inverse problem is shown in the "Fig.4 "

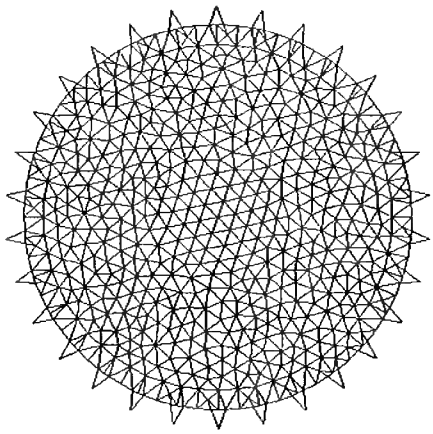

Figure 4. Finite elements mesh to solve the inverse problem with experimental data

The images obtained using simulated data are in figure 6and figure 6. The regularization parameter was $\alpha = 1.0e^{-2}$ when the object is $0.11m$ off the center and $\alpha = 1.0e^{-2}$ when the object is at the center.

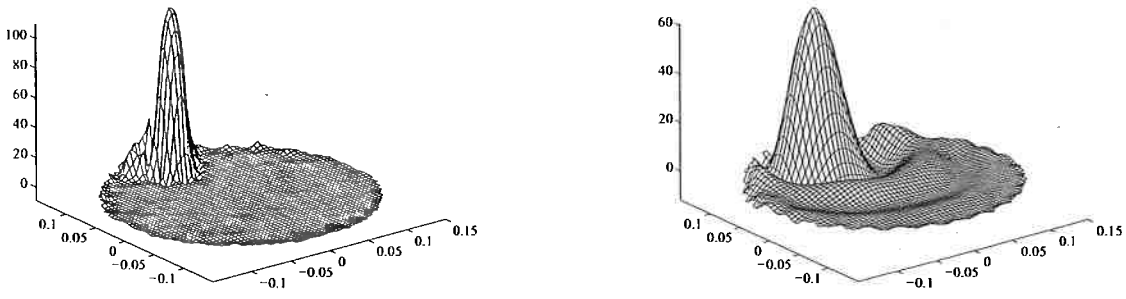

(a) (b)

Figure 5. Variation of resistivity when the object is $0.11m$ off the center of the domain, units in $\Delta\rho[\Omega m]$, and $\alpha = 1.0e^{-2}$ (a) with LP and (b) LU Decomposition

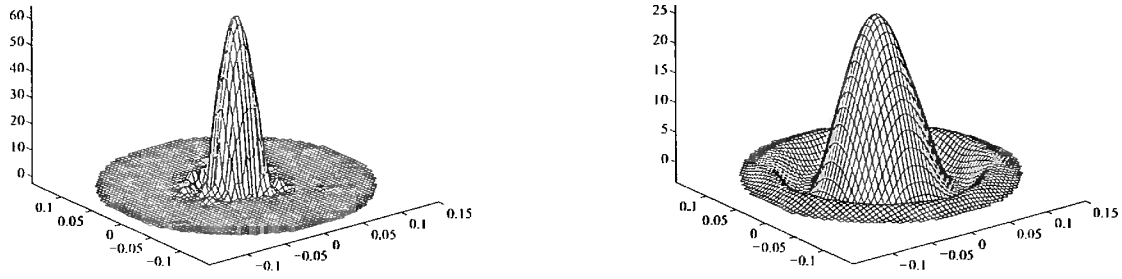

(a) (b)

Figure 6. Variation of resistivity when the object is at the center of the domain, units in $\Delta\rho[\Omega m]$, and $\alpha = 1.0e^{-2}$ (a) with LP and (b) LU Decomposition

The images obtained using experimental data are shown in figure 6and 6. The regularization parameter was $\alpha = 1.0e^{-}3$ when the object is $0.11m$ off the center and $\alpha = 1.0e^{-2}$ when the object is at the center.

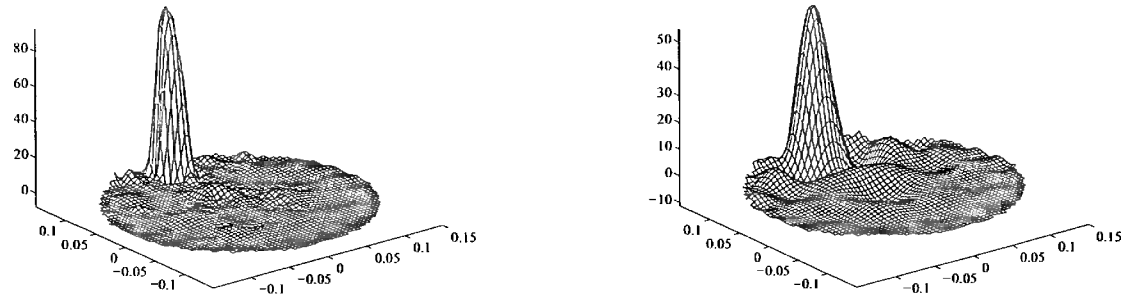

(a) (b)

Figure 7. Variation of resistivity when the object is $0.11m$ off the center of the domain $\Delta\rho[\Omega m]$ and $\alpha = 1.0e^{-3}$ (a) with LP and (b) LU Decomposition

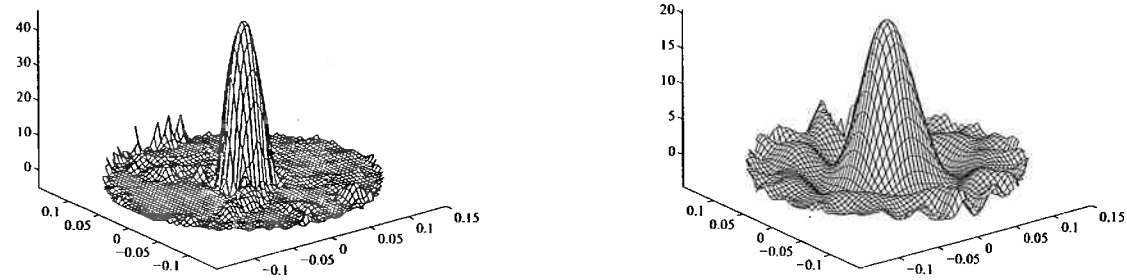

(a) (b)

Figure 8. Variation of resistivity in the center of the tank $\Delta\rho[\Omega m]$ and $\alpha = 1.0e^{-3}$ (a) with LP and (b) LU Decomposition

The resistivity of the saline is expected to be near $20\Omega m$ for the tests with experimental data. The resistivity of the object was estimated 20% lower than the expected resistivity when the object is close to the boundary.

7. Final Comments

The image obtained using Linear Programming to solve the linear system presented higher resistivity distribution, higher resolution in space, with a satisfactory diameter and good position of the object. The image obtained using LU Decomposition and Tikhonov regularization to solve the linear system presented smaller resistivity distribution and smaller spatial resolution than using Linear Programming.

The improvement of the images using LP is partially due to the imposition of restrictions in the variables that reduce the solution space, whithout using a laplacian regularizing term, which penalizes high frequency spatial content. Another reason for improvement of the images using LP is the smaller numerical error propagation during the computation of the solution of linear systems.

8. Acknowledgment

The authors are grateful for the financial support from The State of São Paulo Research Foundation, through a master's scholarship, FAPESP number 04/11159-1, the financial support under FAPESP number 01/05303-4 and from The Brazilian National Research Council for a master's scholarship number CNPq number 134991/2005-2.

9. REFERENCES

Aruca, D.,2002, "Algoritmo de Tomografia por impedância elétrica", Dissertação (Mestrado), Departamento de Engenharia Mecânica, Escola Politécnica, Universidade de São Paulo.

Church, P.M., Philip, M.W, Stephane, G. and John, M., "Performance Assessment of an Electrical Impedance Tomography Detector for Mine-Like Objects", Defence Research Establishment Suffield DRES.

Fehmers, G.,2003, "Volumetric flow rates from impedance tomography in oil/gas flows ", 3rd World Congress on Industrial Process Tomography.

George, D.L., Torczynski, J.R., Shollenberger, K.A., Ohern T.J. and Ceccio, S.L.,2000, "Validation of electrical-impedance tomography for measurements of material distribution in two-phase flows", International Journal of Multiphase Flow.

Hua, J.W.P, Webster, J. and Tompkins, W.,1993, "Finite element modeling of electrode-skin contact impedance in electrical impedance", IEEE Transactions on Biomedical Engineering, Vol.40, No. 4, pp. 335-343.

Lima, C., Silva, E. and Lima, R.,2003, "Topology optimization method applied to obtain images from electrical impedance tomography technique", Proceedings of 17th International Conference of Mechanical Engineering, pp. 535-538.

Murphy, D., Burton, P., Coombs, R., Tarassenko, L. and Rolfe, P., 1987, "Impendace imaging in the newborn", Clin. Phys. Physiol. Meas.

Myer, D., Constable, S. and Key, K., "Electrical Impedance Tomography of a Seafloor Volcano".

Tidswell, T., Gibson, A., Bayford, R.H. and Holder, D.S.,2001, "Three dimensional electrical impedance tomography of human brain activity", Neuroimage.

Trigo, F.,2001, "Filtro estendido de Kalman aplicado à tomografia por impedância elétrica", Dissertação (Mestrado), Departamento de Engenharia Mecânica, Escola Politécnica, Universidade de São Paulo.

Williams, R.A., Dickin, F.J., Gutiérrez, J.A., Dyakowski, T. and Beck, M.S.,1997, "Using electrical impedance tomography for controlling hydrocycolne underflow discharge", Control Engineering Practice.

Woo, E.J., Hua, P., Webster, J.G. and Tompkins, W.,1992, "Measuring lung resistivity using electrical impedance tomography", IEEE Transactions on Biomedical Engineering, Vol.39, No. 7, pp. 756-760.

Yorkey, T.J. and Webster, J.G.,1987, "Comparing reconstruction algorithms for electrical impedance tomography", Transactions on Biomedical Engineering, Vol.34, No.11, pp. 843-852.

Zhang, J. and Patterson, R.P.,2006, "EIT images of ventilation: what contributes to the resistivity changes ?", Institute of Physics Publishing.

10. Responsibility notice

The author(s) is (are) the only responsible for the printed material included in this paper

ANEXO G – TIE via Otimização Topológica

TOPOLOGY OPTIMIZATION APPLIED TO 2D AND 3D ELECTRICAL IMPEDANCE TOMOGRAPHY

Cícero Ribeiro de Lima
Dept. of Mechatronics and Mechanical Systems Engineering - University of São Paulo - 05508-900, Brazil
cicerorl@usp.br

Luis Augusto Motta Mello
Dept. of Mechatronics and Mechanical Systems Engineering - University of São Paulo - 05508-900, Brazil
luis.mello@poli.usp.br

Emílio Carlos Nelli Silva
Dept. of Mechatronics and Mechanical Systems Engineering - University of São Paulo - 05508-900, Brazil
ecnsilva@usp.br

Abstract. *Electrical Impedance Tomography (EIT) is an imaging technique which tries to find conductivity distribution inside a section of body. The EIT deals with an inverse problem in which given the measured voltages on electrodes it estimates the conductivity distribution by using an image reconstruction algorithm. EIT can be used in several applications and, recently, it has been applied for obtaining images in medical applications. Several types of reconstruction algorithms have been reported and used. In this work, images of lungs are obtained by applying Topology Optimization Method as reconstruction algorithm in EIT. Solution of this optimization problem is obtained combining the Finite Element Method and a sequential Linear Programming algorithm (SLP). Since it is an ill-posed problem, regularization schemes based on spatial filters and included constraints are used. The SLP allows to include easily regularization schemes and to work well even though under high noisy measurements. Reconstruction of some 2D and 3D examples using numerical and experimental data are shown.*

Keywords: *Topology Optimization, Electrical Impedance Tomography, Finite Element Method*

1. Introduction

Since the beginning of 90´s years, a technique called Electric Impedance Tomography (EIT) has been studied as an interesting alternative for obtaining images on clinical applications. In fact, EIT has been applied to geophysical sciences (Parker, 1984; Ramirez *et al.*, 1993) and in non-destructive testing (Santosa, Kaup and Vogelius, 1996; Santosa and Vogelius, 1991), however in medical procedures its application is recent (Cheney, Isaacson and Newell, 1999; Borcea, 2002). EIT is based on an inverse problem where, given the voltages measured on electrodes positioned on the boundary of body, it tries to find the conductivity distribution inside of body, and as a consequence its image. A sequence of low intensity electrical currents is applied to the body section, through electrodes positioned around the patient's body and aligned in a plane corresponding to a transverse section of the body (Cheney, Isaacson and Newell, 1999), as illustrated in Figure 1.

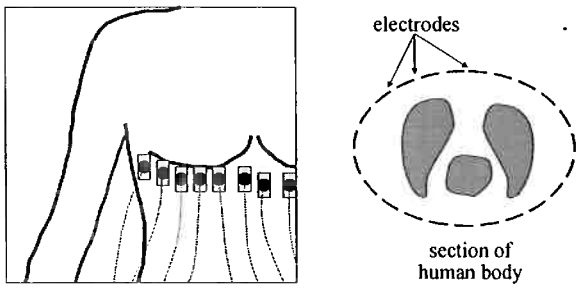

Figure 1 – Electrodes positioned around the body.

Technology of EIT is safer and cheaper than other tomography techniques and although it has poor resolution it has potential for clinical applications such as monitoring mechanical ventilation of lungs (Amato *et al.*, 1998) and monitoring heart function and blood flow (Holder, 1993). Moreover an EIT device is portable which allows its installation for continuous monitoring of bedridden patients, which avoids dangerous patient transportation from ICU (Intensive Care Unit) to the exam room. In this technique the patient does not have exposition to any type of radiation, just to the low electrical current levels that do not cause any harm to the patient (Cheney, Isaacson and Newell, 1999).

This work presents results obtained from application of Topology Optimization Method (TOM) to EIT image reconstruction. TOM tries to find systematically a material distribution inside of a design domain, to extremize an objective function requirement, satisfying some specified constraints (Bendsøe and Sigmund, 2003). The topology

optimization problem applied to EIT consists on finding a material distribution (or conductivity distribution) of a body that minimizes the difference between electrical potentials obtained from electrode measurements at the boundary of the body and electrical potentials simulated numerically from a computational model of this body. This optimization problem is solved by a computational algorithm that combines Finite Element Method (FEM) with an optimizer called Sequential Linear Programming (SLP) (Haftka, Gürdal and Kamat, 1996), which allows us to include easily several constraints in optimization problem than other algorithms applied to obtain image in EIT. It is interesting because it constrains the solution space avoiding images without clinical meaning on tomography examination. Moreover, it is known that SLP provides little numerical error propagation.

The FEM mesh of domain is not changed during the optimization process. The FEM formulation is generated from constitutive equation of the conductive medium, which is given by Poisson's equation (Muray and Kagawa, 1985). Thus, electrical potential distribution in the discretized domain is obtained by the following equilibrium FEM system of equations (Bathe, 1996):

$$\mathbf{K}\,\Phi = \mathbf{I} \tag{1}$$

where $\mathbf{K}$ is the global electric conductivity matrix of FEM model, Φ is a nodal electric potential vector and $\mathbf{I}$ is a nodal electric current vector. In this work, the FEM model of the discretized domain uses quadrilateral elements (2D model) or tetrahedral elements (3D model) and, in addition, a FEM electrode model, proposed by Hua, *et al.* (1993), has been applied to represent the electrical behavior of the electrode-electrolyte interface layer. Figure 2 shows the electrode element that is considered in that model.

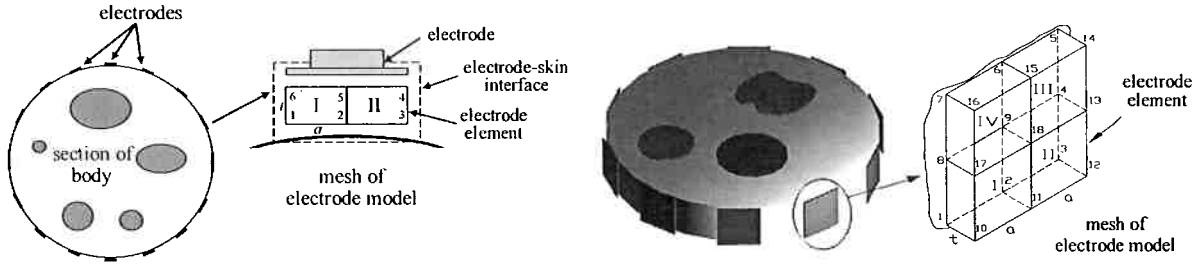

a) 2-D model b) 3-D model

Figure 2 – Electrode model.

For this electrode model, the electric potential on the surface of the metal electrode (nodes 4, 5 and 6 in 2-D model, for example) is assumed to be uniform. The electrical conductivity matrix (kel) of the electrode element depends on width of an electrode, thickness of the contact interface (electrode-electrolyte) and of resistivity value of the contact interface, as demonstrated by Hua, *et al.* (1993). The product between resistivity and thickness of the contact interface is known as contact impedance (or electrode parameter) of electrode elements. Each electrode element matrix kel is inserted in the global matrix $\mathbf{K}$ in according to its connectivity.

In TOM, the material in each point of domain (or in each element) can vary from a material "A" to another one "B" according to a material model, which allows design variables of optimization problem to go from one material to another in a continuous way. For instance, material "A" could be air and material "B" could be the tissue of lungs. In this work, the material model applied is known as Density Method (Bendsøe and Sigmund, 1999) that defines the conductivity properties ($\mathbf{c}_k$) of each element of domain in the following way:

$$\mathbf{c}_k = \rho_k^{\,p}\mathbf{c}_A + \left(1-\rho_k^{\,p}\right)\mathbf{c}_B \qquad \text{with} \qquad 0 \le \rho_k \le 1;\ k = 1...N \tag{2}$$

where $\mathbf{c}_A$ and $\mathbf{c}_B$ are the conductivity properties of base materials of the domain, p is a penalization coefficient of intermediates materials, and N is number of finite elements. The value of each design variable ρ_k is defined between 0 (presence of "B" only) and 1 (presence of "A" only).

In the next section, the formulation of topology optimization applied to EIT and its numerical implementation are presented. In section 3, image reconstruction results using numerical and experimental data are shown. Finally, in section 4, some conclusions are given.

2. Optimization Problem Formulation and Its Numerical Implementation

The image reconstruction by EIT using TOM can be interpreted as a problem of finding the material distribution inside the domain that reproduces the measured electric potential values at electrodes. Thus, the optimization problem could be:

$$\text{Minimize:} \quad F = \frac{1}{2}\sum_{j=1}^{ne}\sum_{i=1}^{np}\left(\phi_{ij} - \phi_{ij0}\right)^2 \tag{3}$$

Such that: *electrical conductivity equation*
$0 \le \rho_k \le 1$; $k = 1...N$
and *additional constraints*

where F is the objective function in which ϕ_{ij0} and ϕ_{ij} are the measured and simulated electrical potential values, respectively. The values ϕ_{ij} are obtained by computational model of the domain. The *ne* and *np* values are the number of applied current load cases and the number of measurement points (electrodes), respectively. The optimization problem above is an ill-posed problem, which finds different distributions of conductivities in the domain that yield the same voltage values on electrodes. However, TOM allows us to include easily some constraints in the optimization problem, restricting the solution space and regularizing the problem. Thus, additional constraints could be included for improvements in problem solution.

The solution of topology optimization problem shown in Eq. (3) is obtained numerically by iterative optimization algorithm sketched in Fig. 3. The FEM model of the design domain is supplied to the algorithm as initial data. By analysis of the FEM model, the electric potentials (ϕ_{ij}) are calculated, allowing us to obtain the objective function and constraints values. In the next step, the optimization is done by using the gradients of the objective function and constraints, relative to design variables (sensitivity analysis). The optimization is done by using the gradients of the objective function and constraints relative to design variables, which are calculated analytically through an adjoint method (Cook and Young, 1985; Byun *et al.*, 1999). The optimization algorithm is started with an uniform distribution of material for the whole design domain and it supplies a new material distribution (design variables), which is updated in the FEM analysis.

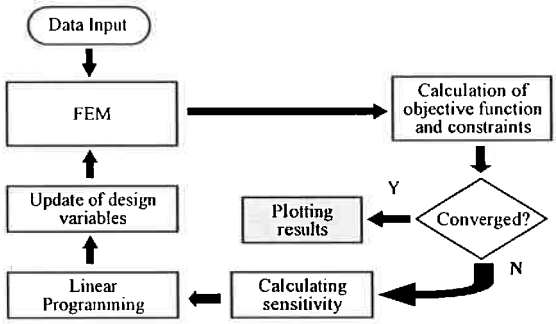

Figure 3 – Flowchart of the TOM algorithm.

The optimization algorithm above, implemented using C language, is known as Sequential Linear Programming (SLP), which has been successfully applied to topology optimization. The SLP allows us to work with a large number of design variables and complex objective functions, and solves a non-linear optimization problem considering it as a sequence of linear sub-problems, which can be solved with Linear Programming (LP) (Haftka, Gürdal and Kamat, 1996). The non-linear problem of Eq. (3) can be linearized by writing a Taylor series expansion of the objective function and keeping only the terms with first order derivatives. For that approach to be valid it is necessary to limit the variation of design variable value in each linear sub-problem by using moving limits (Haftka, Gürdal and Kamat, 1996). In each iteration of topology optimization process, the SLP finds the optimum value for the design variables, that it will be used in the subsequent iteration as initial value. Thus, this process continues successively, until the convergence for the objective function value is achieved.

3. Results

In this section, some 2D and 3D examples will be presented to illustrate image reconstruction using this software with numerical and experimental data. For all examples presented here, electric current load is considered equal to 1 milliampere, which is applied following an adjacent pattern of electrical excitation, as illustrated in Fig. 4. Moreover, in these examples, the topology optimization algorithm uses penalization coefficient value (p) equal to 2.

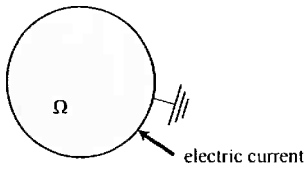

Figure 4 – Adjacent pattern of electrical excitation in EIT.

In this work, to obtain a good quality image for clinical applications in EIT, thirty two 10-mm-wide electrodes are uniformly positioned along the boundary of the design domain (Tang *et al.*, 2002). To find the electrical potentials in these electrodes a pair of them is excited electrically, following the adjacent pattern (see Fig. 4), where the potential in one of them is made to be null ("ground") and the other receives the low intensity electrical current. The pair of electrodes is successively changed until an enough number of observations under different angles is obtained and a high quality image is generated.

3.1. 2-D examples

In this section, the performance of the implemented algorithm is evaluated through 2-D examples and by using numerical and experimental phantoms. First, image of two objects in the domain is obtained by using numerical data and artificial noise. After, the algorithm is applied to obtain an image in a circular domain through using experimental data, in which noise measurements are considerable.

3.1.1. Using numerical data to obtain image of two objects in the domain

The desired image is shown in Fig. 5a, where clear and dark regions simulate a material with 1/17 $(\Omega m)^{-1}$ (clear region) and 10^{-6} $(\Omega m)^{-1}$ (dark regions). In practice, this situation would be equivalent to keep some regions with air in a saline domain, for instance. A numerical phantom, whose domain is uniformly discretized in 3072 four node quadrilateral elements (with thickness equal to 35 millimeters) is considered to simulate accurately the measured electrical potentials (ϕ_{ij0}). On the other hand, a less refined mesh (1120 elements, see Fig. 5b) is applied for image reconstruction. This reduces the computational time to calculate the value of design variables (related to the number of mesh elements) and avoids the inverse crime. The images are obtained from an elliptical domain whose larger axis is 400 millimeters.

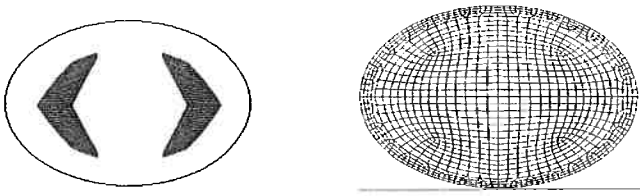

Figure 5 – a) Image to be reconstructed; b) Mesh to obtain image (1120 elements).

In this case, the electrode parameters (see section 1) must also be estimated separately from optimization process. Thus, a numerical phantom (3072 elements) containing only one material (without dark regions) and an electrode parameter value equal to 100 $(\Omega.m^2)^{-1}$ for all electrode elements are adopted to obtain the measured voltages (ϕ_{ij0}) of a saline medium. Based on these voltages values and the less refined mesh (1120 elements), and considering the electrode parameters as design variables, the topology optimization algorithm obtains the optimum electrode parameter values for any initial guess. Since two different domain discretizations are used, numerical errors due this are absorbed by optimized electrode parameters. Therefore, it is noted that most of optimized electrode parameters were not obtained necessarily close to the adopted value of the numerical phantom. In this case, most of them fell in an average error about 10% for adjacent pattern, however some of them were obtained close to 50% of the adopted value.

As mentioned before, the implemented algorithm allows us to include easily some constraint in optimization problem. Thus, in this example, a kind of image tuning could be included to improve the estimated conductivity values. This constraint is given by the following equation:

$$\sum_{k=1}^{N} V_k \rho_k \geq V^* \tag{4}$$

where V_k is the volume of each element and V^* is the material constraint inside of the domain. It is previously known that dark regions in Fig. 5a represents 18% (V^*) of total volume of elliptical domain.

Then, by using this tuning control and the optimized electrode parameters, we obtain the following images and corresponding absolute conductivity values of dark region elements.

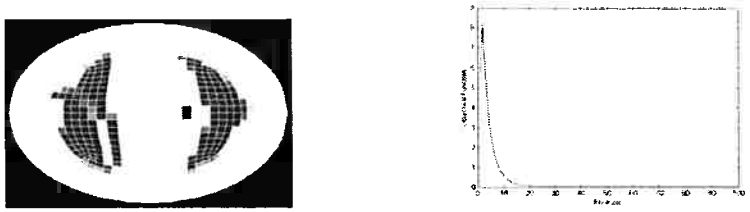

a) obtained image b) convergence curve

Figure 6 – Obtained result with tuning.

From the graph of convergence of the objective function, we observe that it drops quickly to a minimum value, however it continues iteration after iteration with a very small oscillation until the best image is found. Absolute conductivity values of elements of low conductivity (dark regions) are closer to the expected absolute value adopted in this work (10^{-6} $(\Omega m)^{-1}$). In this case, the conductivity values of dark regions have an average of about 82.4% of expected value.

Now, to verify the robustness of the algorithm to work with noise, we have introduced a random variation with standard deviation of about 15% (positive and negative) of the measured electrical potential (ϕ_{ij0}) of each electrode obtained through numerical phantom. Images in Fig. 7 show that the method can absorb this noise level (artificial) in adjacent pattern of electrical excitation.

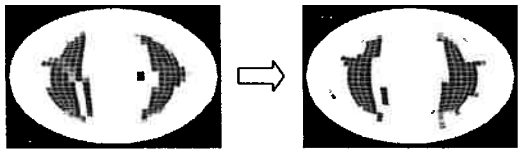

a) without noise b) with noise

Figure 7 – Results considering noise from adjacent pattern.

3.1.2. Using experimental data

Here, the software was evaluated by using data obtained from an experimental phantom. The desired image is shown in Figure 8a. In this case, the experimental phantom is a cylindrical container whose diameter is equal to 230 millimeters and it was filled up to 35 millimeters with a saline solution of concentration 0.3 gram/liter of NaCl, which conductivity value is equal to 1/17 $(\Omega m)^{-1}$. The dashed line in the phantom (see Fig. 8a) represents presence of a immersed glass object, which conductivity value is equal to 10^{-6} $(\Omega m)^{-1}$.

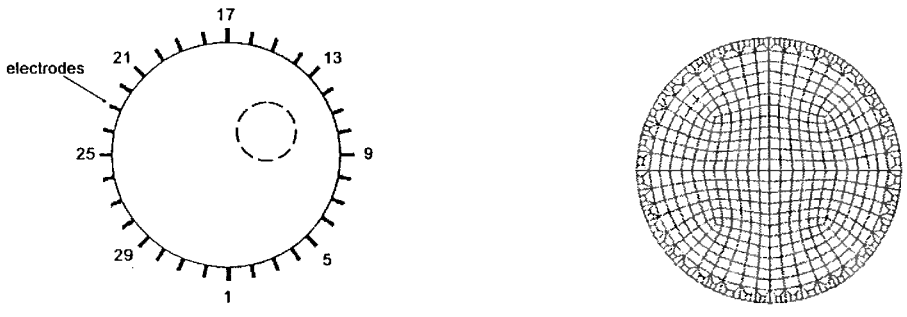

a) b)

Figure 8 – a) Image to be reconstructed; b) Mesh to obtain image (576 elements).

In this example, a "coarse" mesh with 576 four node quadrilateral elements (see Fig. 8b) is applied to image reconstruction. A two-phase method, proposed by Trigo, Lima and Amato (2004), is adopted as strategy to estimate electrode parameters and the conductivity distribution for this case. This strategy considers the problem of estimating electrode contact impedances separated from the problem of image estimation. Thus, in an alternation way of the successive runs of iterative process, first the implemented algorithm estimates the electrode parameters, considering

them as design variables in optimization process, and after that estimates conductivity distribution of the domain with the glass object.

For this example some regularization schemes, based on included constraints, are applied in optimization problem. One of them is a spatial filtering scheme based on smooth distribution of the design variables in whole domain (Swan, Kosaka and Reuss, 1997; Cardoso and Fonseca, 1999), which makes better the control of variation of the design variable values. This filter changes the move limits in the following way (Cardoso and Fonseca, 1999):

$$\rho_i = \frac{\rho_i V_i + \bar{w}\sum_{j=1}^{nv}\rho_j V_j}{V_i + \bar{w}\sum_{j=1}^{nv} V_j} \qquad \text{with} \quad \bar{w} = \frac{\sum_{k=1}^{nv} w_k}{nv} \;;\; w_k = \frac{R_{max} - R_{ij}}{R_{max}} \tag{5}$$

where Vi is the volume of element i, nv is the number of adjacent elements j adopted around of the element i, Rij is the distance between centers of element i and j and $Rmax$ is a radius that accomplishes all adjacent elements j. Here, the image is obtained considering a $Rmax$ value that accomplishes at least a number of eight elements j around of a central element i.

The other regularization scheme is a constraint based on weighted distance interpolation, which is given by following equation:

$$\sum_{k=1}^{N}\frac{1}{d_k^2}\rho_k \geq \sum_{k=1}^{N}\frac{1}{d_k^2}\bar{\rho}_k \tag{6}$$

where $\bar{\rho}$ is average conductivity of the domain and d_k is the distance measured from center of each element up to center of the domain. This constraint makes the balance of conductivity values of each element in the domain. The average conductivity is a parameter of optimization process that can be obtained by considering the domain as a resistor, whose resistance value can be calculated through Ohm's law.

Thus, next figures show the obtained image and its corresponding convergence curve obtained by using the adjacent pattern of electrical excitation.

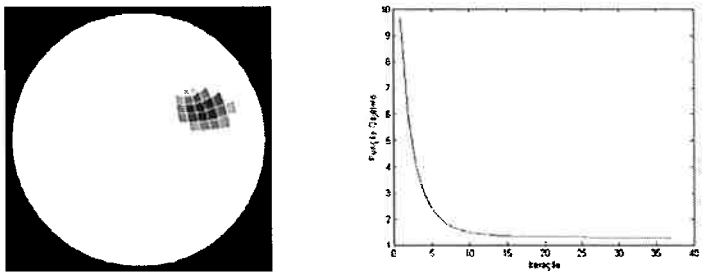

a) obtained image b) convergence curve

Figure 9 – Obtained result with spatial filter and weighted distance interpolation scheme.

According to the obtained image (see Fig. 9a) we note that implemented algorithm is able to detect the glass object inside of phantom. Following the convergence of objective function (see graph of Fig. 9b), we observe that it fells quickly to a minimum value in 20 iterations approximately. However, absolute conductivity values of most elements in dark region (that represents the glass object) have an average of about 70% of expected value.

3.2. 3-D examples

In the 3-D example only numerical data is used to evaluate the implemented algorithm to obtain image. As an alternative to the material model previously presented (and applied in 2-D reconstruction), the algorithm is implemented based on the CAMD (Continuous Approximation of Material Distribution) approach where fictitious densities are interpolated in each finite element, providing a continuum material distribution in the domain (Matsui and Terada, 2004). In CAMD, nodal design variables are introduced, and the material model becomes:

$$\mathbf{c}_k = \left(\sum_{m=1}^{nd} H_m \rho_m\right)^p \mathbf{c}_A + \left[1 - \left(\sum_{m=1}^{nd} H_m \rho_m\right)^p\right]\mathbf{c}_B \qquad \text{with} \qquad 0 \leq \rho_m \leq 1 \tag{7}$$

where ρ_m is the m^{th} nodal design variable, H_m is a FEM shape function (Bathe, 1996) and nd is the number of nodes per element.

The central section of desired image is shown in numerical phantom of Fig. 10b, where clear and dark regions simulate a material with high conductivity (1/17 $(\Omega m)^{-1}$) and low conductivity (10^{-6} $(\Omega m)^{-1}$), respectively. In this case, images are obtained from a cylindrical domain of radius 220 millimeters and 35 millimeters high, and the conductivity distribution is uniform along the axis of the domain.

A numerical phantom whose domain is discretized into 34359 four node tetrahedral elements (see Fig. 10a) is analyzed through FEM and each electrical potential ϕ_{ij0} is obtained. The image reconstruction is then carried out in a less refined mesh with 5548 tetrahedral elements (see Fig. 10c).

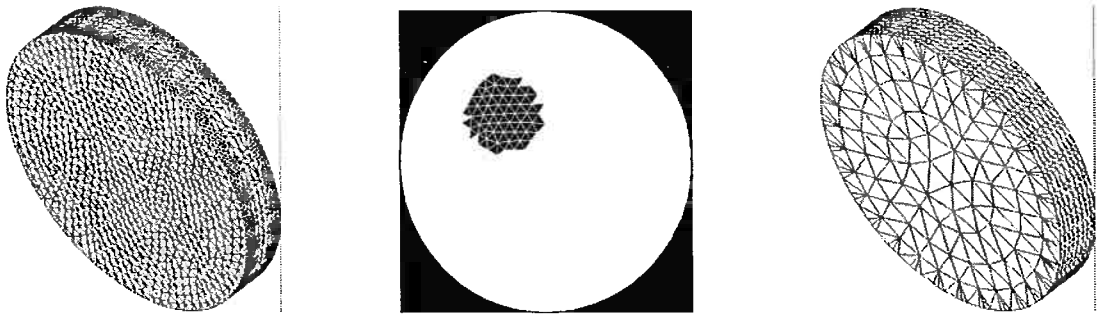

a) numerical phantom b) central section of the phantom c) mesh to obtain image

Figure 10 – a) Numerical phantom (34359 elements) to obtain potentials ϕ_{ij0}; b) The central section of phantom and image to be reconstructed; c) A less refined mesh (5548 elements) applied to obtain the image.

Here, electrode parameters (see section 2) must also be obtained based on numerical data in an analogous way made for 2-D example (see section 3.1.1). Using these optimized electrode parameters, applying the spatial filter and a constraint similar to the constraint based on weighted distance interpolation (shown in section 3.1.2), and considering the same level of artificial noise described in section 3.1.1, the following image is obtained (see Fig. 11a). For simplicity, only the central section is presented (like the phantom, the result is piece-wise uniform along the axis of the domain).

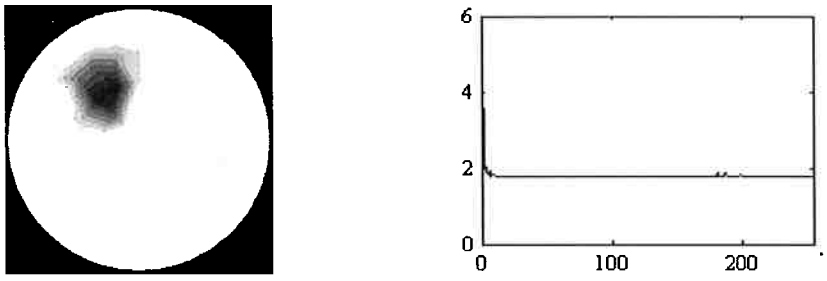

a) obtained image b) convergence curve

Figure 11 – 3-D obtained results with CAMD.

According to the results, the algorithm reduces spatial variation of obtained conductivity distribution. It is mainly attributed to the fact that there is a significant difference between the number of design variables and the amount of information (electrical potentials) available. Following the convergence of objective function (see Fig. 11b), we observe that it fells quickly to a minimum value (1.77). Besides, absolute conductivity values in dark region of the domain have an average of about 45% of expected value.

4. Conclusion

A computational algorithm of Topology Optimization Method (TOM) applied to obtain image in Electrical Impedance Tomography (EIT) was proposed. This algorithm was implemented in software written in C language. According to our results, it is noted that by using numerical and experimental data the software is able to obtain, in few iterations and with a certain level of precision, the contact impedance values of interface electrodes-skin and the values of absolute conductivity of two materials inside of the domain and consequently the image desired, even if noise is introduced. As a future work, other regularization schemes based on included constraints in topology optimization will be tested to improve the precision in obtaining absolute conductivity values.

The implemented algorithm of TOM could be seized for obtaining images of lungs through an EIT device. The TOM allows us to include easily some constraints in the problem of image reconstruction limiting the solution space during tomography examination and avoiding images without clinical meaning. Moreover, it becomes easier to limit the design domain where presence of air in the lung can occur and, therefore, allows us to work with known areas inside of the domain (bone, heart, etc).

5. Acknowledgements

The first and second authors would like to acknowledge the financial support of FAPESP (Fundação de Amparo à Pesquisa do Estado de São Paulo), through a doctoral (nr. 02/01625-0) and a master (nr. 02/10574-0) scholarship. All authors also thank the national research support CAPES (Coordenação de Aperfeiçoamento de Pessoal de Nível Superior).

6. References

Parker, R. L.,1984, "The Inverse Problem of Resistivity Sounding", Geophysics, Vol.142, pp. 2143-2158.

Ramirez, A. *et al.*,1993, "Monitoring an Underground Steam Injection Process Using Electrical Resistance Tomography", Water Resources Res., Vol.29, pp. 73-87.

Santosa, F., Kaup, P. and Vogelius, M.,1996, "A Method for Imaging Corrosion Damage in Thin Plates from Electrostatic Data", Inverse Problems, Vol.12, pp. 279-293.

Santosa, F. and Vogelius, M.,1991, "A Computational Algorithm For Determining Cracks From Electrostatic Boundary Measurements", International Journal Eng. Sci., Vol.29, pp. 917-938.

Cheney, M., Isaacson, D. and Newell, J.C.,1999, "Electrical Impedance Tomography", SIAM review, Vol.41, No. 1, pp. 85-101.

Borcea, A. L.,2002, "Electrical Impedance Tomography", Inverse Problems, Vol.18, pp. 99-136.

Amato, M. B. P. *et al.*,1998, "Effect of a Protective-Ventilation Strategy on Mortality in the Acute Respiratory Distress Syndrome", Journal of Medicine, New England, 338, pp. 347-354.

Holder , D.,1993, "Clinical and Physiological Applications of Electrical Impedance Tomography", UCL, Press, London.

Bendsøe, M. P. and Sigmund, O.,2003, "Topology Optimization: Theory, Methods and Applications", Springer-Verlag, New York.

Haftka, R. T, Gürdal, Z. and Kamat, M. P.,1996, "Element of Structural Optimization", Kluwer Academic Publishers, Boston.

Muray, T. and Kagawa, Y.,1985, "Electrical Impedance Computed Tomography Based on a Finite Elements Model", IEEE Trans. on Biomed. Eng., Vol.32, pp. 177-184.

Bathe, K. J.,1996, "Finite Elements Procedures", Prentice Hall, New Jersey.

Hua, P. *et al.*,1993, "Finite Element Modelling of Electrode-Skin Contact Impedance in Electrical Impedance Tomography", IEEE Trans. on Biomed. Eng., Vol.40, pp. 335-343.

Bendsøe, M. P. and Sigmund, O.,1999, "Material Interpolations Schemes in Topology Optimization", Archive of Applied Mechanics, Vol.69, pp. 635-654.

Cook, R. D. and Young, W. C.,1985, "Advanced Mechanics of Materials", Macmillan, New York.

Byun, J. K. *et al.*,1999, "Inverse Problem Application of Topology Optimization Method with Mutual Energy Concept and Design Sensitivity", Proceed. of IEEE Magnetic, pp. 296-300.

Tang, M. *et al.*,2002, "The Number of Electrodes and Basis Functions in EIT Image Reconstruction", Inst. of Physics Publishing, Physiol. Meas., Vol.23, pp. 129-140.

Trigo, F.C., Lima, R.G. and Amato, M. B. P.,2004, "Electrical Impedance Tomography Using the Extended Kalman Filter", IEEE Transactions on Biomedical Engineering, Vol.51, pp.72-81.

Swan, C., Kosaka, I. and Reuss, V.,1997, "Topology Optimization for Structures with Linear Elastic Material Behaviour", International Journal of Numerical Methos in Engineering, Vol.40, No.1, pp. 3033-3057.

Cardoso, E. L. and Fonseca, J. S. O.,1999, "Intermediate Density Reduction and Complexity Control in the Topology Optimization", Anais do Cobem'99, Águas de Lindóia.

Matsui, K. and Terada, K.,2004, "Continuous Approximation Of Material Distribution for Topology Optimization", International Journal for Numerical Methods In Engineering, Vol.59, No. 14, pp. 1925-1944.

7. Responsibility notice

The authors are the only responsible for the printed material included in this paper.

ANEXO H – TIE 3D via Otimização Topológica

Three-Dimensional Electrical Impedance Tomography: A Topology Optimization Approach

Luís Augusto Motta Mello*, Cícero Ribeiro de Lima, Marcelo Britto Passos Amato, Raul Gonzalez Lima, and Emílio Carlos Nelli Silva

Abstract—**Electrical impedance tomography is a technique to estimate the impedance distribution within a domain, based on measurements on its boundary. In other words, given the mathematical model of the domain, its geometry and boundary conditions, a nonlinear inverse problem of estimating the electric impedance distribution can be solved. Several impedance estimation algorithms have been proposed to solve this problem. In this paper, we present a three-dimensional algorithm, based on the topology optimization method, as an alternative. A sequence of linear programming problems, allowing for constraints, is solved utilizing this method. In each iteration, the finite element method provides the electric potential field within the model of the domain. An electrode model is also proposed (thus, increasing the accuracy of the finite element results). The algorithm is tested using numerically simulated data and also experimental data, and absolute resistivity values are obtained. These results, corresponding to phantoms with two different conductive materials, exhibit relatively well-defined boundaries between them, and show that this is a practical and potentially useful technique to be applied to monitor lung aeration, including the possibility of imaging a pneumothorax.**

Index Terms—**Electrode model, finite element method, medical imaging, three-dimensional electrical impedance tomography, topology optimization.**

I. Introduction

ELECTRICAL impedance tomography (EIT) is a technique to obtain internal images of a domain. Electrodes are attached to the boundary of the domain and low intensity electric alternated currents are applied. Once a reference electrode is chosen, the resulting electric potentials are measured and the unknown electric impedance (conductivity and permittivity) distribution within the domain is obtained by an estimation algorithm (alternatively, electric potentials can be prescribed and electric currents measured [1]). This impedance distribution is represented by an image and constitutes the solution of a nonlinear and ill-posed problem [2]–[4]. Considering invariant the electrode positions, several combinations of current-carrying electrodes and reference electrodes can be chosen and, therefore, many electric potential values may be available for image estimation.

EIT may be used in applications such as medical, geophysical, and industrial, for instance, process tomography [5]. In medical applications, EIT is applied, among several, to detect acute cerebral stroke [6] and breast cancer [7] and to monitor lung aeration imposed by mechanical ventilation [4], [8] (the main interest of our group). The present paper is specially concerned with absolute impedance estimation through iterative algorithms. Some of the works related to this area are reported.

In the double constraint method [9], two finite element method (FEM) solutions for the potentials are obtained in each iteration, given the electric currents and a reference potential on the boundary, and the material distribution within the domain. However, in the second solution, the electric potentials measured are also used as boundary conditions, driving the search for the conductivity distribution. Then, based on a quadratic error index expressing the difference between current densities computed in the two solutions, the conductivities of the elements are updated and an iterative process is established. A large number of iterations were reported.

Hyaric and Pidcock [3] developed a mixed numerical and analytical method: the electric potentials within the domain are obtained analytically and the inverse problem is solved numerically. The current density on the surface of an electrode is assumed to be constant, and equal to the applied electric current divided by its area, and null otherwise, which is the gap model. The inverse problem is solved by the Newton–Raphson scheme [11]—with only one step—and the Levenberg–Marquardt approximation regularizes the problem. A geometric limitation is imposed because only a cylindrical domain is considered. Furthermore, only numerical data was analyzed in the estimation process. Absolute resistivity values were obtained.

Blue, Isaacson, and Newell [12] also addressed a mixed numerical and analytical method, the gap model and the Levenberg–Marquardt method. However, instead of a Newton–Raphson scheme and numerical data, a spectral decomposition solution was obtained and absolute conductivities were estimated based on measurements on an experimental setup.

Vauhkonen *et al.* [13] adopted the "complete electrode model", taking into account the electrode–electrolyte contact impedances. The FEM was employed to model the domain and the Gauss–Newton method (one step) solved the inverse

Manuscript received November 6, 2006; revised March 27, 2007. The first and second authors would like to acknowledge the support of The State of São Paulo Research Foundation (FAPESP) through doctoral scholarships (grant number 2005/00270-1 and 02/01625-0, respectively). The last author acknowledges the support of National Counsel of Technological and Scientific Development (CNPq). All authors are grateful for the research project support from FAPESP, which was granted through a Thematic Project (grant number 01/05303-4). *Asterisk indicates corresponding author.*

*L. A. M. Mello is with the Department of Mechatronics and Mechanical Systems Engineering, School of Engineering, University of São Paulo, São Paulo 01426, Brazil (e-mail: luis.mello@poli.usp.br).

C. R. de Lima and E. C. N. Silva are with the Department of Mechatronics and Mechanical Systems Engineering, School of Engineering, University of São Paulo, São Paulo 01426, Brazil.

M. B. P. Amato is with the Pulmonary Division – Respiratory ICU, Medicine School, University of São Paulo, São Paulo 01426, Brazil.

R. G. Lima is with the Department of Mechanical Engineering, School of Engineering, University of São Paulo, São Paulo 01426, Brazil.

Color versions of one or more of the figures in this paper are available online at http://ieeexplore.ieee.org.

Digital Object Identifier 10.1109/TBME.2007.912637

problem (later, the iterative Gauss–Newton method, the steepest descent method and the conjugate gradient method [14], and the Markov chain Monte Carlo method [15] were implemented). Regularization schemes were applied to improve the condition of the problem and experimental measurements were considered in the image estimation. Their cylindrical agar targets were satisfactorily estimated, both in the case of absolute and relative resistivity values.

Molinari *et al.* [16] implemented the complete electrode model, the FEM and an iterative Newton–Raphson method, as well as important tools such as an auto-adaptive mesh refinement scheme and parallel computing techniques. Only numerical data were used and the resulting absolute conductivities showed poor resolution, which was mainly attributed to the electrodes size.

Finally, Vilhunen *et al.* [17] and Heikkinen *et al.* [18] developed an iterative Gauss–Newton method, based on an FEM framework. The contact impedances were taken into account, obtained together with the remaining properties. In the first work, the relative permittivity and conductivity in a test cell (both assumed constants), and the complex contact impedances corresponding to two electrodes (held equal) were obtained experimentally. Then, simulating a more realistic case, 16 electrodes were placed on the surface of a numerical model of a cylinder and those same parameters and the resistivity distribution within the model were obtained, assuming a homogeneous resistivity distribution and equal contact impedances. In the second work, the authors used real valued properties and experimental results were obtained. Contact impedances and the homogeneous conductivity of tap water within a cylindrical tank were estimated and, based on contact impedance values, the conductivities of the tap water and a plastic object within it were obtained. Accurate results are shown. However, the estimation of the contact impedances together with the conductivity of the tap water and the plastic object was reported only with the knowledge of electric potential measurements of the uniform medium.

An algorithm based on the topology optimization method (TOM) [19] is proposed as a novel approach to the EIT inverse problem. It obtains real valued contact parameters—resistivities of the electrode–electrolyte contact interfaces, multiplied by their thicknesses—and electric conductivities in a three-dimensional model of a domain. Piece-wise constant absolute conductivity distributions are estimated based on numerical and experimental electric potentials, and some different approaches are addressed. In TOM, besides the constraints, which may be considered as regularizations, an objective function is defined. It expresses the difference between electric potentials measured on the electrodes attached to the domain, and the corresponding numerically computed potentials obtained through the solution of a forward problem [8]. The computations are carried out in an FEM framework. The inclusion of constraints is particularly important in EIT since it is an ill-posed problem, which requires prior information. An initial distribution is given to the algorithm, which minimizes the objective function, searching for an optimized absolute distribution within the reduced solution space. Absolute values can be very important in practice since they allow distinguishing some lung pathologies, for instance, a pneumothorax (i.e., the abnormal presence of air inside the pleural cavity, displacing the lung parenchyma) and a proximal blockage of lung ventilation (e.g., bronchial obstruction).

The software implemented allows us to obtain the resistivities of a two-phase piece-wise constant target distribution with high differences between maximum and minimum values (order of 10^6 Ωm) within the domain, which is the main focus of this work. In that sense, the resistivity distribution obtained is almost discrete—that is, with sharp spatial gradient—as demonstrated in the results. Such results are generated by combining the effects of box constraints (constraints for conductivity values) and a material model function that represents the material property at each point of the domain and whose behavior is given by an exponential coefficient (the material model is discussed in Section IV). Therefore, it implies that intermediate values of properties are not likely to happen. However, if required (for instance, when there is no prior concerning the highest resistivity), the intermediate properties can be obtained using a smoothing constraint and a linear material model, which is shown in a numerical example in Section VI. Alternatively, it can be achieved by changing the material model function or by utilizing a segmentation procedure, as it is discussed in Section VII, which contains the conclusions.

The topology optimization method still has the advantage of allowing for parallel computing of FEM solutions and for the easy inclusion of constraints to the conductivity distribution, and the advantage of being relatively robust. Finally, in this work, the method needs only the first derivatives of the objective function and constraints, which are relatively simple to compute. On the other hand, methods based on second order derivatives consume more memory and computing time, and are prone to generate larger numerical errors. Some features of the algorithm are described and its performance is evaluated. The code was implemented in C language.

This paper is organized as follows: in Section II and III, the mathematical model is presented and the corresponding solver is described. In Section IV, TOM is introduced and the formulation applied to the EIT problem is discussed. In Section V, some implementation details are informed. In Section VI, the results are presented and in Section VII some conclusions are offered.

II. Constitutive Equation

In EIT, Maxwell's equations are used to describe the current density flow within the domain. A sinusoidal excitation is imposed and the product $\epsilon\omega$ (where ϵ and ω are the permittivity of the domain and the angular velocity, respectively) can be neglected if ω is low enough. Thus, the medium is considered to be only conductive [10] and Maxwell's equations can be simplified. Then, considering the Ohms's law, the equation which describes the electrical phenomena within the domain Ω is

$$\nabla\cdot(\sigma(\boldsymbol{x})\nabla V(\boldsymbol{x})) = 0, \ \boldsymbol{x} \text{ in } \Omega, \tag{1}$$

an elliptic partial differential equation, where σ and V are the electric conductivity and electric potential, respectively, and $\mathbf{x}$ is the position vector.

The algorithm implemented depends on the solution of (1) for the electric potentials, or the solution of the forward problem.

This solution can be uniquely determined with the knowledge of Newmann's and Dirichlet's boundary conditions on $\partial\Omega$; however, it cannot be obtained analytically for arbitrary geometry, conductivity distributions or boundary data. Thus, a numerical method is employed.

III. Finite Element Modeling

The finite element numerical method is employed, through a variational approach or, alternatively, with the aid of the principle of virtual potentials [11]. It yields the following equation, based on (1) and considering the boundary conditions:

$$\int_{\Omega} \nabla U \cdot (\sigma \nabla V) d\Omega = \int_{\partial\Omega_I} U_S J_n dS \tag{2}$$

where U is the test potential and U_S is the test potential on $\partial\Omega_I$, which is the portion of $\partial\Omega$ where the normal component of the current density J_n (or Newmann's boundary condition) is applied.

Then, the domain is conveniently divided into finite elements and the electric potentials (U and V) are approximated in each of them. A continuous function is used in this task. It depends on the nodal values of the element, new unknowns, as follows:

$$V_m = \boldsymbol{N}_m \boldsymbol{V} \tag{3}$$

where subscript m indicates a finite element (FE), V_m is the continuous function, $\boldsymbol{V}$ is the vector of nodal electric potentials of the entire mesh and $\boldsymbol{N}_m$ is the FE interpolation matrix [11], which is a function of local coordinates.

Equation (2) is computed at each element, the results are added and the problem of finding V is turned into an algebraic problem [11]

$$\boldsymbol{K}\boldsymbol{V} = \boldsymbol{I} \tag{4}$$

where $\boldsymbol{I}$ is the vector of nodal electric currents and $\boldsymbol{K}$ is the conductivity matrix of the system. In this work, the model is represented by four node tetrahedral elements and $\boldsymbol{N}_m$ expresses a linear dependence of V_m on the nodes of the mth finite element and on local coordinates.

A. Electrode Model

The electrode model developed is a three-dimensional version of the model seen in [4]. The latter is a two-dimensional FEM model of the electrode–electrolyte contact interface, and includes the electrode and the periphery of the epidermis (the epidermis is the outermost layer of the skin).

The same assumptions seen in [4] are adopted here, except for neglecting the tangential resistors considered in their work. In other words, the authors keep the effects of the small tangential current flow within the model, and keep the following assumptions, namely, the thickness of the model is small compared to the other dimensions, the electric potential on the metallic surface of the electrode is constant, the whole surface of the electrode is in contact with the skin, and the conductivity of the model is constant.

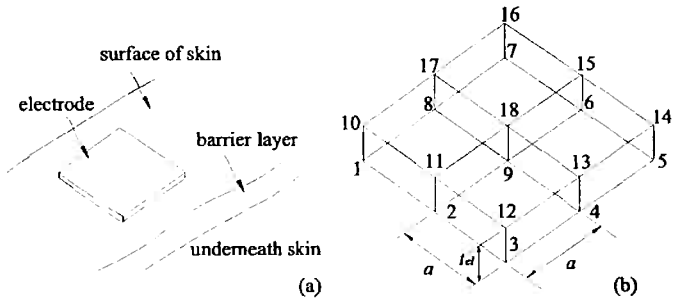

Fig. 1. Elements of an electrode model. Nodes 1–9 are attached to the mesh of domain and nodes 10–18 concern the electrode.

As can be seen in Fig. 1, eight node brick elements are used to match the work of Hua *et al.* [4] (they used four nodes quadrilateral elements). Considering only one electrode and four brick elements (see Fig. 1(b)) and applying the assumptions, the following can be computed:

$$\boldsymbol{K}_{el} = \frac{a^2 \sigma_{el}}{t_{el}} \begin{bmatrix} \frac{1}{9} & \frac{1}{18} & 0 & 0 & 0 & 0 & 0 & \frac{1}{18} & \frac{1}{36} & -\frac{1}{4} \\ & \frac{2}{9} & \frac{1}{18} & \frac{1}{36} & 0 & 0 & 0 & \frac{1}{36} & \frac{1}{9} & -\frac{1}{2} \\ & s & \frac{1}{9} & \frac{1}{18} & 0 & 0 & 0 & 0 & \frac{1}{36} & -\frac{1}{4} \\ & & y & \frac{2}{9} & \frac{1}{18} & \frac{1}{36} & 0 & 0 & \frac{1}{9} & -\frac{1}{2} \\ & & & m & \frac{1}{9} & \frac{1}{18} & 0 & 0 & \frac{1}{36} & -\frac{1}{4} \\ & & & & m & \frac{2}{9} & \frac{1}{18} & \frac{1}{36} & \frac{1}{9} & -\frac{1}{2} \\ & & & & & e & \frac{1}{9} & \frac{1}{18} & \frac{1}{36} & -\frac{1}{4} \\ & & & & & & t & \frac{2}{9} & \frac{1}{9} & -\frac{1}{2} \\ & & & & & & & r & \frac{4}{9} & -1 \\ & & & & & & & & y & 4 \end{bmatrix} \tag{5}$$

$$\boldsymbol{I}_{el}^T = \{0 \quad 0 \quad 0 \quad 0 \quad 0 \quad 0 \quad 0 \quad 0 \quad 0 \quad I_{el}\} \tag{6}$$

where $\boldsymbol{K}_{el}$ is the elth matrix of the electrode model, σ_{el} is the corresponding conductivity, and $\boldsymbol{I}_{el}$ is the elth vector of nodal electric currents of the electrode model. The last term in the array corresponds to the electrode node [4] and I_{el} is the electric current value applied to it. If no current is applied to an electrode, J_n is null and $\boldsymbol{I}_{el} = \boldsymbol{0}$. The derivation of (5) and (6) is described in detail in the Appendix. In (5), t_{el}/σ_{el} is the contact parameter. In practice, this is a value to be estimated.

Finally, assembling the matrices and vectors of the electrode models on (4), we obtain an augmented linear system of equations for the entire problem

$$\boldsymbol{K}_T \boldsymbol{V}_T = \boldsymbol{I}_T. \tag{7}$$

In this work, this system is solved using a preconditioned conjugate gradient algorithm (see [20] for a similar algorithm).

In the experimental study the potentials are measured from a cylindrical container filled with a saline solution, as will be described in detail in Section VI, and a different kind of electrode, a bar electrode, which covers the height of the conductive domain (see Fig. 2), is considered. In this experimental study, the effect of the electrode models is neglected, as discussed in Section VI. Therefore, (5) and (6) are not utilized. Instead, some boundary nodes of the standard mesh—or the mesh without the electrode models—are selected to represent the electrodes and

Fig. 2. Bar electrode attached to the conductive domain.

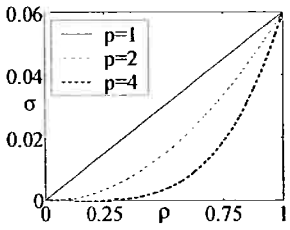

Fig. 3. Curves $\sigma \times \rho$. σ_A and σ_B are equal to 0.06 and 0.000001, respectively.

equality of electric potentials on all nodes representing an electrode is imposed. In other words, the gap model is employed. Finally, a system of equations as (7) is also constructed.

IV. Topology Optimization Method

Essentially, TOM determines a material distribution inside a fixed domain with the purpose of maximizing a performance index of the corresponding system [19], e.g., it solves an optimization problem subjected to some constraints representing limitations to that distribution. The performance index is mathematically represented by an objective function, and the constraints by equality and/or inequality equations, which depend on the material distribution.

This work considers that the properties at each point vary continuously, from the properties of a pure material A to a pure material B. This material model is based on SIMP (Simple Isotropic Material with Penalization) [19], which is an usual material model applied in topology optimization. Its mathematical representation is

$$\sigma(\boldsymbol{x}) = \rho(\boldsymbol{x})^p \sigma_A + (1 - \rho(\boldsymbol{x})^p)\sigma_B, \quad \boldsymbol{x} \text{ in } \Omega \tag{8}$$

where σ_A and σ_B are the limiting electric conductivities of the materials that compose the domain, and ρ is the normalized design variable, ranging from 0 to 1. Additionally, penalization is introduced in the model when p, a positive integer, is larger than 1. Therefore, lower values of σ are favored in the final result. The effect of p can be seen in Fig. 3.

An alternative to the TOM and (8) with p larger than 1, is a binary design (0–1), for which there are several solution methods [19]. However, it is an ill-posed problem with several local minima, which brings numerical instabilities in the solution process, and the algorithms employed to solve it are relatively slow. Thus, the relaxation of the problem by defining a material model, yielding a continuous material design problem, is justified.

In this work, it is assumed that the design variable ρ varies continuously within each finite element and depends on nodal values in the same way as the electric potentials [21]. Thus, the conductivity in the mth element is

$$\sigma_m = \rho_m^p \sigma_A + (1 - \rho_m^p)\sigma_B, \text{ in } \Omega_m \tag{9}$$

and ρ_m is given by

$$\rho_m = \boldsymbol{N}_m \boldsymbol{\rho}. \tag{10}$$

In (9), $\boldsymbol{\rho}$ is the vector of nodal design variables within the domain. The FE interpolation matrix $\boldsymbol{N}_m$ [11] must be selected to provide values of ρ_m between 0 and 1. In this work, this matrix is meant to represent a linear dependence of ρ_m on the nodes of the mth element and on local coordinates.

For σ_{el}/t_{el}, a similar normalization

$$\frac{\sigma_{el}}{t_{el}} = \rho_{el}^{pl}\frac{\sigma_{Ael}}{t_{Ael}} + (1 - \rho_{el}^{pl})\frac{\sigma_{Bel}}{t_{Bel}}, \text{ in } \Omega_{el} \tag{11}$$

is applied, where σ_{Ael}/t_{Ael} and σ_{Bel}/t_{Bel} are convenient limits for σ_{el}/t_{el}, and ρ_{el} is a normalized design variable. The limit σ_{Ael}/t_{Ael} is chosen so that above it the changes of electric potentials on electrodes due to changes of contact parameter values are relatively small. The inferior limit σ_{Bel}/t_{Bel} is zero.

The objective function adopted in this work is the usual square error function for electric potential values [3], [13], [14], [16]

$$F = \frac{1}{2}\sum_{j=1}^{ne}(\boldsymbol{A}_{Pj}\boldsymbol{V}_{Tj} - \boldsymbol{V}_{0j})^T(\boldsymbol{A}_{Pj}\boldsymbol{V}_{Tj} - \boldsymbol{V}_{0j}) \tag{12}$$

where ne is the number of current load cases (they will be defined in the results section) applied to the system, $\boldsymbol{V}_{Tj} = \boldsymbol{V}_{Tj}(\boldsymbol{\rho}, \boldsymbol{\rho}_{el})$ is the vector of nodal electric potentials computed through FE analysis using the conjugate gradient solver, $\boldsymbol{V}_{0j}$ is the corresponding vector of nodal electric potentials obtained in the jth load case, whose components are zero unless they represent a measurement electrode node, and $\boldsymbol{\rho}_{el}$ is the vector of interface design variables related to σ_{el}/t_{el} (see (11)). $\boldsymbol{A}_{Pj}$ is a diagonal and square matrix whose diagonal values are equal to one, indicating potentials on measurement electrodes, or zero, in the position of current-carrying and reference electrodes, and of the remaining nodes (therefore, $\boldsymbol{A}_{Pj}^T$ is equal to $\boldsymbol{A}_{Pj}$ and $\boldsymbol{A}_{Pj}^2$ is equal to $\boldsymbol{A}_{Pj}$; these results are applied to the computation of sensitivities in the next section). This means that only the nodal values of measurement electrodes in $\boldsymbol{V}_{Tj}$ are taken into account in the objective function. It is relevant that, considering only the nonzero components, equal positions in the vectors $\boldsymbol{A}_{Pj}\boldsymbol{V}_{Tj}$ and $\boldsymbol{V}_{0j}$ indicate corresponding locations in the model and the domain (it implies that $\boldsymbol{A}_{Pj}\boldsymbol{V}_{0j}$ is equal to $\boldsymbol{V}_{0j}$; this result is also used in the computation of sensitivities in the next section).

Finally, the problem solved for the conductivity distribution is

$$\begin{aligned} &\text{minimize} \quad F = F(\boldsymbol{\theta}) \\ &\text{w.r.t.} \quad \boldsymbol{\theta} \\ &\text{subject to} \quad \boldsymbol{K}_{Tj}\boldsymbol{V}_{Tj} = \boldsymbol{I}_{Tj} \\ &\qquad\qquad 0 \le \boldsymbol{\theta} \le 1 \end{aligned} \tag{13}$$

where $\boldsymbol{V}_{Tj} = \boldsymbol{V}_{Tj}(\boldsymbol{\theta})$ and $\boldsymbol{\theta}$ is the vector of design variables. It can be either $\boldsymbol{\rho}$ or $\boldsymbol{\rho}_{el}$, since the problem is solved separately

for these two vectors. When $\boldsymbol{\rho}$ is constrained between 0 and 1, ρ_m^p is constrained between 0 and 1; then, σ_m is constrained between σ_B and σ_A. In fact, ρ_m is the equation of a hyperplane containing the nodal values of $\boldsymbol{\rho}$ pertaining to the mth element, which means that the maximum and minimum values of ρ_m are on nodes. Therefore, since all nodal values are constrained between 0 and 1, ρ_m is constrained too. Thus, ρ_m^p is also constrained between 0 and 1.

If the conductivity values are constrained between σ_A and σ_B, given as prior information, the spatial gradients and differences between maximum and minimum values obtained by TOM can be high if compared to the results found in the EIT literature. However, the algorithm tends to reduce the highest resistivity values found and thus, the results are underestimated. Therefore, in the optimization problem, the constraints are made to work with the penalization scheme. When the exponential coefficient p in (9) is larger than 1, lower values of ρ_m^p (close to 0) within the element m are favored (since ρ_m is constrained between 0 and 1). It implies that the resistivity peaks are increased.

On the other hand, when σ_B is unknown and, thus, there is no prior concerning the resistivity contrast, a smoothing constraint and a linear material model ($p = 1$) may be used. This scenario is also addressed through a numerical example in Section VI.

The proposed nonlinear problem (13) is solved by a sequential linear programming (SLP) algorithm [20], which solves a sequence of linear problems through linear programming (LP) [20], [22]. In each LP problem (iteration), (13) is linearized and the design variables are constrained between additional adjustable box constraints, or moving limits. These limits validate the linearization and are also responsible for the convergence. The computation of sensitivities, used in the linearization, is described below.

A. Computation of Sensitivities

The derivatives of F with respect to the design variables are

$$\begin{aligned}\frac{\partial F}{\partial \theta_k} &= \sum_{j=1}^{ne}\left(\boldsymbol{A}_{Pj}\frac{\partial \boldsymbol{V}_{Tj}}{\partial \theta_k}\right)^T(\boldsymbol{A}_{Pj}\boldsymbol{V}_{Tj}-\boldsymbol{V}_{0j})\\ &= \sum_{j=1}^{ne}\frac{\partial \boldsymbol{V}_{Tj}}{\partial \theta_k}^T\boldsymbol{A}_{Pj}^T(\boldsymbol{A}_{Pj}\boldsymbol{V}_{Tj}-\boldsymbol{V}_{0j})\\ &= \sum_{j=1}^{ne}\frac{\partial \boldsymbol{V}_{Tj}}{\partial \theta_k}^T(\boldsymbol{A}_{Pj}\boldsymbol{V}_{Tj}-\boldsymbol{V}_{0j}).\end{aligned}\tag{14}$$

By differentiating (7), the following can be obtained

$$\frac{\partial \boldsymbol{V}_{Tj}}{\partial \theta_k}^T = -\boldsymbol{V}_{Tj}^T\frac{\partial \boldsymbol{K}_{Tj}}{\partial \theta_k}\boldsymbol{K}_{Tj}^{-1}.\tag{15}$$

Substituting this equation into the previous equation, the following is computed:

$$\frac{\partial F}{\partial \theta_k} = -\sum_{j=1}^{ne}\boldsymbol{V}_{Tj}^T\frac{\partial \boldsymbol{K}_{Tj}}{\partial \theta_k}\boldsymbol{K}_{Tj}^{-1}(\boldsymbol{A}_{Pj}\boldsymbol{V}_{Tj}-\boldsymbol{V}_{0j}).\tag{16}$$

The procedure described above is called adjoint method [22]. The vector $\boldsymbol{K}_{Tj}^{-1}(\boldsymbol{A}_{Pj}\boldsymbol{V}_{Tj}-\boldsymbol{V}_{0j})$ is computed by a preconditioned conjugate gradient algorithm and the derivatives of $\boldsymbol{K}_{Tj}$ with respect to θ_k are obtained analytically [23].

V. Implementation

Convergence problems can arise in the iterative optimization process due to large differences between the magnitude of objective function derivatives in relation to interface design variables ($\boldsymbol{\rho}_{el}$) and to nodal design variables ($\boldsymbol{\rho}$), if a distinguishing scheme for the moving limits is not employed. Since adjusting these limits distinctly is not an easy task and the best way to achieve a reasonable updating rule is yet an open question, the optimization procedure is alternatively divided into two nested iterative processes embodied by a global iterative process. In the first stage, the nodal resistivity values obtained from the previous step are kept constant, and only the values of σ_{el}/t_{el} [see (11)] are optimized. Then, at a second stage, a new set of nodal resistivity values is obtained, keeping the contact parameters fixed. These two optimizations form one global step. The algorithm starts from an initial distribution of resistivities and contact parameters, and continues until the convergence is reached. This is called the two-phase approach [8] and it is used in the numerical investigations in the present work.

VI. Results and Discussion

In this section, some images generated using the implemented software will be presented, examining both a numerical [17] and an experimental phantom. In all examples, a low intensity sinusoidal current is applied and all computations are carried out on a PC. The current signal amplitude is 1 mA pk-pk.

The mesh used to represent the numerical phantom for estimation purpose—the estimation mesh—is coarser than the mesh of the phantom, to avoid the inverse crime. Thirty-two square electrodes (10 mm wide) are uniformly placed along the boundary of the estimation mesh and of the numerical phantom. Also, 32 bar electrodes are uniformly attached to the experimental phantom and to its model. Since only 32 electrodes are used to perform measurements, one can not assure uniqueness of the solution [24].

To perform measurements, a pair of adjacent electrodes is electrically excited. The electric potential in one of them is taken as ground. This procedure, which defines a current load case, is repeated, changing the pair of adjacent electrodes. Thirty-two current load cases are applied. Different load patterns could be applied [10].

A. Numerical Phantom

In this section, the electrical potentials $\boldsymbol{V}_{0j}$ are obtained through a FE analysis of the numerical phantom shown in Fig. 4(a). Thus, only numerical data is considered.

The phantom is a 220 mm diameter and 35 mm thick cylindrical domain, divided into 34 359 four node tetrahedral elements (see Fig. 4(b)). The resistivity distribution is approximately uniform along its axis. Fig. 4(a) shows the central section of the mesh. The contact parameters are all equal to 0.01 Ωm^2 and the electrodes are placed on the central layer of the cylindrical boundary of the three-dimensional mesh.

In the first investigations referring to high contrast results, most of the phantom (basal region) has 17 Ωm of resistivity (whose inverse is equal to σ_A in (9)), and the object has 10^6 Ωm of resistivity (whose inverse is equal to σ_B in (9)). In a clinical

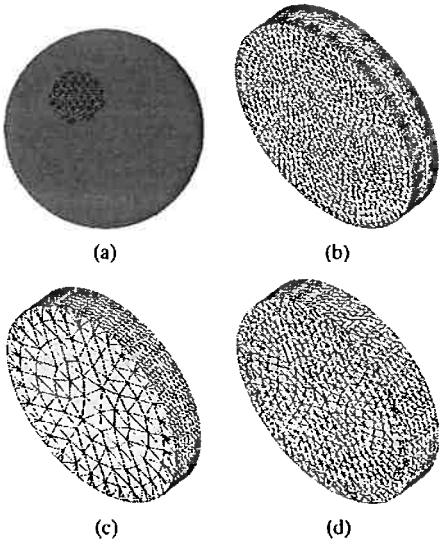

Fig. 4. (a) Central section of numerical phantom (image to be estimated). (b) Numerical phantom model mesh (34 359 elements). (c) Estimation model mesh for the high contrast results (5548 elements). (d) Estimation model mesh for the low contrast results (13 130 elements).

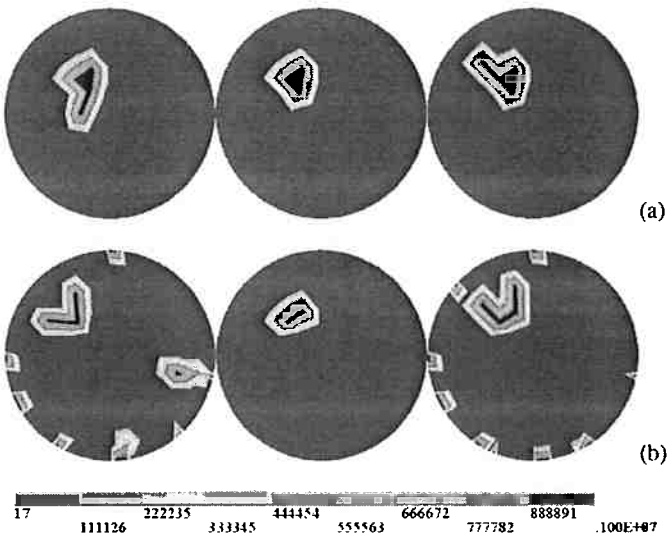

Fig. 5. Resistivity values obtained (units: Ωm; numerical phantom of Fig. 4(a)). (a) Without noise. (b) Considering noise.

perspective, this condition may represent a pneumothorax. Although air has a much larger resistivity, 10^6 Ωm is large enough to inform clinicians the occurrence of a pneumothorax. Of note, a similar order of magnitude, 2×10^5 Ωm, was simulated in a previous work and adopted to represent air inside the thorax in the forward problem [25].

As already shown, the maximum resistivity of the lung parenchyma rarely exceeds 20 Ωm, a value achieved only when breathing close to the total lung capacity. Then, to simulate a situation in which overdistension, massive atelectasis, or pneumonia are the clinical concerns, which are diagnostic hypotheses when the resistivity contrast between the normal versus abnormal parenchymal regions is much lower (2 to 5 times, at a maximum) and the level of contrast is unknown, the resistivities of the numerical phantom are changed to 4 Ωm for the basal region (whose inverse is equal to σ_A in (9)) and 8 Ωm for the inclusion, and the superior constraint to the resistivity is disabled.

The image estimation is carried out using a 5548 elements model (see Fig. 4(c)) for the first scenario and a 13 130 (see Fig. 4(d)) elements model for the last scenario. The number of elements was increased since it is difficult to achieve a satisfactory spatial resolution with the first mesh when the prior comprising inferior conductivity limit is not considered. The following computations are performed using the two-phase approach [8].

1) High Contrast Results: The results obtained are shown in Fig. 5, while the result in Fig. 5(b) includes numerical noise.[1] The middle image corresponds to the central section of the domain and the others to the external sections. In the beginning of the optimization process, the values of pl (see (11)) and p (see (9)) are equal to 1; however, the value of p is changed to 2 after the convergence of the global iterative process is reached. The algorithm starts from a uniform resistivity distribution equal to 17 Ωm, the minimum value allowed (the maximum is 10^6 Ωm). The initial contact parameters are 0.0011 Ωm^2.

According to the results, the right position of the object and correct absolute resistivity values have been obtained, although the geometry is different. In addition, some peripheral artifacts are generated when numerical noise is added to V_{0j}. The final values of contact parameters corresponding to Fig. 5(a) (without noise) range from 0.0192 to 0.0233 Ωm^2. The range increases when noise is introduced (Fig. 5(b)), from 0.0184 to 0.0234 Ωm^2. The authors believe that the discrepancies between the results and the phantom are mainly due to the differences between the phantom and estimation meshes. Moreover, noise aggravates such condition.

In the two-phase approach, the optimal nodal resistivities and the final contact parameters are highly dependent on initial guesses. For instance, when the algorithm starts from 34 Ωm for nodal resistivities, and from 0.0011 Ωm^2 for the contact parameters, the minimum and maximum final values are, approximately, 0.0005 and 0.0017 Ωm^2, respectively. Unlike the other results, the minimum is very close to the imposed limit (σ_{Ael}/t_{Ael} in (11)). This result is shown in Fig. 6, without noise. It suggests that, even if the potentials at current-carrying and reference electrodes are not considered, the algorithm can produce peripheral artifacts and a wrong object diameter if the contact parameters are incorrect.

One way to increase the optimal contact parameters and improve the image quality is to choose an annular domain in the neighborhood of the electrodes and to keep the resistivity fixed at 17 Ωm, the value used in phantom. Another way is to prevent the convergence of the two nested iterative processes, allowing for just one step for each of them. Following these protocols, contact parameters ranging from 0.0074 to 0.0119 Ωm^2 and between 0.0007 and 0.0095 Ωm^2 are obtained, respectively. The corresponding images (Fig. 7(a) and (b)) are more accurate than

[1] A zero-mean uniformly distributed noise (random noise) is considered, meaning that to each potential value of the vector V_{0j}, up to 15% of the value of the respective electric potential is randomly added or subtracted.

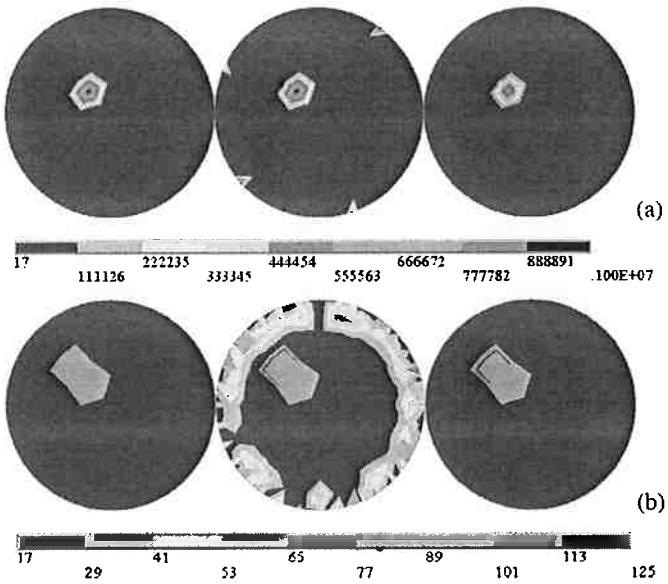

Fig. 6. Resistivity distribution obtained (units: Ωm). Maximum and minimum final values of the contact parameters are 0.0017 and 0.0005 Ωm^2. Range of resistivity values shown: (a) from 17 Ωm to 10^6 Ωm; (b) from 17 Ωm to 125 Ωm (gray color corresponds to resistivities above 125 Ωm).

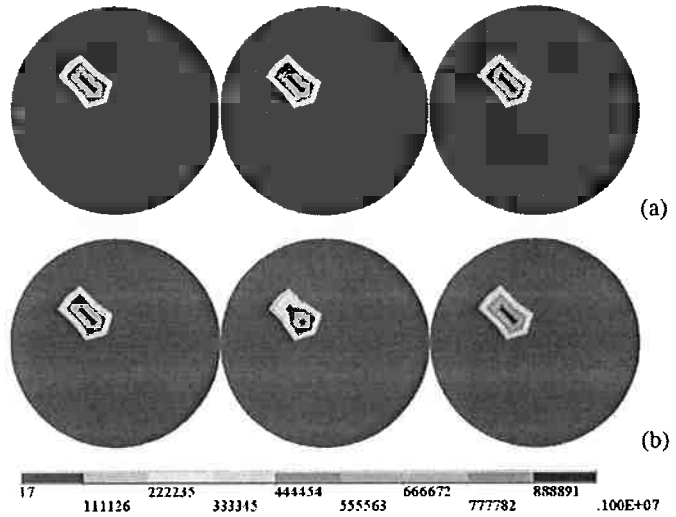

Fig. 7. Resistivity distributions obtained (units: Ωm). (a) The resistivities of the nodes on the lateral surface of the estimation mesh are set to 17 Ωm. (b) It is allowed one step for each of the two nested iterative processes.

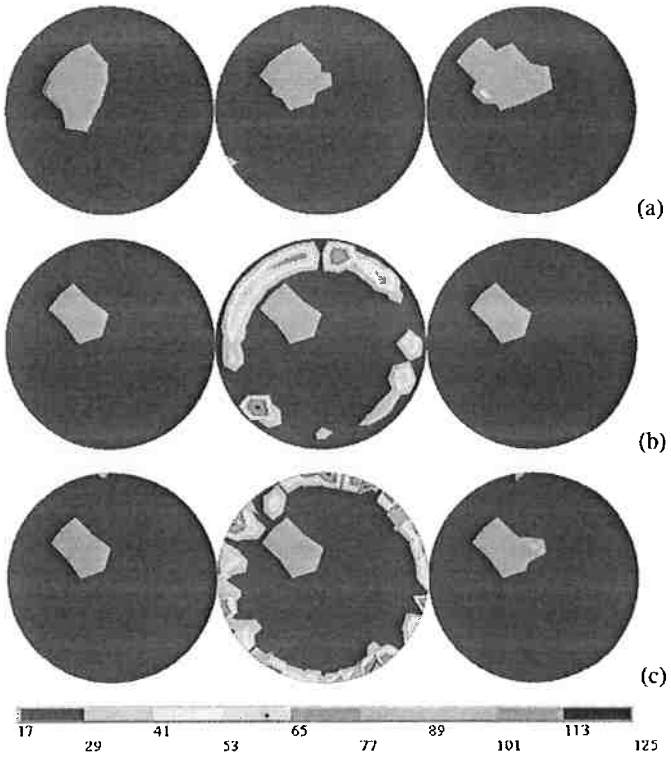

Fig. 8. Resistivity distributions obtained (units: Ωm). (a) The initial guess is 17 Ωm (Fig. 5(a)). (b) The resistivity of an annular domain in the neighborhood of the electrodes is set to 17 Ωm (Fig. 7(a)). (c) It is allowed one step for each of the two nested iterative processes (Fig. 7(b)). Gray color corresponds to resistivities above 125 Ωm.

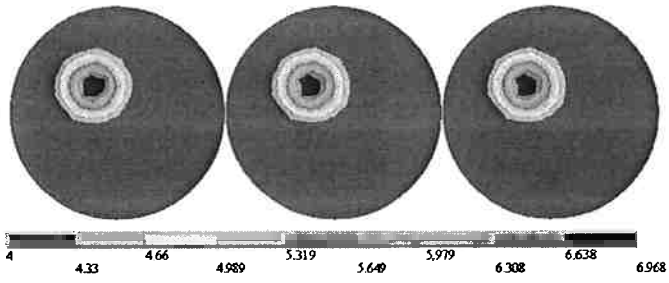

Fig. 9. Low contrast results obtained (units: Ωm; numerical phantom of Fig. 4(a)).

the results of Fig. 6. Differences also become apparent when the plotted range of resistivity values is reduced; see Fig. 8.

Keeping in mind that relatively small errors in the images (comparing with the range of estimated values) occur even when the obtained contact parameters are close to 0.001 Ωm^2 or lower, a new approach can be proposed to be applied in experimental tests. This is discussed in the corresponding section.

2) Low Contrast Results: The results obtained are shown in Fig. 9. The values of pl (see (11)) and p (see (9)) are equal to 1 during the iterative process. The algorithm starts from a uniform resistivity distribution equal to 4 Ωm, the prior used as the minimal value allowed. The maximal value allowed is high enough to prevent that the constraint is active during the optimization, which is equivalent to consider an unknown prior for the highest resistivity value. The initial contact parameters are 0.0011 Ωm^2.

An explicit spatial gradient control scheme [26] is used. In this approach, a linear transformation is applied to the nodal design variables in such a way that each variable, corresponding to one node, is equal to a weighted summation of new nodal variables divided by the sum of the weights. The weights are piecewise constant functions, equal to one within a prescribed radius or zero, otherwise. Therefore, a smooth solution is enforced.

The right position of the object and a reasonable geometry are achieved. Absolute resistivity values within 15% of error have been obtained, which is informative from a clinical point of view. Additionally, there are no artifacts for the range of values plotted and the final values of contact parameters range from 0.0120 to 0.0131 Ωm^2, closer to the values used in the phantom.

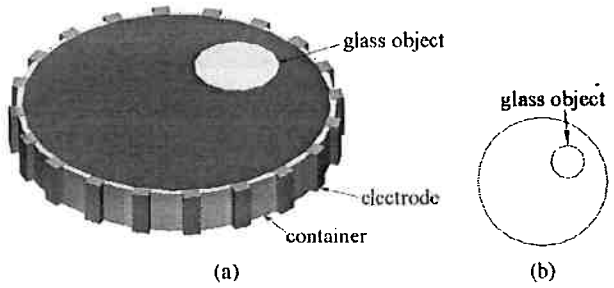

Fig. 10. (a) Sketch of the experimental phantom. (b) Image to be estimated.

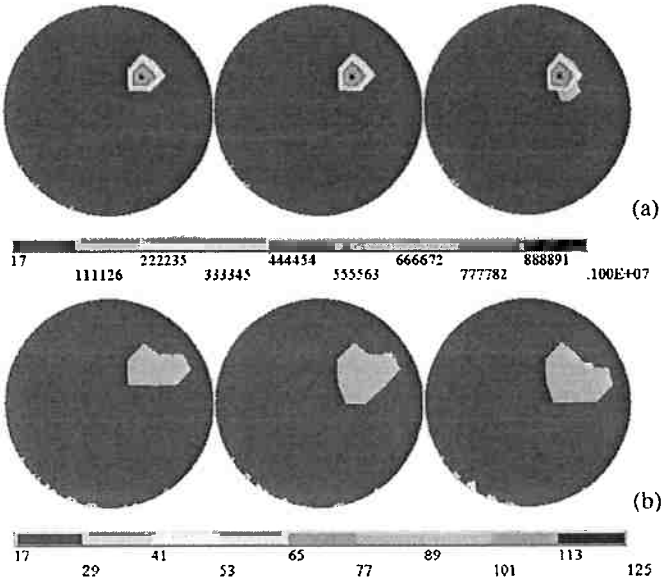

Fig. 11. Resistivity distribution obtained (units: Ωm) (related to experimental phantom of Fig. 10(b)). The effect of the electrode models is neglected. Range of resistivity values shown: (a) from 17 Ωm to 10^6 Ωm; (b) from 17 Ωm to 125 Ωm (gray color corresponds to resistivities above 125 Ωm).

B. Experimental Phantom

In this section an experimental phantom, which provides measured electric potential values, is used. This phantom is a cylindrical container with 32 35-mm by 10-mm bar electrodes (see the sketch in Fig. 10(a)). The container is filled up to 35 mm with a 0.3 g/L saline solution (NaCl). Its resistivity is approximately 17 Ωm and its diameter is 220 mm, which is equal to the inner diameter of the container. The small circle shown in Fig. 10(b) represents a glass object (10^6 Ωm [27]). This large resistivity contrast example is meant to represent a pneumothorax during lung imaging. The conductivities of the saline solution and glass are used as extreme values (σ_A and σ_B, respectively) in (9). The values of pl and p are equal to 1 at the beginning of the optimization process and the value of p is changed to 2 when the convergence of the global iterative process is reached. A new estimation model with 11 623 tetrahedral elements is generated.

According to the numerical results in the previous section, relatively good images were attained even when low contact parameters were estimated. Therefore, assuming relatively small contact parameters, the electrode gap model was used in the experimental evaluation and the two-phase approach was not employed. The results are shown in Fig. 11.

The algorithm implemented is able to detect the glass object inside the experimental phantom. The correct position of the object and correct absolute resistivity values have been found, and few peripheral artifacts remained, which suggests that the gap model is a plausible choice. However, the high resistivity region is smaller than the real one.

VII. Conclusion

In this work, some features of an alternative method to solve the ill-posed nonlinear three-dimensional EIT problem are proposed and studied. According to the numerical results, the corresponding algorithm is able to obtain a resistivity distribution within a domain composed of two materials, even with the addition of numerical noise or when the level of contrast is unknown. Considering also the experimental results, the images suggest that the algorithm is potentially capable of monitoring lung aeration imposed by mechanical ventilation including the possibility of detecting a pneumothorax.

A two-phase approach [8] was implemented for obtaining the images. It is shown that the results are dependent on initial values of design variables. However, when some features of the phantom are known, such as the resistivity values of peripheral areas, the images are consequently better. The experimental results show that the effect of low contact parameters in these cases is smaller. It is believed that this is due to relatively small values of contact resistivities in the experimental setup.

The problems that persist when the estimation is accomplished can likely be overcome by imposing some additional constraints to the nodal resistivity distribution in the optimization problem. Although the best way to define such constraints is still an open question, they should take into account the distance from the center of the domain, since in an EIT system, the sensitivity to resistivity changes in peripheral regions is higher than in central regions [28], [29]. The definition of additional constraints will be the subject of future investigation.

Adaptive mesh refinement and continuously-graded materials [30] could improve the applicability of the algorithm to monitor lung aeration. Furthermore, the sensitivity calculation using the adjoint method formulation allows for parallelization, which can save computation time. These themes will also be matter of future investigation.

Finally, a new strategy, which is explained as follows, can be proposed as an alternative to the use of continuously-graded materials [30]. The implemented algorithm can estimate a large range of resistivities. The idea is to segment the region of highest resistivity and extract it from a subsequent estimation procedure. This reduction on the number of variables is accomplished together with a reduction on the largest resistivity allowed. Then, the subsequent estimation procedure is carried out and a new region, corresponding to this new resistivity limit, can be segmented and extracted from the next parameter estimation procedure. Repeating this steps will result on a better graded image in terms of resistivity and, consequently, on a distribution with better resistivity resolution.

Appendix
Derivation of $\boldsymbol{K}_{el}$ and $\boldsymbol{I}_{el}$

Starting from (2), one can obtain (5) and (6).

Equation (2) can be computed in each finite element and the results added, which is a common practice in FE theory. Following this procedure, (3) is substituted in each term of the summation referent to each finite element in (2), which yields

$$\boldsymbol{U}_T^T \sum_m \int_{\Omega_m} \nabla \boldsymbol{N}_m^T \nabla \boldsymbol{N}_m \sigma_m d\Omega_m \boldsymbol{V}_T = \boldsymbol{U}_T^T \sum_m \int_{\partial\Omega_{1m}} \boldsymbol{N}_{mS}^T J_{nm} dS_m \quad \text{(A.1)}$$

where $\boldsymbol{U}_T$ is the vector of nodal test potentials and the subscript m indicates a finite element. The augmented linear system of (7) is obtained through this last equation. The next step concerning the FE theory is to integrate each term of the summation and add the results.

However, only the nonzero terms of each integral are computed in practice, yielding the element matrices and vectors, which are then assembled using the corresponding element connectivity. The assemblage is out of the scope of this work. For a detailed discussion, please refer to [11].

Focusing on the integral referent to one brick element of the electrode model, as can be seen in Fig. 1(b), and considering its dimensions and a local numbering concerning the nodes of the element, the computation gives rise to (A.2), shown at the bottom of the page, and to

$$\boldsymbol{I}_b^T = \{0 \quad 0 \quad 0 \quad 0 \quad f_{b5} \quad f_{b6} \quad f_{b7} \quad f_{b8}\} \quad \text{(A.3)}$$

where

$$f_{bq} = \int_{\partial\Omega_{1b}} n_{bqS} J_{nb} dS_b \quad \text{(A.4)}$$

and where $\boldsymbol{K}_b$ is the matrix of the bth brick element, $\boldsymbol{I}_b$ is the vector of nodal electric currents of the same brick element and n_{bqS} is the shape function referring to the node whose numbering is given by the qth connectivity of the bth brick element. It is important to note that, following the assumptions mentioned in Section III-A, the contact parameters of the four elements are considered equal.

Assembling four matrices of brick elements—considering their connectivities—and using the assumptions in Section III-A, that are, the electric potential is constant on the metallic surface of the electrode and the thickness t_{el} of the model is small relative to a [see Fig. 1(b)], one obtains (5). Following the same procedure concerning the matrices and using the assumption that the electric potential is constant on the metallic surface of the electrode, one obtains

$$\boldsymbol{I}_{el}^T = \left\{ 0 \quad 0 \quad 0 \quad 0 \quad 0 \quad 0 \quad 0 \quad 0 \quad 0 \quad \sum_b \sum_{q=5}^{8} f_{bq} \right\} \quad \text{(A.5)}$$

where

$$\sum_b \sum_{q=5}^{8} f_{bq} = \sum_b \int_{\partial\Omega_{1b}} (n_{b5S} + n_{b6S} + n_{b7S} + n_{b8S}) J_{nb} dS_b = \sum_b \int_{\partial\Omega_{1b}} J_{nb} dS_b = I_{el} \quad \text{(A.6)}$$

and I_{el} is the electric current applied to the elth electrode. Therefore, (6) is finally obtained and this completes the derivation.

REFERENCES

[1] Y. Kim, J. G. Webster, and W. J. Tompkins, "Electrical impedance imaging of the thorax," *J. Microw. Power*, vol. 18, pp. 245–257, 1983.

[2] A. N. Tikhonov and V. Y. Arsenin, *Solutions of Ill-Posed Problems*. Washington, DC: V.H. Winston & Sons, 1977.

[3] A. L. Hyaric and M. K. Pidcock, "An image reconstruction algorithm for three-dimensional electrical impedance tomography," *IEEE Trans. Biomed. Eng.*, vol. 48, no. 2, pp. 230–235, Feb. 2001.

[4] P. Hua, E. J. Woo, J. G. Webster, and W. J. Tompkins, "Finite element modeling of electrode-skin contact impedance in electrical impedance tomography," *IEEE Trans. Biomed. Eng.*, vol. 40, no. 4, pp. 335–343, Apr. 1993.

[5] A. Ruuskanen *et al.*, "Using process tomography as a sensor for optimal control," *Appl. Numer. Math.*, vol. 56, pp. 37–54, 2006.

[6] M. T. Clay and T. C. Ferree, "Weighted regularization in electrical impedance tomography with applications to acute cerebral stroke," *IEEE Trans. Med. Imag.*, vol. 21, no. 6, pp. 629–637, Jun. 2002.

[7] T. J. Kao, D. Isaacson, J. C. Newell, and G. J. Saulnier, "A 3D reconstruction algorithm for EIT using a handheld probe for breast cancer detection," *Physiol. Meas.*, vol. 27, pp. S1–S11, 2006.

[8] F. C. Trigo, R. G. Lima, and M. B. P. Amato, "Electrical impedance tomography using the extended kalman filter," *IEEE Trans. Biomed. Eng.*, vol. 51, no. 1, pp. 72–81, Jan. 2004.

[9] A. Wexler, B. Fry, and M. R. Neumann, "Impedance computed tomography algorithm and systems," *Appl. Optics*, vol. 24, pp. 3985–3992, 1985.

[10] P. Metherall, "Three dimensional electrical impedance tomography of the human thorax," Ph.D. dissertation, Univ. Sheffield, Western Bank, Sheffield, 1998.

[11] K. J. Bathe, *Finite Element Procedures*. Englewood Cliffs, NJ: Prentice-Hall, 1996.

[12] R. S. Blue, D. Isaacson, and J. C. Newell, "Real-time three-dimensional electrical impedance imaging," *Physiol. Meas.*, vol. 21, pp. 15–26, 2000.

[13] P. J. Vauhkonen, M. Vauhkonen, T. Savolainen, and J. P. Kaipio, "Three-dimensional electrical impedance tomography based on the complete electrode model," *IEEE Trans. Biomed. Eng.*, vol. 46, no. 9, pp. 1150–1160, Sep. 1999.

$$\boldsymbol{K}_b = \frac{\sigma_{el}}{9t_{el}} \begin{bmatrix} 2t_{el}^2+a^2 & -\frac{1}{2}t_{el}^2+\frac{1}{2}a^2 & -t_{el}^2+\frac{1}{4}a^2 & -\frac{1}{2}t_{el}^2+\frac{1}{2}a^2 & t_{el}^2-a^2 & -\frac{1}{4}t_{el}^2-\frac{1}{2}a^2 & -\frac{1}{2}t_{el}^2-\frac{1}{4}a^2 & -\frac{1}{4}t_{el}^2-\frac{1}{2}a^2 \\ & 2t_{el}^2+a^2 & -\frac{1}{2}t_{el}^2+\frac{1}{2}a^2 & -t_{el}^2+\frac{1}{4}a^2 & -\frac{1}{4}t_{el}^2-\frac{1}{2}a^2 & t_{el}^2-a^2 & -\frac{1}{4}t_{el}^2-\frac{1}{2}a^2 & -\frac{1}{2}t_{el}^2-\frac{1}{4}a^2 \\ & & 2t_{el}^2+a^2 & -\frac{1}{2}t_{el}^2+\frac{1}{2}a^2 & -\frac{1}{2}t_{el}^2-\frac{1}{4}a^2 & -\frac{1}{4}t_{el}^2-\frac{1}{2}a^2 & t_{el}^2-a^2 & -\frac{1}{4}t_{el}^2-\frac{1}{2}a^2 \\ & & & 2t_{el}^2+a^2 & -\frac{1}{4}t_{el}^2-\frac{1}{2}a^2 & -\frac{1}{2}t_{el}^2-\frac{1}{4}a^2 & -\frac{1}{4}t_{el}^2-\frac{1}{2}a^2 & t_{el}^2-a^2 \\ & & & & 2t_{el}^2+a^2 & -\frac{1}{2}t_{el}^2+\frac{1}{2}a^2 & -t_{el}^2+\frac{1}{4}a^2 & -\frac{1}{2}t_{el}^2+\frac{1}{2}a^2 \\ & & & & & 2t_{el}^2+a^2 & -\frac{1}{2}t_{el}^2+\frac{1}{2}a^2 & -t_{el}^2+\frac{1}{4}a^2 \\ & & & & & & 2t_{el}^2+a^2 & -\frac{1}{2}t_{el}^2+\frac{1}{2}a^2 \\ & & & & & & & 2t_{el}^2+a^2 \end{bmatrix} \quad \text{(A.2)}$$

[14] P. J. Vauhkonen, M. Vauhkonen, A. Seppänen, and J. P. Kaipio, "Iterative image reconstruction in three-dimensional electrical impedance tomography," in *Proc. Inverse Problems, Design and Optimization Symposium*, Rio de Janeiro, Brazil, 2004.
[15] J. P. Kaipio, V. Kolehmainen, E. Somersalo, and M. Vauhkonen, "Statistical inversion and Monte Carlo sampling methods in electrical impedance tomography," *Inverse Problems*, vol. 16, pp. 1487–1522, 2000.
[16] M. Molinari, S. J. Cox, B. H. Blott, and G. J. Daniell, "Efficient non-linear 3d electrical tomography reconstruction," in *Proc. 2nd World Congress on Industrial Process Tomography*, Hannover, Germany, 2001, pp. 424–432.
[17] T. Vilhunen *et al.*, "Simultaneous reconstruction of electrode contact impedances and internal electrical properties: I. Theory," *Meas. Sci. Technol.*, vol. 13, pp. 1848–1854, 2002.
[18] L. Heikkinen, T. Vilhunen, R. M. West, and M. Vauhkonen, "Simultaneous reconstruction of electrode contact impedances and internal electrical properties: II. Laboratory experiments," *Meas. Sci. Technol.*, vol. 13, pp. 1855–1861, 2002.
[19] M. P. Bendsøe and O. Sigmund, *Topology Optimization: Theory, Methods and Applications*. New York, Berlin, Heidelberg: Springer-Verlag, 2003.
[20] W. H. Press *et al.*, *Numerical Recipes in C – The Art of Scientific Computing*. Cambridge, U.K.: Cambridge Univ. Press, 1999.
[21] K. Matsui and K. Terada, "Continuous approximation of material distribution for topology optimization," *Int. J. Numer. Methods Eng.*, vol. 59, pp. 1925–1944, 2004.
[22] R. T. Haftka and Z. Gürdal, *Elements of Structural Optimization*. Amsterdam, The Netherlands: Kluwer, 1999.
[23] L. A. M. Mello, "Estudo da Obtenção de Imagens Tridimensionais de Tomografia por Impedância Elétrica Pelo método de Otimização topológica," Master's thesis, Sch. Eng., Univ. São Paulo, São Paulo, Brazil, 2005.
[24] R. V. Kohn and A. Mckenney, "Numerical implementation of a variational method for electrical impedance tomography," *Inv. Prob.*, vol. 6, pp. 389–414, 1990.
[25] B. H. Brown *et al.*, "Neonatal lungs – Can absolute lung resistivity be determined non-invasively?," *Med. Biol. Eng. Comput.*, vol. 40, pp. 388–394, 2002.
[26] J. K. Guest, J. H. Prévost, and T. Belytschko, "Achieving minimum length scale in topology optimization using nodal design variables and projection functions," *Int. J. Numer. Meth. Engng.*, vol. 61, pp. 238–254, 2004.
[27] C. J. Phillips, *Glass: Its Industrial Applications*. New York: Reinhold, 1960.
[28] C. C. Bacrie, Y. Goussard, and R. Guardo, "Regularized reconstruction in electrical impedance tomography using a variance uniformization constraint," *IEEE Trans. Med. Imag.*, vol. 16, no. 5, pp. 562–571, Oct. 1997.
[29] J. C. C. Aya *et al.*, "Regularizations for a black box back-projection EIT algorithm," *ABCM Symp. Series in Bioengineering*, vol. 1, no. 11, pp. 1–9, 2006.
[30] F. V. Stump, E. C. N. Silva, and G. H. Paulino, "Optimization of material distribution in functionally graded structures with stress constraints," *Commun. Numer. Meth. Eng.*, vol. 23, no. 6, pp. 535–551, Sep. 2006.

Luís Augusto Motta Mello was born in Brazil on December 31, 1978. He received the B.S. and M.S. degrees (in 2002 and 2005, respectively) in mechanical engineering from the School of Engineering, University of São Paulo, São Paulo, Brazil. He is currently working towards the Ph.D. degree at the University of São Paulo.

His research interests include finite element modeling, inverse problems, iterative methods for linear systems and control theory.

Cícero Ribeiro de Lima was born in Brazil on December 22, 1968. He received the M.S. degree in mechanical engineering from the School of Engineering, University of São Paulo, São Paulo, Brazil, in 2002, and the Ph.D. degree in mechanical engineering from the Department of Mechatronics and Mechanical Systems Engineering at the same university in 2006.

His research interests include topology optimization applications, finite element modeling, inverse problems and reconstruction algorithms applied to electrical impedance tomography.

Marcelo Britto Passos Amato was born in São Paulo, Brazil, in 1962. He began medical studies in 1980 at the Faculdade de Medicina da Universidade de São Paulo, and graduated in December 1985. After graduating, he had a years of training in Internal Medicine and Intensive Care Medicine, as a resident doctor, followed by two years of specialization in pneumology and intensive care medicine at the Pulmonary Division of the Hospital das Clínicas – Medicine School, University of São Paulo. In 1996, he received the Ph.D. degree from the Medicine School, University of São Paulo.

Currently, he is the Supervisor of the Respiratory ICU and Director of the experimental laboratory in pneumology. He is the author of 40 papers and over 100 abstracts published in international journals, focusing on topics related to mechanical ventilation, monitoring, ventilator-induced lung injury, pulmonary physiology, and acute respiratory failure. Since 1997, he has been involved in projects related to electrical impedance tomography, especially the development of the technology for applications in the intensive care environment and the treatment of patients under mechanical ventilation.

Raul Gonzalez Lima was born in Cuba in 1961. He received the degree of Mechanical Engineer in 1984 from the School of Engineering, University of São Paulo, São Paulo, Brazil, and the Master's degree in engineering in 1990 from the same university. In 1996, he received the Ph.D. degree from the Aerospace Engineering Department, University of Texas at Austin.

He has been an Assistant Professor in the Department of Mechanical Engineering, University of São Paulo, since 1996, where he teaches courses on structural dynamics and system identification. His current research areas include parameter identification, dynamics and control of flexible structures, biomechanics, and biomedical inverse problems.

Emílio Carlos Nelli Silva was born in Brazil on September 6, 1968. He received the B.S. and M.S. degrees in mechanical engineering from the School of Engineering, University of São Paulo, São Paulo, Brazil, and the Ph.D. degree in mechanical engineering from the University of Michigan, Ann Arbor, in 1998. During his Ph.D. studies, he received two awards: the Distinguished Achievement award, due to academic and personal excellence, and the Ivo K. McIvor award, due to research performance.

He joined the Department of Mechatronics and Mechanical Systems Engineering, Polytechnic School, University of São Paulo, as an Assistant Professor in 1998. He was promoted to Associate Professor in 2003, and to Professor in 2005. His field of interest is computational mechanics, especially topology optimization and finite element techniques applied to smart materials and structures, such as piezoelectric sensors and actuators, piezocomposite materials, microelectromechanical systems (MEMS), and electrical impedance tomography. He was a Visiting Professor at Kyoto University, Japan, in 2003, and at the University of Illinois at Urbana-Champaign, in 2003, 2004, and 2006. He has published in peer-refereed international journals (in smart materials and structures, computational mechanics, and structural optimization), has given invited lectures at Universities and companies, and has been an engineering consultant to private and federal institutions.

ANEXO I – Filtro de Kalman Estendido

Electrical Impedance Tomography Using the Extended Kalman Filter

Flávio Celso Trigo*, Raul Gonzalez-Lima, and Marcelo Brito Passos Amato

Abstract—**In this paper, we propose an algorithm that, using the extended Kalman filter, solves the inverse problem of estimating the conductivity/resistivity distribution in electrical impedance tomography (EIT). The algorithm estimates conductivity/resistivity in a wide range. The purpose of this investigation is to provide information for setting and controlling air volume and pressure delivered to patients under artificial ventilation. We show that, when the standard deviation of the measurement noise level raises up to 5% of the maximal measured voltage, the conductivity estimates converge to the expected vector within 7% accuracy of the maximal conductivity value, under numerical simulations, with spatial *a priori* information. A two-phase identification procedure is proposed. A cylindrical phantom with saline solution is used for experimental evaluation. An abrupt modification on the resistivity distribution of this solution is caused by the immersion of a glass object. Estimates of electrode contact impedances and images of the glass object are presented.**

Index Terms—**Dynamical imaging, electrical impedance tomography, Kalman filter, parameter estimation.**

I. Introduction

ELECTRICAL impedance tomography (EIT) attempts to reconstruct the admittivity (or impedittivity) field within the body when a low amplitude current pattern is applied to a body surface and the potential at determined points of that surface is measured through electrodes or, alternatively, when a potential is applied and the current flowing through the surface is measured. Since the measured voltages or currents are functions of the admittivity distribution as well as of the overall geometric characteristics of the body under analysis, the problem of estimating the admittivity field, which is governed by Poisson's partial differential equation, is inverse and nonlinear. Additionally, the problem is ill posed [1]–[3].

Although the image resolution of EIT is poor when compared to other imaging techniques such as magnetic resonance, computerized tomography or ultrasonic imaging, EIT presents some advantages such as being harmless to the patient, low cost and portable. EIT also has faster time-response characteristics, which enables it to monitor cyclic changes in the living tissues better than conventional imaging modalities. Many researchers have been making continuous efforts in the pursuit of algorithms that are, at the same time, fast and capable of providing images of good spatial resolution. In order to achieve these high standards, regularization techniques, choice of optimal current patterns, fine and/or three–dimensional (3-D) mesh discretization of the body section and of the electrodes have been tried.

One of these attempts was the so called 'dynamical' method, proposed by Vauhkonen *et al.* [3]. The EIT inverse problem was formulated as a state-estimation problem and the linearized Kalman filter was used to estimate the resistivity distribution (neglecting the permittivity distribution) 31 times faster than with the conventional approach. This result is due to the fact that the Kalman filter provides an estimate for the resistivity distribution immediately after each current pattern is applied to the medium. The application of a complete set of current patterns to obtain one image is not necessary. However, the model linearization required by the linearized Kalman filter imposes a limitation on the estimation range around the linearization state, the resistivity distribution, used for linearization. As a consequence, resistivity estimates can achieve 14% error [3] even using a known linearization state vector.

In order to improve the accuracy of the estimates obtained with the linearized Kalman filter, Kim *et al.* [4], [5] used the state-space approach proposed by [3] and implemented the extended Kalman filter incorporating a Tikhonov regularization and spatial prior information on the cost functional to obtain dynamical images from simulated data and from a phantom with known background resistivity. Their results show that the Tikhonov regularization helps to cope with the ill-posed nature of the problem and, at the same time, has a smoothing effect on the reconstructed images.

In this paper, we are primarily concerned about clinical applications in which the physician is interested in the overall behavior of physiological processes whose dynamics of fluids inside the body affect the conductivity field, such as mechanical ventilation applied in critically ill patients. Patients with severe lung damage are prone to develop marked changes in lung aeration, resulting in either atelectasis or over-stretch, ultimately leading to a superimposed inflammation of the fragile parenchyma. Under this circumstance, early detection and efforts to simultaneously avoid alveolar collapse and overdistention are the cornerstones of a "protective lung strategy," resulting in an improved lung function and survival [6], [7]. The above-mentioned compromise is a challenge inside the intensive care unit (ICU), where the physicians have to manually adjust the mechanical ventilator parameters. Lung condition changes dramatically during the day and a few respiratory cycles under

Manuscript received March 26, 2002; revised May 1, 2003. *Asterisk indicates corresponding author.*

*F. C. Trigo is with the Department of Mechanical Engineering, Polytechnic School, University of São Paulo-SP, R. da Consolação 3064-171A, 01416-000 São Paulo, Brazil (e-mail: ftrigo@netpoint.com.br).

R. Gonzalez-Lima is with the Department of Mechanical Engineering, Polytechnic School, University of São Paulo-SP, Brazil, 05508-900 São Paulo-SP, 01416-000 São Paulo, Brazil (e-mail: rauglima@usp.br).

M. B. P. Amato is with the Pulmonary Department-Respiratory ICU, Medicine School, University of São Paulo-SP, 01246-903, São Paulo-SP, Brazil (e-mail: amato@unisys.com.br).

Digital Object Identifier 10.1109/TBME.2003.820389

an inappropriate airway pressure profile are enough to cause severe inflammation or lung rupture, eventually with pneumothorax. The diagnostic requires several images during the cardiac cycle, which is shorter than the respiratory cycle. Therefore, speed is necessary for lung monitoring applications. Unfortunately, conventional X-ray films and bedside clinical methods lack an appropriate sensitivity to detect such critical lung abnormalities. Presently, X-ray computerized tomography (CT) is still the gold standard procedure to detect those phenomena, despite its drawbacks. The transport of the patient away from his/her bed or from the ICU life support equipment is very risky and the static nature of the CT images is uninformative under such dynamic conditions. Sometimes, when the physician decides that a thorough analysis is required, it is already too late to reverse lung damage. Considering this whole scenario, EIT may be an attractive tool, provided that the method can give us dynamic, online and bedside results.

In order to set and control the positive ventilation parameters, namely, air flow and pressure, the EIT algorithm must provide both fast and reliable estimation of the conductivity field inside the lungs. The algorithm should also track large physiological variations (from total lung collapse to pneumothorax). Real-time images are required to sort out different pathologies. The linearized Kalman filter cannot track accurately the whole range of conductivity changes during cardiac and respiratory cycles. The extended Kalman filter potentially gives speed and accurate conductivity estimates.

This paper proposes an algorithm that uses the extended Kalman filter to estimate time-varying absolute conductivities in a plane domain representing a section of a human thorax at middle-lung level. The domain is discretized through the finite-element method (FEM), see Section II. Algorithm performance is evaluated under numerical simulations and using experimental data from a phantom with unknown resistivity distribution, as described in Sections IV and V. In addition, a procedure to estimate electrode contact impedances is developed.

Tikhonov regularization is not used since, for lung ventilation, accurate mean conductivities of specific regions of interest (ROIs) are required and the smoothness caused by the regularization term on the cost functional may bias the conductivity estimates.

II. Forward and Inverse Problem Formulation

Consider the cross section of an object as a closed domain Γ with stationary charge and conductivity distribution $\sigma(x, y)$, and purely conductive medium through which steady current flows [8]. Under those circumstances, the inner electrical potential Ψ is given by Laplace equation

$$\nabla.(\sigma \nabla \Psi) = 0 \tag{1}$$

At the boundary, currents are injected through electrodes; thus

$$\begin{matrix} \sigma \frac{\partial \Psi(\sigma)}{\partial n} = J_\ell, & \text{on the } \ell\text{th electrode} \\ 0, & \text{elsewhere at the boundary} \end{matrix} \tag{2}$$

where J_ℓ denotes the current density through the surface of the ℓth electrode.

In EIT, it is possible, through the electrodes at the boundary, to impose currents c_ℓ and read voltages v_ℓ or vice-versa. The problem is defined as *inverse* when one wishes to determine what conductivity distribution provided those readings. An inverse problem can be solved iteratively using the solution of its corresponding *forward problem*. When the internal conductivity distribution of the domain is adopted and boundary currents are known, the solution of the forward problem gives an internal voltage distribution. For an irregular domain and isotropic media, analytical solutions to the Laplace (1) with boundary conditions (2) are unknown; thus, we use the FEM to discretize the domain and solve both problems, forward and inverse, numerically.

The FE meshes used in this paper have triangular elements with constant conductivity σ and linear interpolation functions [2], [9]. On numerical simulations, currents are applied directly at a boundary node. The effect of large electrodes of the phantom must be modeled. Additional elements with four nodes are placed at the boundary of the discretized domain to incorporate the simplified complete electrode model [1]. Electrode models take into account the high metal conductivity and the contact impedance between metal and medium.

After assembling the local element matrices into the global admittance matrix [9] we have s nodes, m elements and ℓ electrodes in which p currents are applied; then, the following relation holds:

$$YV = C \tag{3}$$

where $Y(\sigma) \in \mathbb{R}^{s \times s}$ is the admittance matrix calculated at any particular distribution σ_p, $V(\sigma) = [v_1 \dots v_j \dots v_p]$, $v_j \in \mathbb{R}^s$ is a matrix containing nodal voltages corresponding to each applied current pattern, and $C = [c_1 \dots c_j \dots c_p]$, $c_j \in \mathbb{R}^s$ is a matrix of linearly independent bipolar current patterns. On numerical simulations C is

$$C = \begin{bmatrix} -I & -I & \dots & -I \\ +I & 0 & \dots & 0 \\ 0 & +I & \dots & 0 \\ 0 & 0 & \dots & +I \\ \vdots & \vdots & \ddots & \vdots \\ 0 & 0 & 0 & 0 \end{bmatrix}_{s \times p} \tag{4}$$

whereas, with experimental data, C matrix contains diametrical current patterns.

Solving the forward problem for V, we obtain the simulated voltage distribution in the discretized domain. A detailed description of this process is found in [9]. Those voltages are used as input data in the solution of the inverse problem.

The inverse problem can be stated as follows: A domain Γ with nonuniform unknown conductivity distribution $\sigma(x, y)$ is discretized by the FEM into an m-dimensional space. For each $v_j(\sigma)$, $j = 1, \dots, p$, it is possible to write a map $h_j : \sigma \to v_j$

$$v_j(\sigma) = h_j(\sigma) = [Y(\sigma)]^{-1} c_j \tag{5}$$

that is, the nodal voltages vectors are nonlinear functions of the conductivity distribution in the domain Γ. Using a Taylor series to expand $v_j(\sigma)$ around any distribution σ_0 and keeping terms up to the first-order gives

$$v_j(\sigma) \simeq v_j(\sigma_0) + \frac{\partial \mathbf{h}_j}{\partial \sigma}|_{(\sigma_0)}(\sigma - \sigma_0). \tag{6}$$

The derivatives of $\mathbf{h}_j$ with respect to the m conductivities are calculated using the *standard method* [9], in which $\partial Y/\partial\sigma_m$ is obtained directly from the FE model and results in

$$H_j(\boldsymbol{\sigma}_0) = \left.\frac{\partial \boldsymbol{h}_j}{\partial \boldsymbol{\sigma}}\right|_{(\boldsymbol{\sigma}_0)} = -Y^{-1}\frac{\partial Y}{\partial \boldsymbol{\sigma}}Y^{-1}\boldsymbol{c}_j,\ j = 1,\ldots,p. \quad (7)$$

Thus, (6) can be explicitly written as

$$\begin{bmatrix} \boldsymbol{v}_1(\boldsymbol{\sigma}) \\ \vdots \\ \boldsymbol{v}_j(\boldsymbol{\sigma}) \\ \vdots \\ \boldsymbol{v}_p(\boldsymbol{\sigma}) \end{bmatrix} = \begin{bmatrix} \boldsymbol{v}_1(\boldsymbol{\sigma}_0) \\ \vdots \\ \boldsymbol{v}_j(\boldsymbol{\sigma}_0) \\ \vdots \\ \boldsymbol{v}_p(\boldsymbol{\sigma}_0) \end{bmatrix} + \begin{bmatrix} H_1(\boldsymbol{\sigma}_0) \\ \vdots \\ H_j(\boldsymbol{\sigma}_0) \\ \vdots \\ H_p(\boldsymbol{\sigma}_0) \end{bmatrix} (\boldsymbol{\sigma} - \boldsymbol{\sigma}_0). \quad (8)$$

The product $-Y^{-1}(\partial Y/\partial\sigma_m)Y^{-1}\boldsymbol{c}_j = H_j(\boldsymbol{\sigma}_0)$, $j = 1,\ldots,p$, is called the *sensitivity matrix* of the mapping. It must be pointed out that, on each vector $\boldsymbol{v}_j \in \mathbb{R}^s$ of nodal voltages, only the voltages at the ℓ electrodes can be measured. Equation (8) states the *classical frame* of the inverse EIT problem, in which it is assumed that there are no significant changes in the conductivity distribution of the domain Γ during the time it takes to apply all current patterns, make the respective voltage measurements and process those data before an image is reconstructed. In this sense, the formulation can be named "static." In order to increase reconstruction speed and track fast conductivity changes, the EIT inverse problem was dynamically stated [3]–[5], as discussed in Section III.

III. Extended Kalman Filter for EIT

Vauhkonen *et al.* [3] proposed a dynamical formulation of the EIT as a state-estimation problem in which the impedances of the FE model were considered the state to be estimated, and implemented the linearized Kalman filter to observe the state.

In this paper, we take advantage of the state-space formulation to implement the extended instead of the linearized version of the Kalman filter. The rationale follows: In the linearized version, although each image is obtained after a new current pattern is applied, the linearization shown in (6) is always done at the same state vector $\boldsymbol{\sigma}_0$, which brings some limitations in the range of variation of the parameters to be estimated. On the other hand, in the extended Kalman filter, the mapping is linearized at every new estimate. This way, it is possible to estimate conductivity distribution in a wide range [4], [5]. The successive estimates will likely be close to each other, thus decreasing linearization errors.

A detailed discussion on stochastic estimation or on Kalman filtering theory is out of our scope; however, we briefly state the main hypotheses and assumptions necessary for applying the filter equations. An extensive study can be found, for instance, in [10] and [11].

The first requirement for the usage of the filter is that both the observation model and the system model must be in *state-space* form. We return to (6) to start describing the observation model. When any of the p current patterns $\boldsymbol{c}_j$ at time $t = k\Delta t$ is applied, a vector $\boldsymbol{v}_k \in \mathbb{R}^\ell$ of measurable nodal voltages at the electrodes is obtained. Since in our FE mesh the first ℓ nodes correspond to electrodes, taking the first ℓ lines of (6) results

$$\boldsymbol{v}_k(\boldsymbol{\sigma}_k) = \boldsymbol{v}_k(\boldsymbol{\sigma}_{k-1}) + H_k(\boldsymbol{\sigma}_{k-1})[\boldsymbol{\sigma}_k - \boldsymbol{\sigma}_{k-1}] \quad (9)$$

for each k. In addition, every measurement process is inherently corrupted by noise. Thus, from (9), the *observation model* at time t is

$$\boldsymbol{v}_k(\boldsymbol{\sigma}_k) = \boldsymbol{v}_k(\boldsymbol{\sigma}_{k-1}) + H_k(\boldsymbol{\sigma}_{k-1})[\boldsymbol{\sigma}_k - \boldsymbol{\sigma}_{k-1}] + \boldsymbol{\nu}_k \quad (10)$$

where $\boldsymbol{\sigma}_k \in \mathbb{R}^m$ is the conductivity distribution at time t and $\boldsymbol{\nu}_k \in \mathbb{R}^\ell$ is a zero-mean Gaussian white measurement noise vector whose covariance is the symmetrical positive definite matrix $R_k \in \mathbb{R}^{\ell\times\ell}$.

The discrete-time *system model* is given by

$$\boldsymbol{\sigma}_k = \Phi_{k-1}\boldsymbol{\sigma}_{k-1} + \boldsymbol{\omega}_k \quad (11)$$

known as the *state equation*, in which $\Phi_{k-1} \in \mathbb{R}^{m\times m}$ is the discrete-time transition matrix and $\boldsymbol{\omega}_k \in \mathbb{R}^m$ is a zero-mean Gaussian white state noise vector whose covariance is the symmetrical positive semi-definite matrix $Q_k \in \mathbb{R}^{m\times m}$. The hypothesis of zero-mean Gaussian white noise with associated covariance matrices is central in optimal estimation theory. Other important although not necessary assumptions used in this paper are that the process noise and the measurement noise are not correlated, i.e. $E[\boldsymbol{\omega}_k\boldsymbol{\nu}_k^T] = 0$ for all k, and that both process and measurement noise covariance matrices are diagonal with equal and constant elements, or $Q_k = \rho_\omega^2 I_m$ and $R_k = \rho_\nu^2 I_\ell$, with ρ_ω^2 and ρ_ν^2 representing, respectively, process and measurement noise covariances. The validity of these hypotheses depends on several factors including the completeness of model structure. For instance, the elements of Q_k are affected by system model fidelity in describing the physical phenomena. On the other hand, assuming a diagonal R_k implies negligible crosstalk.

Variations of the system do not come from its dynamics, but from exogenous reasons. The transition matrix is the identity matrix [3], characterizing the *random walk model*. With (10) and (11), the state-space representation of the system is complete, and the extended Kalman filter can be readily implemented.

There are several forms to present the filter equations; the one below is based in [10], as follows:

$$\hat{\boldsymbol{\sigma}}_k^{(-)} = \Phi_{k-1}\hat{\boldsymbol{\sigma}}_{k-1}^{(+)} \quad (12)$$

$$P_k^{(-)} = \Phi_{k-1}P_{k-1}^{(+)}\Phi_{k-1}^T + Q_{k-1} \quad (13)$$

$$\hat{\boldsymbol{\sigma}}_k^{(+)} = \hat{\boldsymbol{\sigma}}_k^{(-)} + G_k\left[\boldsymbol{v}_k - \boldsymbol{h}_k\left(\hat{\boldsymbol{\sigma}}_k^{(-)}\right)\right] \quad (14)$$

$$P_k^{(+)} = \left[I - G_k H_k^T\left(\hat{\boldsymbol{\sigma}}_k^{(-)}\right)\right]P_k^{(-)} \quad (15)$$

$$G_k = P_k^{(-)}H_k^T\left(\hat{\boldsymbol{\sigma}}_k^{(-)}\right) \times \left[H_k\left(\hat{\boldsymbol{\sigma}}_k^{(-)}\right)P_k^{(-)}H_k^T\left(\hat{\boldsymbol{\sigma}}_k^{(-)}\right) + R_k\right]^{-1}. \quad (16)$$

Equations (12) and (13) constitute, respectively, the *state estimate propagation* and the *estimation error covariance matrix propagation*, whereas (14)–(16) represent the *state estimate update*, the *estimation error covariance matrix update*, and the *Kalman gain matrix*, respectively. With information about the initial conditions $\boldsymbol{\sigma}(t)$ at $t = 0$ and its associated error covariance P_0, (12) provides the best estimate for the state based on previous information embedded in $\hat{\boldsymbol{\sigma}}_{k-1}^{(+)}$ until the next set of measurements is available; this prediction is then corrected by (14) after processing new data.

IV. Numerical Simulations

A. FEM Meshes

In the dynamical approach via extended Kalman filter, conductivity distribution estimation is a recursive procedure. This paper does not intend to drastically improve image resolution but rather estimate absolute conductivity in a wide range in some major regions and use it for the purpose of setting and controlling air volume and pressure delivered to patients under artificial ventilation. Under such circumstances, estimates of absolute conductivities in five regions in a 2-D image provide sufficient information to allow a reliable evaluation.

From the clinical point of view, the major regions this paper is concerned with, named ROIs, would approximately correspond, in a real situation, to the areas occupied by left and right lungs, heart and other tissues such as backbone and fat around thorax.

From the engineering point of view, any reduction in the dimension of the estimation problem as a consequence of associating elements in ROIs helps improving the speed of the computational process. Also, solution stability tends to improve [3]. In practice, element-association consists in using an average conductivity for all the elements that pertain to the same region of interest.

For numerical simulations, two different meshes were used. A coarse mesh discretization, as in [12], containing $m = 32$ triangular elements and $s = 25$ nodes (from which $\ell = 16$ correspond to the electrodes at the boundary) as shown in Fig. 1(a), and a finer mesh, similar to that presented by [13], with $m = 269$ triangular elements, $s = 157$ nodes and $\ell = 16$ electrodes, see Fig. 1(b).

In order to evaluate the performance of the proposed algorithm, the 32 elements of the coarse FE mesh were associated in 16 ROIs, each region with two neighbor elements. With a finer mesh, it is possible to associate elements in regions whose contours resemble real structures inside the thorax. The 269 elements of the finer mesh were associated in eight ROIs that roughly resemble anatomic structures.

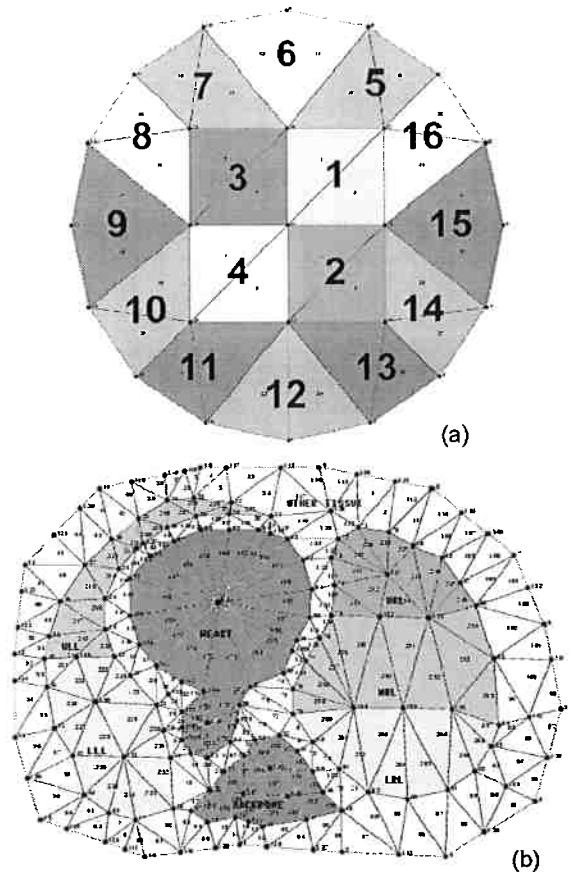

Fig. 1. (a) Coarse FEM mesh with $m = 32$ elements and $s = 25$ nodes used on numerical simulations. Numbers in bold face indicate each ROI formed by two adjacent elements; (b) fine FEM mesh with $m = 269$ elements and $s = 157$ nodes used on numerical simulations (Note: This representation is mirrored according to clinical tomography patterns). The eight ROIs are: *ULL*—upper left lung; *LLL*—lower left lung; *URL*—upper right lung; *MRL*—middle right lung; *LRL*—lower right lung; heart; backbone; and other tissue.

B. Simulation Methods and Parameters

After the discretization of the domain in a FE mesh, the simulation methodology is the following: 1) Adopt a conductivity distribution $\boldsymbol{\sigma} \in \mathbf{R}^m$ that represents typical pulmonary conditions, according to data stated by [8], [14]; 2) Apply p linearly independent current patterns, as in (4), to the 16 nodes representing electrodes and solve the forward problem through (3) to obtain nodal voltages; 3) Add zero-mean Gaussian white noise, with standard deviation 7.5% (coarse mesh) or 5% (fine mesh) of the maximal calculated voltage for each simulation. Computed voltages in 2) plus noise represent "measured" voltages. Zero-mean Gaussian white noise is generated through a routine from [15]; 4) Assuming a clinically acceptable uniform initial distribution $\boldsymbol{\sigma}_0$, use "measured" voltages calculated in 3) for each current pattern as observation data for the extended Kalman filter, (12)–(16), and estimate the conductivity distribution $\boldsymbol{\sigma}$. The above-described procedure characterizes a dynamical situation in the sense that a step function change on the absolute conductivity distribution has to be tracked.

The parameters used on numerical simulations are given on Table I. An initial uniform conductivity $\boldsymbol{\sigma}_0 = 1.0\ (\Omega\mathrm{m})^{-1}$ is assumed for the 16 ROIs of the 32-element mesh. For the 269-element mesh with eight ROIs, the vector of expected conductivities was chosen in order to reproduce the normal pulmonary condition and two levels of severity of an anomaly known as *atelectasis* on the lower right lung. The initial uniform conductivity $\boldsymbol{\sigma}_0 = 0.2\ (\Omega\mathrm{m})^{-1}$ is close to the average value for human tissues inside the thorax. Acronyms *B*, *H*, *ULL*, *LLL*, *URL*, *MRL*, *LRL*, and *OT* stand, respectively, for backbone, heart, upper left lung, lower left lung, upper right lung, middle right lung, lower right lung, and other tissues.

All simulations were carried on an 800-MHz personal computer with 132 Mbytes of RAM.

C. Results From Numerical Simulations

Time-response behavior on simulations 1 and 2 for the 32-element mesh with 16 ROIs are shown in Figs. 2(a) and 3(a). On simulation 1 the estimation error is 4.3% of the maximal conductivity value, and the convergence is achieved in about 6 s, or 180 iterations.

TABLE I
PARAMETERS FOR NUMERICAL SIMULATIONS

Simulation.	1	2	3	4	5
MESH/ROIs	32-element/16 ROIs		269-element 8/ROIs		
Expec. cond. $\hat{\sigma}_k$ $(\Omega m)^{-1}$	0.20 0.80 1.40 0.60†		$B = 0.10$ $H = 0.58$ $ULL = 0.080$ $LLL = 0.087$ $URL = 0.077$ $MRL = 0.083$ $LRL = 0.091$ $OT = 0.20$	0.10 0.58 0.080 0.087 0.077 0.083 0.14 0.20	0.10 0.58 0.080 0.087 0.077 0.083 0.50 0.20
Meas. noise (%) ‡	7.5		5		
$P_0(\times I_{ROIs})$	25	2	0.2		
$Q(\times I_{ROIs})$	$5.5\ e^{-6}$		$3\ e^{-3}$		
$R(\times I_{16})$	$4\ e^{-2}$		$5\ e^{-2}$		
Init. conduc. σ_0 *	1.0		0.2		

† adopted conductivity for 13 ROIs
‡ std. dev. of zero mean Gaussian white noise in % of max. voltage calculated through MEF
* plus additive noise

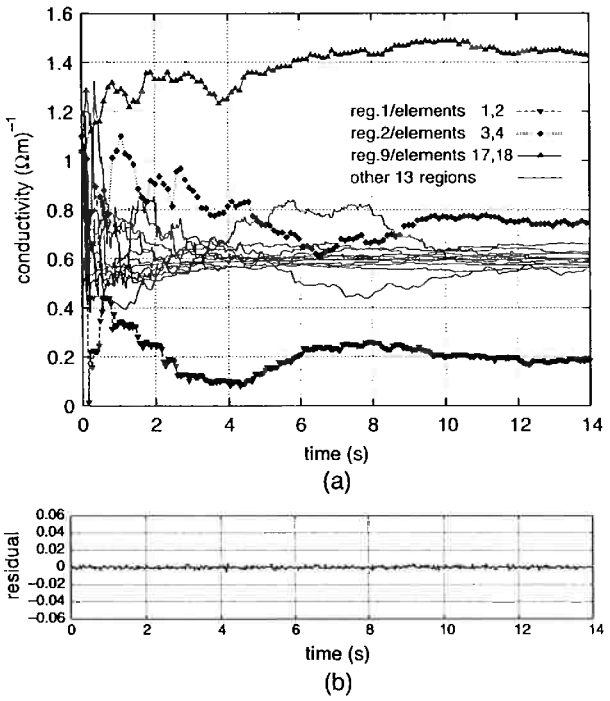

Fig. 2. (a) Simulation Nr. 1: absolute conductivity in 16 ROIs with "measured" voltages standard deviation 7.5% of the maximal voltage calculated through the FEM. The initial conductivity σ_0 is set to 1.00 + additive noise for all regions, and the objective vector is $\hat{\sigma}_k = [0.10\ 0.80\ 1.40\ 0.60\ (13\ regions = background)]^T$. The estimation error is <5% of the maximal conductivity value; (b) normalized residual for simulation Nr. 1.

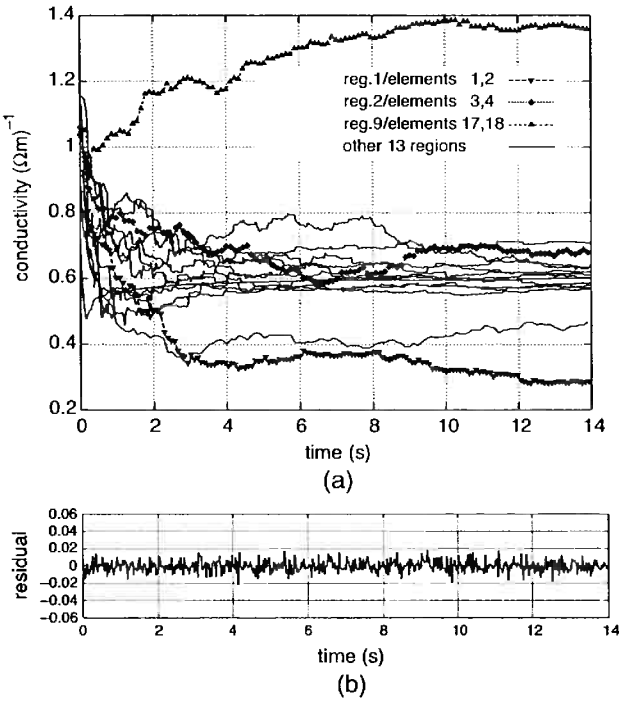

Fig. 3. (a) Simulation Nr. 2: same conditions as in Fig. 2(a), except for a decrease in the variances of the initial error covariance matrix to show its influence on the output. The convergence to the expected vector is slower; (b) normalized residual for simulation Nr. 2.

On numerical simulations, the expected conductivity distributions are known. Then, it is possible to verify if the successive estimates converge to the desired vector. However, in real situations, convergence for some vector *does not imply* that this vector is the right one. For instance, estimates could "converge" for a solution without clinical meaning.

One way to check if the convergence is actually occurring is analyzing the *observation normalized residual*. The normalized residual is the difference between effectively observed values (measured voltages), and the values calculated for the same observation using the state estimated by the filter [16].

The normalized residual for the kth iteration is given by

$$r_\nu = \frac{\left\{\frac{1}{\ell}\sum_{j=1}^{\ell}\left[v_k(\sigma_k) - \hat{v}_k(\hat{\sigma}_k)\right]_j\right\}}{\rho_\nu}, \quad k = 1, 2, \ldots \quad (17)$$

where ℓ is the number of electrodes and ρ_ν is measurement noise level standard deviation. Convergence is considered satisfactory when $E[r_\nu] = 0$ during all the estimation period, and $-3\rho_\nu \leq r_\nu \leq 3\rho_\nu$. The convergence based on the adopted criterion is

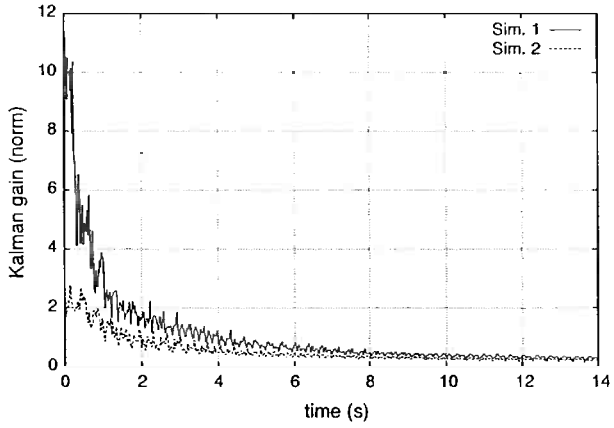

Fig. 4. Simulations 1 and 2—Kalman gain matrix spectral norm.

Fig. 5. Simulation 5—absolute conductivity for dense *atelectasis* on the lower right lung. The estimation error is < 7% of the maximal conductivity value.

achieved for simulations 1 and 2 according to Figs. 2(b) and 3(b).

The initial estimation error covariance matrix P_0 is chosen to indicate the confidence interval of the initial state σ_0. The measurement noise covariance matrix R is defined by the measurement noise. The state covariance matrix Q[1] prevents matrix P_k from getting too small, keeping the filter sensitive to new information [18].

For the 269-mesh with eight ROIs, voltages calculated through the FEM were corrupted by zero-mean Gaussian white noise whose standard deviation was 5% of the maximal voltage. Further simulation parameters are given on Table I. Time-response behavior on simulation 5 is given in Fig. 5; convergence to the expected vector $\hat{\sigma}_k$ is achieved in about 120 iterations, at a rate of four iterations/s. A surface plot for the 300th iteration state vector of simulation 5 is shown in Fig. 6. The anomaly, *dense atelectasis*, was properly identified within 7% accuracy.

[1]The subscript k of Q_k and R_k is dropped since the matrices are admitted constant.

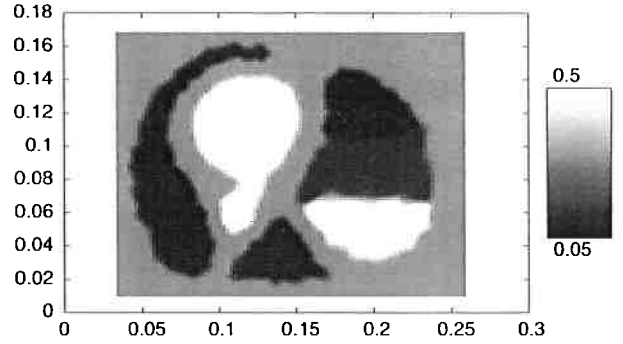

Fig. 6. Absolute conductivity distribution—eight ROIs—lower right lung with dense atelectasis.

D. Discussion

The error covariance matrix P_k is affected by the statistical parameters of the system disturbances as reflected in the components of the covariance matrices Q and R, as shown by (13), (15), and (16). Higher values in components of Q indicate that either the system is driven by stronger state noise or that the adopted model fails to represent system dynamics [10], [11].

The effect of R on the error covariance matrix P_k can be evaluated through

$$P_k^{-1(+)} = P_k^{-1(-)} + \left[H_k^T\left(\hat{\sigma}_k^{(-)}\right) R_k^{-1} H_k\left(\hat{\sigma}_k^{(-)}\right)\right] \quad (18)$$

obtained from the application of the *matrix inversion lemma* [11] and proper manipulation of (15). Larger measurement noise, indicated by higher variances, causes the error covariance matrix P_k and the Kalman gain matrix G_k, (16), to decrease.

The influence of the initial error covariance matrix P_0 on the behavior of the algorithm is not crucial. When no *a priori* information on the parameters to be estimated is available, and P_0 is arbitrarily chosen, its influence is relevant only during the first iterations. After those few iterations, the filter properly adjusts matrix P_k. For instance, on simulations 1 and 2, the initial estimation error covariance matrices, P_0, were selected with variances (elements of the main diagonal) 25.0 and 2.0, respectively, without altering matrices Q and R. Figs. 2(a) and 3(a) show that, for the same simulated time, convergence is slower on simulation 2. On simulation 2, matrix R prevails over Q, and, at each iteration, filter correction provides a smaller decrease of the estimation error.

When P_0 is higher, estimate corrections during the first iterations are increased. However, the effect of the arbitrarily chosen P_0 is gradually suppressed. Fig. 4 presents the *spectral norm* of Kalman gain matrix G_k for simulations 1 and 2. The spectral norm is defined as the largest singular value of a matrix. This can be used as a "measure" of the corrections on the state on each iteration. Observe that, after 8 s, the norms are practically identical, regardless of P_0.

On the smaller mesh, the purpose of associating elements in ROIs is to improve the stability of the filter. On the larger mesh, the association of elements has two purposes: To improve the stability of the filter and to compute accurate average conductivity of specific regions of the lung. These average conductivities can be used to adjust ventilators on ICUs. The choice of

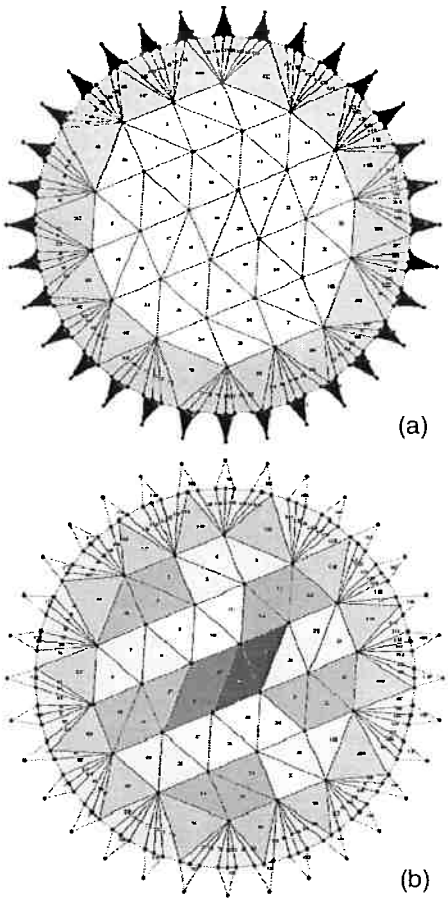

Fig. 7. FE mesh with $m = 182$ elements (32 electrodes) and $s = 156$ nodes used with experimental data: (a) ROIs used to identify the electrodes; (b) ROIs used to identify the glass object.

an initial conductivity distribution, σ_0, is not totally arbitrary. Without a clinically reasonable choice, the convergence will take longer and the local minimum of the error function may not correspond to an acceptable conductivity distribution.

The method can be extended to account for cyclic changes of the shape of the torax and the lung areas during ventilation. On each iteration a different FE-mesh can be used. This research is currently being carried on.

V. Evaluation With Experimental Data

A. FEM Mesh

The performance of the proposed algorithm to estimate resistivity distribution and electrodes contact impedances with experimental data was evaluated using a FE-mesh containing $m = 150$ triangular elements, $\ell = 32$ elements with four nodes, and $s = 156$ nodes, as shown in Fig. 7(a) and (b). The 32 elements with four nodes represent electrodes, modeled using the simplified complete model [1].

B. Experimental Methods and Parameters

The phantom is a 235-mm-diameter cylindrical container with 32 rectangular 12-mm-wide brass electrodes with equal gap between them. The container was filled up to 26.5 mm with a saline solution of concentration 0.23 g/l of NaCl. A current generator, as described in [17], was used to inject bipolar current patterns with frequency 25 kHz and amplitude 2 mA_{pp}. Voltages were measured through a multimeter HP 34401 A. Measured data were processed on an 800-MHz personal computer with 132 Mbytes of RAM.

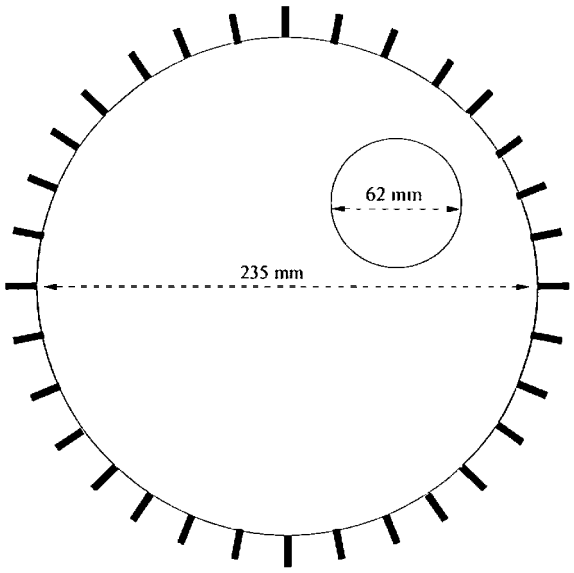

Fig. 8. Schematic representation of the test rig containing 32-brass electrodes and a 62-mm glass object.

Current information and measured voltages were used by the proposed algorithm to estimate electrode contact impedances, and to identify the position of a 62-mm-diameter glass object, which was immersed in the medium, see Fig. 8, in two phases.

First, the Kalman filter is used to estimate the average unknown resistivity of the saline solution and electrode contact impedances. The 182 elements of the mesh were associated in 34 ROIs. The contact impedance of each electrode was considered a parameter to be estimated, whereas the remaining 150 elements were associated in two ROIs with homogeneous resistivity distribution, as shown in Fig. 7(a). Adjacent current patterns were injected to the phantom without the glass object, and voltages were measured. Resistivities of the 34 ROIs were determined through successive runs of the extended Kalman filter until each component of the state-vector presented less than 1% discrepancy when compared to the previous run. The covariance matrices P_0, Q, and R were set, respectively, to $3.5 \times 10^{-1} I_{34}$, $7.8 \times 10^{-4} I_{34}$, and $2.5 \times 10^{-5} I_{32}$.

Keeping estimated electrode contact impedances constant, Kalman filter is used to estimate resistivity distribution of the medium. A cylindrical glass object is immersed in the phantom, without changing the height of the saline medium. This represents a step function change on the resistivity distribution of the medium. The 150 internal elements of the mesh were associated in 16 ROIs as shown in Fig. 7(b). No *a priori* knowledge about the location of the glass object inside the phantom was used to build the ROIs. Diametrical current patterns were injected and voltages measured. The covariance matrices P_0, Q,

TABLE II
ELECTRODE CONTACT IMPEDANCES (Ωm^2)

Electrode	1	2	3	4	5	6	7	8
Impedance	0.0167	0.0260	0.0132	0.0155	0.0211	0.0271	0.0146	0.0195
Electrode	9	10	11	12	13	14	15	16
Impedance	0.0255	0.0100	0.0131	0.0098	0.0088	0.0179	0.0091	0.0143
Electrode	17	18	19	20	21	22	23	24
Impedance	0.0157	0.0164	0.0185	0.0097	0.0190	0.0190	0.0125	0.0090
Electrode	25	26	27	28	29	30	31	32
Impedance	0.0073	0.0152	0.0181	0.0249	0.0272	0.0237	0.0282	0.0201

and R were set, respectively, to $3.5 \times 10^{-5} I_{16}$, $7.8 \times 10^{1} I_{16}$, and $2.5 \times 10^{-3} I_{32}$; all the components of the initial resistivity vector σ_0 were set to 1.0 (Ωm). Kalman filter is used to track the change on the resistivity distribution of the medium.

The two-phase identification procedure is justified since, when matrices Q and R are kept constant, the filter can be interpreted as a deterministic least-squares recursive minimization method [18]. Each Kalman filter iteration is a contraction mapping, $\mathcal{K}$, which contracts the trace of P matrix

$$\hat{\sigma}_k = \mathcal{K}(\hat{\sigma}_{k-1}) \tag{19}$$

and $\hat{\sigma} \in \mathcal{S}$, where $\mathcal{S}$ is a metric space. The Contraction Mapping Theorem states that the filtering process will converge to a fixed-point, $\hat{\sigma}^*$ [19]. Estimating resistivity distribution while keeping contact impedances constant is also a contraction mapping, $\mathcal{K}_1$, on a subspace of $\mathcal{S}$, $\mathcal{S}_1$. Estimating contact impedances while keeping the resistivity distribution constant is a contraction mapping, $\mathcal{K}_2$, on another subspace of $\mathcal{S}$, $\mathcal{S}_2$. Notice that $\mathcal{S}$ is $\mathcal{S}_1 \bigcup \mathcal{S}_2$ and $\mathcal{S}_1 \bigcap \mathcal{S}_2$ is a null space. The sequence of these two estimation procedures, $\mathcal{K}_1$ and then $\mathcal{K}_2$, is necessarily a contraction mapping, $\mathcal{K}_2(\mathcal{K}_1(\cdot))$

$$\hat{\sigma}_k = \mathcal{K}_2\left(\mathcal{K}_1(\hat{\sigma}_{k-1})\right) \tag{20}$$

on the original metric space $\mathcal{S}$. The contraction mapping theorem states that the filtering process will converge to the same fixed-point, $\hat{\sigma}^*$, which is also a minimum of the original error functional. Therefore, phase one should be followed by phase two.

In the present experimental procedure, the estimation method $\mathcal{K}$ with 34 ROIs was initially applied. This is appropriate since the saline solution has uniform resistivity distribution and it can be represented by two ROIs.

With the knowledge of electrode contact impedances, the estimation method $\mathcal{K}_1$ is used with 16 ROIs. According to the two phase identification procedure, one should iterate to solve for contact impedances, $\mathcal{K}_2$. Provided that placing the glass object in the saline solution without changing the liquid level, electrode contact impedances present no significant changes. Under these conditions, $\mathcal{K}_2$ was skipped.

C. Experimental Results

The estimated electrode contact impedances are given on Table II. The mean value is 0.0171 Ωm^2, and the standard deviation is 0.006 Ωm^2. These values were obtained after 30 successive runs of the algorithm, or 960 iterations (each "run" corresponds to 32 patterns of excitation), at a rate of 4 iterations/s. Convergence was achieved according to the criterion stated in Section IV-C.

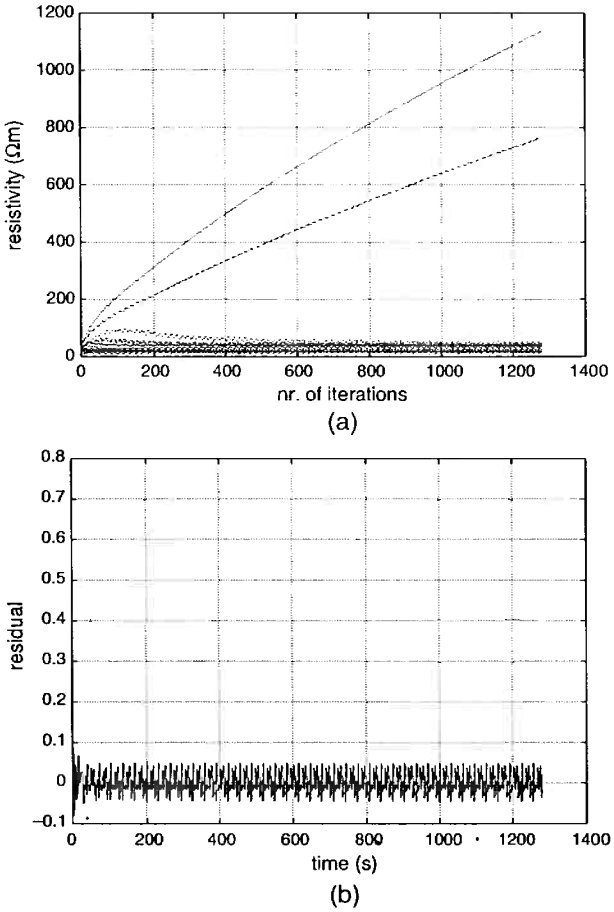

Fig. 9. (a) State-vector evolution for phantom with glass object. (b) Normalized residual—phantom with glass object.

State-vector evolution curves for the phantom with the glass object are shown in Fig. 9(a). At about 100 iterations, or 25 s, it is already possible to identify, on two regions represented by the curves with steeper gradients, resistivity values twice higher than on the other regions. Those two regions, 5 and 9, enclose the glass object. Region 9 presents higher resistivity than region 5 because most of the glass object area belongs to region 9. Fig. 9(b) shows that the residuals fulfill the requisites established on the convergence criterion stated in Section IV-C. A 3-D plot of the state-vector on the 1280th iteration is given in Fig. 10.

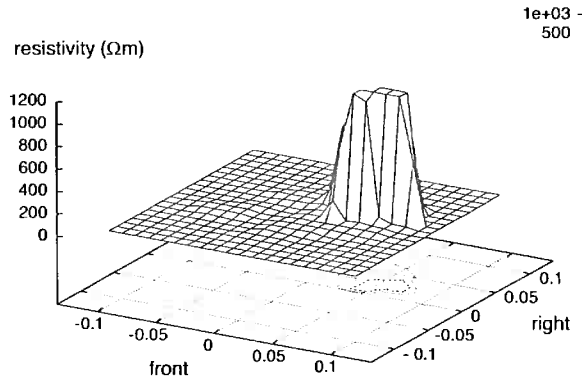

Fig. 10. Phantom with glass object—absolute resistivity distribution—contour plot for the 1280th iteration state vector.

D. Discussion

Initially, electrode contact impedances were estimated together with the average uniform resistivity of the medium. The estimation procedure used was $\mathcal{K}$.

A glass object was immersed in the medium. The estimation of resistivity distribution of the saline solution was performed keeping the contact impedances constant. Although full convergence takes a long time, because the step function modification on resistivity is large, after a few iterations the position and dimension of the glass object are noticeable.

The alternation of the estimation procedures through $\mathcal{K}_1$ and $\mathcal{K}_2$, as described in Section V-B, was relaxed in our experimental methodology. What allows us to repeat $\mathcal{K}_1$ several times, skipping $\mathcal{K}_2$, is the fact that variations on contact impedances are much slower than variations on the resisitivity of the medium when the glass object is immersed, provided that the concentration of the solution and liquid level are kept constant. If the contact impedances changed faster, then alternating $\mathcal{K}_1$ and $\mathcal{K}_2$ would be necessary.

The association of elements in ROIs is used for the sole reason of filter stability. The sensitivity matrix is better conditioned with a small number of ROIs.

VI. Conclusion

This paper has investigated an alternative approach to solve the dynamical resistivity estimation inverse problem in EIT through the extended Kalman filter. The algorithm was able to track a step-function change on the absolute conductivity distribution both with simulated and experimental data. Conductivity estimates obtained with simulated data presented less than 7% discrepancy from the expected values and corroborate the conclusions in [4] and [5], which state the improved accuracy of the extended compared to the linearized Kalman filter. In order to obtain wide-range accurate estimates to be used as control parameters for ICU lung ventilators and keep the algorithm numerically stable, we associated elements in ROIs and adopted a clinically acceptable initial uniform conductivity distribution. This way, we avoided the smoothing effect that a Tikhonov regularization has on the estimated images.

Experimental data from a phantom were used to evaluate the performance of the algorithm. A two-phase method of estimating electrode contact impedances and the resistivity distribution of a medium was proposed. Considering the problem of estimating electrode contact impedances separated from the problem of image estimation has numerical advantages and the final result is necessarily the same as estimating both sets of parameters together. This is shown using the Contraction Mapping Theorem. The proposed two-phase method is particularly suitable for applications in which electrode contact impedances present large variations as, for instance, on lung condition monitoring.

The image rate of 4/s is not satisfactory for real-time control of an ICU lung ventilator. However, the image rate can be improved through hardware and software modifications, for instance, using a faster processor or parallel computing. Furthermore, the limitation on the number of ROIs to keep algorithm stability diminishes the spatial resolution of the estimated images.

References

[1] P. Hua, E. J. Woo, J. G. Webster, and W. J. Tompkins, "Finite element modeling of electrode-skin contact impedance in electrical impedance tomography," *IEEE Trans. Biomed. Eng.*, vol. 40, pp. 335–343, Apr. 1993.

[2] T. Murai and Y. Kagawa, "Electrical impedance computed tomography based on a finite element model," *IEEE Trans. Biomed. Eng.*, vol. BME-32, pp. 177–184, 1985.

[3] M. Vauhkonen, P. A. Karjalainen, and J. P. Kaipio, "A Kalman filter approach to track fast impedance changes in electrical impedance tomography," *IEEE Trans. Biomed. Eng.*, vol. 45, pp. 486–493, Apr. 1995.

[4] K. Y. Kim, B. S. Kim, M. C. Kim, and M. Vauhkonen, "Image reconstruction in time-varying electrical impedance tomography based on the extended Kalman filter," *Meas. Sci. Technol.*, vol. 12, pp. 1032–1039, 2001.

[5] K. Y. Kim, S. I. Kang, M. C. Kim, S. Kim, Y. J. Lee, and M. Vauhkonen, "Dynamic image reconstruction in electrical impedance tomography with known internal structures," *IEEE Trans. Magn.*, vol. 38, pp. 1301–1304, Mar. 2002.

[6] M. B. P. Amato, C. S. Barbas, D. M. Medeiros, R. B. Magaldi, G. P. Schettino, G. Lorenzi-Filho, R. A. Kairalla, D. Deheinzelin, C. Munoz, R. Oliveira, T. Y. Takagaki, and C. R. R. Carvalho, "Effect of a protective-ventilation strategy on mortality in the acute respiratory distress syndrome [see comments]," *New Eng. J. Med.*, vol. 338, no. 6, pp. 347–354, 1998.

[7] M. B. P. Amato, C. S. Barbas, D. M. Medeiros, G. P. Schettino, G. Lorenzi-Filho, R. A. Kairalla, D. Deheinzelin, C. Morais, E. O. Fernandes, T. Y. Takagaki, and C. R. R. Carvalho, "Beneficial effects of the "open lung approach" with low distending pressures in acute respiratory distress syndrome. A prospective randomized study on mechanical ventilation," *Amer. J. Respir. Crit. Care Med.*, pt. 1, vol. 152, no. 6, pp. 1835–1846, 1995.

[8] D. C. Barber and B. H. Brown, "Applied potential tomography," *J. Phys. E: Sci. Instrum.*, vol. 17, pp. 723–733, 1984.

[9] T. J. Yorkey, J. G. Webster, and W. J. Tompkins, "Comparing reconstruction algorithms for electrical impedance tomography," *IEEE Trans. Biomed. Eng.*, vol. BME-34, pp. 843–852, 1987.

[10] A. Gelb, Ed., *Applied Optimal Estimation*. Cambridge, MA: MIT Press, 1979.

[11] P. S. Maybeck, *Stochastic Models, Estimation and Control*. New York: Academic Press, 1979.

[12] F. C. Trigo, "Filtro Estendido de Kalman Aplicado à Tomografia por Impedância Elétrica," M.Sc. dissertation, Universidade de São Paulo, Escola Politécnica, Departamento de Engenharia Mecânica, 2001.

[13] E. J. Woo, P. Hua, J. G. Webster, and W. J. Tompkins, "Measuring lung resistivity using electrical impedance tomography," *IEEE Trans. Biomed. Eng.*, vol. 39, pp. 758–760, July 1992.
[14] T. J. C. Faes, H. A. vanderMeij, J. C. Munck, and R. M. deHeethaar, "The electric resistivity of human tissues (100 Hz–10 MHz): A meta-analysis of review studies," *Physiol. Meas.*, vol. 20, pp. R1–R10, 1999.
[15] W. Press, T. Vetterling, S. A. Teukolsky, and B. P. Flannery, *Numerical Recipes in C: The Art of Scientific Computing*. Cambridge , U.K.: Cambridge Univ. Press, 1992.
[16] A. T. Fleury, "Estimadores de Estado de Sistemas Dinâmicos Baseados no Conceito de Dualidade," Ph.D. thesis, Universidade de São Paulo, Escola Politécnica, Departamento de Engenharia Mecânica, 1985.
[17] P. Bertemes-Filho, B. H. Brown, and A. J. Wilson, "A comparison of modified Howland circuits as current generators with current mirror type circuits," *Physiol. Meas.*, vol. 21, pp. 1–6, 2000.
[18] W. L. Brogan, *Modern Control Theory*, 3rd ed. Upper Saddle River, NJ: Prentice-Hall, 1991.
[19] J. M. Holtzman, *Nonlinear System Theory—A Functional Analysis Approach*. Englewood Cliffs, NJ: Prentice-Hall, 1970.

Flávio Celso Trigo was born in São Paulo, Brazil, in 1961. He received the degree of mechanical engineer from the Polytechnic School, University of São Paulo in 1985, and a Master's degree in engineering from the Mechanical Engineering Department of the Polytechnic School in 2001. He is currently finishing the Ph.D. degree in the same institution.

His research interests include real-time parameter estimation through optimal techniques and its applications to impedance tomography, and modeling/simulation of biological systems.

Raul Gonzalez-Lima was born in Cuba on February 18, 1961. He received the degree of mechanical engineer in 1984 from the Polytechnic School, University of São Paulo, São Paulo, Brazil, and a Master's degree in engineering in 1990 from the same institution. In 1996, he received the Ph.D. degree from the Aerospace Engineering Department at the University of Texas at Austin.

He is an Assistant Professor in the Department of Mechanical Engineering, University of São Paulo since 1996, where he teaches courses on structural dynamics and system identification. His current research areas include parameter identification, dynamics and control of flexible structures, biomechanics, and biomedical inverse problems.

Marcelo Brito Passos Amato was born in São Paulo, Brazil, in 1962. He began medical studies in 1980 at the Faculdade de Medicina da Universidade de São Paulo, and graduated in December 1985. After graduating, he had a year of training in Internal Medicine and Intensive Care Medicine, as a resident doctor, followed by two years of specialization in pneumology and intensive care medicine at the Pulmonary Division of the Hospital das Clínicas—Medicine School, University of São Paulo. In 1996 he received the Ph.D. degree from the Medicine School, University of São Paulo.

Dr. Amato is the author of 19 papers and over 50 abstracts published in international journals. Since 1997, he is a reviser of original papers submitted to the *American Journal of Respiratory and Critical Care Medicine*, *Intensive Care Medicine*, and editor of the electronic journal *ATS Critical Care Website*. His research interests are effects of protective ventilation for the acute respiratory distress syndrome, hemodynamic effects of ideal PEEP on mechanical ventilation, analysis of pressure-volume curves and setting of ventilators using impedance tomography.

ANEXO J – Modelo de evolução Identificado

Dynamic Imaging in Electrical Impedance Tomography of the Human Chest with Online Transition Matrix Identification

Fernando Silva de Moura*, Julio Cesar Ceballos Aya, Agenor de Toledo Fleury, Marcelo Britto Passos Amato, Raul Gonzalez Lima

Abstract—**One of the electrical impedance tomography objectives is to estimate the electrical resistivity distribution in a domain based only on electrical potential measurements at its boundary generated by an imposed electrical current distribution into the boundary. One of the methods used in dynamic estimation is the Kalman filter. In biomedical applications, the random walk model is frequently used as evolution model and, under this conditions, poor tracking ability of the Extended Kalman Filter is achieved. An analytically developed evolution model is not feasible at this moment. The present work investigates the identification of the evolution model in parallel to the EKF and updating the evolution model with certain periodicity. The evolution model transition matrix is identified using the history of the estimated resistivity distribution obtained by a sensitivity matrix based algorithm and a Newton-Raphson algorithm. To numerically identify the linear evolution model, the Ibrahim Time Domain Method is used. The investigation was performed by numerical simulations of a domain with time varying resistivity and by experimental data collected from the boundary of a human chest during normal breathing. The obtained dynamic resistivity values lie within the expected values for the tissues of a human chest. The EKF results suggest that the tracking ability is significantly improved with this approach.**

Index Terms—**Electrical impedance tomography, Kalman filter, parameter estimation, evolution model, Ibrahim Time Domain Method**

I. Introduction

ELECTRICAL Impedance Tomography (EIT) is an imaging method of the resistivity distribution within a domain. The images are estimated from a set of electrical potential measurements at the boundary of a domain, which are caused by applying current through electrodes fixed at its boundary.

Electrical Impedance Tomography have a wide range of applications [1]. It may be used to detect internal hemorrhage and breast cancer, for instance. Examples of non-clinical applications are the visualization of multiphase flow, detection of minerals in the soil, soil pollution monitoring, and crack detection on mechanical components.

The application in mind in the present work is lung monitoring. Lung condition may change dramatically within few respiratory cycles in patients under mechanical ventilation in Intensive Care Units (ICU), as in pneumothorax occurrences [2], [3]. Furthermore, inadequate lung ventilation in ICUs may cause barothrauma or hypoxia.

One of the promises of EIT is the continuous monitoring of lung hyperdistension and/or collapse during daily changes in the parameters of mechanical ventilator [4]. In order to do so, EIT has to accurately track fast changes of lung impedance that occur within the breath. Another promising application of EIT is the detection of complications associated with risky procedures at the bedside, like the occurrence of pneumothorax during recruiting maneuvers[1]. Since conventional clinical parameters are insensitive to detect the initial formation of pneumothoraces, EIT could be of great help by tracking the sudden and localized changes in thoracic impedance happening under this circumstance.

Also, as already pointed out by [3] and [5], the information provided by absolute images could be of great help for any EIT algorithm of pneumothorax detection. In fact, the combination of absolute images, showing the localized increment in impedance, with fast tracking difference images, showing the regional decrease in alveolar ventilation, seems to be necessary for an ideal pneumothorax detector.

The EIT problem can be seen as a state observation problem within the control theory framework. Among several absolute EIT algorithms, the Extended Kalman Filters (EKF) have been investigated due to its ability to track the state of time varying non-linear systems. The EKF is a Bayesian estimation algorithm in the sense that it minimizes the conditional variance of the estimation error.

The first work that solves the EIT problem using the Kalman Filter to track temporal variations of resistivity is Vauhkonen's Ph.D. thesis [6]. In this work, the author implemented the linearized Kalman Filter to estimate the state, the resistivity distribution of a circular domain. Static algorithms, which do not take into account system dynamics, do not use information from past measurements. Kalman filters use past information through the time evolution equation and through covariance matrices.

In [7], the smoothing extension of the Kalman filter is implemented for estimating time-varying impedance distributions. They also discuss how to introduce prior spatial information

F. S. Moura, J. C. C. Aya, A. T. Fleury and R. G. Lima are with the Department of Mechanical Engineering, Polytechnic School, University of São Paulo, 05508-900, São Paulo, Brazil. (e-mail: fernandosmoura@gmail.com)

M. B. P. Amato is with the Respiratory Intensive Care Unit, School of Medicine, University of São Paulo, São Paulo, Brazil.

The authors are grateful for the financial aid from The State of São Paulo Research Foundation, processes 01/05303-4, 05/01088-2, 07/04069-4, and 08/07150-0.

[1]Recruiting maneuvers are temporary use of high pressures during 1-2 minutes, applied through the mechanical ventilator, and intended to recruit a large population of previously collapse alveoli.

in the state space formulation. The authors argue that without the need of online estimations, the filter can use past and future measurements.

The resistivity spatial resolution decreases if the choice of the reference state for the linearization, in the linearized Kalman Filter, is far from the real state. To minimize this problem, in [8] the EKF was implemented. The advantage of EKF is that the linearization is performed at every step, using the last state estimation as reference. One disadvantage of the EKF is the increase of computational time due to the Jacobian matrix computation at every time step. The Tikhonov regularization was used in this work and they show that EKF has better spatial resolution and smaller position errors of objects than the linearized version. In [9], prior information about subregions with known resistivity is included. The results show that the prior information improved tracking ability of EKF.

In [2] and [10], the electrode contact resistivities and the domain resistivity distribution were estimated using the EKF in two phases. In the first phase skin/electrode contact impedance is estimated while the domain resistivity is not updated. In the second phase the domain resistivity is estimated while the skin/electrode contact impedances are not updated. The tracking ability was improved since each EKF was adjusted independently.

The EKF requires a state evolution model. All of the above cited works adopted the *Random Walk* as state evolution model. However, poor tracking ability of the Kalman filters resulted for lung monitoring applications. In [11], a procedure called Interacting Multiple Model, which uses three EKFs running in parallel, was implemented. Each EKF was running with different evolution models, namely, Random Walk, First Order and Second Order. The three resulting images were weighted at the end of the iteration according to a probabilistic criterion.

The present work investigates whether the tracking ability of EKF is improved if the evolution model is frequently estimated using images obtained by a sensitivity matrix algorithm. Once a set of images obtained from the sensitivity matrix algorithm is available, the transition matrix of the evolution model is estimated by the Ibrahim Time Domain Method (ITD) [12], [13]. A preliminary version of this work has been reported [14].

II. Theoretical Background

A. The Problem Formulation

Considering the domain a closed region Γ, with a stationary charge distribution, pure isotropic resistivity media $\rho(x,y)$ and excited by a steady current flow, one can describe the electrical potential $\Psi(x,y)$ in Γ by the generalized Laplace's equation

$$\nabla.(\frac{1}{\rho}\nabla\Psi) = 0, \tag{1}$$

with the following Neumann boundary condition at $\partial\Gamma$ and complete electrode model [15]

$$\int_{\partial\Gamma_{e_i}} \frac{1}{\rho}\frac{\partial\Psi}{\partial\hat{n}}dA = J_i, \quad \text{on the } i\text{-th electrode} \tag{2}$$

$$\frac{1}{\rho}\frac{\partial\Psi}{\partial\hat{n}} = 0, \quad \text{elsewhere in } \partial\Gamma \tag{3}$$

$$\Psi + z_i\frac{1}{\rho}\frac{\partial\Psi}{\partial\hat{n}} = v_i, \tag{4}$$

where $\partial\Gamma_{e_i}$ is the part of the boundary under the i-th electrode[2], $i = 1,\ldots,e$, $\hat{n}$ is the $\partial\Gamma$'s external normal versor, J_i is the injected current, z_i is the skin-electrode interface impedance and v_i is the measured potential.

The *direct problem* solution is obtained when one knows $\rho(x,y)$ and J_i and finds $\Psi(x,y)$. The *inverse problem* solution is obtained when one finds $\rho(x,y)$ that caused known (measured) v_i with known J_i. In practice only a finite number of electrical potential measurements is made through the electrodes, so the Dirichlet boundary condition is incomplete.

In EIT, we are interested in the inverse problem. A common way to solve the inverse problem is by using algorithms that solve a sequence of associated direct problems, since an analytical solution for the inverse problem, when shape of the boundary is arbitrary, is unknown. Unfortunately, the operator associated to the problem is ill-posed.

In this paper, the partial differential equations were approximated by the Finite Elements Method (FEM) and the domain was discretized with triangular linear elements[3] with constant resistivity. The direct problem solution is found by

$$\boldsymbol{v}^j_{\partial\Gamma} = [\boldsymbol{Y}(\boldsymbol{\rho})]^{-1}\boldsymbol{c}_j, \tag{5}$$

where $\boldsymbol{c}_j$ is the j-th current pattern injected ($j = 1,\ldots,p$), $\boldsymbol{Y}(\boldsymbol{\rho})$ is the global conductivity matrix, $\boldsymbol{\rho}$ is a vector containing the finite elements resistivities and $\boldsymbol{v}^j_{\partial\Gamma} \in \mathbb{R}^e$ is the nodal electrical potentials on the nodes which represent the electrodes[4], for more information see [16], [17], [10].

In this paper, the j-th current pattern is composed by a injecting electrical current through a pair of electrodes, following the rule

$$J_i = \begin{cases} +C & , \quad i = j \\ -C & , \quad i = mod(j+3,32)+1 \end{cases}, \tag{6}$$

where C is a scalar value.

B. The Extended Kalman Filter

The Kalman Filters are state space stochastic observers. The state in the present work is a vector composed by the the resistivity of each finite element of the domain. Therefore, the following equations describe the linearized observation model and the discrete time evolution model of the system

$$\boldsymbol{v}_k(\boldsymbol{\rho}_k) = \boldsymbol{v}_k(\boldsymbol{\rho}_{k|k-1}) + \boldsymbol{H}_k[\boldsymbol{\rho}_k - \boldsymbol{\rho}_{k|k-1}] + \boldsymbol{\nu}_k \tag{7}$$

$$\boldsymbol{\rho}_{k|k-1} = \boldsymbol{\Phi}_{k-1,k}\boldsymbol{\rho}_{k-1} + \boldsymbol{\omega}_k, \tag{8}$$

[2]The electrodes are numbered in clockwise order along the boundary of the domain cross section.

[3]Triangular elements represent pentahedrical volumes in the present work.

[4]In fact, the solution is obtained for all nodes and only the nodes of interest are assembled in this last vector.

where $\Phi_{k-1,k}$ is the evolution model's transition matrix, $v_k \in \mathbb{R}^{e \cdot p}$ is a vector composed by the measurements at each electrode for all current patterns, H_k is the observation matrix[5] linearized about the last propagated state $\rho_{k|k-1}$

$$v_k = \begin{Bmatrix} v^1_{\partial\Gamma} \\ \vdots \\ v^p_{\partial\Gamma} \end{Bmatrix}, \quad H_k \triangleq \left[\begin{matrix} \frac{\partial v^1_{\partial\Gamma}}{\partial \rho} \\ \vdots \\ \frac{\partial v^p_{\partial\Gamma}}{\partial \rho} \end{matrix} \right]_{\rho=\rho_{k|k-1}}, \quad (9)$$

ω_k and ν_k are uncorrelated zero-mean Gaussian white noises with covariance matrices Q_k and R_k respectively. The random variables in these equations take into account model uncertainties, including domain shape variations and modeling errors.

It is convenient to define a nominal measurement

$$z_k^{meas.} \triangleq v_k^{meas.} - v_k(\rho_{k|k-1}) + H_k \rho_{k|k-1}, \quad (10)$$

where $v^{meas.}$ is the recent measurement vector at each electrode for all current patterns, so the observation model can be written in standard form

$$z_k(\rho_k) = H_k \rho_k + \nu_k, \quad (11)$$

and the discrete time EKF for $t = kT_s$, $k = 1, 2, \ldots$ can be described by the well known set of equations

$$\rho_{k|k-1} = \Phi_{k-1,k}\rho_{k-1} \quad (12)$$

$$P_{k|k-1} = \Phi_{k-1,k}P_{k-1}\Phi^T_{k-1,k} + Q_{k-1} \quad (13)$$

$$G_k = P_{k|k-1}H_k^T[H_k P_{k|k-1} H_k^T + R_k]^{-1} \quad (14)$$

$$r_k = z_k^{meas.} - H_k\rho_{k|k-1} = v_k^{meas.} - v_k(\rho_{k|k-1}) \quad (15)$$

$$\rho_k = \rho_{k|k-1} + G_k r_k \quad (16)$$

$$P_k = [I - G_k H_k]P_{k|k-1} \quad (17)$$

where (12) and (13) represent the time propagation phase and (14) to (17) represent the update phase [11]. The vector ρ is the state vector, P is the estimation error's covariance matrix, r is called observation residue and G is the Kalman gain matrix.

C. Observation Model for Experimental Data

Even with the complete electrode equations and with a fine mesh, the finite element forward problem solution, given by (5), will be slightly different from the real data collected by an experimental tomograph with the same geometry and resistivity distribution due to simplified modeled phenomena and hardware nonlinearities. This difference is more evident at electrodes that inject current and measure electrical potentials at the same time. Therefore, the observation model is further modified for this case. The intention here is to obtain a close to zero mean random noise.

Let $v_{ref.}^{meas.}$ be a set of measurements collected from an experimental tomograph, and assume the resistivity distribution ρ_{ref} is known for a while. Also, let $v_{ref.}^{comp.}$ be a set of electrical potentials obtained by solving the forward problem (5), using the same reference resistivity distribution, which must be properly converted to the discrete mesh. It is convenient to define the *model-experiment discrepancy* by

$$\varepsilon(\rho_{ref}) = v_{ref.}^{meas.} - v_{ref.}^{comp.}, \quad (18)$$

which can be understood as a persistent bias between the real measurements and the observation model. This discrepancy can be considered as the mean of the observation noise ν_k, provided ρ_{ref} remains stable during a complete observation interval. Using this hypothesis, one can define a new random variable $\zeta_k = \nu_k - \varepsilon(\rho_{ref})$, which is near zero-mean noise. Substituting into (11), the observation model becomes

$$z_k(\rho_k) = H_k\rho_k + \zeta_k + \varepsilon(\rho_{ref}). \quad (19)$$

This equation now is in closer agreement with the hypothesis of zero-mean noise used to develop the set of equations (12) to (17). With this model, the observation residue becomes

$$\begin{aligned} r_k &= z_k^{meas.} - (H_k\rho_{k|k-1} + \varepsilon(\rho_{ref})) \\ &= v_k^{meas.} - \varepsilon(\rho_{ref}) - v_k(\rho_{k|k-1}). \end{aligned} \quad (20)$$

D. The Evolution Model

The EKF requires a transition matrix $\Phi_{k-1,k}$, which is part of the state evolution model. The usual model used in EIT is the random walk, which is given by $\Phi_{k-1,k} = I$, the identity matrix. Using this model, (8) becomes

$$\rho_k = \rho_{k-1} + \omega_k, \quad (21)$$

implying in a purely random behavior along the time. This model tends to slow the Kalman filter convergence.

In this paper, the dynamics of ventilation and perfusion inside the thorax will be represented by a second order homogeneous set of ordinary differential equations (ODEs).

$$M\ddot{\rho}(t) + C\dot{\rho}(t) + K\rho(t) = 0 \quad (22)$$

The evolution model required in Kalman filters is a set of first order ODEs. Therefore, the size of the state must be duplicated, which means that the state vector for the remaining of this work have dimension $2n$, where n is the number of finite elements representing the domain, and will be denoted by $\hat{\rho}$.[6]

$$\frac{d\hat{\rho}}{dt} = A\hat{\rho}(t) \quad (23)$$

$$A = \begin{bmatrix} 0 & I \\ -M^{-1}K & -M^{-1}C \end{bmatrix}, \quad \hat{\rho}(t) = \begin{bmatrix} \rho(t) \\ \dot{\rho}(t) \end{bmatrix} \quad (24)$$

The transition matrix is estimated in this paper through the Ibrahim Time Domain Method (ITD). A detailed description is out of our scope, however it can be found in [18], [12], [13].

The transition matrix can be computed using

$$\Phi_{k,k+1} = X^+(X^{-1}), \quad (25)$$

[5]The observation matrix is obtained by adjoining the Jacobian matrix of the nonlinear equation (5), for each current pattern c_j. For details, see [16], [11].

[6]It is worth to point that the Kalman filter equations will also have its matrices and vectors augmented to take into account the state augmentation.

where $\boldsymbol{X}$ consists of a time increasing sequence of state vectors, from discrete time k_1 to discrete time k_1+m-1 and $\boldsymbol{X}^+$ consists of a time increasing sequence of state vectors, from discrete time k_1+1 to discrete time k_1+m.

$$\boldsymbol{X} = \left[\begin{array}{cccc} \hat{\rho}_{k_1} & \hat{\rho}_{k_1+1} & \cdots & \hat{\rho}_{k_1+m-1} \end{array} \right] \quad (26)$$

$$\boldsymbol{X}^+ = \left[\begin{array}{cccc} \hat{\rho}_{k_1+1} & \hat{\rho}_{k_1+2} & \cdots & \hat{\rho}_{k_1+m} \end{array} \right] \quad (27)$$

$$\hat{\rho}_{k_1} = \left[\begin{array}{c} \rho_{k_1} \\ \rho_{k_1+1} \end{array} \right]. \quad (28)$$

In practice, it is recommended to use $m > 2n$ augmented state vectors to form a least square solution. For this solution, a pseudo-inverse of $\boldsymbol{X}$ is required and a Tikhonov regularization is also necessary [18], [19]. The transition matrix Φ is estimated according to the regularized least square solution

$$\Phi = (\boldsymbol{X}^+\boldsymbol{X}^T)(\boldsymbol{X}\boldsymbol{X}^T + \alpha\boldsymbol{I})^{-1}, \quad (29)$$

where α is the Tikhonov regularization parameter and $\boldsymbol{I}$ is the identity matrix.

For the sequence of absolute images $\boldsymbol{\rho}_k$, a sensitivity matrix algorithm was used [20] and the absolute images were approximated through the addition of the resistivity distribution used for the Taylor series expansion. The sensitivity matrix images are underestimated (see [21] sec. 1.13), but the method is robust, gives good localization of the objects with time varying resistivity and, therefore, are used to estimate the transition matrix. A Gaussian high pass filter was used as regularization. The images resulting from EKF could also be used to compute the transition matrix, but they take a longer time to become informative.

With a certain periodicity, a new transition matrix can be estimated in parallel with the EKF estimation. The periodicity is problem dependent. In the present work, the transition matrix is estimated only once.

III. Methods

A. Numerical Simulation

A finite element numerical phantom comprising a $300mm$ diameter cylindrical domain, $n = 6082$ linear triangular elements, $e = 32$ electrodes, $p = 32$ current patterns and a $40mm$ diameter cylindrical object was developed. The object, which has time varying resistivity, was placed in two positions: at the center of the domain and $126mm$ distant from the center of the domain.

Two different functions were used to represent the time varying resistivity of the object. The first function, a ramp, was used to generate the sequence of voltages $\boldsymbol{v}_k$, in discrete time $k = 0, \ldots, 1500$, that will result in a sequence of images obtained by the sensitivity matrix algorithm [20], which will comprise the input data for ITD.

$$\rho_{object\,(k)} = \left\{ \begin{array}{lll} 35.0 & , & k \leq 0 \\ \frac{10}{50}k + 35.0 & , & k > 0 \end{array} \right. \quad \Omega.m \quad (30)$$

$$\rho_{elsewhere} = 35.0\Omega.m. \quad (31)$$

The second function, a step function, at $k = 0$ was used to generate the sequence of voltages that EKF will use as measurements.

$$\rho_{object\,(k)} = \left\{ \begin{array}{lll} 35.0 & , & k < 0 \\ 100.0 & , & k \geq 0 \end{array} \right. \quad \Omega.m \quad (32)$$

$$\rho_{elsewhere} = 35.0\Omega.m. \quad (33)$$

With these two different functions, the EKF has to estimate a step function using a transition matrix of a ramp function. The ramp function was chosen due to its smooth behavior. Gaussian noise was added to the electrical potential measurements.

Another finite element mesh comprising a $300mm$ diameter cylindrical domain, $n = 514$ linear triangular elements and 32 electrodes was used in the sensitivity matrix algorithm and in the EKF. This mesh is substantially less refined than the one used in the forward problem solution. These two meshes were used to avoid inverse crime [22] and to reduce the size of the state vector in the inverse problem.

Kalman filters require initial data about resistivity and measurement errors. Examples of the initialization of Kalman Filters in EIT are found in [6], [2], [10]. The procedure to adjust the EKF parameters was done adjusting one parameter at a time. The initial uniform resistivity $\rho_0 = 60\Omega m$ was chosen on purpose to overestimate the real resistivity. The initial estimation error covariance matrix was chosen such that $\boldsymbol{P}_0 = 10^1\boldsymbol{I}$.

The Kalman gain matrix $\boldsymbol{G}$ is influenced by errors in $\boldsymbol{H}$ due to wrong linearization states. Therefore, a relaxation factor γ_k was used in (14) according to

$$\boldsymbol{G}_k = \gamma_k(\boldsymbol{P}_{k|k-1}\boldsymbol{H}_k^T[\boldsymbol{H}_k\boldsymbol{P}_{k|k-1}\boldsymbol{H}_k^T + \boldsymbol{R}_k]^{-1}), \quad (34)$$

where γ_k is a relaxation factor defined by

$$\gamma_k = \left\{ \begin{array}{lll} 0.1 & , & k < 5 \\ 0.5 & , & k < 8 \\ 1.0 & , & k \geq 8 \end{array} \right. , \quad (35)$$

to avoid large oscillations of the initial state updates. The authors are aware that $\gamma < 1.0$ will result in a suboptimal update on the first seven iterations but it is worth to use since in the first iterations the $\boldsymbol{H}$ matrix will be computed using a resistivity far form the real resistivity distribution and these first updates can generate strong oscillations in the estimate state.

In this work, $\boldsymbol{R}_k$ is a time invariant matrix, given by $\boldsymbol{R} = \beta\boldsymbol{I}$, where β must be adjusted. By using a diagonal structure, we are admitting uncorrelated measurements. The β parameter was adjusted taking into consideration the *normalized observation residue* statistics as an index of performance. This index is based on [2] and [10]. In this paper, it is given by

$$\bar{r}_k = \frac{1}{e.p}\sum_{i=1}^{e.p}\frac{r_{ik}}{\bar{\sigma}_i}, \quad (36)$$

where r_{ik} is the i-th element of the observation residue vector, given by (15) and $\bar{\sigma}_i$ is the total standard deviation of the observation uncertainty used as normalizing factor. In [2] and [10] the normalizing factor used was the standard deviation of the measurement noise. However, this uncertainty is not only

caused by the measurement noise but also by the observation model errors. Modeling errors in the observation equation effectively increases R [6]. For the simulations, $\bar{\sigma}_i = \sqrt{R_{ii}}$, which takes also into account the observation model errors. It is considered a satisfactory statistical convergence if $E(\bar{r}_k) = 0$, at least within a moving average window, and $\mid \bar{r}_k \mid \leq 3$ within the same moving average.

Matrix Q_k was updated following the rule

$$Q_k = \begin{cases} \lambda P_k^{(+)} & , \ 0 \leq k \leq 3 \\ Q_{k-1} & , \ k > 3 \end{cases} , \tag{37}$$

to keep the filter open to new information [23]. The λ parameter was adjusted taking in account the estimated state evolution and the quantity of artifacts on the images. A reduction of Q_k causes reduction of the tracking ability of EKF and increases the spatial resolution.

B. Experimental Data

In order to test the proposed method, data collected from a volunteer were used. EIT data were acquired using the impedance tomograph Enlight (Dixtal, São Paulo, Brazil), using 32 electrodes. The current pattern is the same of (6) and the equipment has a signal noise ratio of 80dB. The data was collected from a normal male volunteer, without records of previous lung disease or smoking habits, and presenting a normal radiograph. The volunteer was upright during data collection, quietly breathing, with the electrodes placed at the level of the thoracic plane crossing the 5th intercostal space. For each current pattern ($p = 32$ and $C = 5mA$ peak-to-peak at $125kHz$), differential potentials were measured. Considering all current patterns, 1024 measurements were obtained, composing the measurement vector $v_k^{meas.}$. Each vector took 0.02 seconds to be measured in the hardware[7]. The sampling interval of the experiment is $T_s = 0.02s$. A 2D finite element mesh with 469 linear triangular elements was built, with shape and size similar to the cross section of the volunteer's thorax.

Using the sensitivity matrix algorithm, 1700 measurement vectors were used to generate the transition matrix. The initial resistivity guess used in the sensitivity matrix algorithm was a uniform resistivity $\rho^0 = 4.0\Omega.m$. With these images, the transition matrix was estimated with (29), using $\alpha = 0.001$. Due to the damping effect of Tikhonov regularization, the transition matrix computed was further adjusted by removing the damping factor, without changing the frequency. This can be done by converting its eigenvalues z to continuous time by $s = \ln(z)/T_s$, removing the damping by $s' = sign(imag(s)) \mid s \mid i$ (i is the imaginary unit) and converting back to discrete time by $z' = exp(s'T_s)$. Not all eigenvalues were modified, but just those with $\mid z \mid > 0.98$. For these data, 14 eigenvalues were modified.

The reference resistivity ρ_{ref} must be known to estimate ϵ using (18). Since the resistivity distribution inside the thorax is unknown, the reference resistivity was considered to be the resistivity that minimizes the cost function

$$IP = \|\bar{v}^{meas.} - v^{comp.}(\rho)\|_2^2 + \eta \|L(\rho)\|_2^2 \tag{38}$$

$$\bar{v}^{meas.} = \frac{1}{200} \sum_{k=1}^{200} v_k^{meas.}, \tag{39}$$

where L is a high pass Gaussian filter and η is a regularization parameter and $\bar{v}^{meas.}$ is the mean measurement vector of the first 200 measurements. This number was chosen because this was the period of one ventilation cycle in the experiment. The Gauss-Newton algorithm was used in this minimization [16], with $\eta = 6.0 \times 10^{-5}$.

The Kalman filter was adjusted following the same guidelines. The chosen parameters are: $\rho_0 = \rho_{ref}$, $P_0 = 10^{-3}I$, $\lambda = 10^{-4}$, γ_k is the same of (35) and R is a diagonal matrix, with each element being ten percent of the total signal variance.

IV. Results and Discussion

A. Results from the Numerical Simulation

The results will be presented in three parts. The first part shows the estimation of the evolution model, the second part shows the state estimation using the EKF and the third part shows a comparison with the random model.

There are four sets of measurement data $v_k, k = 1, \ldots, 1500$. Two measurement data use the ramp function, one with the object at the center and one with the object off the center. The other two data use the step function, one with the object at the center and one with the object off the center.

1) Part 1: Estimation of the Evolution Model: The sensitivity matrix algorithm was used to generate resistivity distribution images using the measurement data of the object at the center and off the center, both with the ramp function. The initial resistivity guess used in the algorithm was a uniform resistivity $\rho^0 = 35.0\Omega.m$. The chosen regularization parameter for the high pass Gaussian filter in sensitivity matrix algorithm was $\alpha_h = 0.01$, following the criterion described in [20]. With these images, the transition matrices were estimated with (29).

Fig. 1(a) shows the time history of two finite elements taken from the medium region and from the object region, using the estimated transition matrices. They were chosen because they lie inside the object and medium areas respectively. The objects resistivities became smaller than the true resistivities after $k = 708$.

There is also an asymptotic behavior toward a limit resistivity in the estimation. It is caused by the finite precision measurements and the nonlinearity between electrical potential changes and resistivity changes in the object, when there is a large resistivity contrast between object and medium. This behavior is caused by the sensitivity matrix algorithm and not by the ITD method.[8]

[7]Since the hardware generates 50 sets of measurements per second, odd frames can be used for running the Kalman filter, while even frames are being used to estimate a new transition matrix. The periodicity of updating the transition matrix is limited only by the ITD method.

[8]This saturation is due to the fact that if the object has high resistivity compared to the medium resistivity, the electrical current density inside the object is small and further increases of resistivity inside the object will not change the electrical current distribution sufficiently to be measured at the electrodes with finite precision. This asymptotic limit depends on the position of the object relative to the electrodes and the difference between the medium and the object resistivities. See [21] section 1.2.

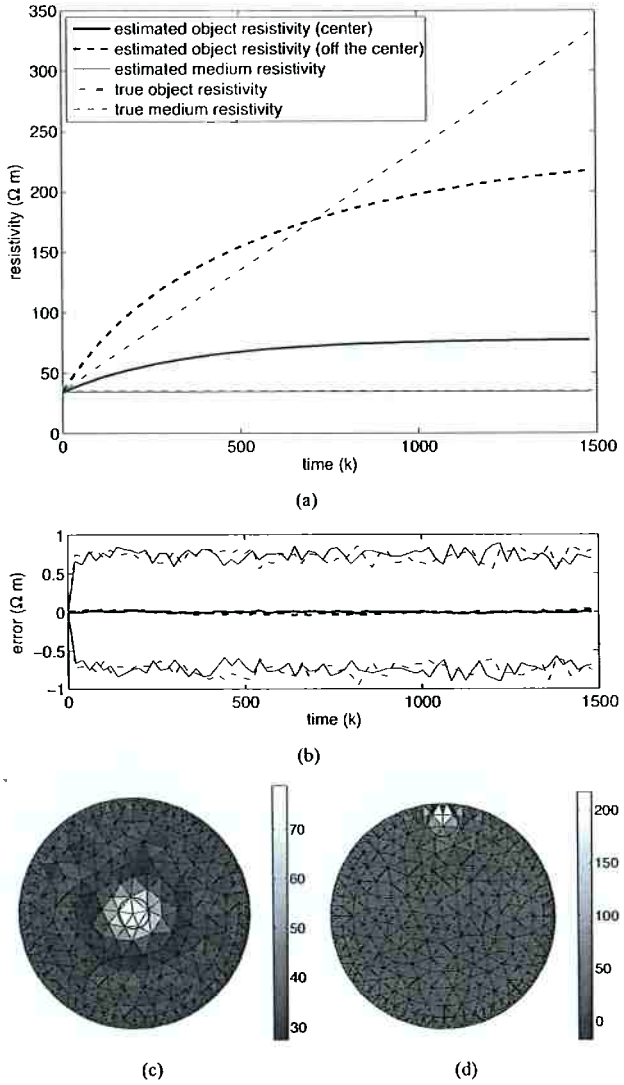

Fig. 1. (a) Time history of the evolution model compared with the time history of the true state; (b) Mean difference between the state evolution using the input data for the ITD and the state evolution using the transition matrix computed with the ITD method. The graph shows the mean difference in thick lines and the mean plus or minus one standard deviation in thin lines. Continuous lines represent the object off the center and dashed lines represent object at the center. (c) Estimated state at $k = 1500$ with object at the center; (d) Estimated state at $k = 1500$ with object off the center. Values in $\Omega.m$.

Since a regularization was used to estimate the transition matrix, the input data to the ITD and the state history computed by the transition matrix were compared to avoid excessive regularization. They have small differences, as can be seen in Fig. 1(b) which shows the mean difference between the state history given as input data for the ITD method and the state history computed by the transition matrix. This difference index is given by

$$e_k = \rho_k^* - \rho_k, \tag{40}$$

where k is the discrete time, ρ^* is the input image for the ITD and ρ is the image obtained from the transition matrix calculated by ITD.[9] The mean difference and its standard deviation are given by the usual equations

$$\bar{e}_k = \frac{1}{n}\sum_{i=1}^{n} e_{ik} \tag{41}$$

$$\sigma_{e_k} = \sqrt{\frac{1}{n-1}\sum_{i=1}^{n}(e_{ik} - \bar{e}_k)^2}. \tag{42}$$

where n is the size of e_k.

Fig. 1(c) and Fig. 1(d) show the state at $k = 1500$ using the estimated transition matrix. The circle marks the correct object location and size. The transition matrix was computed using the regularization parameter $\alpha = 1.0$ to avoid instabilities in the state evolution. Smaller values of α generated unstable transition matrices in our tests.

The model used in this work is a discrete time second order system with n degrees of freedom, so each pair eigenvalue-eigenvector represents one mode of the evolution. Each mode has a damping factor that depends on the magnitude of its eigenvalue. If the magnitude is smaller than one, the mode is stable, if the magnitude is one, the mode is critically stable, if the magnitude is greater than one the mode is unstable. Considering magnitudes smaller than one, the smaller magnitude, the faster the associated mode disappears as time passes.

Fig. 2(a) shows the magnitude plot of the transition matrix's eigenvalues for two different values of Tikhonov regularization parameter α, with the object off the center. All eigenvalues have magnitudes smaller or equal one, configuring a stable system. Increasing α, most of the eigenvalues have their magnitudes reduced, which increases the damping. The eigenvalues with magnitudes close to the unit are not heavily influenced by α.

The dominant modes, those with larger eigenvalues in z plane, have eigenvalues close to the real axis at 1.0 in the complex plane and their associated eigenvectors represent the position of the object, according to Fig. 2(b) to Fig. 2(e). The correlation between the eigenvectors and the most recent image was computed using the Modal Assurance Criterion (MAC) [18] revealing that only the first three eigenvectors have high correlation, $MAC > 0.5$, with the most correct image. These three modes are the same modes that are associated with the most insensitive eigenvalues to the Tikhonov regularization parameter α changes. This result indicates that the Tikhonov regularization helps to remove only the unimportant modes. Very similar results were observed when the object is located at the center of the domain.

2) Part 2: State Estimation: The second part shows the EKF state estimation using computed electrical potentials measurements in agreement with the step change of resistivity and the estimated transition matrix.

The chosen value for β with the object off the center was $\beta = 10^{-4}$, since bigger values slowed down the convergence and smaller values increased the estimation noise. However, with the object at the center, the tracking ability could be

[9]Note that these images are not augmented images $\hat{\rho}$, so they belong to $\mathbf{R}^n$.

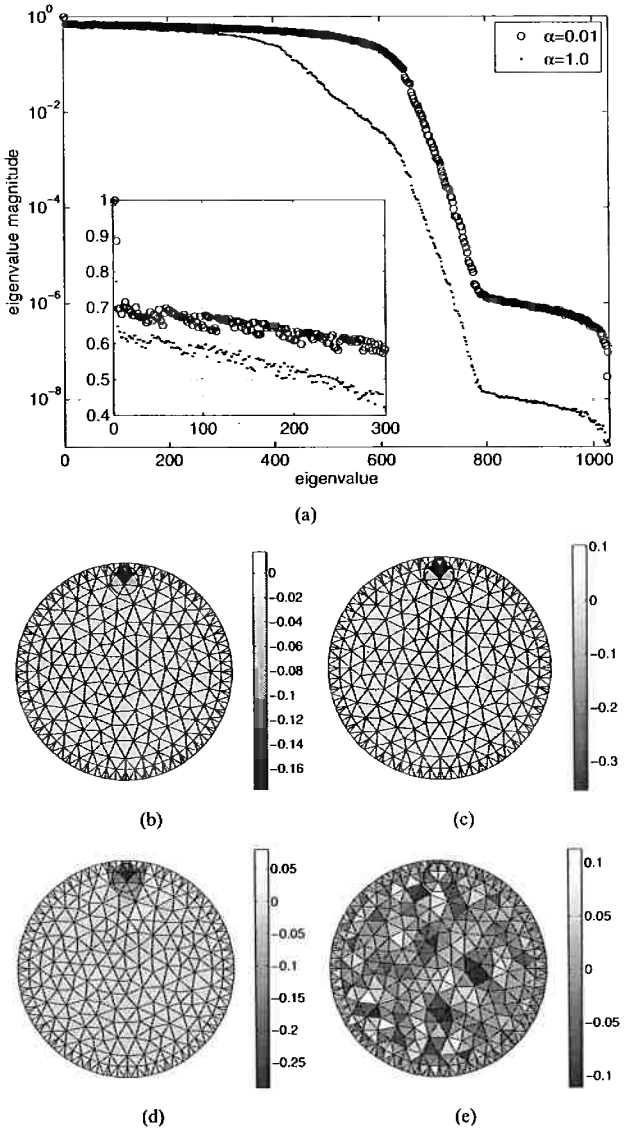

Fig. 2. (a) Eigenvalue magnitude plot of matrix Φ with object off the center for two different Tikhonov regularization parameter. The smaller plot is a detail of the first 300 eigenvalues; (b) eigenvector with eigenvalue magnitude 1.0; (c) eigenvector with eigenvalue magnitude 0.998; (d) eigenvector with eigenvalue magnitude 0.993; (e) eigenvector with eigenvalue magnitude 0.772.

improved. The chosen value for the estimation with the object at the center was $\beta = 10^{-6}$.

The chosen value for λ with the object off the center was $\lambda = 10^{-5}$, since this allowed a good trade-off between tracking ability and spatial resolution. Fig. 3 shows the estimated state history and the normalized observation residue for the data with the object off the center, Fig. 4 shows the same graphs for the data with the object at the center and Fig. 5 shows the estimated state at $k = 300$ using the chosen parameters for each object position. One can note the faster convergence when the object is at the center due to the reduction of R_k.

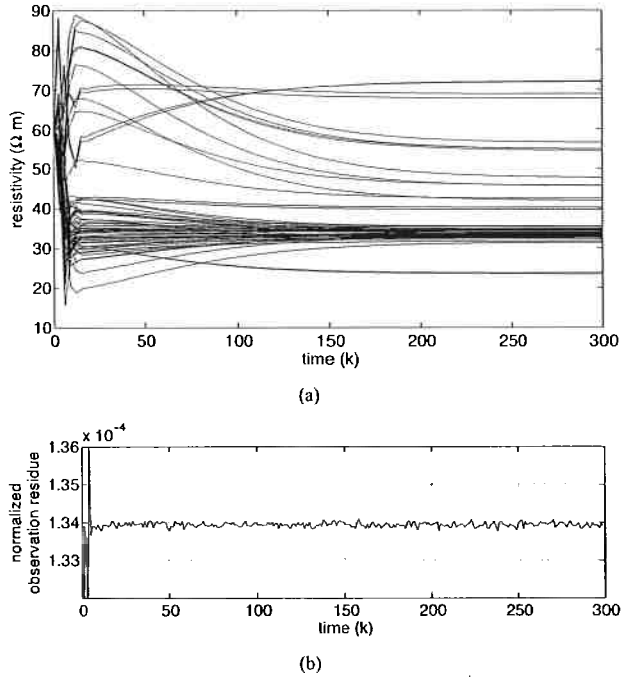

Fig. 3. Estimation using the EKF for the object off the center. (a) State history; (b) Normalized observation residue.

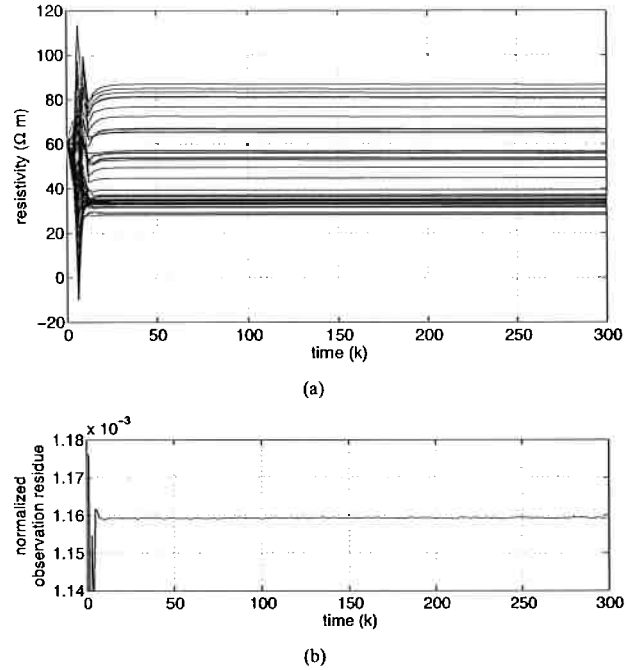

Fig. 4. Estimation using the EKF for the object at the center. (a) State history; (b) Normalized observation residue.

3) Part 3: Comparison with the Random Walk Evolution Model: In this subsection the performance of EKF using the Random Walk Model is presented. Fig. 6 shows the state history, the observation residue and the state at iteration

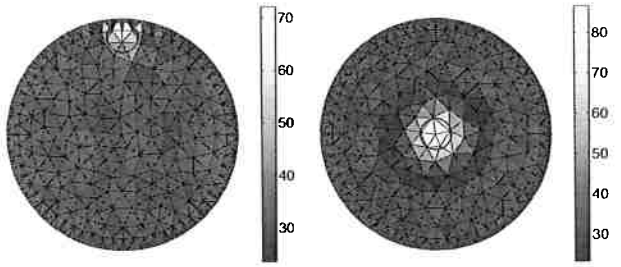

(a) (b)

Fig. 5. Estimated state at $k = 300$. Values in $\Omega.m$. (a) Object off the center; (b) Object at the center. The circles mark the correct object locations and sizes

$k = 800$ for the two different object positions with the Random Walk model. The object was not visible at the center although the observation residue lies within three standard deviation range. It can be observed that there are many artifacts in both images.

The convergence of EKF with the ITD estimated evolution model when the object was at the center of the domain happened after 25 iterations and when the object was off the center happened after 200 iterations. The convergence of EKF with the Random Walk evolution model when the object was at the center of the domain occurred after 800 iterations and when the object was off the center did not happened within 800 iterations. The tracking ability was accelerated 32 times by the use of the ITD estimated evolution model when the object was at the center of the domain and more than 4 times when the object was off the center of the domain.

B. Results from the Experimental Data

In order to make resistivity changes more visible in the results, a mean resistivity distribution was computed by $\bar{\rho} = E\{\rho_k\}$, $k = 0, \ldots, 1700$ and was subtracted from each estimated state. The mean image is shown in Fig. 7(a), which clearly shows the ribcage and the vertebral column. The estimated resistivity values are in accordance with [24] at $125kHz$, namely, deflated lung $3.63\Omega.m$, inflated lung $9.17\Omega.m$, bone (cortical) $47.93\Omega.m$, bone (cancellous) $11.89\Omega.m$, heart $4.50\Omega.m$, fat $40.87\Omega.m$ and muscle $2.72\Omega.m$.

Fig. 7(b) and Fig. 7(c) show the time history of the estimated resistivity variation around the mean image using the EKF with the transition matrix and the noise model proposed in this work in the lung region and outside the lung region. The oscillation phase and period match with the volunteer breathing. The maximum estimated resistivity variation in the lung region is about $1.1\Omega.m$, that is smaller than the results of [24], which is about $5.5\Omega.m$. A smaller variation was indeed expected since the volunteer was upright during the data acquisition and, at this position, the weight of upper part of the lungs tends to compress the lower part, increasing the resistance of the lower part to inflate. The 5th intercostal space, which is the electrodes location in the experiment, is located near the lower part, therefore inflation of this region is smaller than the upper part and the resistivity variation is smaller. Fig. 7(d) and Fig. 7(e) show the estimated resistivity distribution changes at different moments of one ventilation cycle. The resistivity changes in these images match with the lungs positions.

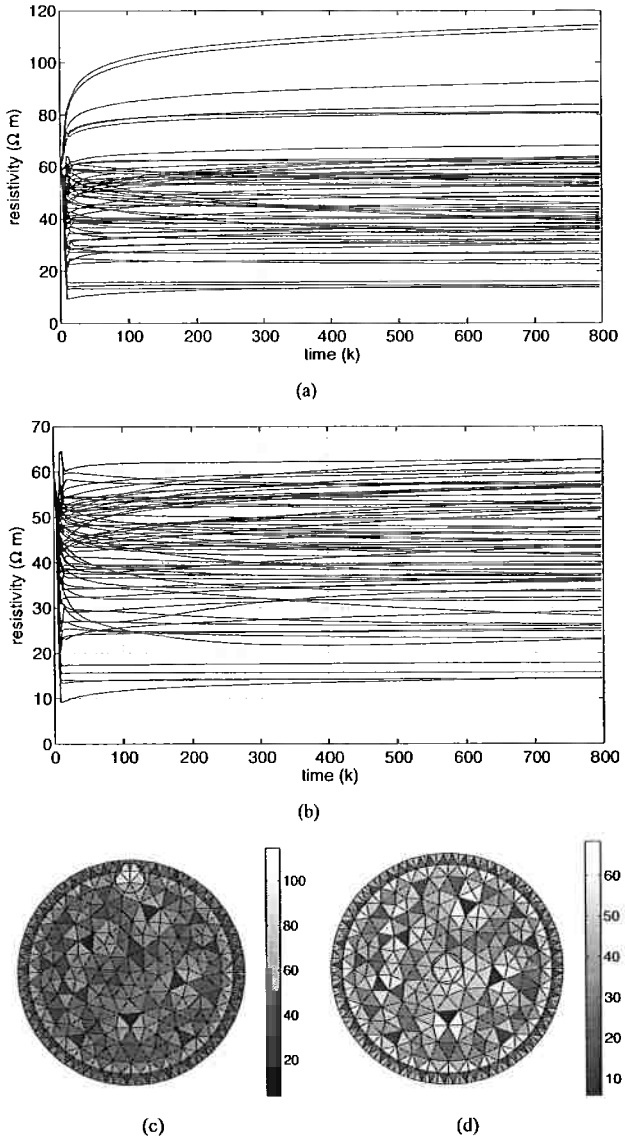

Fig. 6. Results using the Random Walk model in EKF. Values in $\Omega.m$. (a) State history, object at the center; (b) State history, object off the center; (c) Estimated state at $k = 800$, object at the center; (d) Estimated state at $k = 800$, object off the center.

V. Conclusion and Final Comments

The results show that the ITD method can be used to estimate the evolution model based on a sequence of images obtained by a sensitivity matrix and a Newton-Raphson algorithms. Although the resistivity distribution obtained by the sensitivity matrix algorithm is underestimated, the tracking ability of the EKF was improved when compared to the use of the Random Walk model as the evolution model. The Kalman

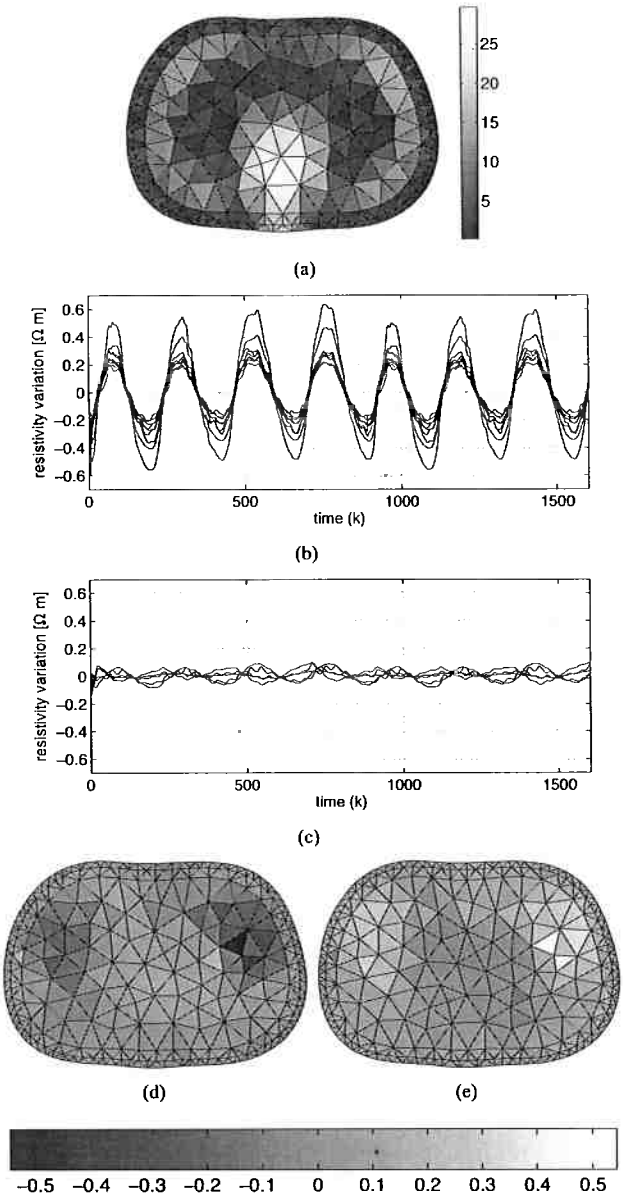

Fig. 7. (a) Mean image obtained with the estimated state vector history. Values in $\Omega.m$; (b) Estimated resistivity history of representative elements of the lungs using the EKF with the noise model and the ITD transition matrix; (c) Estimated resistivity history of representative elements of the other regions using the EKF with the noise model and the ITD transition matrix; (d) Estimated state at $k = 200$. Values in $\Omega.m$; (e) Estimated state at $k = 300$.

Filter is a state observer in Control Theory and should have tracking speed higher than the phenomenon being observed.

The computational effort to implement the direct identification of the transition matrix seems to be justified since the tracking ability improved approximately thirty two times when the object was at the center and more than four times when the object was near the boundary of a cylindrical phantom.

The finite element method used in the observation model can cause persistent bias in the computed measurements due to discretization and skin-electrode contact problems. By subtracting from ν the model-experiment discrepancy, which is the difference of time averaged measurements and computed potentials, the image qualitatively improved considerably.

This is an evidence that the usual hypothesis of zero mean noise on the observation model is not adequate. It was also observed that observation residue to is indeed zero mean, although it is periodic. This behavior indicates that the model could be further improved.

The absolute resistivity values obtained for the tissues of the human thorax lie inside the range of the expected values. Even the peak-to-peak variation of the lungs resistivities is within the expected range for a volunteer quietly breathing and standing up. As already demonstrated during difference EIT imaging analysis, fast and subtle changes in the dynamic behavior pixels may be of great clinical interest. Pathological conditions like lung collapse, lung hyperdistension or cyclic recruitment have been identified by EIT or CT analysis, using algorithms that compare the dynamic behavior of pixels along the time axis or along the airway pressure axis, see [4] and [25]. Thus, by improving the tracking ability of Kalman filters with human data, absolute images are getting closer to be useful in ICU conditions.

References

[1] M. Cheney, D. Isaacson, and J. C. Newell, "Electrical impedance tomography," *Society for Industrial and Applied Mathematics*, vol. 41, no. 1, pp. 85–101, 1999.

[2] F. C. Trigo, R. G. Lima, and M. B. P. Amato, "Electrical impedance tomography using the extended kalman filter," *IEEE Transactions on Biomedical Engineering*, vol. 51, no. 1, pp. 72–81, 2004.

[3] E. V. C. Leite, S. Gomes, M. A. Beraldo, M. S. Volpe, I. A. Schettino, M. R. Tucci, S. H. Bohm, H. Tanaka, R. G. Lima, C. R. R. Carvalho, and M. B. P. Amato, "Real-time detection of pneumothorax using electrical impedance tomography," *Critical Care Medicine*, vol. 36, pp. 1230–1238, 2008.

[4] E. V. L. Costa, J. B. Borges, A. Melo, F. Suarez-Sipmann, C. Toufen, S. H. Böhm, and M. B. P. Amato, "Bedside estimation of recruitable alveolar collapse and hyperdistension by electrical impedance tomography," *Intensive Care Medicine*, vol. 35, pp. 1132–1137, 2009.

[5] G. Hahn, A. Just, T. Dudykevych, I. Frerichs, J. Hinz, M. Quintel, and G. Hellige, "Imaging pathologic pulmonary air and fluid accumulation by functional and absolute eit," *Physiol Meas.*, vol. 27, no. 5, pp. S187–98, 2006.

[6] M. Vauhkonen, P. A. Karjalainen, and J. P. Kaipio, "A kalman filter aproach to track fast impedance changes in electrical impedance tomography," *IEEE Transactions on Biomedical Engineering*, vol. 45, no. 4, pp. 486–493, 1998.

[7] J. P. Kaipio, P. A. Karjalainen, and E. Somersalo, "State estimation in time-varying electrical impedance tomography," *Annals-New York Academy Of Sciences*, no. 873, pp. 430–439, 1999.

[8] K. Y. Kim, B. S. Kim, M. C. Kim, Y. Lee, and M. Vauhkonen, "Image reconstruction in time-varying electrical impedance tomography based on the extended kalman filter," *Measurement Science and Technology*, no. 12, pp. 1032–1039, 2001.

[9] K. Y. Kim, S. I. Kang, M. C. Kim, S. Kim, Y. Lee, and M. Vauhkonen, "Dynamic imagem reconstruction in electrical impedance tomography with known internal structure," *IEEE Transactions on Magnetics*, vol. 38, no. 2, pp. 1301–1304, 2002.

[10] F. C. Trigo, "Estimação não linear de parâmetros através dos filtros de kalman na tomografia por impedância elétrica," Ph.D. dissertation, Escola Politécnica da Universidade de São Paulo, São Paulo, 2005.

[11] B. S. Kim, M. C. Kim, S. Kim, and K. Y. Kim, "Nonstationary electrical impedance tomography with the interacting multiple model scheme," *Measurement Science and Technology*, vol. 15, pp. 2113–2123, 2004.

[12] S. R. Ibrahim and E. C. Mikulcik, "A time domain modal vibration test technique," *Shock and vibration*, vol. 43, no. 4, pp. 21–37, 1973.

[13] ——, "A method for the direct identification of vibrations parameters from the free response," *Shock and vibration*, vol. 47, no. 4, pp. 183–198, 1977.

[14] F. S. Moura, J. C. C. Aya, A. T. Fleury, and R. G. Lima, "On line transition matrix identification of the state evolution model for the extended kalman filter in electrical impedance tomography," *Journal of Physics: Conference Series*, vol. 124, 2008.

[15] P. Hua, E. J. Woo, J. G. Webster, and W. J. Tompkins, "Finite element modeling of electrode-skin contact impedance in electrical impedance tomography," *IEEE Transactions on Biomedical Engineering*, vol. 40, no. 4, pp. 335–343, 1993.

[16] T. J. Yorkey, J. G. Webster, and W. J. Tompkins, "Comparing reconstruction algorithms for electrical impedance tomography," *IEEE Transactions on Biomedical Engineering*, vol. v. BME-34, no. 11, pp. 843–852, 1987.

[17] M. Vauhkonen, "Electrical impedance tomography and prior information," Ph.D. dissertation, University of Kuopio, Finland, 1997.

[18] D. J. Ewins, *Modal Testing: Theory and Pratice*, 1st ed. New York: Research Studies Press LTD., 1984.

[19] L. S. F. Neto, "Um método para análise modal de estruturas submetidas a excitações ambientes," Master's thesis, Escola Politécnica da Universidade de São Paulo, São Paulo, 2004.

[20] F. S. Moura, J. C. C. Aya, L. A. S. Mirandola, P. C. Nan, R. K. Schweder, and R. G. Lima, "A black-box back projection algorithm for electrical impedance tomography," *International Congress of Mechanical Engineering*, 2005.

[21] D. S. Holder, Ed., *Electrical Impedance Tomography Methods, History And Applications*, 1st ed. London: Institute of Physics Publishing, 2005.

[22] J. Kaipio and E. Somersalo, *Statistical and Computational Inverse Problems*, 1st ed. New York: Springer, 2004.

[23] W. L. Brogan, *Modern Control Theory*, 3rd ed. New Jersey: Prentice Hall, 1991.

[24] S. Gabriel, R. W. Lau, and C. Gabriel, "The dielectric properties of biological tissues: Ii. measurements in the frequency range 10 hz to 20 ghz," *Physics In Medicine And Biology*, vol. 41, pp. 2251–2269, 1996. [Online]. Available: http://niremf.ifac.cnr.it/tissprop/

[25] H. Wrigge, J. Zinserling, T. Muders, D. Varelmann, U. Günther, C. Groeben, A. Magnusson, G. Hedenstierna, and C. Putensen, "Electrical impedance tomography compared with thoracic computed tomography during a slow inflation maneuver in experimental models of lung injury," *Critical care medicine*, vol. 36, no. 3, pp. 903–909, 2008.

ANEXO K – Ruído de processo adaptativo

Adaptive iterated extended Kalman filter for electrical impedance tomography

F C Trigo, R G Lima and A T Fleury
Dept. of Mechanical Eng., Polytechnic School, University of São Paulo, Brazil.

1. Introduction

Several approaches describe the EIT inverse problem in dynamical form using a state-space approach [1–3]. The numerical model is obtained by the Finite Element Method (FEM). Associated to each element of the mesh is an unknown resistivity; the whole set of parameters is the state-vector to be estimated through Kalman filters. In this work, we propose to solve the problem through the iterated extended Kalman filter (IEKF) with the inclusion of adaptive state noise covariance (AIEKF). The rationale behind this idea is that Kalman filter performance can range from fast convergence to instability depending on a proper tunning of the process noise covariance matrix [3,4], so far empirically done. The proposed AIEKF scheme uses estimates from the Kalman filter to self-adjust the state noise covariance matrices in real-time and in a stochastic least-squares sense.

2. Methods

The state-space model for EIT of this work comprises a random walk discrete-time state equation and an observation equation obtained through a 2-D FEM model [3],

$$\boldsymbol{\sigma}_k = I\boldsymbol{\sigma}_{k-1} + \boldsymbol{\omega}_k, \quad \boldsymbol{\omega}_k \sim \mathcal{N}(0, Q_k) \quad \text{and} \tag{1}$$

$$\boldsymbol{z}_k = \mathbb{H}_k(\boldsymbol{\sigma}_{k-1})\boldsymbol{\sigma}_k + \boldsymbol{\nu}_k, \quad \boldsymbol{\nu}_k \sim \mathcal{N}(0, R_k). \tag{2}$$

Matrix $\mathbb{H}_k$ is directly obtained from the linearization of the FEM model around the last estimate [3].

In order to characterize Kalman filter divergence, the statistics of the observation residuals must be evaluated. The predicted observation residual (or innovation) is defined as the difference between the real measured value $\boldsymbol{v}_k$ and the value calculated by the filter using the last available state estimate:

$$\boldsymbol{i}_k = \boldsymbol{v}_k(\boldsymbol{\sigma}_k) - \mathbb{H}_k(\hat{\boldsymbol{\sigma}}_k^{(-)}). \tag{3}$$

When the residuals and their expected two first statistical moments, $\boldsymbol{i}_k = \mathbb{E}[\boldsymbol{i}_k] = 0$ and $\mathbb{C}_{\boldsymbol{i}_k} = \mathbb{E}[\boldsymbol{i}_k \boldsymbol{i}_k^T] = \mathbb{H}_k(\hat{\boldsymbol{\sigma}}_k^{(-)}) P_k^{(-)} \mathbb{H}_k^T(\hat{\boldsymbol{\sigma}}_k^{(-)}) + R_k$ ($\mathbb{C}_{\boldsymbol{i}_k} \triangleq$ innovation covariance matrix) are consistent, there is statistical convergence. Defining a random variable *true innovation* as the innovation that would be obtained from an ideal sensor, i.e.,

$$\boldsymbol{i}_k^{\mathbf{V}} \triangleq \boldsymbol{i}_k - \boldsymbol{\nu}_k \tag{4}$$

and considering equation 2, one has

$$\boldsymbol{i}_k^{\mathbf{V}} = \boldsymbol{v}_k(\boldsymbol{\sigma}_k) - \boldsymbol{z}_k(\hat{\boldsymbol{\sigma}}_k^{(-)}), \tag{5}$$

whose statistics are $\mathbb{E}[i_k^{\mathbf{v}}] = 0$ and $\mathbb{E}[i_k^{\mathbf{v}}(i_k^{\mathbf{v}})^T] = \mathbb{C}_k^{\mathbf{v}}$. The method, described in detail by [5] for real-time satellite orbit tracking, attempts to attain diagonal matrices $Q_{d_k\ 1}$, with diagonal $q_k \geq \mathbf{0}$, so as to maximize the probability of realization of true innovation and, therefore, ensure consistency between observed and expected statistics of the residuals. The core idea is to describe the problem of obtaining $Q_{d_{k-1}}$ as a state-space problem, using q_k as the state-vector and a random-walk model for its dynamics, besides an auxiliary Kalman filter to predict the state. This auxiliary filter runs "inside" the main one, responsible for estimating the state σ_k.

Experimental validation of the model was done using a 235 mm-diameter cylindrical tank with saline and 32 electrodes equally spaced around the container's border. This domain is discretized by the FEM in 240 triangular elements (medium) and 32 four-noded ones (electrodes); the total number of nodes is 201. Bipolar 25 kHz 2 mA_{pp} diametrical current patterns were injected. The AIEKF is used to estimate electrode contact impedances, and to identify the position of a 62 mm-diameter cylindrical glass object according to a two-phase identification procedure [3].

3. Results and Conclusion

We performed 8 identification sequences (phase one - electrode; phase two - medium impedances) with the AIEKF/IEKF and 15 with the EKF. The adaptive noise estimates generated innovations whose statistics were consistent with their expected values. When both methods are compared, as shown in figure 1 by their resulting images after the last estimation sequence, one realizes that object localization and size are better estimated with the proposed method, due to its improved convergence and accuracy.

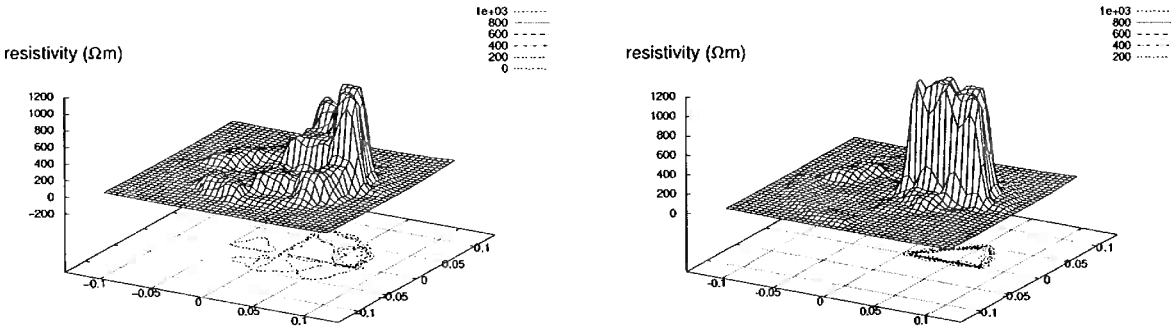

Figure 1. Absolute resistivity distribution: EKF (left); AIEKF/IEKF (right)

References

[1] Vauhkonen M, Karjalainen P A and Kaipio J P 1998 *IEEE Transactions on Biomedical Engineering* **45-4** 486-93.

[2] Kim K Y, Kim B S, Kim M C, Lee Y J and Vauhkonen M 2001 *Measurement Science and Technology* **12** 1032-39.

[3] Trigo F C, González-Lima R and Amato M B P 2004 *IEEE Transactions on Biomedical Engineering* **51-1** 72-81.

[4] Kaipio J P, Karjalainen P A, Somersalo E and Vauhkonen M 1999 *Annals New York Acad. Sci* **873** 430-439.

[5] Rios Neto A and Kuga H K 1985 *Annals of the ELECON'85* (Rio de Janeiro, Brazil)

ANEXO L – Posicionamento ótimo de eletrodos

EngOpt 2008 - International Conference on Engineering Optimization
Rio de Janeiro, Brazil, 01 - 05 June 2008.

On the Design of Electrodes through the Topology Optimization Method applied to Electrical Impedance Tomography

Luis Augusto Motta Mello[1], Raul Gonzalez Lima[2], Marcelo Britto Passos Amato[3] and Emílio Carlos Nelli Silva[1]

1 - Department of Mechatronics and Mechanical Systems Engineering, School of Engineering, University of São Paulo, São Paulo, Brasil, luis.mello@poli.usp.br, ecnsilva@usp.br

2 - Department of Mechanical Engineering, School of Engineering, University of São Paulo, São Paulo, Brasil, lima.raul@gmail.com

3 - Pulmonary Division - Respiratory ICU, Medicine School, University of São Paulo, São Paulo, Brasil, amato@unisys.com.br

1. Abstract

Electrical Impedance Tomography (EIT) images internal objects within a body. Electrodes are attached to the boundary of the body, low intensity alternated currents are applied and the resulting electric potentials are measured. Then, an estimation algorithm obtains the internal admittivity distribution, which corresponds to the image. There are several problems inherent to the admittivity estimation, for instance, high sensitivity to noise and poor conditioning of the sensitivity matrix (which relates changes of conductivity to changes of electric potentials and is utilized in algorithms based on Newton-type techniques). Some authors reported the reduction of the effects of such problems for some configurations of electrodes. In this work, we propose a systematic way to reduce the sensitivity to noise and the poor conditioning by obtaining the optimal position of electrodes and also their shapes based on the Topology optimization Method (TOM). The 2D results showing the obtained electrodes suggest that this method can be applied to design electrodes, considering the optimization of the condition number of the sensitivity matrix as well as the summation of the singular values of that matrix as objective function.

2. Keywords: Electrodes, design, electrical impedance tomography, topology optimization.

3. Introduction

EIT finds the admittivity distribution in a given model of a body which reproduces the boundary measurements of currents and potentials on electrodes attached to that body [1]. The admittivity distribution represents the solution of a non-linear and ill-posed inverse problem. Several combinations of current-carrying electrodes can be chosen and, therefore, many induced electric potential values may be available for the admittivity estimation, which is meant to reduce the solution space.

EIT applications range from medical to industrial (for instance, process tomography [2]). In medical applications, it is applied to detect breast cancer and to monitor lung aeration [1], for instance. In the last case, the main interest of our group, the reconstruction of absolute admittivity values has shown its relevance, since these values allow distinguishing some lung pathologies [1].

The Finite Element Method (FEM) is frequently employed to model the body. It means that electric potentials are obtained through FEM, given the material properties and electric currents. Based on this model, the error function, that is, the square of a vector containing the differences between measured electric potentials and the corresponding computed values is minimized to estimate the admittivities.

Several algorithms have been proposed to solve this non-linear inverse problem for the absolute admittivity values. They are usually based on iterative methods such as Newton-type [3] or gradient-based methods [1], but relatively small perturbations can be recovered utilizing a linear approximation method [4]. Essentially, Newton-type techniques minimize the error function by setting its derivatives with respect to the admittivity distribution equal to zero, and by solving the obtained non-linear system utilizing the Newton-Raphson approach. These techniques give rise to the sensitivity matrix [3], or Jacobian matrix [5], which relates a vector of admittivity changes in pixels and the vector containing the corresponding changes in computed potentials. On the other hand, the linearized error function is iteratively minimized through gradient-based methods.

The sensitivity matrix is rank-deficient in most cases [4]. It can also be ill-conditioned, giving rise to an unstable problem and therefore, a highly biased solution [3]. Generally, regularization methods are employed [3–5], which enforce a stable solution. The Tikhonov method and the truncated generalized

singular value decomposition (TGSVD) [4] are examples of regularization methods, and the first is likely to be the most utilized technique.

In the case of Tikhonov regularization, a regularization term is added to the error function, which comprises a positive regularization parameter multiplied by a smoothing functional. A regularization parameter for both the TGSVD and Tikhonov method controls the trade-off between the ill-conditioning of the regularized matrix and the smoothness of the estimated admittivity distribution. The distribution can be smooth since the smallest singular values of the Jacobian matrix, which generate the high-frequency components of the distribution and therefore, its detailed features, are filtered out by the regularization procedure.

Graham and Adler [6] have reported the dependence of the ill-conditioning of the sensitivity matrix with electrode positions. However, the best placement and geometry of the electrodes is not addressed. Therefore, we utilize a TOM [7] algorithm to optimize the position and shape of the electrodes, in order to reduce the ill-conditioning of the sensitivity matrix. The ill-conditioning is reduced by minimizing the squared difference between the maximum and minimum singular values of the sensitivity matrix. We show that, in the absence of noise, the ill-conditioning is drastically decreased when it is compared to the ill-conditioning of a simulated EIT system with a practical configuration of electrodes.

However, some singular values of the sensitivity matrix can be vulnerable to noise (mainly the smallest ones) [4]. We show that the optimized ill-conditioning can give rise to singular values sensible to particular noise levels. In this case, it is desirable to keep the singular values above a certain level, which depends on the noise variance [4]. Polydorides and McCann [4] obtained an improved resolution and immunity to noise with less electrodes utilizing the segmentation approach. Following this technique, sets of more than one electrode apply electric currents to the body and the potentials are measured as usual (utilizing one electrode). In addition, Dehghani *et al.* [5] have shown that some types of electric current excitation are more robust to noise. However, the optimization of the shape and position of electrodes has not been addressed so far.

Therefore, we also propose to utilize TOM to find the optimum position and shape of the electrodes by maximizing the summation of singular values of the sensitivity matrix maintaining a reasonable value of the regularization parameter, in order to reduce the reconstruction of noise signal in the admittivity distribution. The maximum value of the regularization parameter is verified at the end of the optimization process to avoid ill-conditioning due to the acquisition of high singular values.

We test our results with a numerical phantom, utilizing a Newton-Raphson approach to estimate its properties distribution (a numerical phantom emulates a body, providing "measured" electric potentials). Therefore, the optimized electrodes are employed in the image estimation.

This paper is organized as follows: in Sections 4 and 5, the mathematical model of the body is presented and the method utilized to obtain an EIT image in this work is described. In Section 6, TOM is introduced and the formulation applied to the present problem (the design of electrodes) is discussed. In Section 7, the results are presented and in Section 8 some conclusions are offered.

4. Finite Element Model

Maxwell's equations can describe the electromagnetic fields in the body [2]. Based on these equations and considering the quasi-static approximation for a linear and isotropic medium and a sufficiently small excitation frequency, a conductive medium is assumed (see [2]) and we can obtain using matrix notation:

$$\boldsymbol{K}(\boldsymbol{\sigma})\boldsymbol{V}_j(\boldsymbol{\sigma}) = \boldsymbol{I}_j \tag{1}$$

which, together with Newmann's and Dirichlet's boundary conditions, corresponds to the FEM model of a typical EIT setup (for simplicity, we consider a 2D model). Three nodes triangular finite elements comprise the FEM mesh, $\boldsymbol{\sigma} \in \Re^{nd\times 1}$ is the vector of nodal conductivities (we assume that the conductivity of each finite element depends on nodal values, varying linearly within the element in the same way as the electric potentials [8]) and nd is the number of nodes. The reason why triangular elements are considered is that they allow us to obtain an analytical expression for the gradient of the objective function (defined in Section 6). $\boldsymbol{K}(\boldsymbol{\sigma}) \in \Re^{nd\times nd}$ is the conductivity matrix and $\boldsymbol{I}_j, \in \Re^{nd\times 1}$ and $\boldsymbol{V}_j(\boldsymbol{\sigma}) \in \Re^{nd\times 1}$ are the vectors of nodal electric currents and electric potentials, respectively. The index j indicates different current-carrying electrodes.

5. Estimation of the Conductivities of the Body

As it was mentioned, the EIT inverse problem is often based on the minimization of a square error function for potential values

$$F = \frac{1}{2}(\boldsymbol{V}(\boldsymbol{\sigma}) - \boldsymbol{V}_0)^T(\boldsymbol{V}(\boldsymbol{\sigma}) - \boldsymbol{V}_0), \tag{2}$$

where $\boldsymbol{V}(\boldsymbol{\sigma}) \in \Re^{(ne.np)\times 1}$ contains computed electric potentials on electrodes, ne is the number of different configurations of current-carrying electrodes (that is, the number of current patterns), np is the number of measurements for each current pattern and $\boldsymbol{V}_0 \in \Re^{(ne.np)\times 1}$ contains measurement values.

In this work, the function given by F plus the regularization term [3] is minimized by enforcing its gradient equal to zero and solving the obtained nonlinear system using a Newton-type technique [8]. The usual Levenberg-Marquardt method [3] was chosen (it is similar to the standard Tikhonov solution [4]), which iteratively solves the following linear problem [5]

$$\boldsymbol{\sigma}_{it+1} = \boldsymbol{\sigma}_{it} + (\boldsymbol{J}^T(\boldsymbol{\sigma}_{it})\boldsymbol{J}(\boldsymbol{\sigma}_{it}) + \lambda \boldsymbol{I})^{-1}\boldsymbol{J}^T(\boldsymbol{\sigma}_{it})(\boldsymbol{V}(\boldsymbol{\sigma}_{it}) - \boldsymbol{V}_0), \tag{3}$$

where the subscript it represent an iteration and λ is the positive regularization parameter, which controls the trade-off between the ill-conditioning of the regularized matrix $(\boldsymbol{J}^T\boldsymbol{J} + \lambda \boldsymbol{I}) \in \Re^{nd\times nd}$ and the smoothness of the conductivity distribution. The matrix $\boldsymbol{J} \in \Re^{(ne.np)\times nd}$ is the sensitivity or Jacobian matrix, which can be given by

$$\boldsymbol{J} = \begin{bmatrix} \boldsymbol{T}\frac{\partial \boldsymbol{V}_1}{\partial \sigma_1} & \boldsymbol{T}\frac{\partial \boldsymbol{V}_1}{\partial \sigma_2} & \cdots & \boldsymbol{T}\frac{\partial \boldsymbol{V}_1}{\partial \sigma_{nd}} \\ \boldsymbol{T}\frac{\partial \boldsymbol{V}_2}{\partial \sigma_1} & \boldsymbol{T}\frac{\partial \boldsymbol{V}_2}{\partial \sigma_2} & \cdots & \boldsymbol{T}\frac{\partial \boldsymbol{V}_2}{\partial \sigma_{nd}} \\ \vdots & \vdots & \ddots & \vdots \\ \boldsymbol{T}\frac{\partial \boldsymbol{V}_{ne}}{\partial \sigma_1} & \boldsymbol{T}\frac{\partial \boldsymbol{V}_{ne}}{\partial \sigma_2} & \cdots & \boldsymbol{T}\frac{\partial \boldsymbol{V}_{ne}}{\partial \sigma_{nd}} \end{bmatrix} \tag{4}$$

where the matrix $\boldsymbol{T} \in \Re^{(ne.nc)\times nd}$, given in the next section, selects computed potentials of $\boldsymbol{V}_j$ compared to measurements.

It is relevant to mention that gradient-based algorithms such as Seqüetial Linear Programming (SLP) [1] obtain the conductivity distribution that minimizes the linearized F within a constrained solution space (in order to assure that the linearized function is a good approximation to F), following a iterative process. On the other hand, it can be shown that the the gradient of F is a linear combination of the lines of $\boldsymbol{J}$ (see [1]). Therefore, changing the singular values of $\boldsymbol{J}$ in order the improve the performance of the EIT system does have a positive impact on the gradient and thus, on the performance of gradient-based methods applied to EIT.

The singular value decomposition (SVD) [4] of $\boldsymbol{J}$ yields the equation:

$$\boldsymbol{J} = \boldsymbol{U}\boldsymbol{S}\boldsymbol{V}^T \tag{5}$$

where $\boldsymbol{U} \in \Re^{(ne.nc)\times(ne.nc)}$ and $\boldsymbol{V} \in \Re^{nd\times nd}$ are orthonormal matrices containing the singular vectors of $\boldsymbol{J}$ and $\boldsymbol{S} \in \Re^{(ne.nc)\times nd}$, a diagonal matrix, contains the singular values of $\boldsymbol{J}$. Since $\boldsymbol{U}$ and $\boldsymbol{V}$ are orthonormal matrices, the following can be computed based on Eq.(5) and Eq.(3):

$$\begin{gathered} (\boldsymbol{V}\boldsymbol{S}^T\boldsymbol{U}^T\boldsymbol{U}\boldsymbol{S}\boldsymbol{V}^T + \lambda \boldsymbol{I})(\boldsymbol{\sigma}_{it+1} - \boldsymbol{\sigma}_{it}) = \boldsymbol{V}\boldsymbol{S}^T\boldsymbol{U}^T(\boldsymbol{V} - \boldsymbol{V}_0) \Rightarrow \\ \Rightarrow \boldsymbol{V}^T(\boldsymbol{V}\boldsymbol{S}^T\boldsymbol{S}\boldsymbol{V}^T + \lambda \boldsymbol{I})(\boldsymbol{\sigma}_{it+1} - \boldsymbol{\sigma}_{it}) = \boldsymbol{V}^T\boldsymbol{V}\boldsymbol{S}^T\boldsymbol{U}^T(\boldsymbol{V} - \boldsymbol{V}_0) \Rightarrow \\ \Rightarrow \boldsymbol{\sigma}_{it+1} - \boldsymbol{\sigma}_{it} = \boldsymbol{V}(\boldsymbol{S}^T\boldsymbol{S} + \lambda \boldsymbol{I})^{-1}\boldsymbol{S}^T\boldsymbol{U}^T(\boldsymbol{V} - \boldsymbol{V}_0). \end{gathered} \tag{6}$$

In addition, the last equation of Eq.(6) can be given by

$$\boldsymbol{\sigma}_{it+1} - \boldsymbol{\sigma}_{it} = \sum_{n=1}^{ne.nc} \boldsymbol{E}_n = \sum_{n=1}^{ne.nc} \frac{\nu_n^2}{\nu_n^2 + \lambda}\frac{\boldsymbol{U}_n^T(\boldsymbol{V} - \boldsymbol{V}_0)}{\nu_n}\boldsymbol{V}_n, \tag{7}$$

where $\boldsymbol{E}_n \in \Re^{nd\times 1}$ is a component of the solution, $\boldsymbol{V}_n \in \Re^{nd\times 1}$ is the n-th column of $\boldsymbol{V}$, ν_n is a singular value of $\boldsymbol{J}$ and $\boldsymbol{U}_n \in \Re^{(ne.nc)\times 1}$ is the n-th column of $\boldsymbol{U}$.

This last equation is an alternative way to express the standard Tikhonov solution based on the SVD of $\boldsymbol{J}$. It shows how each component of the solution $(\boldsymbol{E}_n)$ at each iteration can be filtered out when the

regularization parameter is relatively high. In addition, it illustrates why the smallest singular values can be more subjected to noise. Therefore, it motivates our studies.

6. Topology Optimization Method

As it is mentioned in Section 1, we consider TOM [7] to obtain the position and shape of the electrodes: (a) to reduce the ill-conditioning of the sensitivity matrix and (b) to maximize the summation of singular values of the sensitivity matrix. The reason why TOM is utilized is that it can be based on the SLP, which solves a non-linear problem through a sequence of solutions of linearized problems, subjected to constraints. Therefore, some constraints that are necessary to reduce the solution space can be enforced, allowing only possible solutions. In addition, TOM can favor a 0-1 result (void and the material of the electrode, for instance), as it is explained in the current section.

In order to obtain a simple expression for the gradient of the objective function, avoiding to differentiate the SVD problem, we work with the eigenvalues γ_n of $\boldsymbol{J}^T\boldsymbol{J} \in \Re^{nd \times nd}$ instead of the singular values of $\boldsymbol{J}$, which are related by (for $n \leq (ne.nc)$):

$$\gamma_n = \nu_n^2. \tag{8}$$

Therefore, the following function is minimized to reduce the ill-conditioning:

$$F_{min}(\boldsymbol{\sigma}, \boldsymbol{\rho}) = (\gamma_{max} - \gamma_{min})^2 \tag{9}$$

where $\boldsymbol{\rho} \in \Re^{no \times 1}$ is the vector of parameters which determine the electrode shapes and positions and γ_{max} and γ_{min} are the maximum and minimum values of the eigenvalues of $\boldsymbol{J}^T\boldsymbol{J}$, respectively. The minimum value utilized is higher than zero.

On the other hand, we optimize the following function to maximize the summation of singular values:

$$F_{max}(\boldsymbol{\sigma}, \boldsymbol{\rho}) = \sum_{n=1}^{ne.nc} \gamma_n. \tag{10}$$

In order to obtain the optimum shapes and positions, we consider conductive domains connected to the image domain, in which the electrodes can exist. The domains are depicted in Fig.(1). In this case, the problem becomes to find the discontinuous conductivity functions at each domain (the optimization domain), which represents electrodes and void.

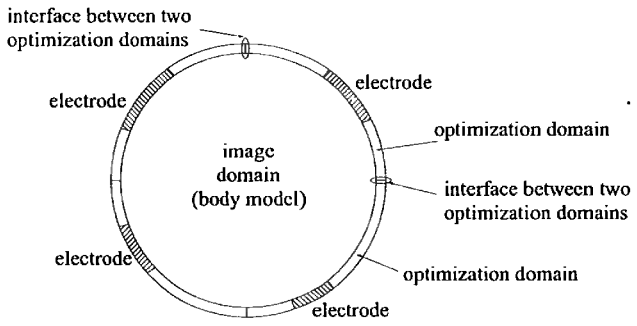

Figure 1: Image and optimization domains. Electrodes are also depicted.

Then, the TOM theory is applied to make this problem tractable (see [7]). Therefore, each domain is divided into finite elements and a material model is defined. In this work, the continuous approximation of material distribution [9] is chosen as the material model, which means that the conductivity of the m-th finite element is given by

$$\sigma_{em} = \rho_{em}^p \sigma_A = +(1 - \rho_{em}^p)\sigma_B \tag{11}$$

and ρ_{em} depends on nodal values, varying linearly within the element in the same way as the electric potentials, that is:

$$\rho_{em} = \boldsymbol{N}_m \boldsymbol{\rho} \tag{12}$$

where $\boldsymbol{N}_m$ is the FEM interpolation matrix [8], which is a linear function of local coordinates. It can be seen that $\boldsymbol{\rho}$ contains the nodal values on which ρ_{em} depends. It implies that $\boldsymbol{\rho}$ is composed of nodal optimization variables.

In Eq.(11), σ_A and σ_B are the electric conductivities of the materials that compose the domains, that is, the conductivity of an electrode and the conductivity of the void (assumed to be slightly higher than zero in order to avoid numerical instabilities), which implies that ρ_{em} is constrained between zero and one. Additionally, the exponent p introduces penalization into the model when it is higher than one. In this case, lower values of conductivities are favored. It is worth noting that if $\boldsymbol{\rho}$ is constrained between $\mathbf{0}$ and $\mathbf{1}$, ρ_{em} will also be constrained between zero and one.

At this point, we need to assure that the correct amount of electric current is applied to the electrodes. Therefore, we consider a technique to prescribe their boundary conditions. The following nodal electric current is imposed to each superficial node of a current-carrying electrode

$$I_c = \frac{I\rho_{es}}{n_T}, \tag{13}$$

where I is the nominal current applied to the electrode, n_T is the number of nodes which correspond to that electrode and ρ_{es} is the optimization variable of a superficial node. This means that the current imposed to each superficial node is equal to zero when ρ_{es} is equal to zero (void) or equal to $\frac{I}{n_T}$ when delta is equal to one. In addition, we consider the following constraint to the minimization problem, applied to each current-carrying electrode:

$$\sum_{k=1}^{n_D} I_{ck} = \sum_{k=1}^{n_D} \frac{I\rho_{esk}}{n_T} = I, \tag{14}$$

where k represents a superficial node of a current-carrying electrode and n_D is the number of superficial nodes of an optimization domain.

Finally, in order to obtain the electric potentials to compare with the measured values in the image estimation, we consider that the potential on an electrode is given by

$$V_c = \sum_{k=1}^{n_D} \frac{V_k \rho_{esk}}{n_T}, \tag{15}$$

where V_k is a nodal potential in a superficial node of a measurement electrode and it is also an element of $\boldsymbol{V}_{ej}$, the extended version of $\boldsymbol{V}_j$ which contains the nodes of the optimization domains. The matrix $\boldsymbol{T}$ in Eq.(4) is given by the coefficients of this last equation, positioned to obtain each value of V_c compared to the measured electric potentials.

Based on all equations proposed in this section, the following optimization problem is defined

$$\begin{array}{ll} \text{optimize} & F_g = F_g(\boldsymbol{\sigma}, \boldsymbol{\rho}) \\ \text{w.r.t. } \boldsymbol{\rho} & \\ & \\ \text{subject to} & \sum_{k=1}^{n_D} I_{ck} = I \\ & \mathbf{0} \leq \boldsymbol{\rho} \leq \mathbf{1} \end{array} \tag{16}$$

where F_g is equal to F_{min} as well as F_{max}, depending on the problem considered and the first constraint (Eq.(14)) is applied to each current-carrying electrode, considering each current pattern.

6.1. Sensitivity Analysis

The gradient of F_g is given by

$$\boldsymbol{grad}(F_g) = \left[\begin{array}{cccc} \frac{\partial F_g}{\partial \gamma}\frac{\partial \gamma}{\partial \rho_1} & \frac{\partial F_g}{\partial \gamma}\frac{\partial \gamma}{\partial \rho_2} & \cdots & \frac{\partial F_g}{\partial \gamma}\frac{\partial \gamma}{\partial \rho_{no}} \end{array} \right]^T \in \Re^{no \times 1}. \tag{17}$$

where

$$\gamma = \begin{bmatrix} \gamma_1 & \gamma_2 & \cdots & \gamma_{(ne.nc)} \end{bmatrix}^T \in \Re^{(ne.nc)\times 1}. \tag{18}$$

The matrix $\frac{\partial F_g}{\partial \gamma} \in \Re^{1\times(ne.nc)}$ is given by

$$\begin{cases} 2(\gamma_{max} - \gamma_{min}) & \text{if} \quad \gamma_n = \gamma_{max} \\ -2(\gamma_{max} - \gamma_{min}) & \text{if} \quad \gamma_n = \gamma_{min} \\ 0 & \text{otherwise} \end{cases} \tag{19}$$

if F_g is equal to F_{min} and by $\mathbf{1} \in \Re^{1\times(ne.nc)}$, otherwise.

In order to obtain $\frac{\partial \gamma}{\partial \rho_l} \in \Re^{(ne.nc)\times 1}$, we set $\boldsymbol{D} = \boldsymbol{J}^T\boldsymbol{J} \in \Re^{nd\times nd}$ and differentiate the following eigenproblem:

$$(\boldsymbol{D} - \gamma_q \boldsymbol{I})\boldsymbol{G}_q = 0, \tag{20}$$

where $\boldsymbol{G}_q \in \Re^{nd\times 1}$ is the qth eigenvector of $\boldsymbol{D}$.

Therefore, by choosing a particular value of $\boldsymbol{G}_q$, $\boldsymbol{G}_{pq}$, which satisfies

$$\boldsymbol{G}_{pq}^T\boldsymbol{G}_{pq} = 1, \tag{21}$$

the following can be obtained:

$$\frac{\partial \gamma_q}{\partial \rho_l} = \boldsymbol{G}_{pq}^T \frac{\partial \boldsymbol{D}}{\partial \rho_l}\boldsymbol{G}_{pq}. \tag{22}$$

The derivative of $\boldsymbol{D}$ is given by

$$\frac{\partial \boldsymbol{D}}{\partial \rho_l} = (\frac{\partial \boldsymbol{J}}{\partial \rho_l})^T\boldsymbol{J} + \boldsymbol{J}^T\frac{\partial \boldsymbol{J}}{\partial \rho_l} \tag{23}$$

where

$$\frac{\partial \boldsymbol{J}}{\partial \rho_l} = \begin{bmatrix} \boldsymbol{T}\frac{\partial^2 \boldsymbol{V}_1}{\partial \sigma_1 \partial \rho_l} + \frac{\partial \boldsymbol{T}}{\partial \rho_l}\frac{\partial \boldsymbol{V}_1}{\partial \sigma_1} & \boldsymbol{T}\frac{\partial^2 \boldsymbol{V}_1}{\partial \sigma_2 \partial \rho_l} + \frac{\partial \boldsymbol{T}}{\partial \rho_l}\frac{\partial \boldsymbol{V}_1}{\partial \sigma_2} & \cdots & \boldsymbol{T}\frac{\partial^2 \boldsymbol{V}_1}{\partial \sigma_{nd} \partial \rho_l} + \frac{\partial \boldsymbol{T}}{\partial \rho_l}\frac{\partial \boldsymbol{V}_1}{\partial \sigma_{nd}} \\ \boldsymbol{T}\frac{\partial^2 \boldsymbol{V}_2}{\partial \sigma_1 \partial \rho_l} + \frac{\partial \boldsymbol{T}}{\partial \rho_l}\frac{\partial \boldsymbol{V}_2}{\partial \sigma_1} & \boldsymbol{T}\frac{\partial^2 \boldsymbol{V}_2}{\partial \sigma_2 \partial \rho_l} + \frac{\partial \boldsymbol{T}}{\partial \rho_l}\frac{\partial \boldsymbol{V}_2}{\partial \sigma_2} & \cdots & \boldsymbol{T}\frac{\partial^2 \boldsymbol{V}_2}{\partial \sigma_{nd} \partial \rho_l} + \frac{\partial \boldsymbol{T}}{\partial \rho_l}\frac{\partial \boldsymbol{V}_2}{\partial \sigma_{nd}} \\ \vdots & \vdots & \ddots & \vdots \\ \boldsymbol{T}\frac{\partial^2 \boldsymbol{V}_{ne}}{\partial \sigma_1 \partial \rho_l} + \frac{\partial \boldsymbol{T}}{\partial \rho_l}\frac{\partial \boldsymbol{V}_{ne}}{\partial \sigma_1} & \boldsymbol{T}\frac{\partial^2 \boldsymbol{V}_{ne}}{\partial \sigma_2 \partial \rho_l} + \frac{\partial \boldsymbol{T}}{\partial \rho_l}\frac{\partial \boldsymbol{V}_{ne}}{\partial \sigma_2} & \cdots & \boldsymbol{T}\frac{\partial^2 \boldsymbol{V}_{ne}}{\partial \sigma_{nd} \partial \rho_l} + \frac{\partial \boldsymbol{T}}{\partial \rho_l}\frac{\partial \boldsymbol{V}_{ne}}{\partial \sigma_{nd}} \end{bmatrix}. \tag{24}$$

Based on the derivative of Eq.(1), one can obtain

$$\frac{\partial \boldsymbol{V}_j}{\partial \sigma_s} = -\boldsymbol{K}^{-1}\frac{\partial \boldsymbol{K}}{\partial \sigma_s}\boldsymbol{V}_j, \tag{25}$$

and

$$\frac{\partial^2 \boldsymbol{V}_j}{\partial \sigma_s \partial \rho_l} = \boldsymbol{K}^{-1}\frac{\partial \boldsymbol{K}}{\partial \sigma_s}\boldsymbol{K}^{-1}\frac{\partial \boldsymbol{K}}{\partial \rho_l}\boldsymbol{V}_j + \boldsymbol{K}^{-1}\frac{\partial \boldsymbol{K}}{\partial \rho_l}\boldsymbol{K}^{-1}\frac{\partial \boldsymbol{K}}{\partial \sigma_s}\boldsymbol{V}_j. \tag{26}$$

The derivative $\frac{\partial \boldsymbol{T}}{\partial \rho_l}$ can be obtained by differentiating Eq.(15). The derivative of the equality constraint in Eq.(14) for each design variable is equal to $\frac{I}{n_T}$ if the corresponding node is a superficial node, and zero otherwise. Finally, $\frac{\partial \boldsymbol{K}}{\partial \rho_l}$ can be found in [1] and $\frac{\partial \boldsymbol{K}}{\partial \rho_l}$ can be obtained in a similar manner.

7. Results and Discussion

In this section we compare the results obtained by the proposed TOM algorithm with a conventional placement of electrodes (see Fig.(2(b))). A particular set up with wide electrodes is chose since this type of electrode is known to reduce the sensitivity of the EIT system to the contact resistivity [10]. The two sets of electrodes are compared qualitatively (through estimated images), as well as quantitatively based on the normalized error:

$$e = \frac{\| \sigma_{exact} - \sigma_{estimated} \|_2}{\| \sigma_{exact} \|_2}. \tag{27}$$

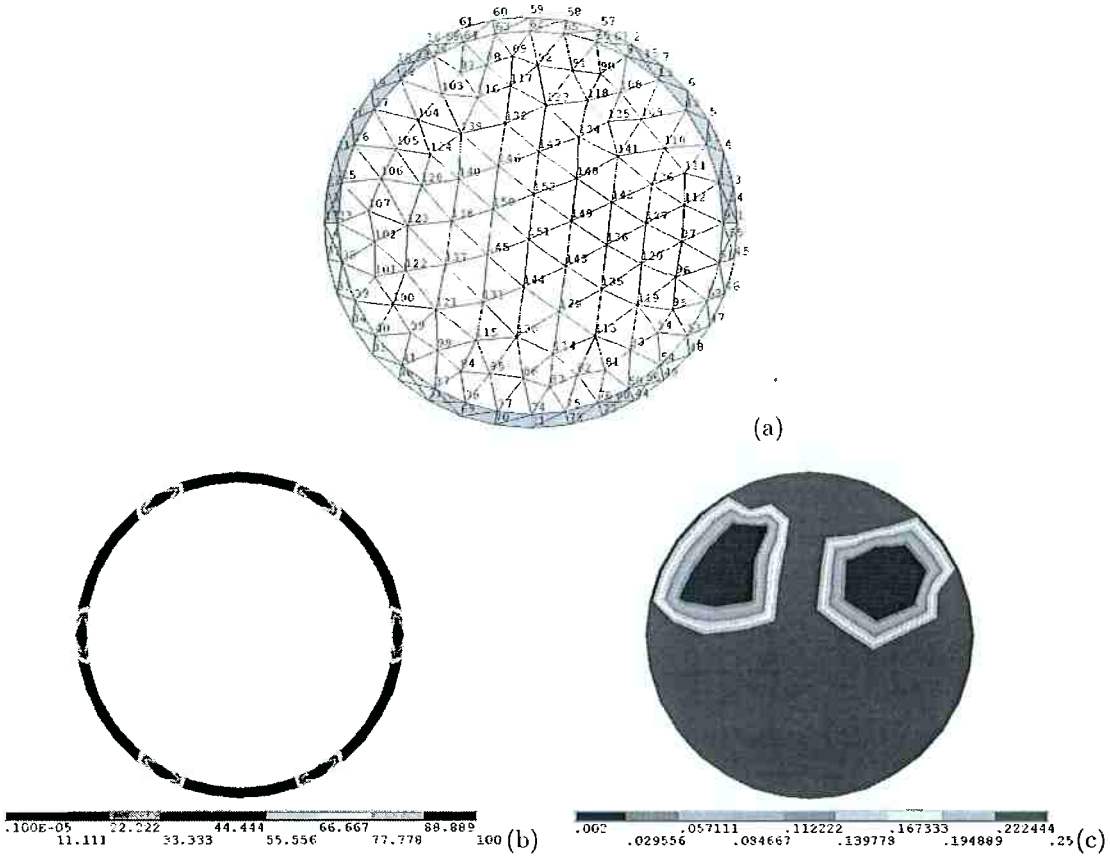

Figure 2: (a) The FEM mesh considered, showing the optimization domains in different colors; (b) conventional placement of electrodes; (c) image to be estimated. (units: $(\Omega m)^{-1}$)

As it can be seen in Fig.(2(a)), only six optimization domains are considered, corresponding to six electrodes. Additionally, one of the six possible measurements for each current pattern are discarded (therefore, np=5) in order to emulate a real case, and the adjacent current pattern is considered (in a real case, all measurements on current-carrying electrodes are usually discarded [10]). Following the adjacent pattern [1], neighbor electrodes are excited with electric currents of the same magnitude and opposite values (ne=6).

The mesh (with 266 elements and 152 nodes) is utilized to obtain the positions and shapes of the electrodes by TOM given the conductivity distribution of the image. It is also employed to generate the measured potentials (numerical phantom) given the optimized electrodes and the image, and to estimate the image based on the measurements and the electrodes. Since the mesh of the numerical phantom is the same mesh utilized to estimate the images, which means that an exact model for the image estimation is considered, the so-called inverse crime is committed in this preliminary study [2]. However, the authors believe that the main features of the results will be kept by more realistic cases, since the optimization of F_{min} and F_{min} will always have a positive impact on the performance of the system (specially in the case of the high changes obtained in the singular values with the proposed methodology).

Fig.(2(a)) also depicts boundary nodes between optimization domains (nodes: 1, 9, 2, 8, 16, 24, 17, 23, 31, 37, 44, 50), which are not included into the optimization to avoid the connection of two electrodes.

The image utilized to obtain the measurements and to optimize the positioning and geometry of the electrodes is the same and it is depicted in Fig.(2(c)) (in practice, the image employed to optimize the electrodes can be a mean image over the time).

The electric currents and the exponent p (in Eq.(11)) are equal to 0.001mA and 1, respectively. The values of σ_A and σ_B are equal to $100(\Omega\text{m})^{-1}$ and $10^{-6}(\Omega\text{m})^{-1}$, respectively. The value of σ_A is utilized for illustrative purposes and can be even higher in practice for copper electrodes, for instance. In all cases, the electric potential in the same node (which models a point electrode) is taken as ground. The convergence criterion for the image estimation is that the modulus of the change of $|| V(\sigma) - V_0 ||_2$ (see Eq.(2)) is less than 10^{-11}. Finally, the initial image utilized in the estimation corresponds to a uniform distribution of $0.25(\Omega\text{m})^{-1}$.

First, the problem given by the objective function F_{min} is solved and the corresponding results are discussed. Then, the images obtained with the optimized electrodes and the conventional electrodes are shown. In the sequence, a similar procedure regarding F_{max} is considered.

7.1. Minimization of F_{min}

The optimized electrodes are shown in Fig.(3). In the same figure, the singular values of the conventional set up and the singular values of the optimized electrodes are depicted, showing that the magnitude of the optimized singular values are closer. The optimal conductivities suggest that the value of p could be increased to favor 0-1 solutions, which is not addressed in this work.

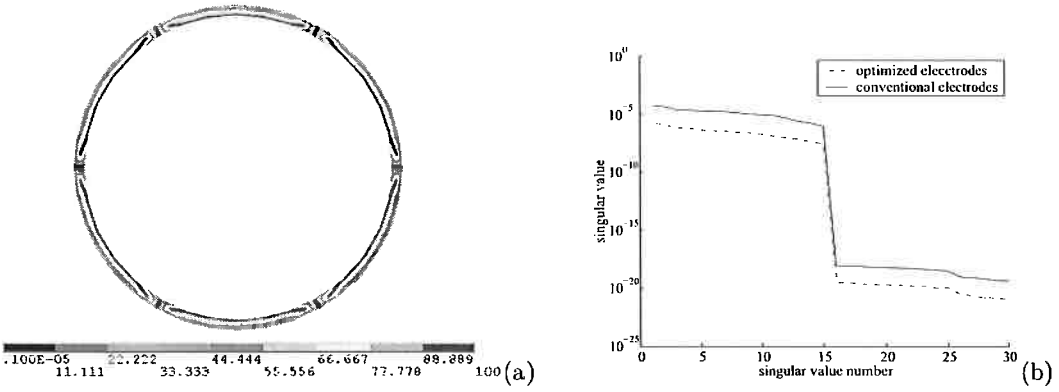

Figure 3: Minimization of F_{min} (γ_{min} in Eq.(9) is the 15th value). (a) Optimized electrodes (units: $(\Omega m)^{-1}$); (b) singular values of $\boldsymbol{J}$.

If the conventional set up is utilized to obtain the images, a stable iterative process can be achieved for $\lambda = 10^{-21}$, and a useful solution for $\lambda = 10^{-12}$, at most. Considering the optimized electrodes on the other hand, a stable solution can be achieved for $\lambda = 10^{-24}$, and a useful solution for $\lambda = 10^{-15}$. For useful solutions, the values of the normalized error e for the conventional and optimized electrodes are equal to 1.029 and 0.744, respectively. The images are shown in Fig.(4). However, for a Gaussian white noise of zero mean and 10^{-4} standard deviation superimposed on the measurements, a useful image could not be obtained (the images are blurred for higher values of λ or absolute conductivity values higher than $100(\Omega m)^{-1}$ are obtained for smaller values of the regularization parameter).

7.2. Maximization of F_{max}

The optimized electrodes and the singular values of both the conventional set up and the optimized electrodes are shown in Fig.(5). In this figure, it can be seen that optimized singular values are significantly different from the values of the conventional set up. It is also seen that a 0-1 solution is obtained.

The images obtained with the conventional set up and the optimized electrodes for $\lambda = 10^{-10}$ are shown in Fig.(6). The noise is similar to the one described in the last subsection. The mean value of

the normalized error e and the standard deviation for the conventional electrodes are equal to 3.908 and 0.502, respectively, considering four estimated images (it is important to mention that the images depicted are the best images obtained within the set of four images). On the other hand, the mean value of e and the corresponding standard deviation for the optimized electrodes are equal to 1.093 and 0.187, respectively. The smaller standard deviation shows that the optimized set up is more robust to noise. In addition, the results suggest that the increase in the singular values was sufficient to reduce the occurrence of image artifacts caused by the noise signals. It is worth noting that the conditioning of the regularized matrix is not an issue for the singular values obtained and the λ considered.

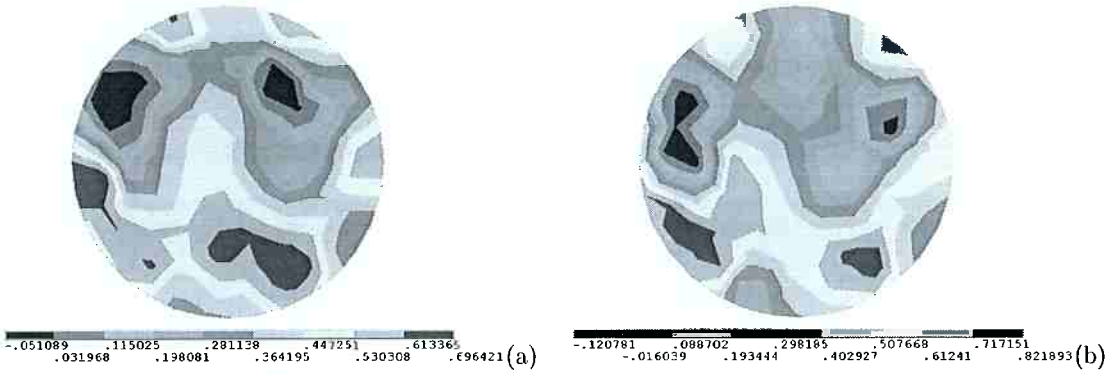

Figure 4: Conductivity images obtained with the conventional electrodes ((a)) and with the optimized electrodes (considering F_{min}) ((b)). (units: $(\Omega m)^{-1}$)

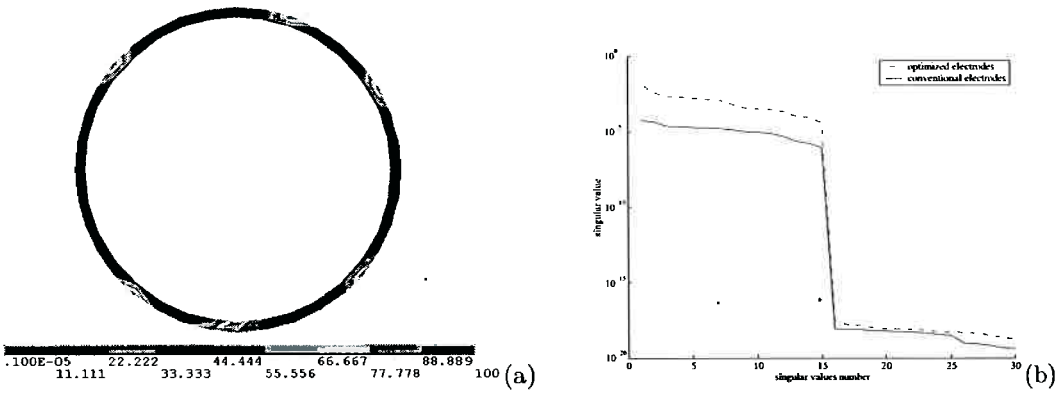

Figure 5: Maximization of $Fmax$. (a) Optimized electrodes (units: $(\Omega m)^{-1}$); (b) singular values of $\boldsymbol{J}$.

Finally, considering six uniformly-placed electrodes of approximately the same size of the optimized electrodes, the mean value of the normalized error e and the standard deviation are equal to 2.394 and 0.497, respectively. This result shows that the size and also the positioning of the electrodes are issues and therefore, need to be optimized.

8. Conclusions

In this work, we propose a methodology for the design of electrodes applied to EIT. An extremely ill-conditioned problem, as well as a high noise level [4] are addressed by considering the methodology, showing that the optimized electrodes achieved a superior performance. It is also shown that the geometry and position of the electrodes can have significant impact on the image estimation.

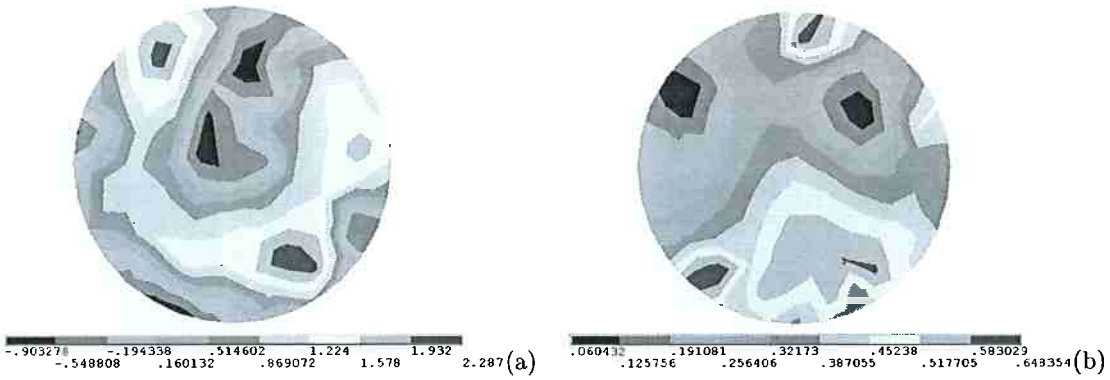

Figure 6: Conductivity images obtained with the conventional electrodes ((a)) and with the optimized electrodes (considering F_{max}) ((b)). (units: $(\Omega m)^{-1}$)

We intend to extend the implemented algorithm in order to minimize the sensitivity of the EIT system to electrode placement errors [6]. We also intend to utilize more finite elements, 3D elements and a model for the contact interface between the electrodes and the body [1] in order to refine the FEM model. We can propose a linear combination between F_{min} and F_{max} as an objective function, in order to reduce the ill-conditioning of the EIT problem and, at the same time, to obtain a configuration of electrodes immune to noise. Finally, we intend to avoid the inverse crime in future tests. These will be matter for future works.

The authors acknowledge the financial support of FAPESP and CNPq.

9. References

[1] L.A.M. Mello *et al.*, Three-Dimensional Electrical Impedance Tomography: A Topology Optimization Approach, *IEEE Transactions on Biomedical Engineering*, 2008, 55(2), 531-540.

[2] Kaipio J and Somersalo E. Statistical and Computational Inverse Problems. *New York: Springer Science+Business Media, Inc.*, 2005

[3] Päivi J V. Image Reconstruction in Three-Dimensional Electrical Impedance Tomography. *Department of Applied Physics, University of Kuopio: Doctoral Dissertation*, 2004.

[4] N. Polydorides and McCann H., Electrode Configurations for Improved Spatial Resolution in Electrical Impedance Tomography, *Meas. Sci. Technol.*, 2002, 13, 1862-1870.

[5] H. Dehghani, *et al.*, Excitation Patterns in Three-Dimensional Electrical Impedance Tomography, *Physiol. Meas.*, 2005, 26, S185-S197.

[6] B.M. Graham and A. Adler, Electrode Placement Configurations for 3D EIT, *Physiol. Meas.*, 2007, 28, S29-S44.

[7] Bendsøe M P and Sigmund O. Topology Optimization: Theory, Methods and Applications. *New York: Springer-Verlag Berlin Heidelberg*, 2003.

[8] Bathe K J. Finite Element Procedures. *New Jersey: Prentice-Hall*, 1996

[9] K. Matsui and K. Terada, Continuous Approximation of Material Distribution for Topology Optimization, *International Journal for Numerical Methods in Engineering*, 2004, 59, 1925-1944.

[10] K.S. Paulson, M.K. Pidcock and C.N. McLeod, A Probe Organ Impedance Measurement, *IEEE Transactions on Biomedical Engineering*, 2004, 51(10), 1838-1844.